NEW METHODS TOWARDS SYNTHESIS AND CONTROLLED FUNCTIONALISATION OF INORGANIC NANOPARTICLES

THESIS SUBMITTED TO THE UNIVERSITY OF PUNE
FOR THE DEGREE OF

DOCTOR OF PHILOSOPHY

IN

CHEMISTRY

BY

S. PRATHAP CHANDRAN

UNDER THE GUIDANCE OF

DR. B. L. V. PRASAD

AND CO-GUIDANCE OF

DR. MURALI SASTRY

PHYSICAL AND MATERIALS CHEMISTRY DIVISION
NATIONAL CHEMICAL LABORATORY
PUNE – 411008, INDIA

JANUARY 2009

NEW METHODS TOWARDS SYNTHESIS AND CONTROLLED FUNCTIONALISATION OF INORGANIC NANOPARTICLES

THESIS SUBMITTED TO THE UNIVERSITY OF PUNE
FOR THE DEGREE OF

DOCTOR OF PHILOSOPHY

IN

CHEMISTRY

BY

S. PRATHAP CHANDRAN

UNDER THE GUIDANCE OF

DR. B. L. V. PRASAD

AND CO-GUIDANCE OF

DR. MURALI SASTRY

PHYSICAL AND MATERIALS CHEMISTRY DIVISION
NATIONAL CHEMICAL LABORATORY
PUNE – 411008, INDIA

JANUARY 2009

CERTIFICATE

This is to certify that the work presented in the thesis entitled **"NEW METHODS TOWARDS SYNTHESIS AND CONTROLLED FUNCTIONALISATION OF INORGANIC NANOPARTICLES"** by **S. Prathap Chandran**, submitted for the degree **Doctor of Philosophy in Chemistry** was carried out under my supervision at the Physical and Materials Chemistry Division of National Chemical Laboratory, Pune. Such material as has been obtained by other sources has been duly acknowledged in this thesis. To the best of my knowledge, the present work or any part thereof has not been submitted to any other University for the award of any other degree or diploma.

Date: Dr. B. L. V. Prasad

Place: Pune (Research Guide)

CERTIFICATE

This is to certify that the work presented in the thesis entitled **"NEW METHODS TOWARDS SYNTHESIS AND CONTROLLED FUNCTIONALISATION OF INORGANIC NANOPARTICLES"** by **S. Prathap Chandran**, submitted for the degree **Doctor of Philosophy in Chemistry** was carried out under my joint supervision at the Physical and Materials Chemistry Division of National Chemical Laboratory, Pune. Such material as has been obtained by other sources has been duly acknowledged in this thesis. To the best of my knowledge, the present work or any part thereof has not been submitted to any other University for the award of any other degree or diploma.

Date: Dr. Murali Sastry

Place: Pune (Research Co-Guide)

DECLARATION

I hereby declare that the thesis entitled "**NEW METHODS TOWARDS SYNTHESIS AND CONTROLLED FUNCTIONALISATION OF INORGANIC NANOPARTICLES**" submitted for the degree Doctor of Philosophy in Chemistry to the University of Pune, has been carried out by me at the Physical and Materials Chemistry Division of National Chemical Laboratory, Pune under the joint supervision of Dr. B. L. V. Prasad and Dr. Murali Sastry. Such material as has been obtained by other sources has been duly acknowledged in this thesis. The work is original and has not been submitted in part or full by me for any other degree or diploma to other University.

Date: S. Prathap Chandran

Place: Pune (Research Student)

Acknowledgements

I like to thank my guides Dr. B. L. V. Prasad and Dr. Murali Sastry to start with. I joined Dr. Sastry and was initiated in to the field of nanoscience by him. I am grateful to him, for it was under his guidance that I learnt key aspects of scientific methodology and writing. I am grateful to Dr. Prasad for being supportive and ever enthusiastic in trying out new ideas and without whose support this thesis would have been a difficult job. It would be an understatement if I say that they have left an indelible impression on my scientific thinking and practice. I am grateful to both for their constant support and guidance.

I like to thank our director, Dr. Sivaram, for giving me an opportunity to work in NCL. CSIR's financial support is gratefully acknowledged. I thank Dr. Sourav Pal, head of the physical and materials chemistry division, for always being supportive. I thank all scientists of the physical and materials chemistry division for being very supportive.

I had an opportunity to work in collaboration with a number of scientists during my stay at NCL. I thank Dr. Srinivas Hotha for his constant guidance. He was ever ready to clear doubts, however trivial they were. Support of Dr. C. V. Ramana, Dr. Sayam Sen Gupta and Dr. Absar Ahmad is gratefully acknowledged. I like to thank Dr. C. S. Gopinath for many fruitful discussions regarding XPS. I also had the opportunity to work with Dr. Guruswamy and thank him for his support and practical guidance. Dr. Suresh Bhat's help with some preliminary DLS experiments is also gratefully acknowledged. I thank Dr. P. A. Joy and Prof. S. K. Kulkarni of Pune University for their constant guidance.

It was a pleasure working with Dr. P. V. Satyam of IOP, Bhuvaneshwar. His support with HRTEM characterisation was important to this thesis work. His student Mr. Umananda was very helpful during my visit to Bhuvaneshwar. I like to thank Dr. Easwaramoorthy, JNCASR and his student Mr. Sai Krishna for helping us with SEM characterisation. Dr. Avadhani helped me out with the all important data analysis software. His help is gratefully acknowledged. I also thank Dr. C. V. Sathyanarayana and Mr. Ramesh for helping me out with TGA analysis. Similar help was extended to me by Dr. George Thomas and his student Mr. Pramod of RRL Trivandrum. I am grateful to them for their timely assistance.

CMC scientists, particularly Dr. (Mrs) Renu Pasricha, Mr. R. S. Gholap and Dr. Patil went out of their way in helping with TEM and XPS measurements. Mr. Gaikwad was always supportive during SEM characterisation. Dr. Pasricha was very kind enough to train me on the TEM.

The support infrastructure at NCL is very good. The efforts of library, DIRC, glass blowing section, administrative section and stores is gratefully acknowledged. Mr. Dipak Jori of physical chemistry office is always there to help with a smile on his face.

The group members of Dr. Hotha were very supportive during my time there. They are Sushil, Sudhir, Ashish, Suresh, Rao and others. Pitamber synthesised the ascorbic acid sample that was tried out by me for shape controlled synthesis. I thank him for this. Sudarshan Tamang was also very supportive during many discussions. He gave me a large stock of organic compounds that he had an opportunity to synthesise during his stay here. I thank him for his support. It was a pleasure collaborating with Kamendra who tried out many of my silica samples in his work. We heavily relied on the fluorescence instrument of Dr. Badigar and he was ever obliging. His support is gratefully acknowledged. I thank Ritwik for help with fluorescence measurements during his time at the Pune University. Malli was ever helpful by sharing his glassware and knowledge with regard to experimental skills.

I thank all my seniors for teaching me instrumental and data analysis techniques that are relevant to nano work. They are Dr. Senthil, Debu, Sumanth, Anita, Saikat, Kannan, Shankar, Ambarish, Hrushi, Akhilesh, Atul, Tanushree, Vipul, Amit and Sourabh. Special thanks to Kannan as the HDA gold nanorods work was conceived by him and his effort during the initial stages is the core of the entire work. He is very supportive and it's a pleasure to know them. I spent a lot of time with Sourabh and our inquisitiveness w.r.t. good cuisine and movies helped kill a lot of time! My present lab mates Vijay, Deepti, Manasi, Sanjay, Priyanka, Maggie, Vilas, Anal, Ravi, Sheetal, Prakash and Vivek have been very supportive. I appreciate the same. They always took me positively. I thank Manasi, Vilas and Ravi for helping me out with XRD measurements. It was a pleasure knowing Prakash and working with him was a good experience. Vijay always impressed with his earnestness. Deepti, Manasi, Vijay and Eashwar helped me out with the thesis corrections. I am grateful to them.

Other NCL guys like Malli, Ramanujam, Khaja, Kannan, Bala, Shankars, Selva, Pradeep, Vijay, Nazrul, Bhuvan, Satish, Suresh, Ramesh helped create a relaxing atmosphere. Eashwar and Subbu were great guys and one can always look up to them. Their clarity of thought always inspired me. Since the time Eshwar's parents moved to Pune, some of us didn't miss home food. I thank them for their support. The hummers group from HCU was always there for encouragement and support. Subbu and Trishul, of IITM, helped me out whenever there was a need.

Ashwin and Talpak, both from my alma matter were very friendly and I enjoyed their company in Pune. I have known Bhaktha and Jaggu for a long time now and they have been very supportive and kind to me.

My loving parents have always been there for me. I hope to bring them joy and happiness and live up to their expectations. My brothers and their families have been very supportive and ever encouraging. Abhi particularly has been a bundle of joy. Fresh from Swami, he would light up your mood at any point of time. I thank Anand for his love. Stay in Pune was made an easy task by my patti and mama. I thank them for their love and support. All this is but Swami's grace. Even as I let him down, he is there to correct me. I am sure to live up to his expectations and make him happy.

Prathap

Table of contents

Chapter 1

Introduction

This chapter provides an introduction to the thesis. Salient features of reported synthetic procedures of anisotropic and core-shell nanoparticles, their characterisation, properties and applications are presented. In addition, important aspects of nanoparticle functionalisation are discussed and the advantages of "click" reactions and silica coatings are presented. Using these discussions as a backdrop, the objective of the thesis work and the chapter-wise organisation of the same is presented.

1.1. Introduction

Whilst they captured the imagination of artisans of yore and were also mentioned to have curative powers in their potable "soluble" form [1], it was not until the year 1857 when Michael Faraday published his work on "divided" gold [2] that a systematic scientific study of nanoparticles actually gained prominence. Following Faraday's footsteps, modern day scientists are occupied in unravelling and understanding the intriguing shape and size dependent properties of colloidal/divided/nanoparticulate metals. The size dependent properties of quantum dots [3], fascinating electronic and mechanical properties of carbon nanotubes [3], catalytic properties of transition and noble metal nanoparticles [1,3], super-paramagnetism [3] and super-hydrophobicity [4] are other examples (fig. 1.1) that have stimulated scientists and common man alike. It is thus not surprising to see innumerable methods devoted to the synthesis of such nanoparticles.

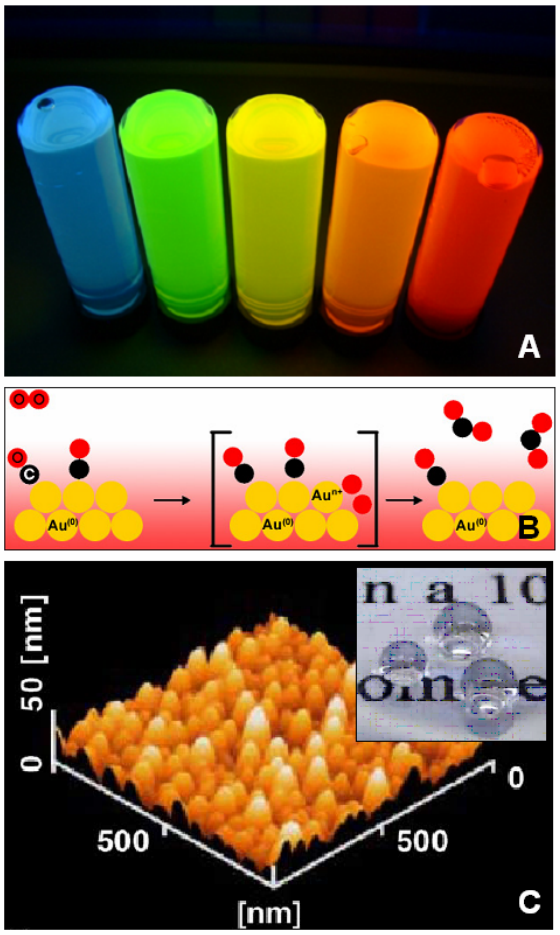

Figure 1.1: *Some interesting properties of nanomaterials: (A) Size dependent luminescence of semi-conductor CdSe quantum dots, (B) Catalytic activity of gold nanoparticles, (C) Superhydrophobicity achieved in PET films due to perfluoro functionalisation on nanoscale features. [Figure courtesy: References 4, 5, 6].*

Since the nanoparticle properties are sensitive to size and shape variation, it is important that synthetic procedures ensure selectivity and uniformity of size thereby enabling best usage of nanosize properties [7]. Wet chemical procedures and sometimes bio-synthetic techniques have been used to achieve the desired property by controlling the size and shape of the nanoparticle as part of the bottom-up approach to nanoparticle synthesis [3e,7]. Apart from synthesis, functionalisation of the nanosized object with a suitable material helps in utilisation of its properties. Functionalisation acts to provide stability, control size, modulate interparticle interactions and direct their assembly. Thus functionalisation is a key aspect that enables application of nanoparticles in different fields [7].

This thesis presents work wherein new methods for the synthesis of noble metal nanoparticles are described. In addition, a method to achieve effective surface functionalisation of inorganic nanoparticles is presented. The following sections of this chapter serve to bring out the salient features concerning synthesis, characterisation, properties and applications of anisotropic noble metal nanoparticles which served as the motivation to carry out the work presented in this thesis. In addition, a discussion on surface functionalisation of nanoparticles is presented.

1.2. Synthesis of anisotropic and core-shell nanoparticles of gold and silver

Noble metal nanoparticles are one of the oldest known and first studied nanomaterials. The surface plasmon resonance absorbance of these materials is an important property that is dependent on the nanoparticle size, shape, composition and refractive index of the surrounding medium. Shape anisotropy in nanoparticles such as nanotriangles, nanorods and hollow nanoparticles enables tunability of surface plasmon resonance more efficiently in comparison to the other factors. In addition to these, a core-shell system which has a varying core and shell composition, allows utilisation of the advantages and suppression of any negative aspect of the materials effectively. Numerous synthetic procedures exist for their synthesis. The following sections present some of these.

Anisotropic nanoparticles

A variety of procedures exist for the synthesis of anisotropic nanoparticles of gold and silver [7c,d]. These methods offer good control over the yield and dimensions of the nanoparticles. Apart from the metal salt and reducing agent, synthetic protocols

usually involve one or more of the following; surfactant, seed particles and reaction temperature (fig. 1.2). Though a variety of parameters decide the shape of the nanoparticle, these would not be discussed in this chapter. These would be taken up as part of appropriate discussions in the relevant chapters. Herein we present some of the popular methods for the synthesis of anisotropic nanostructures.

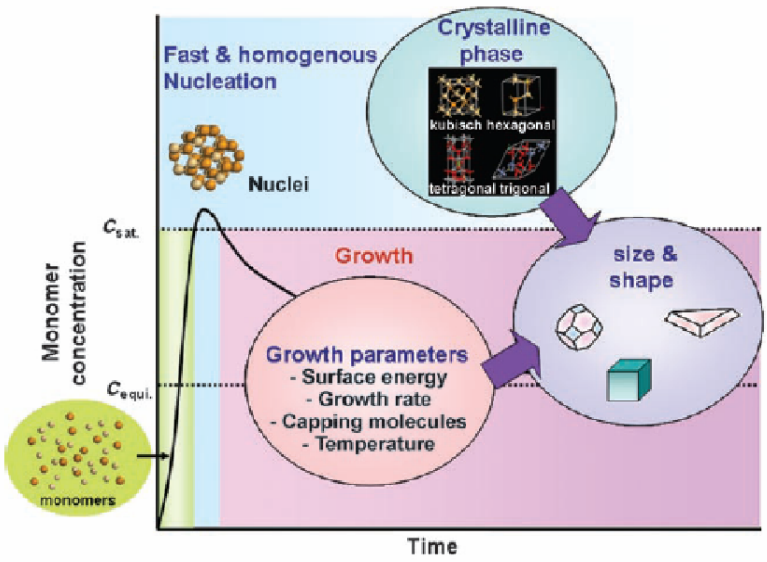

Figure 1.2: *The cartoon above illustrates that crystal growth starts when the growth solution is supersaturated with the monomer. This is referred to as seeding. Further growth of the crystal and its final shape depends on the crystal structure of the system and other growth parameters such as surface energy, growth rate, presence of capping molecules and temperature.* C_{sat} *and* C_{equi} *indicate saturation and equilibrium concentration respectively.[Figure courtesy: Reference 7e].*

Template method

One of the first methods for the synthesis of gold nanorods involved the electro-less deposition of metallic gold in polycarbonate membranes [8]. In this method, the membranes were first sensitised by immersing in a solution of Sn^{2+}. These adsorbed ions acted as sacrificial templates for the deposition of metallic Ag from $AgNO_3$ solution by way of galvanic exchange. Another round of galvanic exchange with Au^{3+} ions now led to the formation of gold islands on the inner walls of the membrane. This was followed by slow reduction of Au^{3+} ions using a mild reducing agent such as formaldehyde. Constrained growth of gold nanorods with the gold islands acting as seeds took place. The polycarbonate membrane itself was dissolved using dichloromethane to yield unsupported gold nanorods. As is characteristic of membrane

based methods, the dimensions of the gold nanorods were tuned by altering the membrane dimensions.

Electrochemical method

Bohmer and co-workers used anodised alumina membranes for the electro-deposition of gold nanorods [9]. They demonstrated tunability of the gold nanorod length from 39 to 730 nm and the width from 12 to 22 nm (fig. 1.3). Consequently, the method offered control over the nanorod optical properties. Here again the membrane was dissolved using NaOH to give stable nanorod dispersions in the presence of poly(vinylpyrrolidone) (PVP). Electrochemical reduction could also be carried out in the solution phase. This was demonstrated by Wang and co-workers wherein cetyltrimethylammoniumbromide (CTAB) and tetraoctylammoniumbromide (TOAB) were used as surfactants [10].

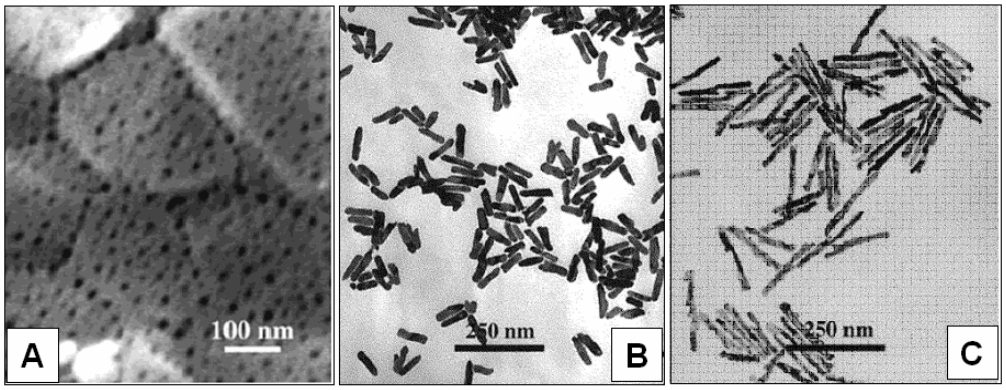

Figure 1.3: *Anodised alumina membranes (A) were used in the synthesis of gold nanorods of varying lengths (B) and (C) by Bohmer and co-workers. [Figure courtesy: Reference 9].*

Seed mediated growth

The seed mediated growth method developed by Catherine Murphy's group is one of the widely used methods for nanorods synthesis. Here, reduction of gold ions in the presence of gold seeds and a surfactant was carried out. The mild reducing agent (ascorbic acid) ensures that fresh nucleation does not occur and so all the gold atoms deposit on the gold seeds. A surfactant, usually CTAB, was used to achieve surface directed growth of the seed particles resulting in formation of nanorods [11]. A Similar procedure for the synthesis of silver nanorods has been demonstrated [12]. The review

on this topic by Murphy and co-workers covers important aspects of controlling nanoparticle synthesis, assembly and optical properties [11].

Other methods, which are essentially modifications of this method for gold nanorod synthesis, have also been conceived. For example, El-Sayed and co-workers achieved better control over yield and aspect ratio of the gold nanorods by adding varying amounts of silver ions to the reaction mixture [13]. In another report, Gil Markovich and co-workers have demonstrated the synthesis of gold nanorods on mica surfaces using a seeded growth procedure [14]. The review by Liz Marzan describes the synthesis, characterisation and applications of gold nanorods comprehensively [15].

Mirkin and co-workers have optimised conditions for the synthesis of high yields of gold nanotriangles [16a] by a modification of the seed mediated procedure developed by Murphy and co-workers [11]. An efficient way to control the edge length of the gold nanotriangles was presented [16b] (fig. 1.4).

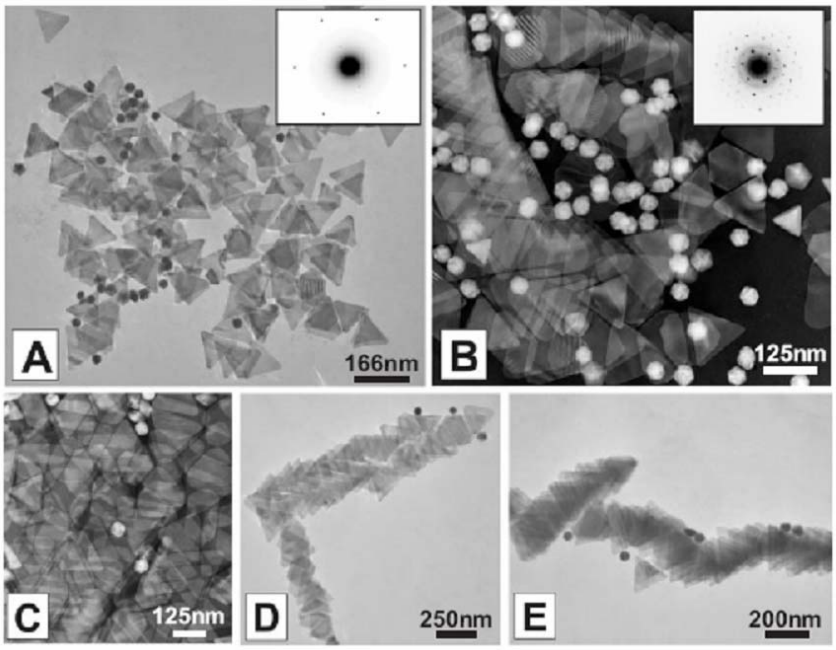

Figure 1.4: *images of gold nanotriangles of varying thickness synthesised by Mirkin and co-workers. The average edge length can be controlled. For instance, figs. (A) to (E) show triangles with average edge lengths of 114, 148, 192, 207 and 220 nm respectively. [Figure courtesy: Reference 16b].*

Polyol synthesis

The polyol method popularised by Xia and co-workers [17] uses the reductive action of poly(ethylene glycol) on silver nitrate to synthesize anisotropic

nanostructures. Here, poly(ethylene glycol) acts even as the solvent medium. PVP added to the reaction mixture was the shape directing agent. By varying the reaction conditions, such as silver nitrate and PVP concentration, different shapes such as nanowires and nanocubes were obtained (fig. 1.5). By using citrate ion as the capping agent in place of PVP, a good yield of silver nanotriangles was obtained [17]. Using a similar method, Peidong Yang and co-workers have synthesised platonic gold nanocrystals such as cubes, tetrahedron and icosahedron [18].

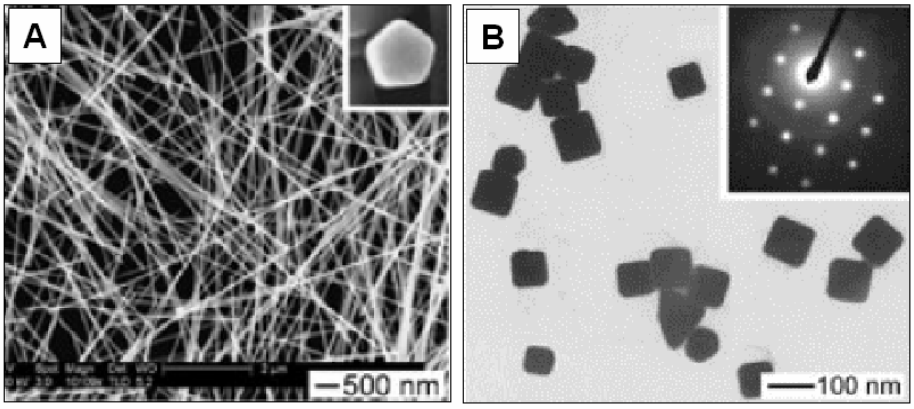

***Figure 1.5**: (A) Silver nanowires obtained by Xia and co-workers using the polyol method. The pentagonal cross-section of a broken nanowire is shown in the inset. (B) Nanocubes obtained by the same method were single crystalline. Inset shows its electron diffraction pattern. [Figure courtesy: Reference 17].*

DMF reduction of gold and silver salts yielded interesting anisotropic nanostructures. It is similar to the polyol method in the sense that DMF serves as both the solvent and reductant [19].

Besides these, a number of methods that use photo thermal [20], sonochemical [21] and microwave [22] sources of energy for the synthesis of anisotropic gold and silver nanoparticles exist. It needs to be noted that the photo thermal conversion of spherical silver nanoparticles to nanoprisms as demonstrated by Mirkin and co-workers was one of the first reports on high yielding synthesis [20] of anisotropic nanoparticles.

Biological methods

In one of the first reports of anisotropic gold nanoparticle synthesis using biological methods, Jose Yacaman and co-workers reported the synthesis of multiply twinned gold nanorods using the extract of the alfalfa (*Medicago sativa*) [23]. Sastry

and co-workers reported the synthesis of gold nanotriangles using the lemon grass plant [*Cymbopogon flexuosus*] extract [24a]. The edge length and hence the optical properties of the gold nanotriangles were tuned by varying the extract amount [24b]. It was further demonstrated that the strong NIR absorbance of the gold nanotriangles could be used for the fabrication of heat absorbing coatings [24b]. Similar reports followed which use *Aloe vera* [24c] and brown sea weed (*Sargassum*) extract [25a] for the synthesis of gold nanotriangles. Recently Gu and co-workers reported the synthesis of gold nanowires using the cell-free extract of *Rhodopseudomonas capsulate* [25b].

Synthesis of gold and silver core-shell nanoparticles

In comparison to anisotropic nanoparticles, the synthesis of core-shell nanoparticles is relatively simple and is based on seeded growth. A few examples are illustrated as follows. Methods that use an external reducing agent for the controlled deposition of the second metal on to seed particle are many. Arnim Henglein and co-workers [26a] demonstrated the synthesis of Ag@Au core-shell and Au@Ag core-shell systems using radiolytic reduction. Similarly, they have also demonstrated the synthesis of a multiple shelled system such as Pd@Au@Ag core-shell-shell [26b] nanoparticle. Zhu and co-workers reported the synthesis of Au@Ag core-shell nanoparticles using an electrochemical method [27].

Mirkin and co-workers have reported an interesting protocol for the synthesis of anisotropic core shell nanoparticles [28]. Physical mixtures of gold and silver nanoparticles when excited at the surface plasmon resonance band of gold nanoparticles resulted in the formation of Au@Ag spherical core-triangular shell nanoparticles. The silver nanoparticles were stated to act as a source of silver atoms that deposit on the surface of the gold cores. The hypothesis that these reactions proceed by way of excitation of the plasmon band of the core was verified as follows: Mixtures of gold nanotriangles (λ_{max} = 1100 nm) and spherical nanoparticles were excited at 550 nm and 1064 nm. Whereas the former did not yield core-shell structures, excitation of the longitudinal plasmon band of the gold nanotriangles led to the formation of Au@Ag triangular core-shell nanoparticles [28].

Sastry and co-workers demonstrated the synthesis of Au@Ag core-shell systems using a reducing agent bound to the surface of the seed particle (fig. 1.6). For example, Tyrosine molecules present on the surface of pre-formed gold nanoparticles were used to reduce silver ions [29a]. The advantage of this method was the

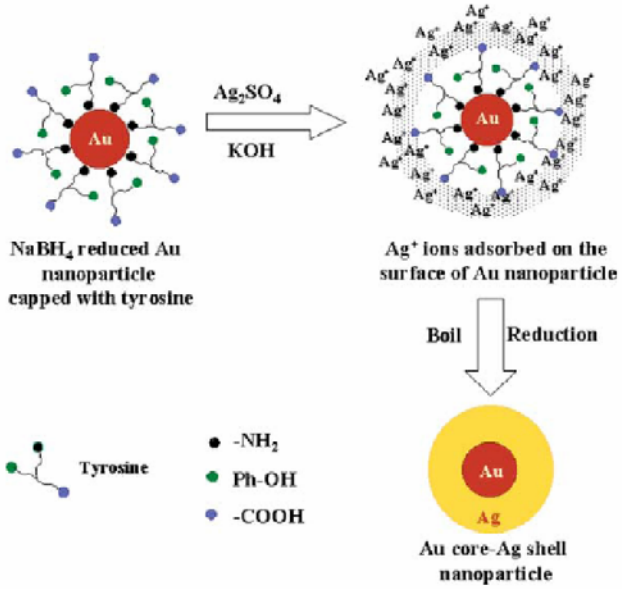

Figure 1.6: *Strategy outlining the synthesis of Au@Ag core-shell nanoparticles using surface bound tyrosine as a reducing agent. [Figure courtesy: Reference 29a].*

minimisation of the external nucleation that is possible when an external reducing agent is used. Similarly phosphotungsticacid (PTA) was used as surface bound reducing agent for the synthesis of Au@Ag core-shell nanoparticles [29b], where UV light was used to switch on or switch off the reductive ability of surface bound PTA.

Lee and co-workers have synthesised Ag@Au core-shell nanoparticles (fig. 1.7) starting from silver seeds in the organic media [30]. The shell was formed by a simple galvanic exchange between the gold ions and the metallic silver seed. This resulted in the formation of a metallic gold coating and release of silver ions. This process of spontaneous reduction of a metal ion with a greater redox potential by another with a lower redox potential is referred to as galvanic exchange [30]. The procedure of galvanic exchange has also led to the development of a wide variety of hollow nanoparticles [31].

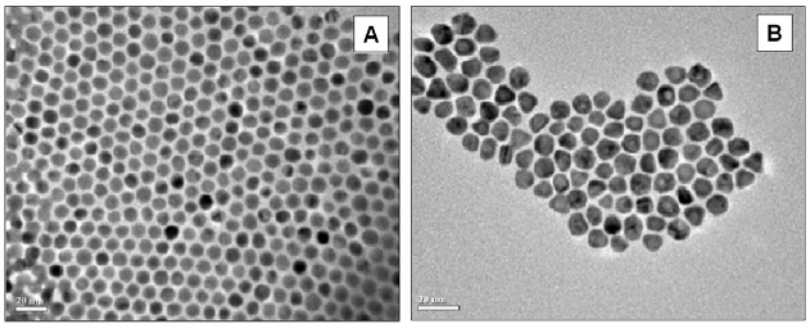

Figure 1.7*: Controlled galvanic exchange between Ag nanoparticles (A) and gold ions results in formation of Ag@Au core-shell nanoparticles (B). Note the lighter contrast of the core in B. [Figure courtesy: Reference 30].*

A combination of seeded growth and galvanic exchange has been used by Liz Marzan and co-workers [32] for the synthesis of multishell Au-Ag bimetallic nanoparticles. They used a mild reducing agent like ascorbic acid that selectively facilitated seeded growth. The resulting particles were highly facetted as shown in fig. 1.8. Despite the presence of a mild reducing agent, it was believed that galvanic exchange occurred when a second layer of gold was deposited on Au@Ag core-shell nanoparticles.

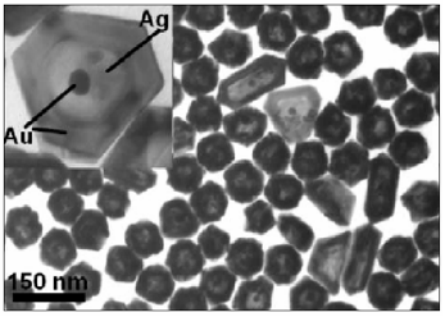

Figure 1.8: *A gold core multishell nanoparticle synthesised by Liz Marzan and co-workers. [Figure courtesy: Reference 32].*

1.3. Properties of anisotropic and core-shell nanoparticles of gold and silver

The most studied and utilised property in terms of applications for noble metal nanoparticles in general and gold and silver anisotropic nanostructures in particularly that of the surface plasmon resonance. Besides these, other properties of gold and silver anisotropic and core-shell nanoparticle are discussed here. It also needs to be noted that purely by virtue of their shape, anisotropic nanoparticles interact differently with cells in comparison to spherical nanoparticles [33].

Surface plasmon resonance

The coherent oscillation of free electrons in response to an oscillating electric field of electromagnetic radiation is called surface plasmon resonance (fig. 1.9) [34].

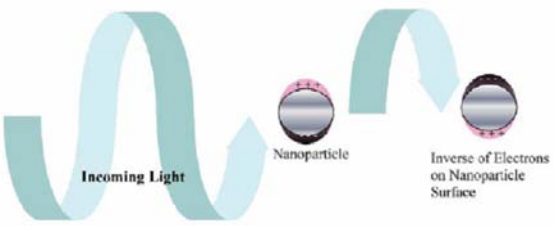

Figure 1.9: *The phenomenon of surface plasmon resonance. [Figure courtesy: Reference 35b].*

Consequently, noble metal nanoparticles absorb intensely in the visible region of the electromagnetic spectrum [35]. The surface plasmon resonance band of spherical nanoparticles of gold and silver occur at 520 and 400 nm respectively [35].

In case of anisotropically shaped nanoparticles of gold and silver such as nanorods and nanotriangles, multiple modes of resonances are observed [35c]. This is due to the fact that polarisation of the free electrons can occur at different length scales in the same nanoparticle. For a nanorod, the polarisation can occur across the rod cross-section and also along its length. These two resonance modes are referred to as the transverse and longitudinal surface plasmon resonance modes. In case of nanotriangles and other flat structures, the polarisation can take place perpendicular to the plane and also along the plane of the particle. These are referred to as the out-of-plane and the in-plane surface plasmon resonance modes. The nanorod longitudinal and triangular in-plane surface plasmon resonance modes occur at longer wavelengths in comparison to the transverse and out-of-plane resonance modes respectively. The position of the

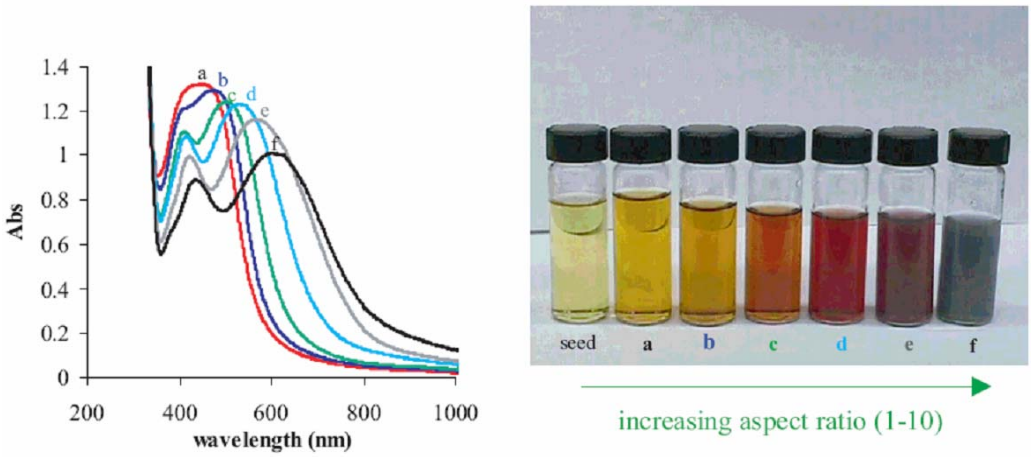

***Figure 1.10**: Murphy and co-workers have demonstrated the tunability of the aspect ratio of silver nanorods using the CTAB assisted seeded growth. Aspect ratio is tuned by varying the amount of spherical silver seeds used. From (a) to (f) the aspect ratio increases. This is illustrated in the UV-visible-NIR spectra and the corresponding photographs of the nanorods. [Figure courtesy: Reference 12].*

longer wavelength absorbance band is sensitively dependent on dimensions of the nanoparticle. Increase in the aspect ratio (length/width) of the nanorods or the edge length of the nanotriangle results in a red shift of the longer wavelength absorbance band [12] (fig. 1.10). The longer wavelength surface plasmon band is several orders of magnitude more intense in comparison to conventional molecular dyes [34]. The above discussion pertains to dipolar surface plasmon modes. In addition to this, higher modes

are also observed. For example, silver [20] and gold nanotriangles [16] exhibit the quadrapolar mode. In general quadrapolar modes are observed in larger sized nanoparticles [19].

As a consequence of the intense absorption of the gold nanorods, it was observed that their fluorescence increased by six orders of magnitude in comparison to bulk gold. This is referred to as the lightning effect in gold nanorods [34]. This emission results from interband to sp transition [34].

Following energy absorption due to surface plasmon resonance, nanoparticles participate in non-radiative relaxation processes [34]. Herein, the energy acquired by the electrons, is lost by way of electron-phonon relaxation and further phonon-phonon relaxation. The former is the result of collision with lattice ions [34]. When nanorods are subjected to laser irradiation, shape transformation to spherical nanoparticles was observed [34]. When the energy of the laser was beyond a threshold, fragmentation of the nanorods to smaller spherical nanoparticles has been observed [34].

In case of core shell nanoparticles, the UV-visible absorbance spectrum exhibits characteristics of both gold and silver due to collective oscillations of electrons [36]. An example of the characteristic UV-visible absorbance of Au@Ag core-shell system is shown in fig. 1.11. It needs to be noted that with increasing silver layer thickness, the spectrum bears greater resemblance to that of pure silver nanoparticles. Similar behaviour was observed in case of Ag@Au core-shell nanoparticles [36].

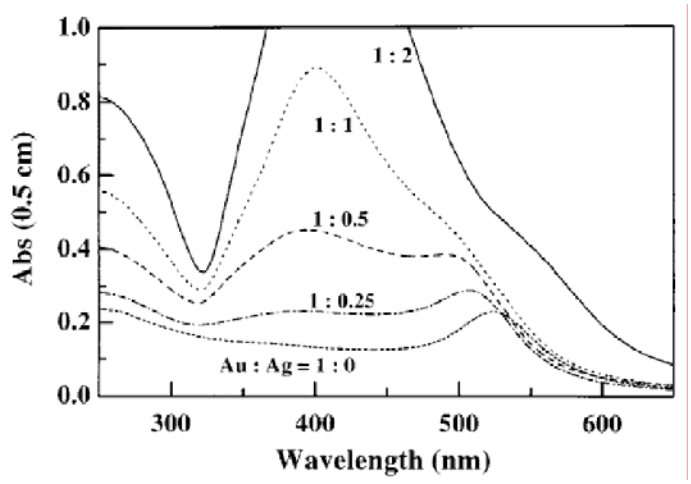

Figure 1.11: *UV-visible profile of Au@Ag core-shell nanoparticles. The nanoparticle spectra acquire greater silver character on increasing silver layer thickness. [Figure courtesy: Reference 36].*

Anisotropic chemical reactivity of gold nanorods

The reasons to the anisotropic chemical reactivity of nanorods can be attributed to both the surface crystal structure of nanorods and the influence of adsorbed molecules. For instance, the surface of gold nanorods is comprised of high energy {110} and {100} faces [15] that coordinate better with ligands [7d] and other metal atoms [37]. This specifically is the reason for the under-potential deposition of silver atoms on the lateral sides of gold nanorods in comparison to the tips that are bound by {111} faces [37]. The higher energy faces also facilitate preferential binding of CTAB molecules [7d]. As a consequence of both these arguments, the tips tend to be more reactive and open to deposition of new metal atoms. This was seen in the deposition of platinum preferentially at the nanorod tips in the presence of silver ions (fig. 1.12) [38]. In a similar context, Herrero and co-workers [39] have used surface sensitive electrochemical reactions for the characterisation of gold nanoparticle surfaces.

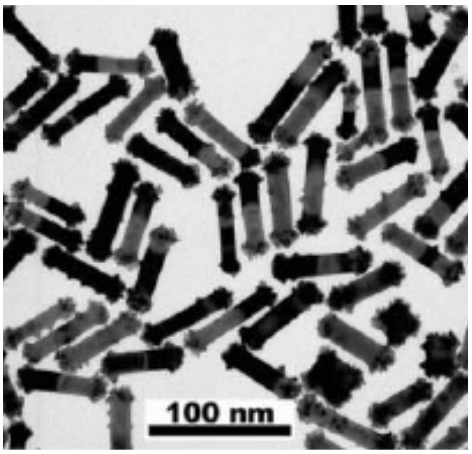

Figure 1.12: *The crystal structure of gold nanorods is the reason behind their anisotropic reactivity. Shown here is the selective deposition of Pt at the nanorod tips. [Figure courtesy: Reference 38].*

The presence of CTAB bilayer on the surface of gold nanorods imparts a positive zeta potential to its surface. This decays more rapidly at the tips. Consequently, species with a positive zeta potential are directed to the tip of a nanorod. This hypothesis is behind the electric field directed mechanism used to explain growth of gold nanorods [40a]. Herein, CTAB-Au(I) micelles, having a positive zeta potential, are directed to the tips facilitating growth of gold nanorods. Similarly anisotropic chemical reactivity has been observed during reactions of gold nanorods with CTAB-Au(III) micelles [40b] leading to the etching of nanorod tips preferentially.

1.4. Characterisation of anisotropic and core-shell gold and silver nanoparticles

In case of gold nanorods which are usually either single crystalline or have a penta-twinned structure, HRTEM and electron diffraction analysis are valuable tools that give crystal structure information of the nanostructures. Rods synthesised by the surfactant assisted seed mediated method have a structure similar to a multiply twinned decahedral nanoparticle stretched along its [110] axis [41]. The nanorod has five crystal variants bound to each other at the [111] twin boundaries. The five lateral sides are bound by [100] faces and the tips are bound by five [111] faces [41]. The twin boundaries can be imaged using HRTEM [41]. Moreover, there are reports of their [200] surface being imaged using HRTEM [42]. Two kinds of electron diffraction patterns are obtained from penta-twinned gold nanorods (fig. 1.13). This was attributed to the two possible orientations a gold nanorod can assume during deposition on a TEM grid [41]. Each of these arises from two different sets of zone axes. The two combinations are <112> and <100> or <110> and <111> zone axes of the gold nanorods [41]. A similar structure has been observed for silver nanowires and nanorods synthesised using the polyol method [17,43].

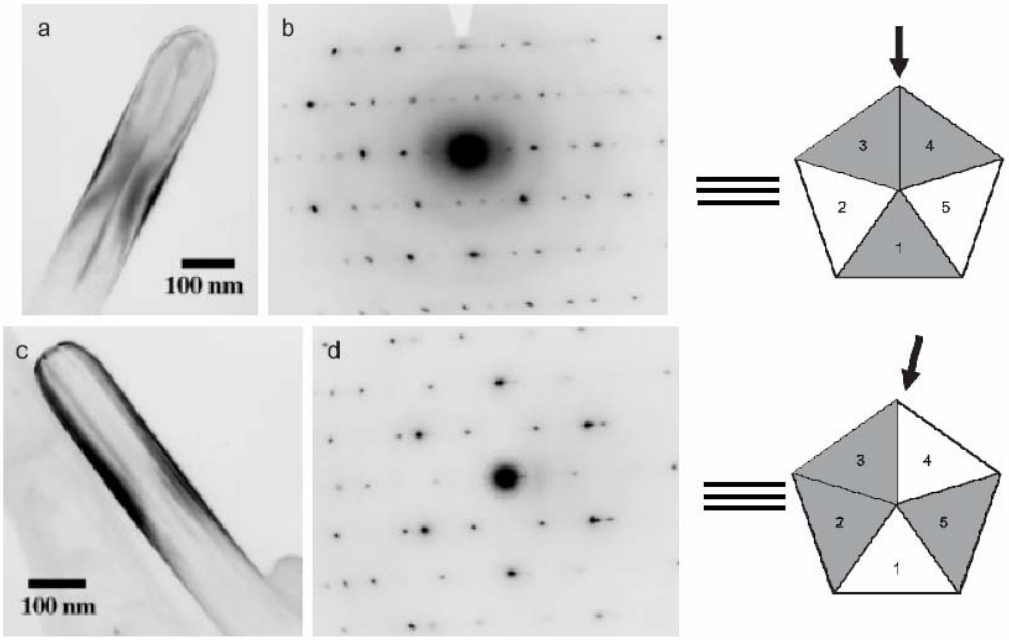

Figure 1.13: *(a) TEM image of a penta-twinned silver nanorod revealing the {111} twin plane as the central dark feature running along the length of the nanorod. The corresponding electron diffraction pattern (b) arises from <112> and <100> zone axes. The corresponding nanorod orientation w.r.t the electron beam is shown to the right of (b). The TEM image (c) and diffraction pattern (d) arising out of the <110> and <111> zone axes are also shown. The corresponding nanorod orientation w.r.t the electron beam is shown to the right of (d). [Figure courtesy: Reference 43].*

The nanorods synthesised by surfactant assisted seeded growth in presence of silver ions [13] were single crystalline with the surface being bound by {110} and {100} faces. In this case growth occurred along the [100] direction. Consequently, these crystalline faces are detected using HRTEM and electron diffraction.

Guyot-Sionnest and co-workers [37] have determined that the crystal structure of the nanorod is dependent on that of the seed particle. In the surfactant assisted seed mediated growth [41], the seed particles are multiply twinned decahedra. Consequently, the nanorods formed have a penta-twinned structure. In case of the silver ion assisted method [13], the seed particles are single crystalline. Hence single crystalline nanorods are formed (fig. 1.14). They have also clearly delineated the function of silver ions during the formation of gold nanorods. It was demonstrated that silver ions participate in under-potential deposition on high energy {110} and {100} faces. Consequently, they act as hard surfactants and restrict growth along certain directions resulting in the formation of gold nanorods [37].

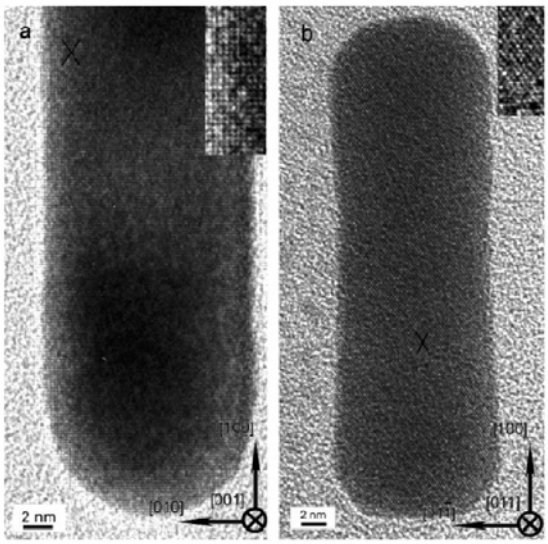

Figure 1.14: *Single crystalline gold nanorods synthesised using the silver ion assisted method are single crystalline. HRTEM images reveal presence of both {100} and {110} surfaces as shown in (a) and (b) respectively. [Figure courtesy: Reference 37].*

Nanotriangles of gold and silver exhibit similar structures [16b,20a,24b,44]. Single crystalline nanotriangles have atomically flat {111} surfaces. Consequently the electron diffraction corresponds to the [111] zone axis. However, an interesting feature in them is the occurrence of the forbidden 1/3{422} spots in the electron diffraction

pattern [16b,20a,24b,44] (fig. 1.15). This has however been ascribed recently to the presence of a HCP phase in the nanotriangles [44b]. This phase is detected in HRTEM and electron diffraction studies of gold and silver nanotriangles as a feature with *d* value of 0.25 nm (fig. 1.15). Moreover, the thickness of the nanotriangles can also be detected using cross sectional viewing [44b,c] (fig. 1.15).

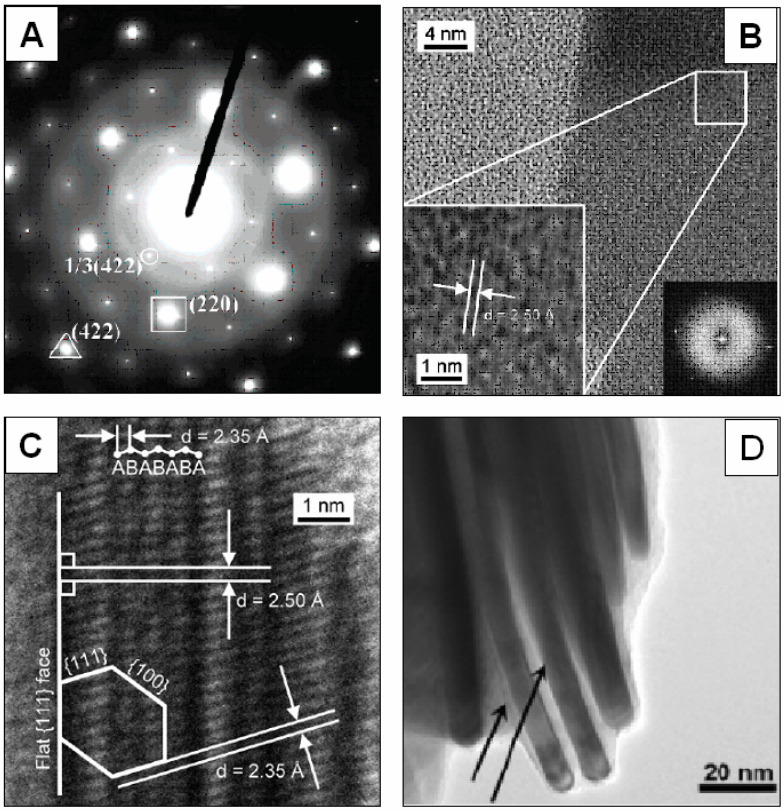

Figure 1.15: *(A) Nanotriangles of silver reveal diffraction pattern corresponding to [111] zone axis of the FCC phase. This is in addition to spots corresponding to the forbidden 1/3{422} Miller planes. (B) HRTEM images also reveal lattice fringes corresponding to 1/3{422} Miller planes with "d" spacing of 0.25 nm. (C) Kelly and co-workers however reveal these forbidden features to be due to a HCP phase with "d" spacing of 0.25 nm. Cross section TEM analysis can also be used for determination of the thickness of silver nanotriangles as shown in (D). [Figure courtesy: Reference 44].*

XRD analysis has also been used to analyse the anisotropic nanostructures. For example, due to the [111] oriented growth, ratio of {111} Bragg reflection's intensity to other reflections would be significantly higher for nanotriangles and other flat nanostructures [45] of gold and silver in comparison to their respective bulk phases.

Characterisation of core-shell noble metal nanoparticles can be performed using a variety of techniques such as UV-visible spectroscopy, HRTEM and XPS. For the gold-silver system, UV-visible analysis provides valuable information as has already been outlined. Only in terms of differing contrast of the core and shell can HRTEM and TEM be useful in characterising gold silver core shell nanoparticle systems. This is due to the fact that the lattice parameters of gold and silver do not vary significantly. Consequently no distinction can be made out in their "d" spacings. The same reasoning makes XRD characterisation redundant. However, information regarding the increase in size can be obtained from TEM and HRTEM images. XPS elemental surface characterisation is very useful in studying layered materials and nanoparticles [46]. These techniques have been used for characterisation of the Au@Ag core-shell nanoparticles synthesised in the organic media (chapter 3).

1.5. Applications of anisotropic and core-shell nanoparticles of gold and silver

It needs to be noted that most applications of anisotropic noble metal nanoparticles have their basis on the phenomenon of surface plasmon resonance. The sensitivity of surface plasmon resonance absorbance to factors such as interparticle distance and refractive index of the surroundings has found interesting applications. The following section presents illustrative examples of the applications of anisotropic and core-shell nanoparticles of gold and silver.

Spectroscopy and plasmonics

Raman cross-sections are extremely small as a result of which low intensity signals are obtained. Nanostructures have been observed to provide up to 10^6 to 10^7 times enhancement in the intensity of the Raman signal. This effect is referred to as the Surface Enhanced Raman scattering (SERS) [47]. Two mechanisms namely chemical and electromagnetic enhancements are known to operate [35b]. Chemical enhancement is specific to a given molecule and it's binding to the nanoparticle surface. Electronic effects that are similar to resonance Raman scattering are believed to operate here. In the electromagnetic enhancement mechanism, the intense electromagnetic fields in places such as nanoparticle junctions, as in aggregates, tips of nanorods and nanotriangles, enhances the electric field of incoming light and also amplifies outgoing radiation. This is due to surface plasmon resonance. Consequently signal enhancement is observed [35b]. For example, at gold nanotriangle tips, the electric field intensity is

enhanced by 500 times due to field effects [48]. In an interesting report, Nie et al obtained enhancement by 10^{14} to 10^{15} times for the dye R6G (rhodamine 6G) during single molecule measurements on silver substrates [49].

Core-shell and alloy nanoparticles of gold and silver also find interesting applications in SERS [50a]. For example, Loo and Furtak show that by coating gold electrodes with a monolayer of silver, SERS enhancement was obtained using a 514.5 nm excitation. At this wavelength, gold does not provide any SERS effect. Thus we see that the silver provides the SERS enhancement [50b]. In a similar report, Mirkin and co-workers obtain no Raman signals from oligonucleotides bound to the surface of gold nanoparticles. However, after deposition of silver nanoparticles on the gold-oligonucleotide conjugate, Raman signals were obtained [50c]. Such a particle combines the surface chemistry of gold and the SERS enhancement provided by silver.

The enhancement of molecular fluorescence due to coupling of fluorescence and surface plasmons is referred to as metal enhanced fluorescence (MEF) [35b,51]. This is observed when a fluorophore molecule is situated 10 nm or beyond from the nanoparticle surface. The enhancement in these cases is as much as 100 fold [35b]. However when the molecule is closer to the metal surface, electronic interaction leads to the donation of excited electrons to the metal. This is a non-radiative decay process and leads to quenching of the nanoparticle fluorescence [35b]. To avoid quenching and obtain fluorescence, various methodologies are adopted including using a spacer molecule or having a thin silica shell around the metal nanoparticle (fig. 1.16) [35b,52].

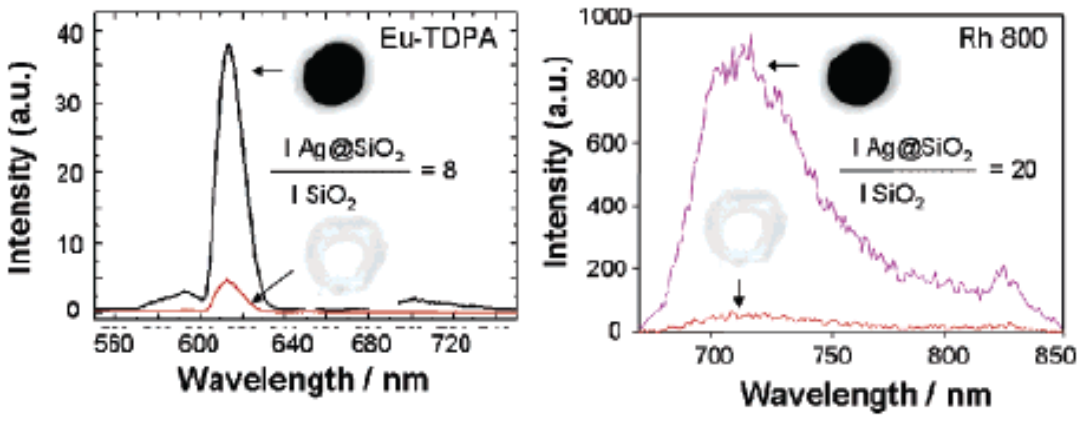

Figure 1.16: *Enhancement of fluorescence signal from dyes (Eu-TDPA and Rh 800) doped on $Ag@SiO_2$ nanoparticles. Note the enhancement factors w.r.t control samples having no silver core. [Figure courtesy: Reference 52].*

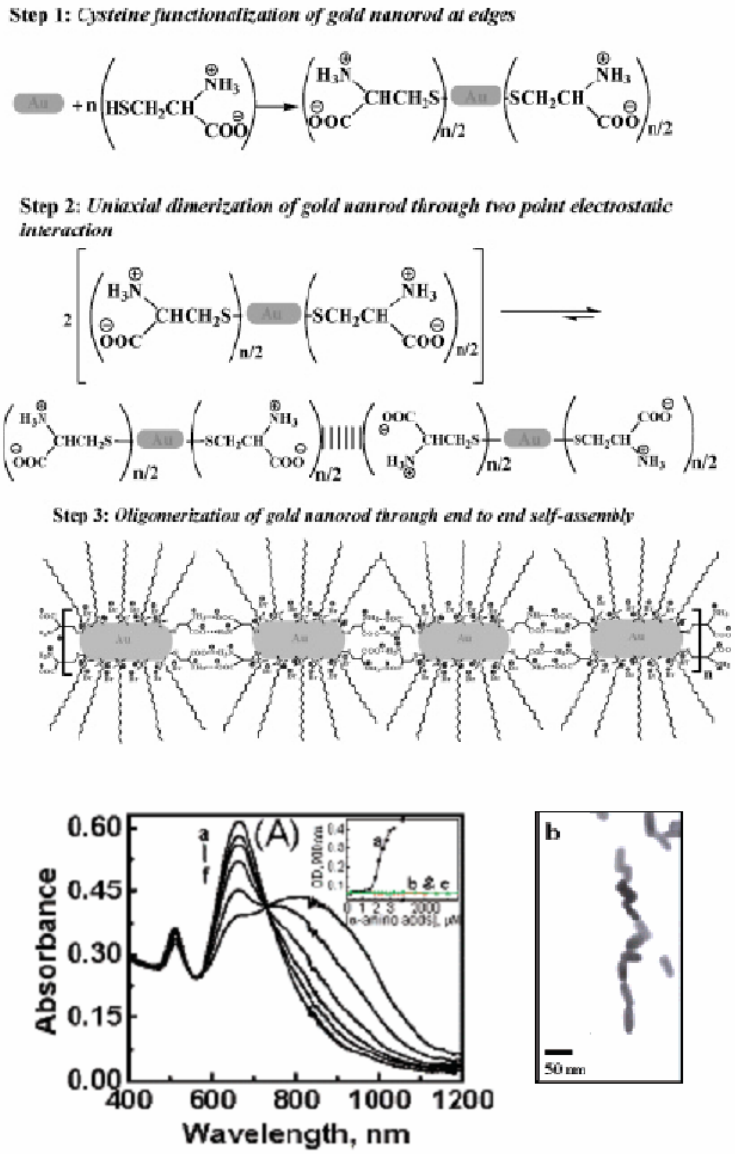

Figure 1.17: *Detection of cysteine using gold nanorods. The uni-axial binding promotes UV-visible-NIR spectral changes. TEM image of end to end assembled rods is also shown. [Figure courtesy: Reference 53].*

The preferential reactivity of gold nanorods to thiol containing molecules has been elegantly used by George Thomas and co-workers to sense thiol containing amino acids; cysteine and glutathione [53]. Hydrogen bonding interactions between amino acids bound to different rods enables tip to tip orientation of the rods (fig. 1.17). The evolution of the gold nanorod UV-visible-NIR absorbance profile accompanying such a process, even at low concentrations of such amino acids, was used to signal and hence detect their presence. Interestingly this detection of cysteine and glutathione can be carried out even in the presence of other amino acids without any interference. The

selective binding of thiol bearing molecules to the tips is due to the presence of a CTAB bilayer on the lateral sides of gold nanorods. Similarly, the nanorod tip reactivity was used to detect ultra low levels of mercury (6.6×10^{-13} gL^{-1}) in water [54]. Herein, mercury forms amalgams with gold at the exposed nanorod tips leading to modification of the longitudinal surface plasmon resonance absorbance of the nanorods.

The absorbance of light by anisotropic nanorods to convert the same in to surface plasmons and the re-conversion of surface plasmon to light radiation by nanostructures has facilitated the fabrication of nano-optical devices [55]. A large number of metallic nanostructures have been used for the construction of waveguides and other optoelectronic devices [55].

Nanobiotechnology

Interesting applications in the field of nanobiotechnology have been demonstrated using anisotropic nanostructures. These applications can be categorised as follows; drug/gene delivery, therapeutics and contrast agents. In the following discussion, two representative examples to this effect are presented:

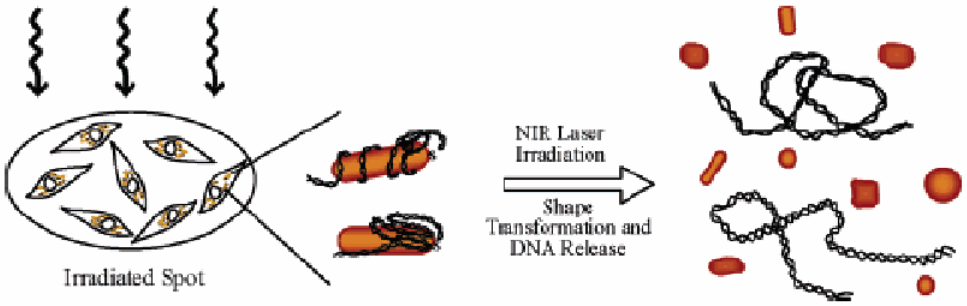

Figure 1.18: *A DNA gold nanorod conjugate has been used for remote control of localised gene expression using NIR laser irradiation. [Figure courtesy: Reference 56].*

Wu and co-workers coated gold nanorods with the gene of enhanced green fluorescence protein (EGFP) through an Au-S linkage (fig. 1.18) [56]. These conjugates were then delivered to cultured HeLa cells. Upon delivery, NIR laser irradiation was used to transform the shape of the gold nanorods to spherical particles. This is accompanied by release of the gene which then expresses itself. This induced expression was found only in cells that were irradiated with the NIR laser. In this case,

we see that the shape transformation property of gold nanorods was used for localised gene delivery.

The property of nanoparticles to undergo non-radiative relaxation following surface plasmon absorbance has been used to envisage cancer hyperthermia applications. It was mentioned that by tuning the dimensions of the anisotropic nanoparticles of gold and silver such as nanorods and nanotriangles, it is possible to push their absorbance to the NIR region of the electromagnetic spectrum. Hyperthermia is based on the fact that such anisotropic nanostructures can absorb intensely in the NIR region, where absorbance by tissues is minimal (650 – 1300 nm). The absorbed energy is released as heat to cause localised cell death. For instance, El-Sayed and co-workers [57] demonstrated that gold nanorods conjugated to anti-epidermal growth factor receptor (anti-EGFR) monoclonal antibodies bind with greater affinity to malignant cells due to the over expression of EGFR in malignant cells. Once bound to the malignant cells, irradiation of gold nanorods (continuous laser 800 nm) enabled heat transfer to the malignant cell and causes their death. Moreover the strong scattering of red light by the gold nanorods was used to image malignant cells and differentiate them from non-malignant cells [57].

1.6. Surface functionalisation of nanoparticles: Interaction of functionalisation agents with nanoparticle surface

The use of nanomaterials in diverse fields as described above is essentially dependent on their surface functionalisation. A key aspect to this functionalisation is the type of interaction that the capping agent has with the nanoparticle surface [58]. Consequently the adaptability of the functionalised particle to different conditions is decided. These interactions belong to one of the following categories; covalent bonding, electrostatic assembly or weaker interactions such as the van der Waal's and dipolar. In addition to interacting with the bare nanoparticle surface, the first round of capping molecules participate in a variety of interactions aiding in further functionalisation and applications.

Covalent linkage

A variety of nanoparticle surface functionalisation procedures rely on covalent bond formation between the surface of the nanoparticle and ligand functional group. An important example is the case of Au-S bond. A variety of sulphur bearing compounds

such as alkanethiols, dialkanethiols, dialkanedithols form self assembled monolayers (SAMs) on gold surfaces and have been thoroughly investigated [59]. Thiol bearing amino acids [60], supramolecules with the thiol functionality [61] and ω-functionalised alkanethiols [59,61] are widely used to impart functionality to gold nanoparticle based nanostructures. Formation of the siloxane bond between silane bearing ligands, such as alkoxysilanes and chlorosilanes, and surfaces bearing a hydroxyl group also come under the category of covalent functionalisation. Stober silica, quartz, glass, aluminium oxide and mica are some of the surfaces functionalised through the Si-O-Si siloxane bond [59].

Electrostatic binding

Electrostatic assembly has been used for the construction of layer by layer assemblies (fig. 1.19) [62], immobilisation of biomolecules [58] and synthesis of monolayer protected clusters of nanoparticles [63] in various solvent media. It needs to be noted that electrostatic interactions are susceptible to changes of pH or ionic strength [64] and may affect the stability of the nanoparticle.

One of the initial reports of electrostatic force driven functionalisation of nanoparticles was that of layer by layer assembly of charged polyelectrolytes on polystyrene spheres [62a]. Following this a variety of reports with such a type of interaction as basis for functionalisation have appeared [62c,64,65].

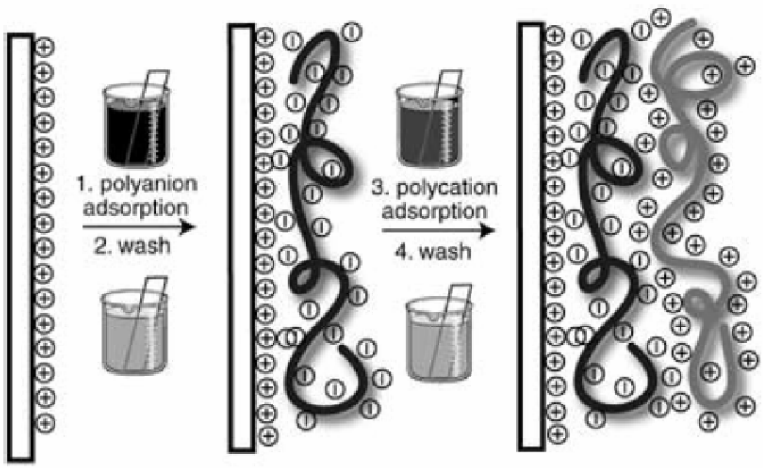

Figure 1.19: *A cartoon illustrating layer by layer assembly of oppositely charged polyelectrolytes. Such functionalisation is possible in aqueous media, and the material stability is susceptible to fluctuations in the ionic strength. [Figure courtesy: Reference 62c].*

It is worth noting that in such procedures, covalent cross linking is finally used to increase the stability of capping [64,66]. A typical feature of electrostatically driven layer by layer functionalisation procedure is that they are performed in aqueous solvents due to the involvement of polyelectrolytes [62c,64,65]. Consequently they are limited in their application as compared to covalent functionalisation procedures that can be carried out in a range of solvents.

Electrostatic interactions also aid phase transfer of nanoparticles to organic media using primary amines [63]. The protonated amine group of the amphiphile interacts with the negatively charged nanoparticle surface in such a procedure. Similar interactions come to play during the capping of gold nanoparticles with amino acids that do not bear a thiol group like tyrosine [29a] and tryptophan [67b].

In the above two instances, the interaction of the charged capping agent is not with the bare nanoparticle surface as the nanoparticle is usually stabilised by the presence of ions which impart charge to the surface. Interaction of alkyl carboxylates with alumina or silver oxide surfaces and that of phosphonate with transition metal surfaces however, belong to cases where a direct electrostatic interaction with the nanoparticle surface is reported to take place [59].

Other interactions

Apart from covalent and electrostatic interactions, a variety of weak non-specific interactions such as van der Waal's [59], dipolar [68] and π-π interactions bind molecules to nanoparticle surfaces and provide stability. Binding of oligonucleotides to gold surfaces [68] and interaction of polyethylene glycol with nanoparticle surfaces [69] are instances of the same. It is seen in such cases that van der Waal's and dipolar forces come in to play.

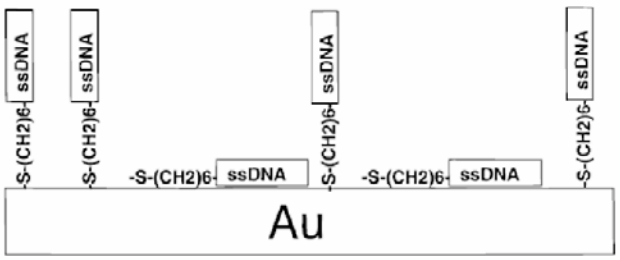

Figure 1.20: *Binding of thiolated oligonucleotides involve non-covalent dipolar interactions apart from the covalent Au-S bond. [Figure courtesy: Reference 68a].*

The following three illustrations demonstrate that in functional nanoparticle systems two or more of the above mentioned interactions that are working in tandem, exist between the ligand and the nanoparticle surface [58]. This is particularly so if the capping agent is as complex as a protein or DNA. For example investigations on interaction between thiolated oligonucleotides and gold nanoparticle surface reveal that apart from the Au-S covalent bond, secondary interactions, between the gold surface and the phosphate (back bone) [68b,c] or amine (exposed bases) [68b] groups exist. Indeed dipolar and induced dipolar interactions are involved in the adsorption of oligonucleotides, that do not bear any thiol functionality, to gold thin film (fig. 1.20) [68a] and gold nanoparticle surfaces [68b,c].

Recently Schubert and Hoeppener [70] demonstrated functionalisation of silicon surfaces with terpyridine ligands through click chemistry. The switchable nature of the coordination complexes that these ligands form with transition metals such as Fe(II) and Zn(II) on the silicon surface is demonstrated. Such a system involving covalent and coordinate covalent interactions has been predicted to have important consequences in sensor technology [70].

In general, due to the robust nature of covalent bonds [71] they have been preferred over non-specific electrostatic interaction driven adsorption protocols [72]. However, in certain cases weak non-covalent interactions that do not alter the electronic structure of the material are preferred. For example, due to the change in electronic properties of carbon nanotubes [73] accompanying covalent functionalisation, van der Waal's forces [73], chemical adsorption [73,74] and other non-covalent forces, such as π-π stacking of aromatic groups [75], are preferred.

Covalent functionalisation protocols are counterproductive in certain cases. This is particularly true during bioconjugation where site-specific functionalisation is critical. For instance the amide bond formation or reductive amination, the most widely used covalent bond formation procedures in nanoparticle bioconjugation processes, are very random in nature [76]. Hence they lack the required specificity. It has been observed that the probability of Cytochrome c bound to gold nanoparticles undergoing denaturation was more when bound covalently than the electrostatically bound cases [58]. Indeed supramolecular interactions such as those between biotin and avidin are preferred for bioconjugation of nanoparticles. It is also encouraging to know that biotin incorporated surface ligands are easily accessible [58].

Another important aspect during functionalisation is the control over the density of surface groups. Controlling the stoichiometry of surface ligands during bond formation processes in solution phase, however, does not yield precise and reproducible control over the ligand surface density [77,78]. This is probably due to the fact that not many covalent bond formations proceed quantitatively and reproducibly. A classic example in this regard is the irreproducible results obtained during silane functionalisation procedures under identical conditions [78]. They are also affected by the occurrence of a variety of side reactions.

Exact control over the number of functional groups on nanoparticle surface would allow their use as building blocks in nanoarchitectures; analogous to molecular building blocks [77]. Precise control over the surface density of nanosized gold particles has been achieved for the Au_{55} cluster. It has been demonstrated that the cluster can be functionalised using appropriately designed thioether ligands to bear a single functional group [79]. Apart from this, there have been sporadic reports of control over the relative density of multiple ligands on the surface of a nanoparticle [80].

1.7. Click Chemistry

From the above discussion it is clear that there is need for more efficient functionalisation procedures. Addressing the above shortfalls of conventional organic reactions is the family of reactions referred to as “click” reactions [81]. These reactions are characterised by their modular nature, very high reaction yields, no or inoffensive by-products, simple reaction conditions and use of benign solvent conditions [81]. A variety of reactions fall under his category: Huisgen’s 1,3 dipolar cycloaddition, Diels-Alder reaction, ring opening nucleophilic substitution reactions such as epoxides and aziridines are some examples [81].

Notable among the “click” reactions is the Huisgen’s 1,3 dipolar cycloaddition reactions. As depicted in fig. 1.21, the reaction occurs between a terminal alkyne and an azide leading to the formation of 1,2,3 triazoles. The reaction can be carried out in a variety of solvent systems [83] under the influence of transition metal catalysts such as Cu(I), Ru, Pd(II), Pt(II) and Ni(II). Cu(I), though, is extensively used facilitating near quantitative yields even under room temperature conditions. The reaction is regioselective in the presence of a Cu(I) resulting in selective formation of 1,4-disubstituted 1,2,3-triazoles [84]. 1,5-disubstituted 1,2,3-triazoles can however be

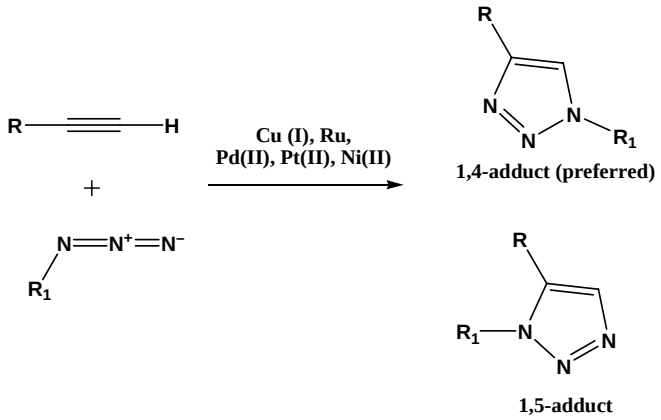

Figure 1.21: *The Huisgen's 1,3 dipolar cycloaddition "click" reaction. [Figure Adapted from reference 82].*

obtained selectively using ruthenium catalysts [85]. Generally for aqueous systems a combination of Cu(II) salt and a reducing agent like sodium ascorbate are used [84]. However one can directly use Cu(I) salts or even metallic copper in combination with a nitrogen base [83,84] in other solvent systems. Copper removal from biologically relevant systems is very crucial due to its cytotoxicity at high concentrations [86]. However ligands such as EDTA and sodium diethyl dithionate come in handy as they complex with copper strongly making them water soluble. Consequently, their removal becomes easy [87]. Alternatively, the triazole linkage can be obtained in the absence of copper catalyst under certain conditions. Lutz and co-workers have demonstrated that novel substituted cyclooctynes participate in 1,3 dipolar cycloaddition in the absence of a copper catalyst even at room temperature [88]. These reactions have been found to be a fast and efficient way to achieve the 1,2,3 triazole linkage [88].

The scope, efficiency and predictability of the Huisgen's 1,3 dipolar cycloaddition reactions are so impressive that the term "click" in recent literature predominantly refers to the Huisgen's 1,3 dipolar reaction. The same will be followed hence forth in this thesis. This is indeed justified given its wide applicability in organic synthesis [85], materials and polymer chemistry [82,86] and bio-conjugation [86]. Examples of "click" functionalisation of nanoparticulate systems and surfaces are many [82,86,89].

The "click" reaction has extensive applicability in bio-conjugation procedures. This is facilitated by the fact that azide functionality is not prevalent [89] in naturally occurring biomolecules. Consequently, once the azide and alkyne groups are incorporated in a biomolecule at a desired position using biotechnological [90a] or

semi-synthetic methods [90b], their selectivity towards each other does not interfere with the other functional groups present. Moreover the facile nature of the reaction even under benign conditions point to exciting prospects [81-83,86,89]. The following instances are illustrative examples of the same.

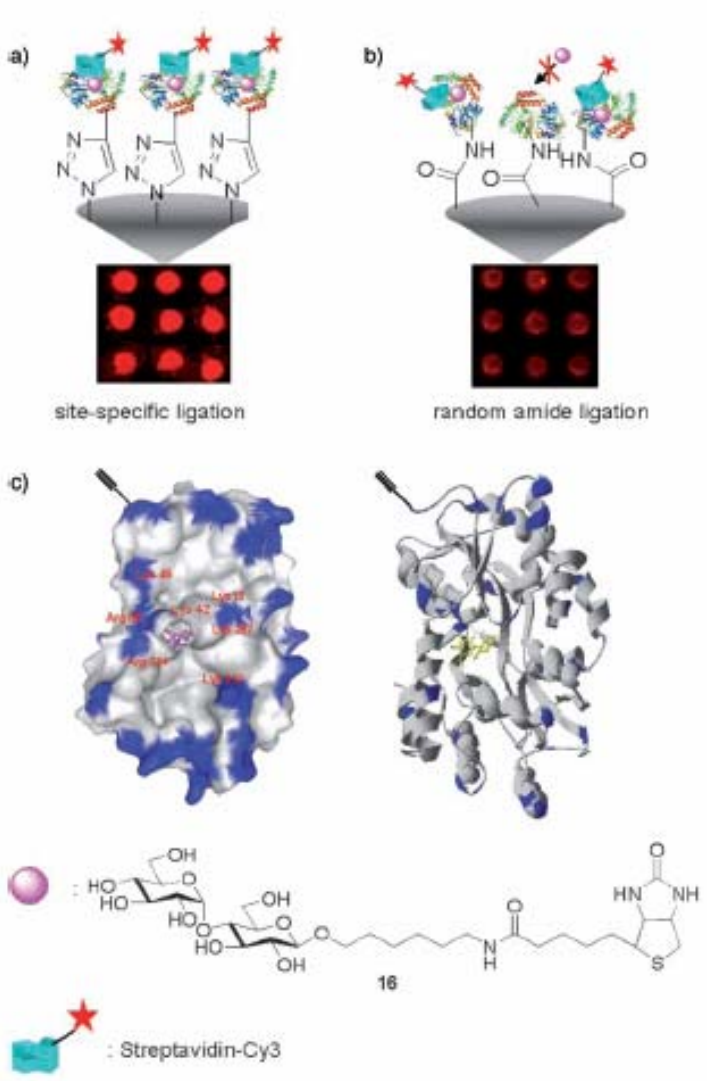

Figure 1.22: *Site specific labelling of the maltose binding protein using "click" reaction does not affect its biological activity (a) as the incorporated alkyne group is situated far from the active site (c). Activity is lost when amide bond formation is used for bioconjugation due to lack of site specificity. Amide bond formation results in random linkage and hence random orientation of the protein (b). See text for details. [Figure courtesy: Reference 76]*

Lin and co-workers have shown that click chemistry can be used to efficiently carry out site specific modification of proteins [76]. To demonstrate this, the maltose binding protein (MBP) in *Eschericia coli* was modified to express a single alkyne

group at a specified position not involved in maltose binding. Azide bearing fluorescein was then "clicked" to the MBP to yield a fluorescent adduct. This process of ligation of incorporated functional groups is generally referred to as expressed protein ligation (EPL). The ligation process efficiency was monitored using electrospray mass spectroscopy that confirmed complete conversion of all alkyne bearing MBP with time. Electrospray mass spectroscopy confirmed that no side products were obtained as each MBP was specifically bound to only one fluorescein molecule. Furthermore they demonstrated that site specific labelling through the "click" reaction does not affect the biological activity of the enzyme. For this purpose, the alkyne bearing MBP were immobilised on an azide bearing glass surface using the "click" protocol (fig. 1.22). Since the alkyne residue position was identical in all proteins, their orientation on the glass surface remains identical too. Moreover the protein was expected to retain its activity as the alkyne groups have been incorporated away from the active site. As a control experiment, unmodified MBPs were also bound to the glass surface through amide bonds. It was observed that only in case of site specifically "clicked" proteins, biotinylated maltose could bind efficiently as all the active sites were free for interaction. On the other had, random amide bond formation, and hence random protein orientation, resulted in cases where biotinylated maltoses are sterically blocked from accessing the active site. The maltose binding was detected using a tagged streptavidin molecule (Cy3). Thus it was demonstrated that "click" chemistry can be used for site specific labelling of proteins without altering their biological activity [76]. Apart from this there have been other instances of site specific conjugation of protein on to surfaces and particles [91].

In another interesting account, Schuber and co-workers [92] have shown that the "click" reaction can be used to functionalise preformed vesicles. The modified vesicles having surface alkyne groups were reacted with azido mannose to yield functionalised vesicles. It needs to be noted that the mild reaction conditions do not damage the vesicles. Vesicle damage would have led to release of the entrapped fluorescein. Such functionalised vesicles are part of liposomal formulations that find applications in diagnostics and drug/gene delivery. Asymmetrically functionalised micron sized polymer spheres and tapes were fabricated by Lahaan and co-workers [93] using the "click" reaction. Such functionalisation helps in mimicking nature's complex architectures [93]. These examples demonstrate the modular nature of the click reactions.

Thus it is clear that Huisgen's 1,3 dipolar cycloaddition can be effectively used for covalent functionalisation of nanoparticle systems and surfaces. The robustness of the triazole linkage coupled with high reaction efficiency and benign reaction conditions provide an efficient alternative to traditional functionalisation protocols in a range of materials.

1.8. Silane functionalisation and silica coatings

Amorphous silica coatings have been achieved on a wide variety of nanoparticles [94]. The coatings themselves can be achieved through hydrolytic (Stober methodology) [95] or non-hydrolytic routes [96]. Usually the coating uses nucleating species, such as (3-mercaptopropyl)-triethoxy silane, (3-aminopropyl)-triethoxy silane or the polymer poly(vinyl pyrrolidone), and can be executed in a variety of solvents.

Following coating the particle size becomes more monodisperse. This is due to fact that the relative size distribution of the particles is narrowed. Moreover, the nanoparticle surfaces become uniformly smooth as the coating proceeds by way of monomer addition on to surfaces [94b]. Such monodisperse materials have been used for the construction of metallo-dielectric opals [97a] and inverse opals [97b,c] with photonic band gap properties.

Silica being electronically inert (i.e. prevent electron transfer), the coatings cause little or no change to the individual material properties [55a,94b,98]. However, their thickness can be varied to modulate interparticle interactions. For instance, by varying the silica shell thickness the interparticle surface plasmon coupling between gold cores in silica coated gold colloids has been modulated [99]. The individual surface plasmon resonance behaviour though remains intact. Likewise, in the case of magnetic nanoparticles, the magnetic dipolar interaction between the particles was modulated to prepare stable magnetic nanoparticle dispersions [100].

In case of silica coated quantum dots, besides concealing the toxicity of the core material, surface coating also acts to passivate the surface defects that are typical of the nanoscale [98]. This results in enhancement of the photo stability of the quantum dots [98]. Moreover the coatings are robust and problems associated with polymeric coatings such as solvent assisted swelling and de-swelling are absent [101].

The amorphous nature of the silica coating also facilitates incorporation of smaller nanoparticles [102] or dyes molecules [101] in the nanostructure. This enables the synthesis of multifunctional materials. For instance, Tan and co-workers [101] have

synthesised monodisperse silica nanoparticles encasing three organic dyes (FITC, R6G and ROX). The dye ratios are then varied to tune the fluorescence using the process of fluorescence resonance energy transfer (FRET) (fig. 1.23).

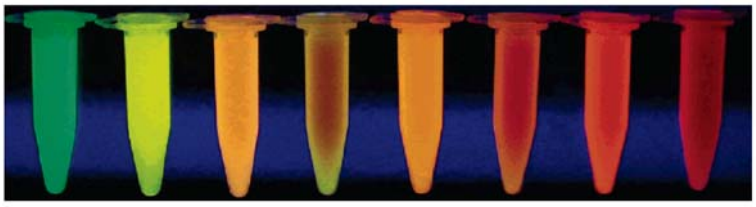

Figure 1.23: *Incorporation of FRET enabled dyes in the silica matrix can be used for synthesis of versatile fluorescent nanomaterials. See text for details. [Figure courtesy: Reference 101].*

In another report Hyeon and co-workers demonstrated synthesis of multifunctional magnetic composites [103] possessing optical and catalytic functionalities by assembling smaller Au, CdSe@ZnS and Pd nanoparticles on to Fe_3O_4 loaded silica spheres (fig. 1.24). Herein smaller nanoparticles were attached to silica through bi-functional silane coupling agents (e.g.: aminopropyltriethoxysilane).

A wide variety of bi-functional silane coupling agents are available. Consequently, the polarity of the silica surface can be tuned. The ability to tune the

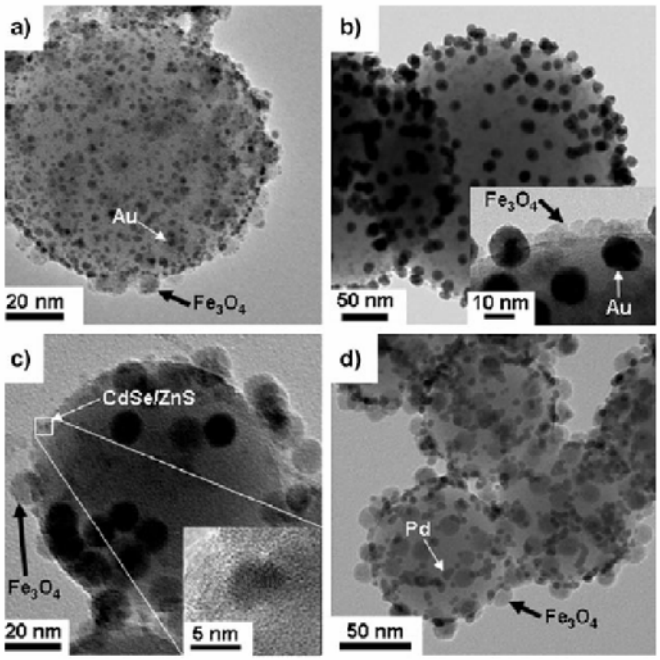

Figure 1.24: *Hyeon and co-workers demonstrate the fabrication of multifunctional nanoparticles that incorporate optical, catalytic and magnetic functionalities. [Figure courtesy: Reference 103].*

surface polarity of a silica coated material, through suitable surface modification, facilitates phase transfer across the oil-water interface. For instance, technologically important gold nanorods synthesised in the aqueous media were transferred to the non-polar organic media using this method [104]. Such a methodology has even been employed for phase transfer and Langmuir-Blodgett assembly of silver nanoprisms [105]. In these cases, the coating methodology serves to overcome the short comings of synthetic protocols that are restricted to certain solvent.

The biocompatibility of a silica coating also enables in-vivo applications following suitable surface modification [58]. However bio-functionalisation of silica poses some challenges. For example, silica is known to be unfavourable towards adsorption of proteins [58]. In general, functionalisation of silica based surfaces using silane functionalisation usually does not give reproducible surface coverage [78]. Consequently better functionalisation protocols need to be developed that enable biological applications. Not withstanding these drawbacks, it can be said that the generic nature of silica coatings in combination with efficient functionalisation tools such as click chemistry, can be used to functionalise most nanomaterials.

1.9. Objectives of work and chapter wise summary

Noble metal nanoparticles by virtue of their properties, find wide applicability as has been described above. This is particularly true for anisotropic nanoparticles where tunability of properties is an added attraction. A majority of synthetic protocols have however been carried out in the aqueous media or in polar organic solvents such as DMF and poly (ethylene glycol). This is true to a great extent even for the gold-silver core-shell systems.

It has been traditionally observed that non-hydrolytic pathways to nanoparticles and methods based in organic media give better control over nanoparticle size and shape [7b,e]. Moreover hydrophobically stabilised nanoparticles facilitate better functionalisation and hence more conceivable applications that include fabrication of sensors [106], self assembly to form interesting architectures [107], catalysis [108] and preparation of polymer nanocomposites [107c,109]. Moreover, storage and easy transport of dry re-dispersible nanoparticle powders, a consequence of hydrophobic stabilisation, would enhance their applicability in industry [107d].

Consequently, in the first part of this thesis, we endeavour to address this aspect by investigating seeded growth protocols in organic media for synthesis of gold

nanorods and Au@Ag core-shell nanoparticles. In addition to this, we attempt to use biogenic methods for synthesis of anisotropic gold nanotriangles to address the increasing need for "green" synthetic procedures [110].

In the second part of this thesis we address issues pertaining to functionalisation of nanoparticles. We investigate silane coating in combination with the versatile "click" reaction to present a generic protocol for functionalisation of inorganic nanoparticles [111]. It needs to be noted that though silane coupling agents suffer from drawbacks, they cannot be ruled out when covalent functionalisation of silica surfaces is desired. However incorporation of an efficient reaction such as the "click" would improve the overall efficiency of a multi-step functionalisation procedure. The important issue of estimation of chemically reactive groups in nanoparticles is also addressed. The thesis is organised as follows:

In **chapter two**, two new seed mediated growth methodologies for the synthesis of gold nanorods in organic media such as toluene and chloroform are discussed. Thorough structural characterisation of the nanorods was carried out. Efforts were made to understand the mechanistic aspects of the formation of the nanorods in light of previous reports.

In **chapter three** a novel method for the synthesis of Au@Ag core-shell nanoparticles in toluene has been discussed. This method follows established bi-phasic procedures for simultaneous reduction and phase transfer of silver ions, in the aqueous phase, to metallic silver nanoparticles in the organic phase. The Au@Ag nanoparticles thus formed were characterised using UV-visible absorbance spectroscopy, TEM, HRTEM and XPS.

In an attempt to investigate environmentally benign methods for synthesis of nanoparticles, a biogenic method for the synthesis of gold nanotriangles and silver nanoparticles is investigated and presented in **chapter four**. The leaf extract of the medicinal plant *Aloe vera* was employed to reduce the respective metal ions. The single crystalline gold nanotriangles and spherical silver nanoparticles were characterised using techniques such as UV-visible-NIR absorbance spectroscopy, Fourier transform infra-red spectroscopy (FTIR), transmission electron microscopy (TEM) and atomic force microscopy (AFM). Mechanistic aspects of gold ion reduction and nanotriangle formation are discussed.

"Click" chemistry based approach for the surface functionalisation of silica nanoparticles is the theme of **chapter five**. The "click" reaction between an azide and a

terminal alkyne (catalysed by cuprous ions) resulting in 1, 2, 3 triazoles is used to functionalise appropriately modified silica nanoparticle surfaces. The aim here was to develop a method to reliably vary the density of surface functional groups. In the second part of this chapter, 9-fluorenylmethylchloroformate and its derivative were used as a probe to develop an assay to quantify surface functional groups in nanoparticles. UV-visible absorbance spectroscopy, FTIR and fluorescence spectroscopy were used in these studies to monitor the reactions. Electron microscopy was used to characterise the silica nanoparticles.

In **chapter six**, the generic "click" chemistry methodology developed in chapter five for silica nanoparticle functionalisation has been extended to graft them with a known anti-cancer drug berberine. Moreover, inorganic nanoparticles of γ-AlOOH and iron oxide were functionalised with pyrene groups using the "click" reaction. This was facilitated by silica coatings on the respective nanoparticles. In addition, the plausible applications of such materials in catalysis, and understanding phase transitions in liquid crystals are listed.

C**hapter seven** concludes the thesis by presenting the salient points of the work described and presenting avenues for future investigations.

1.10. References

[1] Daniel, M.; Astruc, D. *Chem. Rev.* **2004**, *104*, 293.

[2] Faraday, M. *Philos. Trans.* **1857**, *147*, 145.

[3] (a) *The Chemistry of Nanomaterials*; Rao, C. N. R.; Muller, A.; Cheetham, A. K., Eds.; WILEY-VCH Verlag GmbH & Co.: Weinheim, 2004. (b) *Nanoscale Materials in Chemistry*; Klabunde, K. J., Ed.; John Wiley & Sons: New York, 2001. (c) *Colloids and Colloid Assemblies*; Caruso, F., Ed.; WILEY-VCH Verlag GmbH & Co.: Weinheim, 2004. (e) *Nanobiotechnology*; Niemeyer, C. M.; Mirkin, C. A., Eds.; WILEY-VCH Verlag GmbH & Co.: Weinheim, 2004.

[4] (a) Erbil, H. Y.; Bemeril, A. L.; Avci, Y.; Mert, O. *Science* **2003**, *299*, 1377. (b) Ma, M.; Hill, R. M. *Curr. Opin. Colloid Interface Sci.* **2006**, *11*, 193. (c).

[5] http://www.ruf.rice.edu/~wonglab/Improving%20the%20Synthesis.html

[6] http://www.esrf.eu/news/spotlight/spotlight35catalysts/

[7] (a) Yin, Y.; Alivisatos, A. P. *Nature* **2005**, *437*, 664. (b) Park, J.; Joo, J.; Kwon, S. G.; Jang, Y.; Hyeon, T. *Angew. Chem. Int. Ed.* **2007**, *46*, 4630. (c) Tao, A. R.; Habas, S.; Yang, P. *Small* **2008**, *4*, 310. (d) Grzelczak, M.; Perez-Juste, J.; Mulvaney, P.; Liz-

Marzan, L. M. *Chem. Soc. Rev.* **2008**, *37*, 1783. (e) Jun, Y. ; Choi, J.; Cheon, J. *Angew. Chem. Int. Ed.* **2006**, *45*, 3414.

[8] Menon, V. P.; Martin, C. R. *Anal. Chem.* **1995**, *67*, 1920.

[9] van der Zande, B. M. I.; Bohmer, M. R.; Fokkink, L. G. J.; Schnenberger, C. *Langmuir* **2000**, *16*, 451.

[10] Yu.; Chang, S.; Lee, C.; Wang, C. R. C. *J. Phys. Chem. B* **1997**, *101*, 6661.

[11] Murphy, C. J.; Sau, T. K.; Gole, A. M.; Orendorff, C. J.; Gao, J.; Gou, L.; Hunyadi, S. E.; Li, T. *J. Phys. Chem. B* **2005**, *109*, 13857.

[12] Murphy, C. J.; Jana, N. R. *Adv. Mater.* **2002**, *14*, 80.

[13] Nikoobakht, B.; El-Sayed, M. A. *Chem. Mater.* **2003**, *15*, 1957.

[14] Taub, N.; Krichevski, O.; Markovich, G. *J. Phys. Chem. B* **2003**, *107*, 11579.

[15] Perez-Juste, J.; Pastoriza-Santos, I.; Liz-Marzan, L. M.; Mulvaney, P. *Coord. Chem. Rev.* **2005**, *249*, 1870.

[16] (a) Millstone, J. E.; Park, S.; Shuford, K. L.; Qin, L.; Schatz, G. C.; Mirkin, C. A. *J. Am. Chem. Soc.* **2005**, *127*, 5312. (b) Millstone, J. E.; Metraux, G. S.; Mirkin, C. A. *Adv. Funct. Mater.* **2006**, *16*, 1209.

[17] Wiley, B.; Sun, Y.; Mayers, B.; Xia, Y. *Chem. Eur. J.* **2005**, *11*, 454.

[18] Kim, F.; Connor, S.; Song, H.; Kuykendall, T.; Yang, P. *Angew. Chem. Int. Ed.* **2004**, *43*, 3673.

[19] Pastoriza-Santos, I.; Liz-Marzan, L. M. *Adv. Funct. Mater.* **2009**, *19*, 1.

[20] (a) Jin, R.; Cao, Y.; Mirkina, C. A.; Kelly, K. L.; Schatz, G. C.; Zheng, J. G. *Science* **2001**, *294*, 1901. (b) Jin, R.; Cao, Y. C.; Hao, E.; Metraux, G. S.; Schatz, G. C.; Mirkin, C. A. *Nature* **2003**, *425*, 487.

[21] Carbo-Argibay, E.; Rodriguez-Gonzalez, B.; Pacificio, J.; Pastoriza-Santos, I.; Perez-Juste, J.; Liz-Marzan, L. M. *Angew. Chem. Int. Ed.* **2007**, *46*, 8983.

[22] Tsuji, M.; Hashimoto, M.; Nishizawa, Y.; Kubokawa, M.; Tsuji, T. *Chem. Eur. J.* **2005**, *11*, 440.

[23] Canizal, G.; Ascencio, J. A.; Gardea-Torresday, J.; Yacaman, M. J. *J. Nanopart. Res.* **2001**, *3*, 475.

[24] (a) Shankar, S. S.; Rai, A.; Ankamwar, B.; Singh, A.; Ahmad, A.; Sastry, M. *Nat. Mater.* **2004**, *3*, 482. (b) Shankar, S. S.; Rai, A.; Ahmad, A.; Sastry, M. *Chem. Mater.* **2005**, *17*, 566. (c) Chandran, S. P.; Chaudhry, M.; Pasricha, R.; Ahmad, A.; Sastry, M. *Biotechnol. Prog.* **2006**, *22*, 577.

[25] (a) Liu, B.; Xie, J.; Lee, J. Y.; Ting, Y. P.; Chen, J. P. *J. Phys. Chem. B* **2005**, *109*, 15256. (b) He, S.; Zhang, Y.; Guo, Z.; Gu, N. *Biotechnol. Prog.* **2008**, *24*, 476.

[26] (a) Mulvaney, P.; Giersig, M.; Henglein, A. *J. Phys. Chem.* **1993**, *97*, 7061. (b) Henglein, A. *J. Phys. Chem. B* **2000**, *104*, 6683.

[27] Zhu, J.; Wang, Y.; Huang, L.; Lu, Y. *Phys. Lett. A* **2004**, *323*, 455.

[28] Xue, C.; Millstone, J. E.; Li, S.; Mirkin, C. A. *Angew. Chem. Int. Ed.* **2007**, *46*, 8436.

[29] (a) Selvakannan, PR.; Swami, A.; Srisathyanarayanan, D.; Shirude, P. S.; Pasricha, R.; Mandale, A. B.; Sastry, M. *Langmuir* **2004**, *20*, 7825. (b) Mandal, S.; Selvakannan, PR.; Pasricha, R.; Sastry, M. *J. Am. Chem. Soc.* **2003**, *125*, 8440.

[30] Yang, J.; Lee, J. Y.; Too, H. *J. Phys. Chem. B* **2005**, *109*, 19208.

[31] (a) Sastry, M.; Swami, A.; Mandal, S.; Selvakannan, PR. *J. Mater. Chem.* **2005**, *15*, 3161. (b) Shukla, S.; Priscilla, A.; Banerjee, M.; Bhonde, R. R.; Ghatak, J. Satyam, P. V. Sastry, M. *Chem. Mater.* **2005**, *17*, 5000. (c) Skrabalak, S. E.; Chen, J.; Sun, Y.; Lu, X.; Au, L.; Cobley, C. M.; Xia, Y. *Acc. Chem. Res.* **2008**, *41*, 1587.

[32] Rodriguez-Gonzalez, B.; Burrows, A.; Watanabe, M.; Kiely, C. J.; Liz Marzan, L. M. *J. Mater. Chem.* **2005**, *15*, 1755.

[33] (a) Champion, J. A.; Mitragotri, S. *PNAS* **2006**, *103*, 4930. (b) Chithrani, B. D.; Ghazani, A. A.; Chan, W. C. W. *Nano. Lett.* **2006**, *6*, 662.

[34] El-Sayed, M. A. *Acc. Chem. Res.* **2001**, *34*, 257.

[35] (a) Mulvaney, P. *Langmuir* **1996**, *12*, 788. (b) Eustis, S.; El-sayed, M. A. *Chem. Soc. Rev.* **2006**, *35*, 209. (c) Link, S.; El-Sayed, M. A. *Int. Rev. Phys. Chem.* **2000**, *19*, 409.

[36] Hodak, J. H.; Henglein, A.; Giersig. M, Hartland, G. V. *J. Phys. Chem. B* **2000**, *104*, 11708.

[37] Liu, M.; Guyot-Sionnest, P. *J. Phys. Chem. B* **2005**, *109*, 22192.

[38] Grzelczak, M.; Perez-Juste, J.; Rodriguez-Gonzalez, B.; Liz Marzan, L. M. *J. Mater. Chem.* **2006**, *16*, 3946.

[39] Hernndez, J.; Solla-Gulln, J.; Herrero, E.; Aldaz, A.; Feliu, J. M. *J. Phys. Chem. B* **2005**, *109*, 12651.

[40] (a) Perez-Juste, J.; Liz Marzan, L. M.; Carnie, S.; Chan, D. Y. C.; Mulvaney, P. *Adv. Funct. Mater.* **2004**, *14*, 571. (b) Rodrguez-Fernndez, J.; Prez-Juste, J.; Mulvaney, P.; Liz Marzan, L. M. *J. Phys. Chem. B* **2005**, *109*, 14257.

[41] Johnson, C. J.; Dujardin, E.; Davis, S. A.; Murphy, C. J.; Mann, S. *J. Mater. Chem.* **2002**, *12*, 1765.

[42] Chandran, S. P.; Pasricha, R.; Bhatta, U. M.; Satyam, P. V.; Sastry, M. *J. Nanosci. Nanotechnol.* **2007**, *7*, 2808.

[43] Lofton, C.; Sigmund, W. *Adv. Funct. Mater.* **2005**, *15*, 1197.

[44] (a) Yang, Y.; Matsubara, S.; Xiong, L.; Hayakawa, T.; Nogami, M. *J. Phys. Chem. C* **2007**, *111*, 9095. (b) Aherne, D.; Ledwith, D. M.; Gara, M.; Kelly, J. M. *Adv. Funct. Mater.* **2008**, *18*, 2005. (c) Rodrguez-Fernndez, J.; Pastoriza-Santos, I.; Liz Marzan, L. M. *J. Phys. Chem. B* **2006**, *110*, 11796.

[45] (a) Wang, T.; Hu, X.; Dong, S. *J. Phys. Chem. B* **2006**, *110*, 16930. (b) Bharde, A.; Kulkarni, A.; Rao, M.; Prabhune, A.; Sastry, M. *J. Nanosci. Nanotechnol.* **2007**, *7*, 4369. (c) Chen, S.; Carroll, D. L. *Nano. Lett.* **2002**, *2*, 1003.

[46] (a) Idla, K.; Johansson, L. S.; Campbell, J. M.; Inganas, O. *Surf. Interface Anal.* **2000**, *30*, 557. (b) Johansson, L. S.; Juhanoja, J. *Thin Solid Films* **1994**, *238*, 242. (c) Xu, X.; Cortie, M. B. *J. Phys. Chem. C* **2007**, *111*, 18135.

[47] Kneipp, K.; Kneipp, H.; Itzkan, I.; Dasari, R. R.; Feld, M. S. *Chem. Rev.* **1999**, *99*, 2957.

[48] Kelly, K. L.; Coronado, E.; Zhao, L. L.; Schatz, G. C. *J. Phys. Chem. B* **2003**, *107*, 668.

[49] Nie, S.; Emory, S. R. *Science* **1997**, *275*, 1102.

[50] (a) Freeman, R. G.; Hommer, M. B.; Grabar, K. C.; Jackson, M. A.; Natan, M. J. *J. Phys. Chem.* **1996**, *100*, 718. (b) Loo, B. H.; Furtak, T. E. *Chem. Phys. Lett.* **1980**, *71*, 68. (c) Cao, Y. C.; Jin, R.; Mirkin, C. A. *Science* **2002**, *297*, 1536.

[51] Pompa, P. P.; Martiradonna, L.; Della Torre, A.; Della Sala, F.; Manna, L.; De Vittorio, M.; Calabi, F.; Cingolani, R.; Rinaldi, R. *Nat. Nanotech.* **2006**, *1*, 126.

[52] Aslan, K.; Wu, M.; Lakowicz, J. R.; Geddes, C. D. *J. Am. Chem. Soc.* **2007**, *129*,1524.

[53] Sudeep, P. K.; Joseph, S. T. S.; Thomas, K. G. *J. Am. Chem. Soc.* **2005**, *127*, 6516.

[54] Rex, M.; Hernandez, F. E.; Campiglia, A. D. *Anal. Chem.* **2006**, *78*, 445.

[55] (a) Hutter, E.; Fendler, J. H. *Adv. Mater.* **2004**, *16*, 1685. (b) Maier, S. A.; Brongersma, M. L.; Kik, P. G.; Meltzer, S.; Requicha, A. A. G.; Atwater, H. A. *Adv. Mater.* **2001**, *13*, 1501.

[56] Chen, C. C.; Lin, Y. P.; Wang, C. W.; Tzeng, H. C.; Wu, C. H.; Chen, Y. C.; Chen, C. P.; Chen, L. C.; Wu, Y. C. *J. Am. Chem. Soc.* **2006**, *128*, 3709.

[57] Huang, X.; El-Sayed, I. H.; Qian, W.; El-Sayed, M. A. *J. Am. Chem. Soc.* **2006**, *128*, 2115.

[58] Aubin Tam, M. E.; Hamad Schifferli, K.; Biomed. Mater. 2008, 3, 034001

[59] Ulman, A. *Chem. Rev.* **1996**, *96*, 1533.

[60] Mandal, S.; Gole, A.; Lala, N.; Gonnade, R.; Ganvir, V.; Sastry, M. *Langmuir* **2001**, *17*, 6262.

[61] Tshikudo, T. R.; Demuru, D.; Wang, Z.; Brust, M.; Secchi, A.; Arduini, A.; Pochini, A. *Angew. Chem. int. Ed.* **2005**, *44*, 2913.

[62] (a) Caruso, F.; Lichtenfeld, H.; Donath, E.; Mhwald, H. *Macromolecules* **1999**, *32*, 2317. (b) Sastry, M.; Rao, M.; Ganesh, K. N. *Acc. Chem. Res.* **2002**, *35*, 847. (c) Peyratout, C. S.; Dahne, L. *Angew. Chem. Int. Ed.* **2004**, *43*, 3762.

[63] (a) Leff, D. V.; Brandt, L.; Heath, J. R. *Langmuir* **1996**, *12*, 4723. (b) Kumar, A.; Mandal, S.; Pasricha, R.; Mandale, A. B.; Sastry, M. *Langmuir* **2003**, *19*, 6277. (c) Ha, J.; Solovyov, A.; Katz, A. *Langmuir* **2009**, *25*, 153.

[64] Buck, M. E.; Zhang, J.; Lynn, D. M. *Adv. Mater.* **2007**, *19*, 3951.

[65] (a) Decher, G. *Science* **1997**, *277*, 1232. (b) Bertrand, P.; Jonas, A.; Laschewsky, A.; Legras, R. *Macromol. Rapid Commun.* **2000**, *21*, 319.

[66] (a) Yang, S. Y.; Rubner, M. F. *J. Am. Chem. Soc.* **2002**, *124*, 2100. (b) Zelikin, A. N.; Quinn, J. F.; Caruso, F. *Biomacromolecules* **2006**, *7*, 27.

[67] Selvakannan, PR.; Mandal, S.; Phadtare, S.; Gole, A.; Pasricha, R.; Adyanthaya, S.; Sastry, M. *J. Colloid Interface Sci.* **2004**, *269*, 97.

[68] (a) Herne, T. M.; Tarlov, M. J. *J. Am. Chem. Soc.* **1997**, *119*, 8916. (b) Storhoff, J. J.; Elghanian, R.; Mirkin, C. A.; Letsinger, R. L. *Langmuir* **2002**, *18*, 6666. (c) Sandstorm, P.; Boncheva, M.; Akerman, B. *Langmuir* **2003**, *19*, 7537.

[69] (a) Kane, R. S.; Deschatelets, P.; Whitesides, G. M. *Langmuir* **2003**, *19*, 2388. (b) Liufu, S.; Xiao, H.; Li, Y. *Powder Technol.* **2004**, *145*, 20. (c) Yang, W.; Thordarson, P.; Gooding, J. J.; Ringer, S. P.; Braet, F. *Nanotechnology* **2007**, *18*, 412001.

[70] Haensch, C.; Chiper, M.; Ulbricht, C.; Winter, A.; Hoeppener, S.; Schubert, U. S. *Langmuir* **2008**, *24*, 12981.

[71] Wei, Q.; Ji, J.; Shen, J. *Macromol. Rapid. Commun.* **2008**, *29*, 645.

[72] (a) Gorelikov, I.; Field, L. M.; Kumacheva, E. *J. Am. Chem. Soc.* **2004**, *126*, 15938. (b) Das, M.; Sanson, N.; Fava, D.; Kumacheva, E.; *Langmuir* **2007**, *23*, 196. (c) Kumar, V. R. R.; Samal, A. K.; Sreeprasad, T. S.; Pradeep, T. *Langmuir* **2007**, *23*, 8667.

[73] Richard, C.; Balavoine, F.; Schultz, P.; Ebbesen, T. W.; Mioskowski, C. *Science* **2003**, *300*, 775.

[74] Dieckmann, G. R.; Dalton, A. B.; Johnson, P. A.; Razal, J.; Chen, J.; Giordano, G. M.; Muoz, E.; Musselman, I. H.; Baughman, R. H. Draper, R. K. *J. Am. Chem. Soc.* **2003**, *125*, 1770.

[75] Chen, R. J.; Zhang, Y.; Wang, D.; Dai, H. *J. Am. Chem. Soc.* **2001**, *123*, 3838.

[76] Lin, P.; Ueng, S.; Tseng, M.; Ko, J.; Huang, K.; Yu, S.; Adak, A.; Chen, Y.; Lin, C. *Angew. Chem. Int. Ed.* **2006**, *45*, 4286.

[77] Huo, Q.; Worden, J. G. *J. Nanopart. Res.* **2007**, *9*, 1013.

[78] Bruce, I. J.; Sen, T. *Langmuir* **2005**, *21*, 7029.

[79] Pankau, W. M.; Monninghoff, S.; von Keidrowski, G. *Angew. Chem. Int. Ed.* **2006**, *45*, 1889.

[80] (a) Ipe, B. I.; Thomas, K. G. *J. Phys. Chem. B* **2004**, *108*, 13265. (b) Jackson, A. M.; Myerson, J. W.; Stellacci, F. *Nat. Mater.* **2004**, *3*, 330.

[81] Kolb, H. C.; Finn, M. G.; Sharpless, K. B. *Angew. Chem. Int. Ed.* **2001**, *40*, 2004.

[82] Binder, W. H.; Sachsenhofer, R. *Macromol. Rapid Commun.* **2007**, *28*, 15.

[83] Meldal, M.; Tornoe, C. W. *Chem. Rev.* **2008**, *108*, 2952.

[84] Rostovtsev, V. V.; Green, L. G.; Fokin, V. V.; Sharpless, K. B. *Angew. Chem. Int. Ed.* **2002**, *41*, 2596.

[85] Zhang, L.; Chen, X.; Xue, P.; Sun, H. H. Y.; Williams, I. D.; Sharpless K. B.; Fokin, V. V.; Jia, G. *J. Am. Chem. Soc.* **2005**, *127*, 15998.

[86] Nandivada, H.; Jiang, X.; Lahann, J. *Adv. Mater.* **2007**, *19*, 2197.

[87] Terry, T. J.; Stack, T. D. P. *J. Am. Chem. Soc.* **2008**, *130*, 4945.

[88] Lutz, J. *Angew. Chem. Int. Ed.* **2008**, *47*, 2182.

[89] Moses, J. E.; Moorhouse, A. D. *Chem. Soc. Rev.* **2007**, *36*, 1249.

[90] (a) Wang, L.; Schultz, P. G. *Angew. Chem. Int. Ed.* **2005**, *44*, 34. (b) Muir, T. W. *Annu. Rev. Biochem.* **2003**, *72*, 249.

[91] (a) Sun, X.; Stabler, C. L.; Cazalis, C. S.; Chaikof, E. L. *Bioconjugate Chem.* **2006**, *17*, 52. (b) Duckworth, B. P.; Xu, J.; Taton, T. A.; Guo, A.; Distefano, M. D. *Bioconjugate Chem.* **2006**, *17*, 964.

[92] Hassane, F. S.; Frisch, B.; Schuber, F. *Bioconjugate Chem.* **2006**, *17*, 849.

[93] Bhaskar, S.; Roh, K.; Jiang, X.; Baker, G. L.; Lahann, J. *Macromol. Rapid Commun.* **2008**, *29*, 1655.

[94] (a) Alejandro-Arellano, M.; Ung, T.; Blanco, A.; Mulvaney, P.; Liz Marzan, L. M. *Pure Appl. Chem.* **2000**, *72*, 257. (b) Liz-marzan, L. M.; Giersig, M.; Mulvaney, P. *Langmuir* **1996**, *12*, 4329. (c) Selvan, S. T.; Tan, T. T.; Ying, J. Y. *Adv. Mater.* **2005**, *17*, 1620. (d) Rebolledo, A. F.; Bomati-Miguel, O.; Marco, J. F.; Tartaj, P. *Adv. Mater.* **2008**, *20*, 1760.

[95] Stober, W.; Fink, A.; Bohn, E. *J. Colloid lnterface Sci.* **1968**, *26,* 62.

[96] Hay, J. N.; Raval, H. M. *Chem. Mater.* **2001**, *13*, 3396.

[97] (a) Garca Santamara, F.; Salgueirio Maceira, V.; Lopez, C.; Liz-Marzan, L. M. *Langmuir* **2002**, *18*, 4519. (b) Wang, D.; Li, J.; Chan, C. T.; Salgueirio Maceira, V.; Liz-Marzan, L. M.; Romanov, S.; Caruso, F. *Small* **2005**, *1*, 122. (c) Wang, D.; Salgueirio Maceira, V.; Liz-Marzan, L. M.; Caruso, F. *Adv. Mater.* **2002**, *14*, 908.

[98] Nann, T.; Mulvaney, P. *Angew. Chem. Int. Ed.* **2004**, *43*, 5393.

[99] Liz-Marzan, L. M.; Mulvaney, P. *J. Phys. Chem. B* **2003**, *107*, 7312.

[100] Philipse, A. P.; van Bruggen, M. P. B.; Pathmamanoharan, C. *Langmuir* **1994**, *10*, 92.

[101] Wang, L.; Tan, W. *Nano Lett.* **2006**, *6*, 84.

[102] Tartaj, P.; Gonzalez-Carreno, T.; Serna, C. *Adv. Mater.* **2001**, *13*, 1620.

[103] Kim, J.; Lee, J. E.; Lee, J.; Jang, Y.; Kim, S.; An, K.; Yu, J. H.; Hyeon, T. *Angew. Chem. Int. Ed.* **2006**, *45*, 4789.

[104] Pastoriza Santos, I.; Perez-Juste, J.; Liz Marzan, L. M. *Chem. Mater.* **2006**, *18*, 2465.

[105] Xue, C.; Chen, X.; Hurst, S. J. Mirkin, C. A. *Adv. Mater.* **2007**, *19*, 4071.

[106] (a) Ipe, B. I.; Mahima, S, Thomas, K. G. *J. Am. Chem. Soc.* **2003**, *125*, 7174. (b) Ipe, B. I.; Yoosaf, K.; Thomas, K. G. *J. Am. Chem. Soc.* **2006**, *128*, 1907.

[107] (a) Kiely, C. J.; Fink, J.; Brust, M.; Bethell, D.; Schiffrin, D. J. *Nature* **1998**, *396*, 444. (b) Peng, G.; Qiu, F.; Ginzburg, V. V.; Jasnow, D.; Balasz, A. C. *Science* **2000**, *288*, 1802. (c) Nie, Z.; Fava, D.; Kumacheva, E.; Zou, S.; Walker, G. C.; Rubinstein, M. *Nature Mater.* **2007**, *6*, 609. (d) Mitamura, K.; Imae, T.; Saito, N.; Takai, O. *J. Phys. Chem. B* **2007**, *111*, 8891.

[108] (a) Jaramillo, T. J.; Baeck, S. –H.; Cuenya, B. R.; McFarland, E. W. *J. Am. Chem. Soc.* **2003**, *125*, 7148. (b) Chen, M.; Goodman, W. *Acc. Chem. Res.* **2006**, *39*, 739.

[109] (a) Corbierre, M. K.; Cameron, N. S.; Lennox, R. B. *Langmuir* **2004**, *20*, 2867. (b) Perez-Juste, J.; Rodriguez-Gonzalez, B.; Mulvaney, P.; Liz-Marzan, L. M. *Adv.*

Func. Mater. **2005**, *15*, 1065. (c) Balazs, A. C.; Emrick, T.; Russell, T. P. *Science* **2006**, *314*, 1107.

[110] Dahl, J. A.; Maddux, B. L. S.; Hutchison, J. E. *Chem. Rev.* **2007**, *107*, 2228.

[111] Shen, R.; Camargo, P. H. C.; Xia, Y.; Yang, H. *Langmuir* **2008**, *24*, 11189.

Chapter 2

Synthesis of gold nanorods in organic media

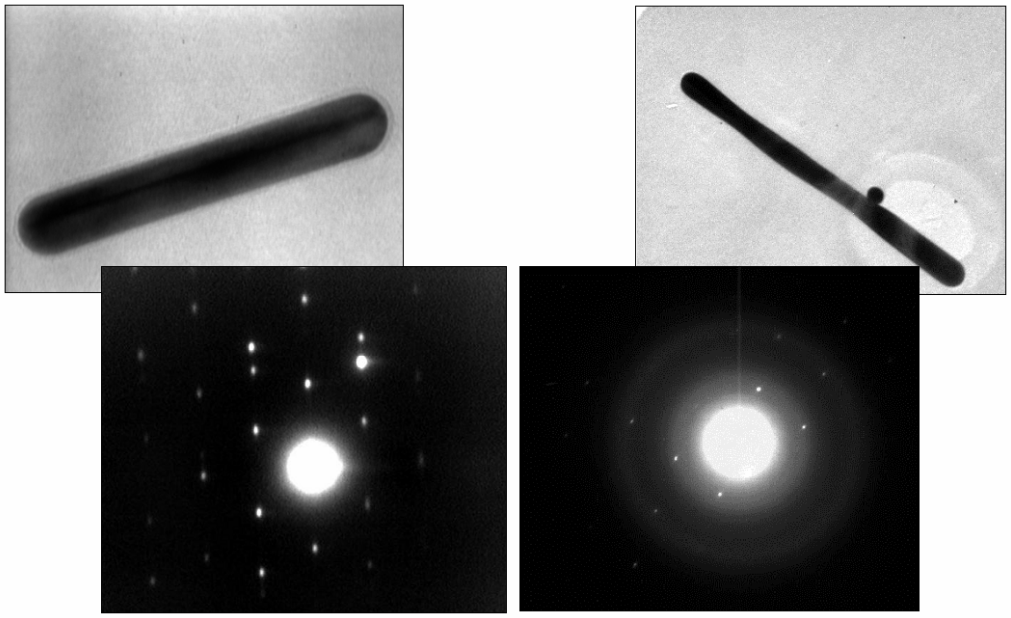

This Chapter describes two new seeded growth methods in organic media for the synthesis of hydrophobic gold nanorods. In the first method, hydrophobised chloroaurate ions are reduced by an aniline derivative in the presence of gold nanoparticle seeds, wherein, the reductant 4-hexadecylaniline (HDA) is present capping the surface of the seed particles. Under certain conditions, gold nanorods are obtained. The second method uses derivatised ascorbic acid as the reducing agent of chloroaurate ions. Whereas reduction by HDA results in formation of nanorods that incorporate five twin planes running along the length of particle, the latter method selectively results in the formation of single crystalline rods. The nanorod structure and mechanism of formation are discussed using HRTEM analysis besides other techniques.

Part of the work discussed in this chapter has been published in

Prathap Chandran, S.; Pasricha, R.; Bhatta, U. M.; Satyam, P. V.; Sastry, M. *J. Nanosci. Nanotechnol.* **2007**, *7*, 2808.

2.1. Introduction

The study of metal nanorods, particularly gold nanorods, has been the central theme of many research investigations [1]. Due to interesting optical properties, applications in fields that include sensor technology, spectroscopy, plasmonics and biomedicine have been conceived and demonstrated [2]. To address such diverse needs, various synthetic procedures have been developed that offer good control over the nanorod yield, dimensions and hence their properties. Seeded growth based protocol developed by Murphy and co-workers, silver ion assisted growth processes and photochemical procedures are some of the well established methodologies [1]. A detailed account on these issues has been provided in chapter 1.

Given the inherent symmetry in FCC crystal systems, the breaking of symmetry under the influence of various factors is held responsible for the evolution of such an anisotropic structure. Minimisation of strain during growth of seed particles [3], electric field directed growth [4] and preferential adsorption of surfactants on high energy crystal faces formed during nanorod growth [1d] are some of the theories that have been invoked to explain the growth of gold nanorods.

Factors common to the synthetic methods are usage of seed, surfactant and a mild reducing agent to facilitate directed seeded growth. The crystal structure of the seed has been found to influence the crystal structure of the nanorods [5]. In addition, the seed quantity has been used to control the dimensions of the gold nanorods [1a]. Most methods employ CTAB as the shape directing agent and ascorbic acid as the reducing agent. Ascorbic acid is a well known reducing agent used in synthesis of gold and silver nanoparticles [1a-e,6]. During such processes ascorbic acid undergoes oxidation to form dehydroascorbic acid [6]. The concentration of ascorbic acid itself has been found to be critical in seeded growth procedures that result in gold nanorods [7]. Its weak reducing nature when used in combination with a surfactant such as CTAB is known to bring about seeded growth leading to formation of nanorods [1a-e].

Methods highlighted till now provide stable nanorods in the aqueous media. However as stated earlier in chapter 1, hydrophobic stabilisation widen the scope nanoparticle applicability in general. Though methods that achieve phase transfer of gold nanorods to organic media exist, they involve coating of the nascent gold nanorods with silica before further hydrophobisation [8]. This ultimately leads to a lengthy functionalisation protocol. Consequently we investigate two methods in this chapter that address the synthesis of gold nanorods directly in the organic media.

It is understood that the reduction of gold ions and the deposition of metallic gold on seeds is a pre-requisite to achieve maximum yield of gold nanorods [9]. With this as the rationale we use gold nanoparticles that are stabilised by 4-hexadecylaniline (HDA) as seeds in the first method. The choice of this reagent is based on the well known reductive action of anilines accompanied by their oxidative polymerisation [10]. The presence of the reducing agent on the surface of the seed is expected to minimise fresh nucleation and aid seeded growth. The seeded growth is performed in toluene under different concentrations of the amine amphiphiles to utilise the shape directing ability of amines. This approach stems from reports wherein alkylamines have been found to have greater affinity towards low index crystal faces [11], those that are common in gold nanorods [12]. In the second method, we have derivatised ascorbic acid to utilise its reductive action in chloroform. Similar derivatives of ascorbic acid have been used for the synthesis of gold nanoparticle based gels and liquid crystals [13]. The study of alternative methods for synthesis of gold nanorods in organic media such as toluene and chloroform forms the central theme of this chapter.

2.2. Seeded growth using 4-hexadecylaniline capped gold nanoparticle seeds in toluene

In this section, results of the seeded growth procedure with HDA capped gold nanoparticle seeds are presented.

2.2.1. Synthesis of aqueous gold nanoparticles

To a 1 L solution of 10^{-4} M $HAuCl_4$ in de-ionised water (Milli-Q®), 0.1 g of $NaBH_4$ was added followed by vigorous stirring. This reaction is accompanied by the

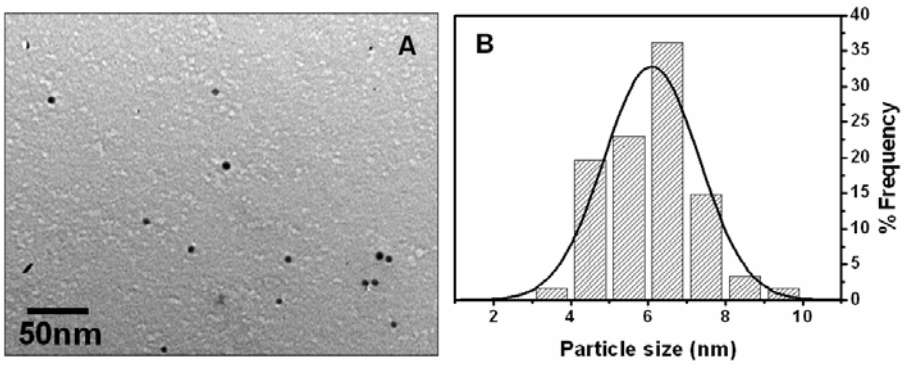

Figure 2.1: *(A) Representative TEM micrograph and (B) size distribution of sodium borohydride reduced gold nanoparticles. The mean particle size was determined to be 6.1 ± 2.5 nm following a Gaussian fit to the size distribution.*

immediate appearance of deep ruby red colour characteristic of gold nanoparticles. This solution was allowed to stand for a period of 24 h before further use. These particles were found to have a mean diameter of 6.1 ± 2.5 nm based on TEM analysis (fig. 2.1).

2.2.2. Preparation of hydrophobised 4-hexadecylaniline capped gold nanoparticles

In a typical reaction, 1 L of 10^{-4} M gold nanoparticle were stirred vigorously with 100 mL of 10^{-3} M 4-hexadecylaniline (HDA) in toluene for 6 h. Complete phase transfer of the gold nanoparticles was seen by the aqueous solution turning colourless and the toluene phase assuming a deep ruby red colour. The toluene phase was thereafter separated and the concentration of gold nanoparticles was taken to be 10^{-3} M. The particle size distribution was fitted to a bimodal distribution revealing mean diameters of 11.0 ± 1.9 nm and 20.7 ± 1.5 nm (fig. 2.2). It is interesting to note that the size of the gold nanoparticles has changed following capping with HDA. Such variation in nanoparticle size at room temperature and elevated temperature in the presence of surface active ligands is well documented [14].

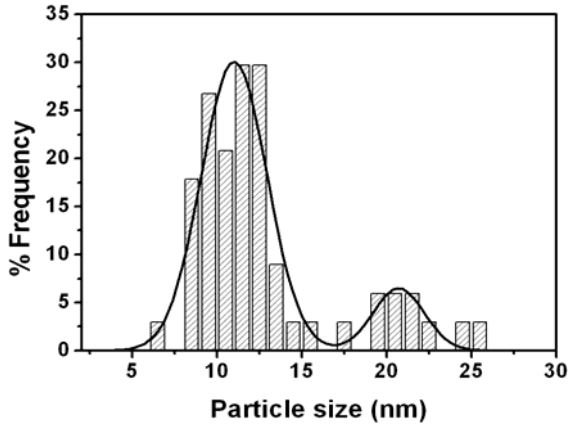

Figure 2.2: *Size distribution analysis of HDA capped gold nanoparticles.*

2.2.3. Preparation of hydrophobic $HAuCl_4$

In a typical reaction, 50 mL of aqueous 10^{-3} M $HAuCl_4$ was stirred with 50 mL of 10^{-3} M ODA in toluene for a period of 2 h. This led to the phase transfer of chloroaurate ions to toluene as evidenced by the complete transfer of yellow colour to the toluene phase. The toluene phase was separated to yield 10^{-3} M ODA hydrophobised chloroaurate ions. A similar procedure for the phase transfer of aqueous chloroaurate ions into toluene was carried out using hexadecylamine, dodecylamine,

octylamine, benzyldimethylstearylammoniumchloride (BDSAC) and tetraoctylammoniumbromide (TOAB).

For the preparation of ODA–TOAB hydrophobised chloroaurate ions, 5 mL of 10^{-2} M ODA in toluene and 0.5 mL of 10^{-2} M TOAB in toluene were added to 44.5 mL of toluene. This solution was 10^{-3} M and 10^{-4} M in ODA and TOAB respectively. This was then stirred with 50 mL of 10^{-3} M aqueous $HAuCl_4$ for a period of 2 h to yield ODA – TOAB hydrophobised chloroaurate ions.

2.2.4. Seeded growth experiment

In a series of experiments, 1, 3, 5, 7 and 9 mL of 10^{-3} M HDA capped gold nanoparticle seeds in toluene were added to 9, 7, 5, 3 and 1 mL of 10^{-3} M ODA hydrophobised chloroaurate ions in toluene respectively. It was observed that solutions with smaller amount of seed particles (1, 3 and 5 mL) changed colour from ruby red (characteristic of the seed - HDA capped gold nanoparticles) to turbid brownish red and formed precipitates after 12 h of reaction. It needs to be noted that since the reductant HDA is present on the seed particles its concentration in these cases in low. The colour change for cases with greater amount of seed particles was not discernible to the naked eye unlike for cases with smaller amount of seed. These were redispersed by sonication for further UV-visible-NIR spectroscopic and transmission electron microscopy (TEM) characterization.

2.2.4.1. UV-visible-NIR absorbance studies

Fig. 2.3 shows the UV-visible-NIR absorbance spectra of nanoparticulate solutions obtained when varying amounts of 10^{-3} M HDA capped gold nanoparticle seeds were added to ODA hydrophobised chloroaurate ions in toluene. The increase in surface plasmon resonance intensities in all cases relative to HDA capped gold nanoparticle seeds (curve 1, fig. 2.3) indicates reduction of ODA hydrophobised gold ions by the surface bound HDA molecules. It is known that aniline derivatives undergo oxidative polymerisation in the presence of gold ions facilitating reduction of gold ions. The aniline species themselves undergo concomitant oligomerisation or polymerisation [10c]. It can be seen that for solutions having smaller amount of seed (1, 3 and 5 mL) the absorbance due to surface plasmon resonance is broad (curves 2, 3 and 4, fig. 2.3). As the seed amount increases (7 and 9 mL) the surface plasmon resonance band sharpens (curves 5 and 6, fig. 2.3). Broadening of the surface plasmon resonance

absorption bands in metal nanoparticles has been observed to occur due to formation of anisotropic structures or aggregated structures [15].

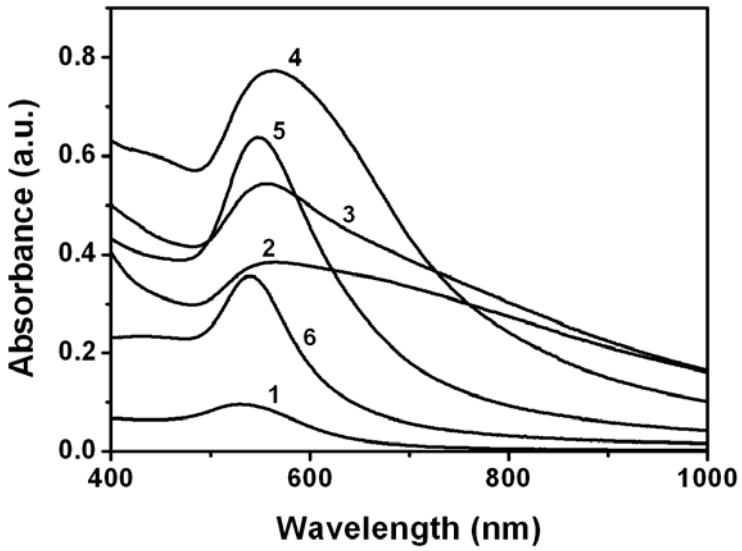

Figure 2.3: *UV-visible-NIR absorbance spectrum of HDA capped gold nanoparticle seeds is shown in curve 1. Curves 2 to 6 show the UV-visible-NIR absorbance spectra of the nanoparticles formed when 1, 3, 5, 7 and 9 mL of 10^{-3} M HDA capped gold nanoparticle seeds react with 9, 7, 5, 3 and 1 mL of 10^{-3} M ODA hydrophobised chloroaurate ions respectively.*

One of the above reactions (5 mL of 10^{-3} M HDA capped gold nanoparticle seeds with 5 mL of 10^{-3} M ODA hydrophobised chloroaurate ions) was monitored using UV-visible-NIR absorbance spectroscopy as a function of time (fig. 2.4). Within a minute of addition of ODA hydrophobised chloroaurate ions to HDA capped gold nanoparticle seeds, (curve 1, fig. 2.4) the transverse surface plasmon absorbance of the nanoparticulate solution centred at 530 nm increased in intensity (curve 2, fig. 2.4). After 45 mins (curve 3, fig. 2.4) of reaction, a fall in the intensity of transverse surface plasmon resonance band at 530 nm along with its broadening is observed. Such a trend has been observed during anisotropic gold nanostructure formation [16] or the aggregation of spherical gold nanoparticles [17]. After 2.5 h of reaction (curve 4, fig. 2.4), an increase in intensity of the transverse surface plasmon resonance band in addition to development of a shoulder near 620 nm is observed. Further reaction sees a shift in the shoulder position from 640 nm (after 5 h, curve 5, fig. 2.4) to 700 nm (after 12.5 h, curve 8, fig. 2.4). Such evolution of UV-visible-NIR profiles with time is characteristic of growth of anisotropic nanostructures [16,18]. The time taken for completion of reaction is approximately 12.5 h after which the reaction saturates.

Although a very marginal increase in the intensity of the surface plasmon resonance with time after 12.5 h is observed, the features essentially remain unchanged (fig. 2.4, compare curves 8 and 9 – 14.5 h). TEM analysis was conducted to analyse the nanostructures formed as a product of seeded growth process.

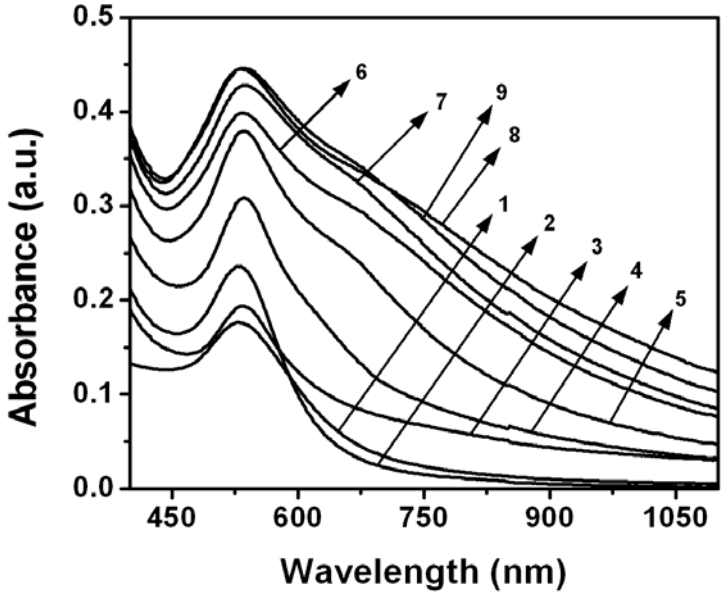

Figure 2.4: *Temporal evolution of UV-visible-NIR absorbance profiles of nanoparticulate products formed when 5 mL of 10^{-3} M ODA hydrophobised chloroaurate ions were reacted with 5 mL of 10^{-3} M HDA capped gold nanoparticle seeds. Curve 1 corresponds to HDA capped gold nanoparticle seeds, curves 2 – 9 correspond to reaction products formed at different time intervals after onset of the reaction: less than 1 min, 45 mins, 2.5, 5, 8, 10, 12.5 and 14.5 h respectively.*

2.2.4.2. TEM studies

TEM measurements were carried out on nanoparticulate solutions where 1, 5 and 7 mL of the 10^{-3} M HDA capped gold nanoparticle seeds were reacted with 9, 5 and 3 mL of 10^{-3} M ODA capped chloroaurate ions respectively. Fig. 2.5A shows a representative TEM image of HDA capped gold nanoparticle seeds which were used as seeds. The particles have a quasi-spherical morphology and polydisperse size. The size distribution was fitted to a bimodal distribution with mean diameters of 11.0 ± 1.9 nm and 20.7 ± 1.5 nm (fig. 2.2). Figs. 2.5B and 2.5C show representative TEM image corresponding to the nanoparticulate solution with 7 mL of 10^{-3} M HDA capped gold nanoparticle seeds and 3 mL of 10^{-3} M ODA hydrophobised chloroaurate ions. The formation of nanorods as seen from the TEM images account for the occurrence of the broad surface plasmon band centred at 555 nm (curve 5, fig. 2.3). Gold nanorods are

known to exhibit a longitudinal surface plasmon resonance absorbance whose position is a function of the aspect ratio of the nanorods [1c,19]. This is in addition to the transverse surface plasmon resonance absorbance which occurs at the same position where spherical gold nanoparticles absorb (ca. 520 nm).

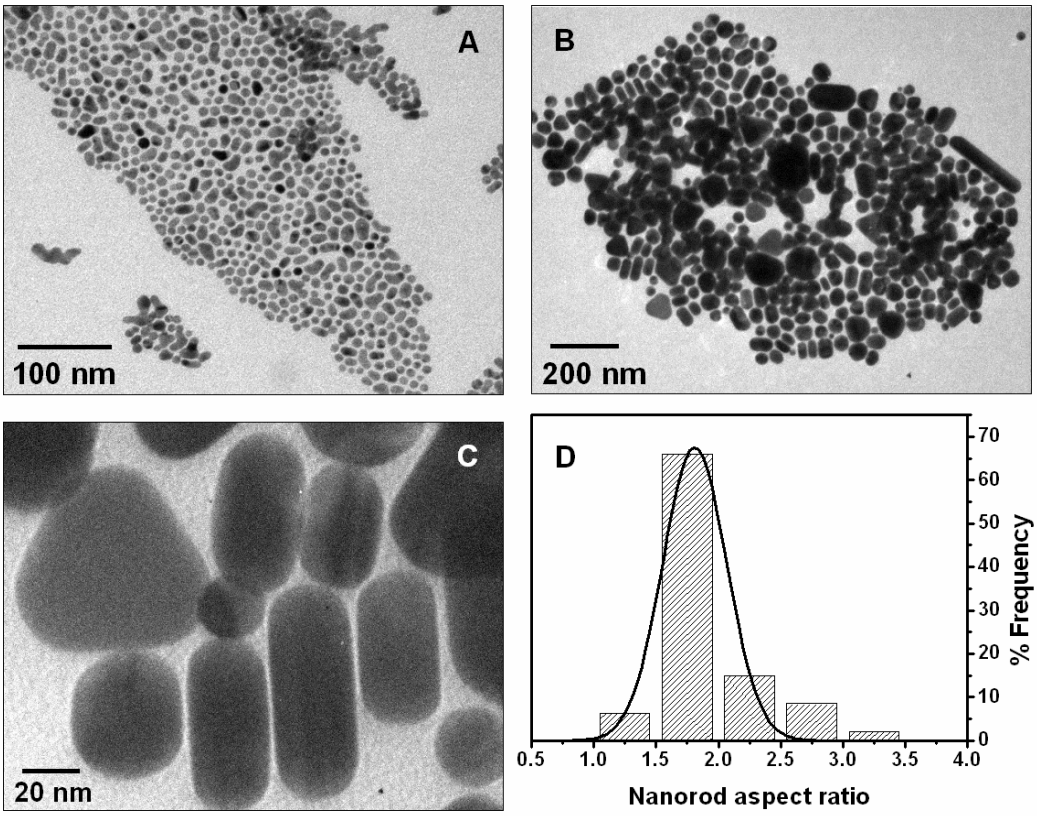

Figure 2.5: *Representative TEM images of HDA capped gold nanoparticle seeds (A) and of the gold nanoparticles formed when 7 mL 10^{-3} M HDA capped gold nanoparticle seeds and 3 mL 10^{-3} M ODA hydrophobised chloroaurate ions in toluene react (B and C). The aspect ratio distribution (D) of gold nanorods shown in images (B) and (C) has been fitted to a Gaussian curve.*

Based on TEM analysis, the average length of the nanorods was determined to be 55.9 ± 14.1 nm. The width distribution was fitted satisfactorily to a bimodal distribution centred at 26.6 ± 3.2 nm and 41.5 ± 3.2 nm. The aspect ratio of these nanorods was measured to be 1.8 ± 0.3 (fig. 2.5D). It is interesting to note that there are high contrasting regions that run along the length of the nanorods (fig. 2.5C) and indicate that the particles are not single crystalline in nature [12a,20]. Further analysis regarding the crystal structure of the nanorods is obtained from HRTEM and electron diffraction analysis as described in section 2.2.6.

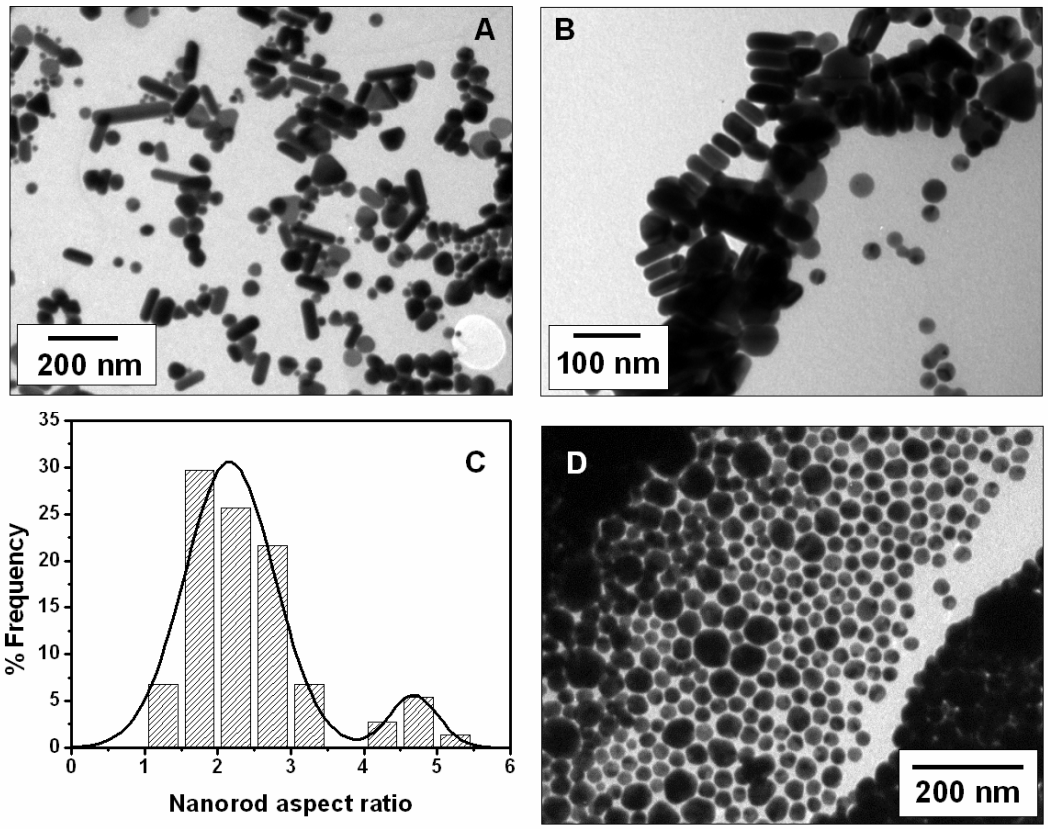

Figure 2.6: *(A) and (B) Representative TEM images of gold nanoparticles formed when 5 mL 10^{-3} M HDA capped gold nanoparticle seeds and 5 mL 10^{-3} M ODA hydrophobised chloroaurate ions in toluene react. (C) The aspect ratio distribution of these nanorods has been fitted to a Gaussian curve.(D) Shows a representative TEM image of gold nanoparticles formed when 1 mL 10^{-3} M HDA capped gold nanoparticle seeds and 9 mL 10^{-3} M ODA hydrophobised chloroaurate ions in toluene react.*

As the seed amount was decreased to 5 mL (in which case volume of 10^{-3} M ODA hydrophobised chloroaurate ions is 5 mL), relatively longer nanorods were formed (figs. 2.6A and 2.6B). Size distribution analysis based on these images and others indicate the mean length and width of the nanorods to be 79.5 ± 41.7 nm and 34.4 ± 11.8 nm respectively (fig. 2.6C). The nanorod aspect ratio distribution exhibited a bimodal behaviour with majority of the nanorods having an aspect ratio of 2.2 ± 0.6 and a smaller percentage having an aspect ratio of 4.7 ± 0.3. Thus it is observed that the amount of seed added initially to the growth solution determines the aspect ratio and dimensions of the nanorods formed (figs. 2.5 and 2.6). It can be observed that growth of the nanorods is accompanied by the formation of spherical particles and a small population of flat triangular or disc shaped nanoparticles. With further decrease of seed amount to 1 mL, the formation of large quasi spherical nanoparticles was observed (fig.

2.6D). This is due to the excess concentration of ODA present in the growth mixture as discussed in section 2.2.7. These results are summarised in table 2.1.

Table 2.1: *Summary of results when different amounts of HDA capped gold nanoparticle seeds were reacted with different amounts of octadecylamine hydrophobised chloroaurate ions.*

Nanoparticle system	**Morphology**	**Average size (nm)/ Aspect ratio (for nanorods)**	**Average length (nm)**	**Average width (nm)**
Aqueous Au nanoparticles (BH_4^- reduced)	Spheres	6.1 ± 2.5	-	-
HDA-Au nanoparticles	Spheres	11.0 ± 1.9 20.7 ± 1.5	-	-
7 mL 10^{-3}M HDA-Au + 3 mL 10^{-3}M ODA-$AuCl_4^-$	Nanorods + spheres	1.8 ± 0.3	55.9 ± 14.1	26.6 ± 3.2 41.5 ± 3.2
5 mL 10^{-3}M HDA-Au + 5 mL 10^{-3}M ODA-$AuCl_4^-$	Nanorods + spheres	2.2 ± 0.6 4.7 ± 0.3	79.5 ± 41.7	34.4 ± 11.8
1 mL 10^{-3}M HDA-Au + 9 mL 10^{-3}M ODA-$AuCl_4^-$	Large quasi-spherical nanoparticles	-	-	-

In reasonably monodisperse gold nanorods, the two plasmon bands observed are usually narrow and well separated [1a,5]. The broad absorbance patterns observed here can be attributed to two factors: low yield of the rods and a broad distribution of the nanorod dimensions. Consequently a series of experiments were done to examine the factors that affect nanorod growth. In concurrence with earlier reports [11], we speculate the shape directing ability of alkyl amine to be responsible for the formation of rod shaped particles during the seeded growth process. In order to establish the same, the chloroaurate ion phase transfer agents were varied.

2.2.5. Effect of chloroaurate ion phase transfer agent on seeded growth process

Murphy and co-workers have investigated the effect of chain length of the shape directing agent on the aspect ratio of gold nanorods formed. It was observed that greater chain lengths led to greater aspect ratios [21]. In the following set of experiments, HDA capped gold nanoparticle seeds were treated with chloroaurate ions hydrophobised using different phase transfer agents such as alkylamines of varying chain lengths and quaternary ammonium ion amphiphiles.

2.2.5.1. Alkylamines of varying chain lengths as chloroaurate ion phase transfer agents

The role of the chloroaurate ion phase transfer agent on the morphology of the nanoparticles formed was studied by employing alkylamines of different chain lengths. The molecules employed here were hexadecylamine, dodecylamine and octylamine.

In the first case, hexadecylamine hydrophobised chloroaurate ions were reacted with HDA capped gold nanoparticle seeds. A broad peak centred at 584 nm is observed in the UV-visible-NIR spectra (curve 2, fig. 2.7A). This is red shifted in comparison to the seed particles (curve 1, fig. 2.7A). TEM analysis of the products revealed the presence of spherical particles and a small population of rods and flat structures (fig. 2.7B). The presence of a small amount of rods and spherical nanoparticles in an aggregated form justifies the red shifted broad peak in the UV-visible-NIR absorbance spectra. The spherical particles are about 40 nm in size and indicate the occurrence of seeded growth on the HDA capped gold nanoparticle seeds (compare with fig. 2.2). In the second case when dodecylamine hydrophobised chloroaurate ions were reacted with HDA capped gold nanoparticle seeds, growth of nanorods was observed. This was concluded from TEM analysis which showed the presence of a large number of rods along with a small population of spherical nanoparticles (fig. 2.7C). UV-visible-NIR absorbance spectra revealed the surface plasmon peak centred at 570 nm characteristic of gold nanoparticles (curve 3, fig. 2.7A). The hump at 670 nm is attributed to the longitudinal surface plasmon resonance peak of gold nanorods that were formed (curve 3, fig. 2.7A). Size distribution analysis on the TEM images was used to determine the average length and width to be 132 ± 48.2 nm and 39.5 ± 6.4 nm. The aspect ratio of the gold nanorods was determined to be 2.9 ± 0.9 (fig. 2.7D).

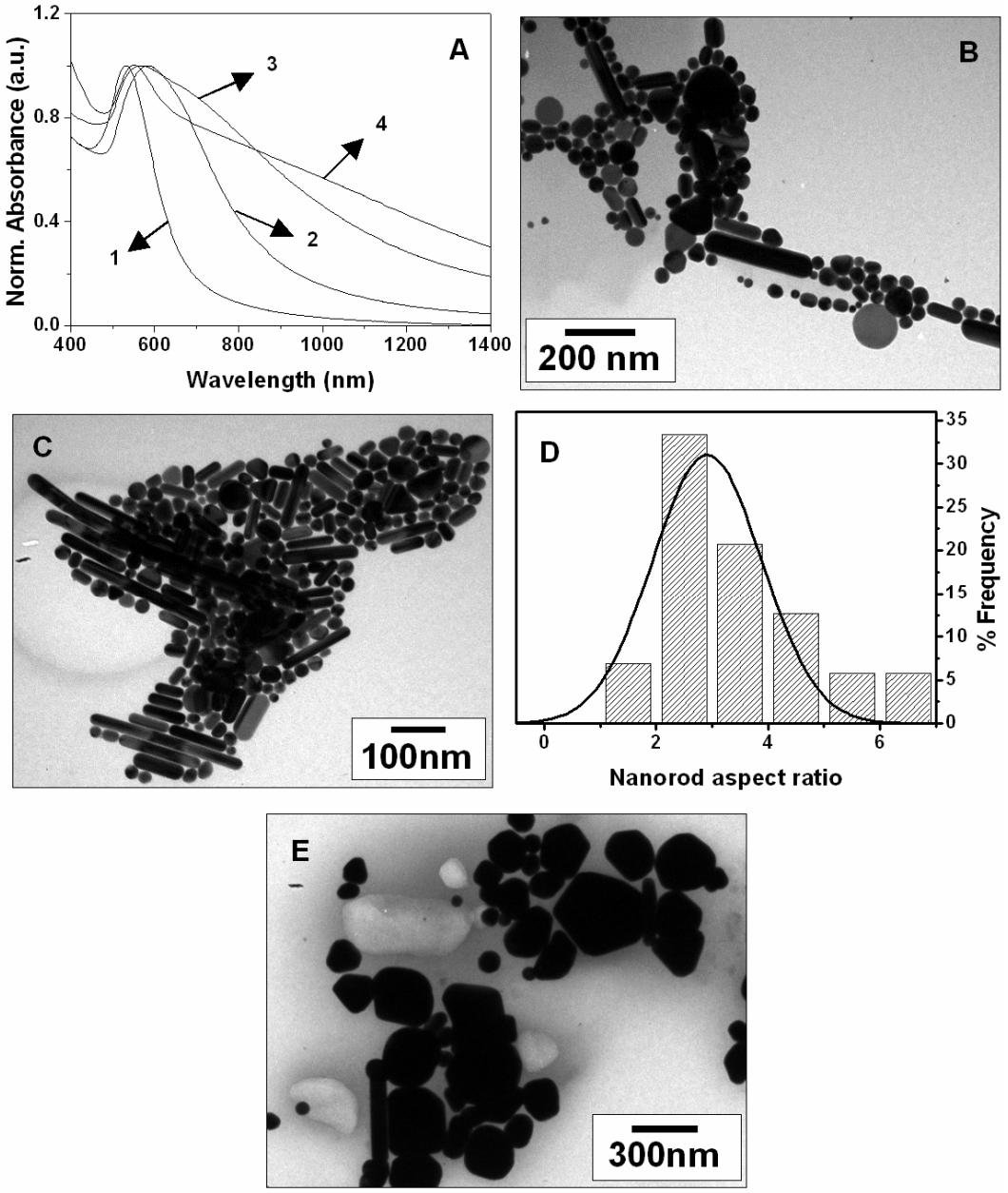

Figure 2.7: *(A) UV-visible-NIR absorbance spectra: curve 1 corresponds to HDA capped gold nanoparticle seeds. Curves 2, 3 and 4 correspond to samples shown in B, C and E respectively. (B) Representative TEM image of nanoparticles formed when 5 mL of 10^{-3} M hexadecylamine hydrophobised chloroaurate ions were reacted with 5 mL of 10^{-3} M HDA capped gold nanoparticle seeds.(C) Representative TEM image of nanoparticles formed when 3 mL of 10^{-3} M dodecylamine hydrophobised chloroaurate ions were reacted with 7 mL of 10^{-3} M HDA capped gold nanoparticle seeds. Aspect ratio distribution of the nanorods shown in (C) is fitted to a Gaussian curve in (D). (E) Representative TEM image of nanoparticles formed when 5 mL of 10^{-3} M octylamine hydrophobised chloroaurate ions were reacted with 5 mL of 10^{-3} M HDA capped gold nanoparticle seeds.*

In the final case when octylamine hydrophobised chloroaurate ions were reacted with HDA capped gold nanoparticle seeds, seeded growth led to the formation of nanoparticles of no particular shape. Very rarely the TEM grid revealed the presence of a nanorod but mostly aggregates of nanostructures were observed (fig. 2.7E). This again explains the surface plasmon resonance feature in the UV-visible-NIR absorbance spectrum wherein a peak at 550 nm and a broad absorbance in the NIR region was revealed (curve 4, fig. 2.7A). The broad feature in the NIR region occurs due to the aggregates that were formed. The results of the above experiment are summarized in table 2.2.

Table 2.2: *Summary of results when HDA capped gold nanoparticle seeds was reacted with chloroaurate ions hydrophobised using alkylamines of different chain lengths.*

Nanoparticle system	Morphology	Size details (average)
5 mL 10^{-3}M HDA-Au + 5 mL 10^{-3}M hexadecylamine-$AuCl_4^-$	Spherical nanoparticles and few nanorods	-
7 mL 10^{-3}M HDA-Au + 3 mL 10^{-3}M dodecylamine-$AuCl_4^-$	Nanorods	Aspect ratio – 2.9 ± 0.9 Length – 132 ± 48.2 nm Width – 39.5 ± 6.4 nm
5 mL 10^{-3}M HDA-Au + 5 mL 10^{-3}M octylamine-$AuCl_4^-$	Aggregated nanostructures	-

2.2.5.2 Quaternary ammonium ion amphiphiles as chloroaurate ion phase transfer agents

As in earlier cases, various amounts of HDA capped gold nanoparticle seeds were reacted with different amounts of chloroaurate ions phase transferred with quaternary ammonium amphiphiles. For brevity only relevant results are presented here. Curve 1 in fig. 2.8A shows the UV-visible-NIR absorbance spectrum of the nanoparticulate product formed when HDA capped gold nanoparticle seeds were reacted with BDSAC hydrophobised chloroaurate ions. A fall in the intensity of the surface plasmon resonance of the nanoparticulate solution centred at 534 nm, in comparison to HDA capped gold nanoparticle seeds (fig. 2.8A), is accompanied by a broad absorbance centred at 725 nm. Representative TEM image (fig. 2.8B) shows the

formation of highly faceted nanoparticles which are parts of larger aggregates. The presence of such aggregates accounts for the broad absorbance centred at 725 nm. Curve 2, fig. 2.8A shows the UV-visible-NIR absorbance of the nanoparticulate solutions formed when TOAB hydrophobised chloroaurate ions were reacted with HDA capped gold nanoparticle seeds. Apart from fall in the intensity of the surface plasmon absorbance band at 542 nm, in comparison to seed nanoparticles, an absorbance feature at 1010 nm is observed. TEM analysis of this sample (fig. 2.8C) shows the formation of long interconnected structures accounting for the absorbance at 1010 nm. This is in concurrence with reports where aggregated nanostructures are known to result in absorbance feature in the NIR region [17].

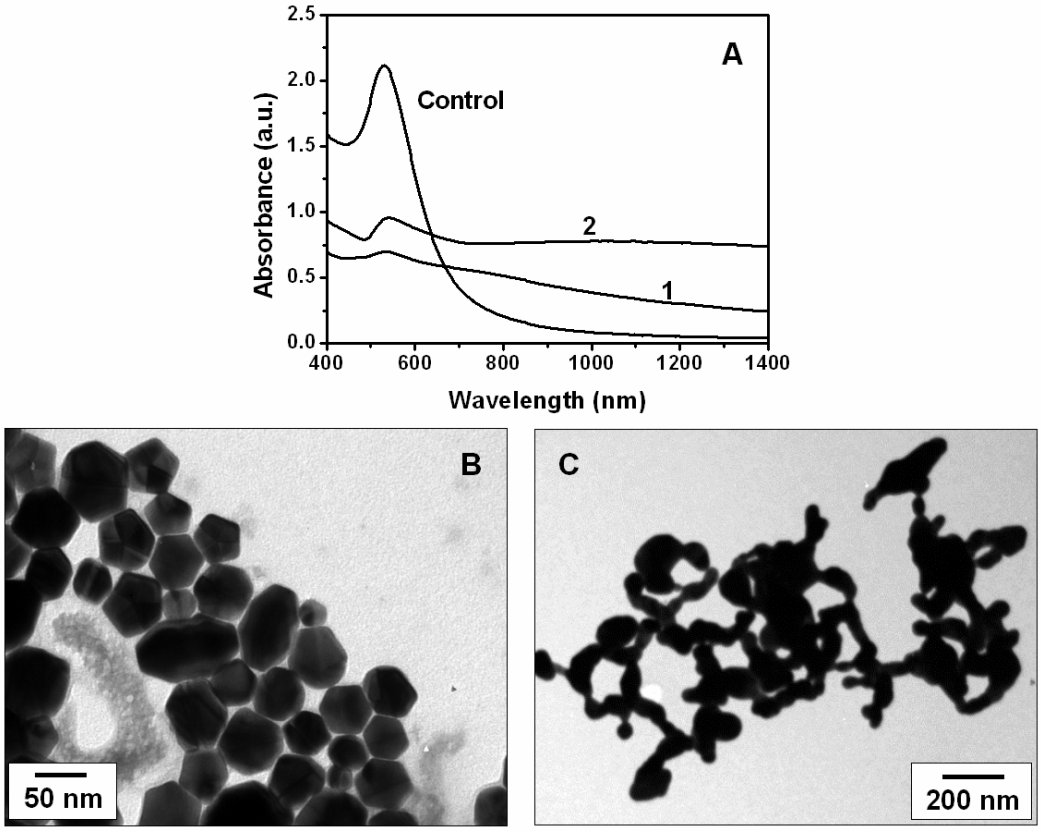

Figure 2.8: *(A) Curve labelled control corresponds to HDA capped gold nanoparticle seeds. Curve 1 shows the absorbance profile of the nanoparticulate product formed when 5 mL of 10^{-3} M BDSAC hydrophobised chloroaurate ions were reacted with 5 mL of 10^{-3} M HDA capped gold nanoparticle seeds. Curve 2 shows absorbance profile of the nanoparticulate product formed after 3 mL of 10^{-3} M TOAB hydrophobised chloroaurate ions react with 7 mL of 10^{-3} M HDA capped gold nanoparticle seeds. (B) Representative TEM image of sample corresponding to curve 1 in A. (C) Representative TEM image of sample corresponding to curve 2 in A.*

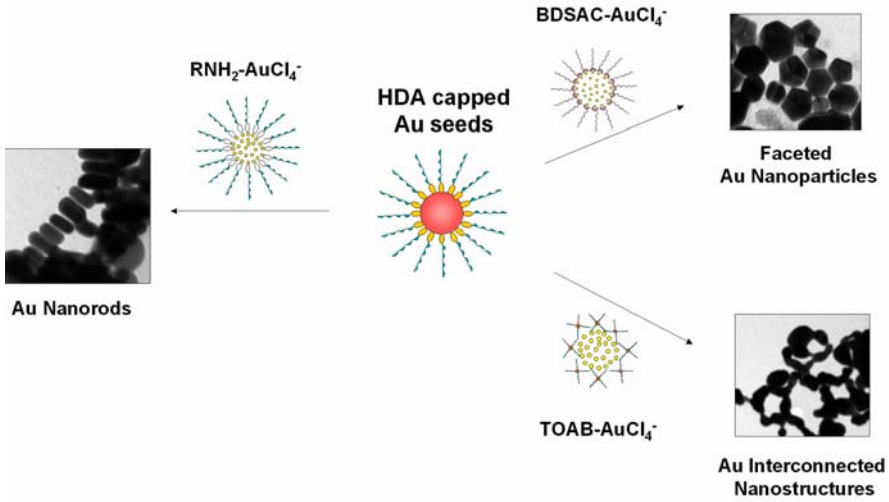

Figure 2.9: *Effect of nature of chloroaurate ion phase transfer agent on the morphology of the seeded growth product when HDA capped gold nanoparticle seeds was used.*

Results of the above experiments are summarised in fig. 2.9. It is clear from experiments carried out using alkylamines and quaternary ammonium ions as phase transfer agents that the presence of aliphatic amines is essential for the formation of gold nanorods. It is known that amines preferentially interact with specific crystallographic faces of gold nanoparticles [11]. In order to verify this, it is important to examine the surface crystallographic structure of the gold nanorods. The following section details HRTEM analysis and electron diffraction studies carried out on gold nanorods synthesised here.

2.2.6. HRTEM analysis of gold nanorods

Detailed HRTEM analysis to elucidate the structure of the gold nanorods was performed. Fig. 2.10A shows HRTEM image of a section of a gold nanorod synthesized by reacting HDA capped gold nanoparticle seeds and dodecylamine hydrophobised chloroaurate ions (see inset for a lower magnification image of the gold nanorod analyzed here). The image reveals {111} lattice fringes running along the longitudinal axis of the nanorod parallel to a {111} twin plane. Fig. 2.10B reveals the surface structure of the nanorod to be made up of a {200} face. This is evident from the lattice spacing and the square symmetry characteristic of a {200} face.

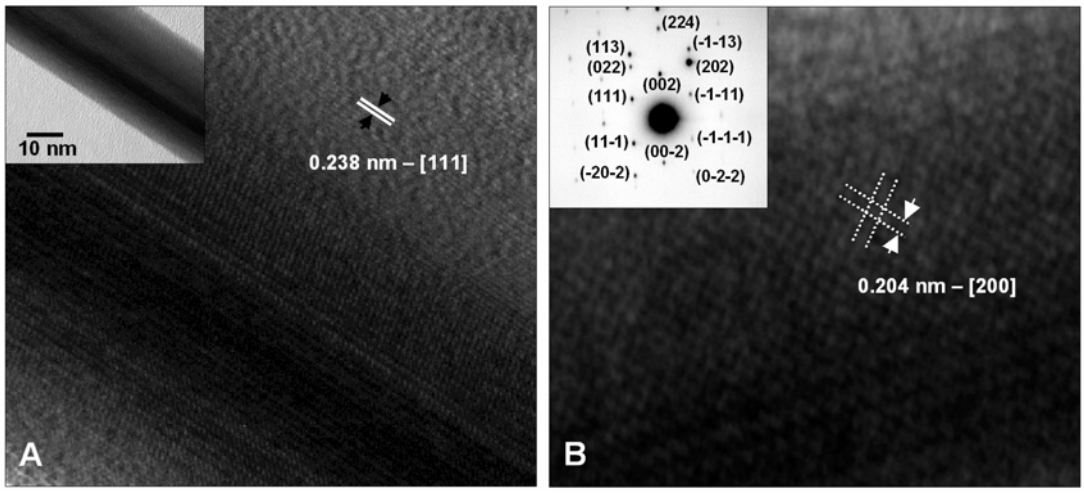

Figure 2.10: *HRTEM analysis: (A) shows a higher magnification image of the gold nanorod shown in the inset of (A). It can be seen that {111} lattice planes run parallel to {111} twin boundary along the length of the nanorod. (B) HRTEM image shows the surface of the nanorod to be made up of a {200} face. The square symmetry and d-spacing obtained are characteristic of {200} faces. Electron diffraction pattern shown in the inset of (B) originates from two different zone axes namely <-110> and <-1-11>.*

This is further supported by electron diffraction analysis (inset fig. 2.10B) performed on a single nanorod which shows a pattern originating from two different zone axis namely <-110> and <-1-11>. Such a structure is similar to what has been observed in gold nanorods synthesized in aqueous media [12a].

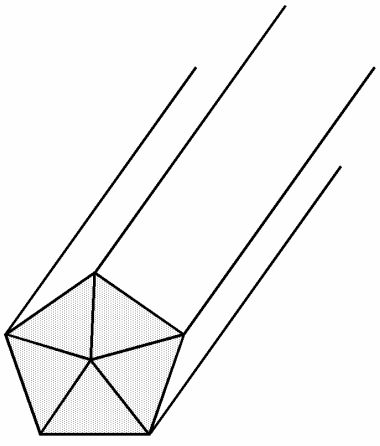

Figure 2.11: *Cartoon illustrating the crystallography of one end of the gold nanorod synthesized as described here. The nanorod has a five-fold symmetry and can be seen as a decahedral particle stretched along the common [110] axis. The nanorod is bound by five {111} faces at the tips (shaded region) and five {100} faces at the sides (plain region). Adapted from reference 12a.*

The gold nanorod can thus be visualized as a decahedral particle stretched along the common [110] axis. Such a particle with a five-fold symmetry axis is made up of five single crystal variants in contact with each other at {111} twin boundaries. The tip of such a particle has five {111} faces and the surface of the nanorod is bound by five {100} faces (see fig. 2.11 for a cartoon illustrating the structure of the nanorod).

2.2.7. Mechanism of growth of gold nanorods

From the experimental results described so far it can be summarised that 4-hexadecylaniline which passivate the gold nanoparticles, acts as the chloroaurate ion reducing agent leading to occurrence of seeded growth and nanorod formation.

The formation of gold nanorods is critically dependent on the concentration and chain length of the alkylamine phase transfer agent. Though there is a dependence of the nanorod dimension on chain length of the alkylamine used (compare results obtained with octadecylamine and dodecylamine – table 2.2), the lack of a trend cannot be explained. It is possible that the alkylamine amphiphiles organize themselves on the nanorod surfaces thus stabilizing them. The chain length variance could lead to differing degrees of stabilization thus affecting the yield and dimensions of the product. Such an explanation has already been invoked to explain the systematic dependence of gold nanorod dimensions on the surfactant chain length in an aqueous medium growth procedure [21]. It is also important to note that other experiments performed using quaternary ammonium amphiphiles as the chloroaurate ion phase transfer agent did not result in nanorod formation (fig. 2.8). Further, the necessity of primary alkyl amines for the formation of gold nanorods is unequivocally proved by the formation of nanorods when octadecylamine was used in combination with quaternary ammonium amphiphiles. This is illustrated as follows: To varying amounts of 10^{-3} M HDA capped gold nanoparticle seeds, different amounts of 10^{-3} M ODA-TOAB hydrophobised chloroaurate ions were added and the resultant solutions were studied using UV-visible-NIR absorbance and TEM. Fig. 2.12A shows the UV-visible-NIR absorbance profile of the nanoparticulate solutions. In the case corresponding to reaction of 5 mL of 10^{-3} M HDA capped gold nanoparticle seeds with 5 mL of 10^{-3} M hydrophobised chloroaurate ions (curve 3, fig. 2.12A) a shoulder appears at 670 nm apart from the red shifted surface plasmon absorbance at 550 nm. Further TEM analysis (fig. 2.12B) reveals the formation of nanorods. The mean nanorod width, length and aspect ratio were determined to be 75.5 ± 29.9 nm, 28.1 ± 4.7 nm and 2.5 ± 0.9 respectively (fig.

2.12C). A particular region where a collection of high aspect ratio nanorods was observed is shown in fig. 2.12B. It is important to note that rod formation is not observed in the absence of alkylamine (fig. 2.8B).

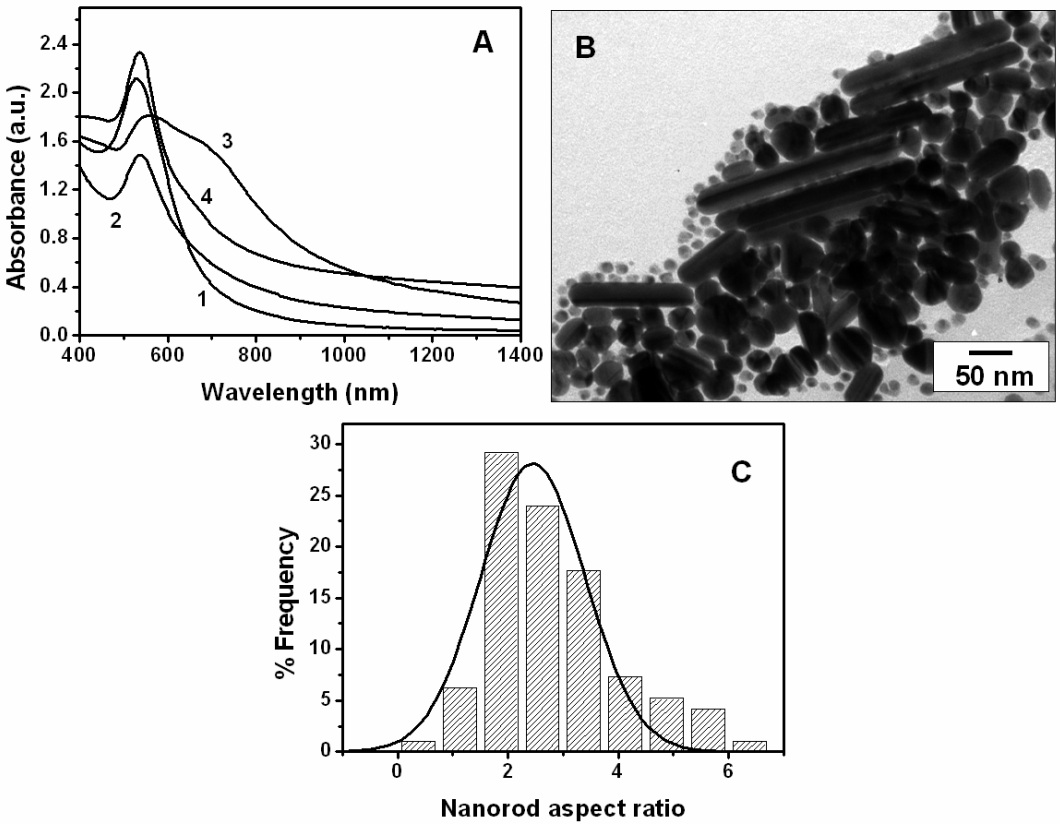

Figure 2.12: *(A) UV-visible-NIR absorbance spectra: curve 1 - HDA capped gold nanoparticle seeds; curve 2 – product formed when 2 mL of ODA-TOAB hydrophobised chloroaurate ions react with 8 mL of HDA capped gold nanoparticle seeds; curve 3 - product formed when 5 mL of ODA-TOAB hydrophobised chloroaurate ions react with 5 mL of HDA capped gold nanoparticle seeds; curve 4 - product formed when 8 mL of ODA-TOAB hydrophobised chloroaurate ions react with 2 mL of HDA capped gold nanoparticle seeds. (B) Representative TEM image of the sample corresponding to curve 3 in (A). (C)The aspect ratio distribution of gold nanorods shown in (B) is fitted to a Gaussian curve.*

Thus, it is seen that the presence of alkylamine amphiphiles is essential for the growth of gold nanorods. It is quite possible that alkylamines bind to specific crystallographic faces of the seed particles and further intermediates that are formed during the seed mediated process thus promoting the formation of gold nanorods. It is well known that the stability of the low index crystallographic faces of gold decreases in the order {111} > {100} > {110} [22]. It can be concluded that for the stability of gold nanorods with such a large exposure of the high energy {100} face as is the case

here, they need to be capped with stabilizing agents that are present in the reaction mixture. It is well documented that amines cap and stabilize gold nanoparticles [23]. Moreover, theoretical results indicate that amines bind to {100} faces with greater affinity in comparison to the {111} faces [11]. Such a binding will have a stabilizing effect on the {100} face and its greater surface exposure.

Based on these observations and our own results already described we conclude that the alkylamines employed here stabilize the {100} faces that are exposed during the growth of gold nanorods. Previous reports suggest that multiply twinned decahedral particles act as seeds for the formation of gold nanorods [12a]. Here too we believe that multiply twinned particles observed in the reaction mixture are likely to act as precursors for the nanorod growth. The gold adatoms formed due to the reducing action of HDA on chloroaurate ions deposit themselves on the {111} defect sites of the multiply twinned decahedral leading to growth along the common [110] axis. The {100} faces that are exposed during such a process are stabilized by the alkylamine amphiphiles present in the reaction environment thus restricting the growth in the [100] direction. The nanorods thus formed have five {111} faces at each of the tips and the five surface faces are bound by five {100} faces (see fig. 2.11).

The capping action of HDA can be ruled out based on the observation that in reactions wherein HDA was present along with quaternary ammonium amphiphiles, no nanorods were formed. The fact that the products formed are not all rods can be explained from the fact that not all seeds have the same multiply twinned structure. An examination of the HRTEM image of HDA capped gold nanoparticle seeds (fig. 2.13)

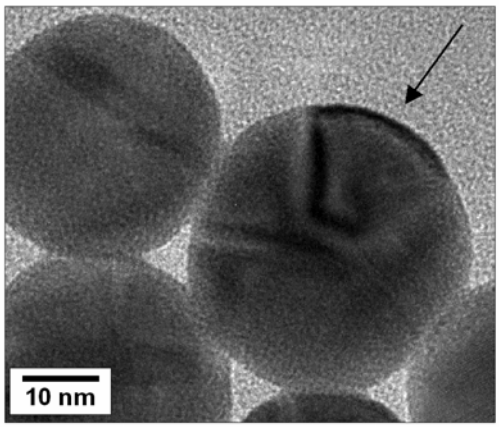

Figure 2.13: *Representative TEM image showing HDA capped gold nanoparticle seeds. The particle indicated by the arrow is the only one with a multiply twinned structure here.*

shows that not all particles have the multiply twinned decahedral structure. This highlights the role of seed structure in determining the final morphology of the products [5].

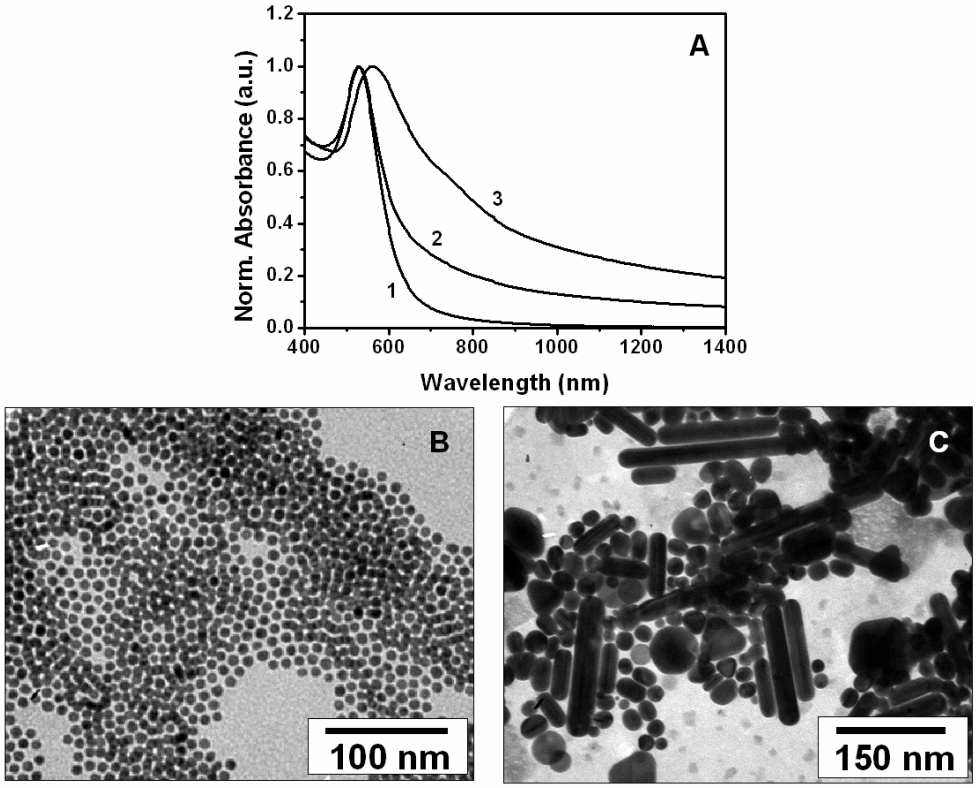

Figure 2.14: *Effect of concentration of dodecylamine: (A) curves 1, 2 and 3 correspond to UV-visible-NIR spectra of HDA capped gold nanoparticle seeds and nanoparticles shown in (B) and (C) respectively. (B) and (C) respectively are representative TEM images of nanoparticles formed when the seeded growth process was carried out with 10 times excess dodecylamine (10^{-2} M) and 10 times less dodecylamine (10^{-4} M) – See text for details.*

In order to validate our claim with regard to the surface directing ability of the alkylamine amphiphile, additional experiments were performed wherein the concentration of the amphiphile was varied keeping other parameters constant. It was observed that when HDA capped gold nanoparticle seeds were reacted with chloroaurate ions stabilized by 10^{-2} M dodecylamine (10 times excess amphiphile), only spherical nanoparticles were formed. This was evident from the nature of the surface plasmon absorbance in the UV-visible-NIR spectrum (curve 2, fig. 2.14A) and confirmed using TEM analysis (fig. 2.14B). On the other hand when the amount of the dodecylamine used was 10^{-4} M (10 times less), growth of anisotropic nanostructures was observed. TEM analysis of the products in this case revealed the presence of a

relatively small population of gold nanorods in the TEM grid and a smaller population of gold nanotriangles (fig. 2.14C). This observation of low nanorod yield also explains the lack of any prominent contribution from the longitudinal surface plasmon resonance of the gold nanorods to the UV- visible -NIR absorbance spectra (curve 3, fig. 2.14A) besides the slight broadening of surface plasmon peak in comparison to that of pure HDA capped gold nanoparticle seeds (curve 1, fig. 2.14A).

These observations can be explained based on the argument that excess dodecylamine amphiphile capping agent leads to indiscriminate binding of the amine to all the faces of the gold seed and intermediates formed thereof due to its high concentration. Spherical nanoparticles are formed as the end products of the seeded growth process since growth takes place in all directions with equal propensity. In reactions where the concentration of the amphiphile is low enough (10^{-3} M and 10^{-4} M) to facilitate selective binding to the high energy {100} faces, growth takes place by way of deposition of the adatoms of gold on the exposed {111} faces and the twin boundaries separating the same in the precursor MTPs.

In experiments with ODA as the chloroaurate ion phase transfer agent (section 2.2.4) wherein the concentration of ODA is high predominantly spherical nanoparticles are formed. These are actually instances where alkylamines bind indiscriminately with all the crystal faces of the seeds and the particles formed thereof. For instance addition of 1 mL of 10^{-3} M HDA capped gold nanoparticle seeds to 9 mL of 10^{-3} M ODA hydrophobised chloroaurate ions (fig. 2.6D) yielded only spherical nanoparticles as product of seeded growth. These observations are summarised in fig. 2.15.

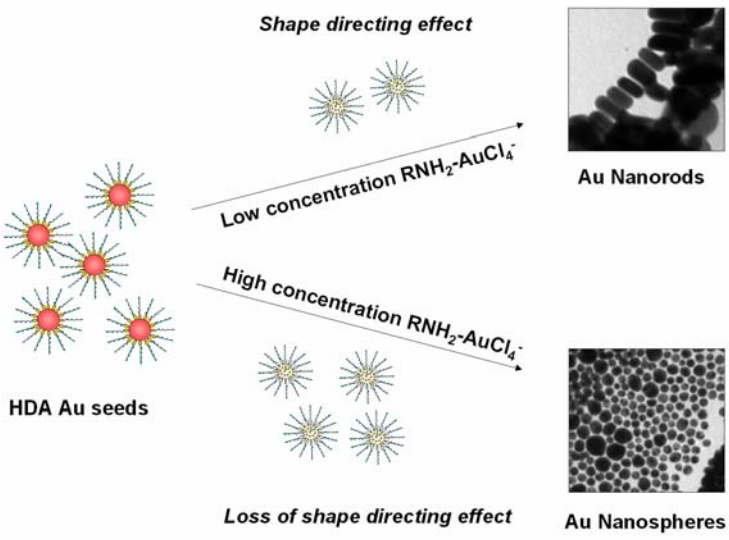

Figure 2.15: *Shape directing effect of alkylamines during seeded growth in toluene.*

2.3. Synthesis of gold nanorods in chloroform using ascorbic acid derivatives

In the second part of this chapter, we describe another organic media based seed mediated method for synthesis of gold nanorods using an ascorbic acid derivative as the reducing agent.

2.3.1. Experimental details

2.3.1.1. Synthesis of 5,6-*O*-Isopropylidene-2-*O*-tertadecyl-L-ascorbic acid (2AAIP)

2AAIP was provided by Dr. C. V. Ramana's group at NCL Pune, India. The following is the NMR characterisation of 2AAIP.

^{1}H NMR (200 MHz, $CDCl_3$) : δ 0.87 (t, 3H, J = 6.7 Hz), 1.25 (br s, 22H), 1.37 (s, 3H), 1.41 (s, 3H), 1.58-1.68 (m, 2H), 4.02 (dd, 1H, J = 6.9, 8.7 Hz), 4.07 (t, 2H, J = 7.0 Hz), 4.16 (dd, 1H, J = 6.9, 8.7 Hz), 4.41 (ddd, 1H, J = 3.2, 6.5, 9.8 Hz), 4.69 (d, 1H, J = 3.2 Hz) ppm. ^{13}C NMR (50 MHz, $CDCl_3$) : δ 14.2 (q), 22.7 (t), 25.3 (q), 25.6 (t), 25.8 (q), 29.4 (t), 29.5 (t), 29.7 (t), 29.7 (t), 31.9 (t), 65.0 (t), 71.9 (t), 73.8 (d), 74.5 (d), 96.1 (s), 110.5 (s), 121.8 (s), 156.6 (s), 170.2 (s) ppm. *Calcd. Mol. Wt. of* $C_{28}H_{31}N_3O_2$: 412.55, Found: 412. 58; FTIR: 3330 (s), 3293 (s), 2947 (m), 2871 (m), 1690 (m) and 1145 (m) cm^{-1}.

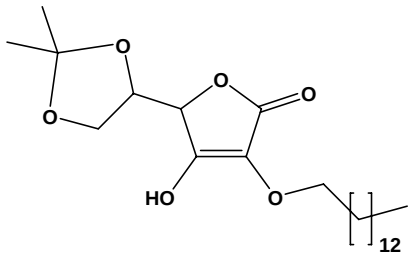

Figure 2.16: *Structure of 5,6-O-Isopropylidene-2-O-tertadecyl-L-ascorbic acid (2AAIP).*

2.3.1.2. Preparation of hydrophobised chloroaurate ions

In a typical reaction, 50 mL of aqueous 10^{-3} M $HAuCl_4$ was stirred with 50 mL 10^{-3} M of ODA in chloroform for a period of 2 h. This led to the phase transfer of chloroaurate ions to chloroform as evidenced by the complete transfer of yellow colour to the organic phase. The chloroform phase was separated to yield 10^{-3} M ODA hydrophobised chloroaurate ions.

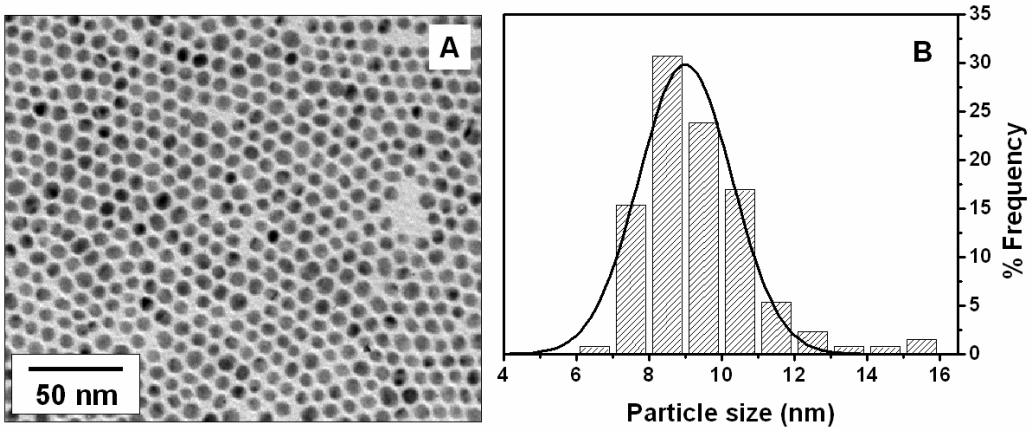

Figure 2.17: *Representative TEM image of ODA capped gold nanoparticles stabilised in chloroform (A) and their corresponding size distribution (B) fitted to a Gaussian curve.*

2.3.1.3 Preparation of hydrophobised gold nanoparticle seeds

In a typical reaction, 1 L of 10^{-4} M gold nanoparticles (prepared as outlined in section 2.2.1) were stirred vigorously with 100 mL of 10^{-3} M ODA in chloroform for 6 h. The complete phase transfer of the gold nanoparticles was seen by the aqueous solution turning colourless and the chloroform phase assuming a deep ruby red colour. The organic phase was thereafter separated and the concentration of gold nanoparticles in the same was taken to be 10^{-3} M. Fig. 2.17A shows a representative TEM image of the hydrophobised gold nanoparticle seeds prepared as outlined above. The average particle size was determined to be 9.0 ± 1.3 nm (fig. 2.17B).

2.3.1.4. Reduction of hydrophobised ions using ascorbic acid derivatives

In a typical seeded growth reaction procedure, varying amounts of seed solutions (10^{-3} M ODA capped gold nanoparticles) were added to 5 mL of 10^{-3} M ODA hydrophobised chloroaurate ions in chloroform. The seed amount was varied from 25 μL to 1000 μL. To this mixture 2 mg of 2AAIP (10^{-3} M) was added. The reaction mixture was allowed to stand for a period of 12 h before characterisation using UV-visible-NIR absorbance spectroscopy and TEM measurements.

The same reaction was carried out in the absence of seeds by mixing 5 mL of 10^{-3} M ODA hydrophobised chloroaurate ions in chloroform and 2 mg of 2AAIP (10^{-3} M). Here too the reaction mixture was allowed to stand for a period of 12 h before characterisation of the products formed using UV-visible-NIR absorbance spectroscopy and TEM measurements.

2.3.2. UV-visible-NIR absorbance and TEM characterisation

Fig. 2.18 shows the UV-visible NIR absorbance of nanoparticulate products formed when hydrophobised chloroaurate ions were reduced using 2AAIP under the influence of ODA capped gold nanoparticle seeds. Whereas ODA capped seeds exhibit a single peak at 524 nm (curve 1, fig. 2.18) due to surface plasmon resonance, the product of the seeded growth with 25 μL of seed shows two peaks at 536 nm and 580 nm (curve 2, fig. 2.18). It can be concluded that the excess chloroaurate ions that are added to the reaction mixture are reduced leading to formation of newer nanostructures. The reducing action of ascorbic acid is well documented and forms the basis for well established protocols for the preparation of gold nanostructures [1a-e,6]. The multiple resonances observed are characteristic of nanostructures that are either aggregates of smaller particles or are anisotropically shaped like rods and triangles [17,24]. The products formed with greater amount of seed show broad absorbance. No discrete multiple resonances were observed in contrast to the case when low amount of seed was present (curve 2, fig. 2.18). For instance when the amount of seed used was 500 μL, the absorbance maxima occurred at 556 nm (curve 3, fig. 2.18). The same shifted to 563 nm (curve 5, fig. 2.18) when 1000 μL of seed was used in the reaction mixture.

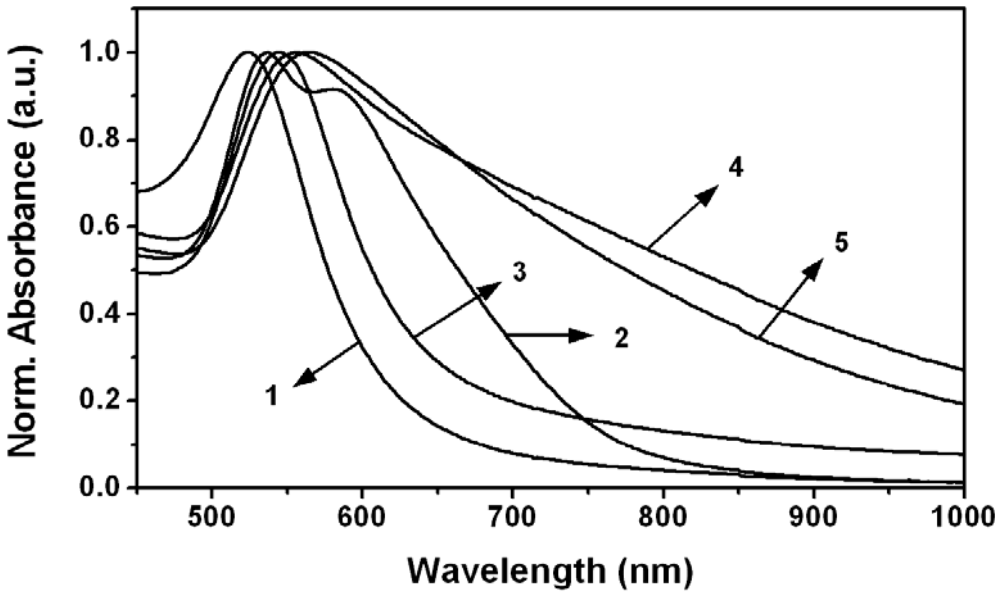

Figure 2.18: *Curve 1 shows the absorbance profile of ODA capped gold nanoparticles. Curves 2 - 5 respectively show the UV-visible-NIR absorbance profiles of products formed when the amount of seed added to the growth solution were 25 μL, 250 μL, 500 μL and 1000 μL. All spectra have been normalised w.r.t their absorbance maxima occurring in the region from 500 to 570 nm. See text for details.*

Transmission electron microscopy was employed to study the morphology of the particles formed. Fig. 2.19A shows the presence of gold nanorods in the reaction mixture when 25 µL of ODA capped gold nanoparticle seeds was used. This explains the occurrence of the two resonance peaks in the UV-visible-NIR absorbance spectra of this sample (curve 2, fig. 2.18). The peak at 536 nm and 580 nm respectively correspond to absorbance arising due to transverse and longitudinal surface plasmon resonances. The nanorods length was determined to be 62.8 ± 6.1 nm. The distribution of widths was fitted to a bimodal distribution yielding average widths of 33.7 ± 2.8 nm and 43.7 ± 2.8 nm. The mean aspect ratio was determined to be 1.6 ± 0.3 (fig. 2.19B). Earlier reports of nanorod synthesis have demonstrated tunability in the dimensions, aspect ratio and hence the UV-visible-NIR absorbance properties of the gold nanorods formed by varying the amount of seed used [1a]. However in the present procedure, we observe that when higher amount of seed (500 µL) was used, only a few nanorods were formed. This is evident from fig. 2.19C which also reveals the presence of aggregates. Consequently the broad absorbance observed for such cases can be explained (curve 4, fig. 2.18).

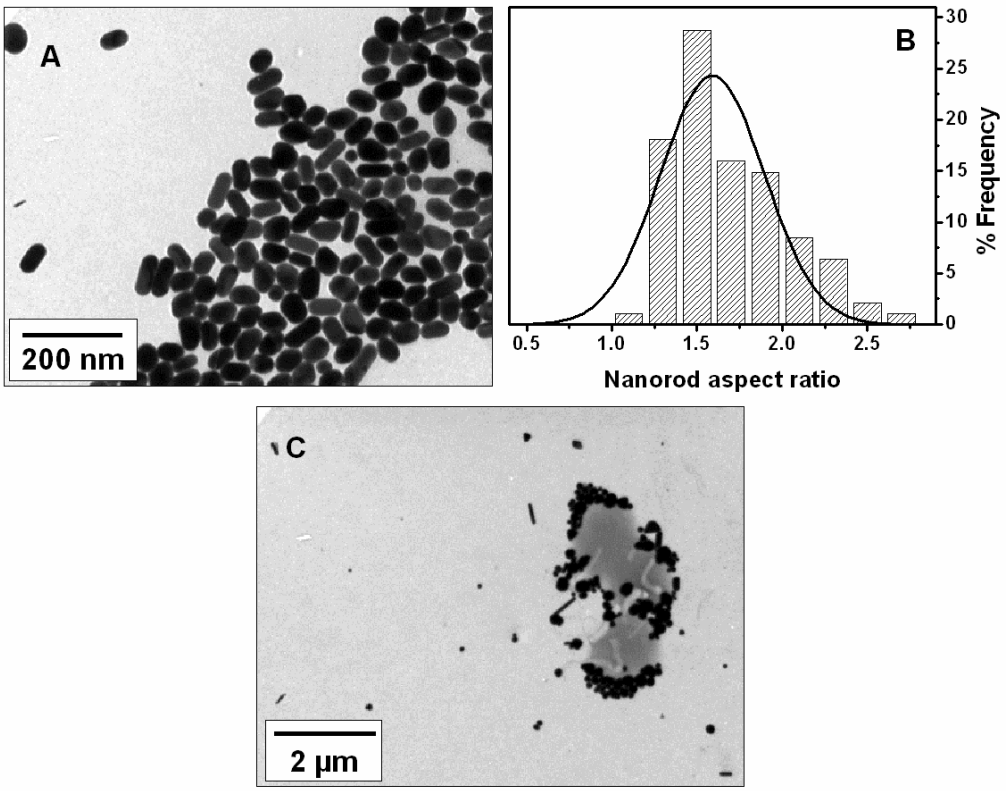

Figure 2.19: *Representative TEM images of the nanoparticulate products formed when the amount of seed in the reaction mixture was (A) 25 µL and (C) 500 µL. (B) shows the distribution of aspect ratio of the nanorods shown in (A) fitted to a Gaussian curve.*

It can be seen that in comparison to the dimension of the seed particles (average diameter 9.0 ± 1.3 nm), the length and width of the gold nanorods are greater indicting that growth occurs selectively along certain crystallographic directions of the seed particles resulting in the formation of gold nanorods. To study the crystallographic structure of the particles formed, the particles shown in fig. 2.19A were subjected to HRTEM and electron diffraction analysis.

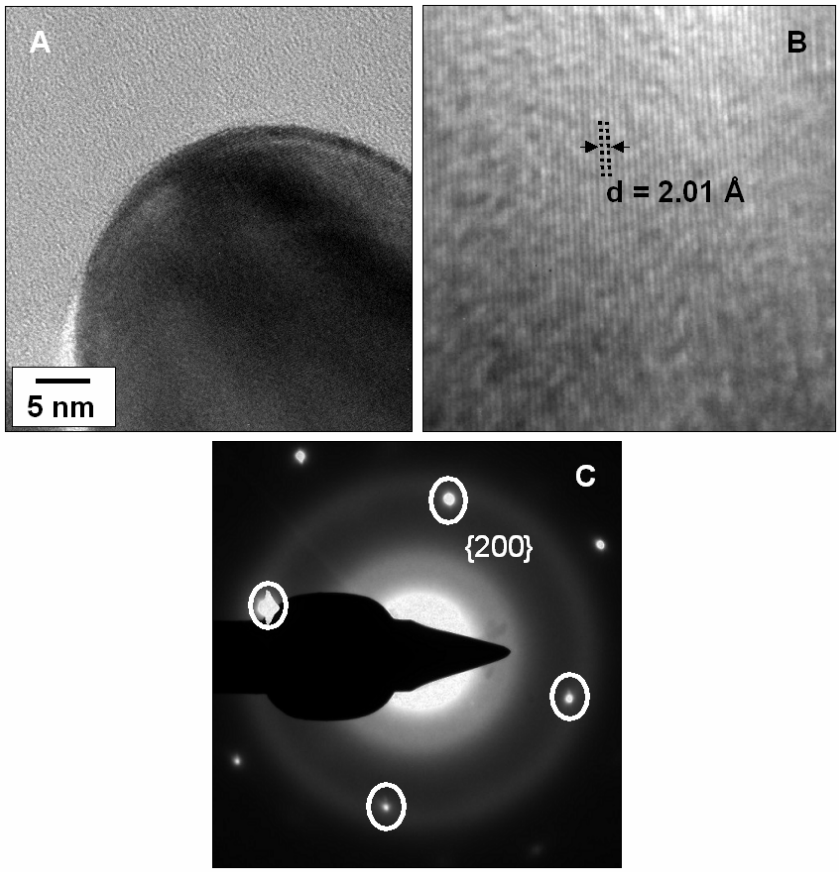

Figure 2.20: *A low magnification HRTEM image of gold nanorods prepared by the reductive action of 2AAIP in the presence of 25 µL of seed. B is a higher magnification HRTEM image showing the {200} lattice fringes of FCC gold. C shows the SAED from a single gold nanorod indicating its single crystalline nature. See text for details.*

Fig. 2.20A shows a nanorod tip imaged using HRTEM. The un-uniform contrast suggests that the nanorods either have a defect feature or have a facetted single crystalline structure. The relatively high energy {200} face is exposed at the surface of the nanorod. This is seen from fig. 2.20B wherein the lattice fringes corresponding to {200} Miller planes (d = 2.01 Å) are visible. The single crystalline nature of the gold

nanorod is seen from the SAED pattern shown in fig. 2.20C. The pattern corresponds to a [100] zone axis [12a,25]. Thus it is evident that the surface of the gold nanorods is comprised of {100} miller planes. The contrast seen in fig. 2.20A is thus due to the facetted nature of the gold nanorod. Single crystalline facetted gold nanorods have been reported earlier [1a]. These were synthesised either electrochemically [1a] or under the influence of silver ions [1a,e]. The surfaces of the single crystalline nanorods in these cases were bound by the {100} and the higher energy {110} crystallographic faces. In the present case (figs. 2.20B and 2.20C), the nanorod could be resting on the TEM grid in such a way that only the {100} surface is exposed. It is seen that in anisotropic nanoparticles of gold, silver and copper, relatively high energy low index planes are exposed [1a-b,12,25,26]. The stabilising effect of capping agents is invoked to explain the stability of this. Here too it can be tentatively said that presence of amines (ODA) could play a role in stabilising the high energy surfaces. It is known that amines interact with certain crystallographic faces of gold nanoparticles and stabilise the same [11,23]. This was also observed during the seeded growth of nanorods from HDA capped gold nanoparticle seeds in section 2.2.7 (fig. 2.14).

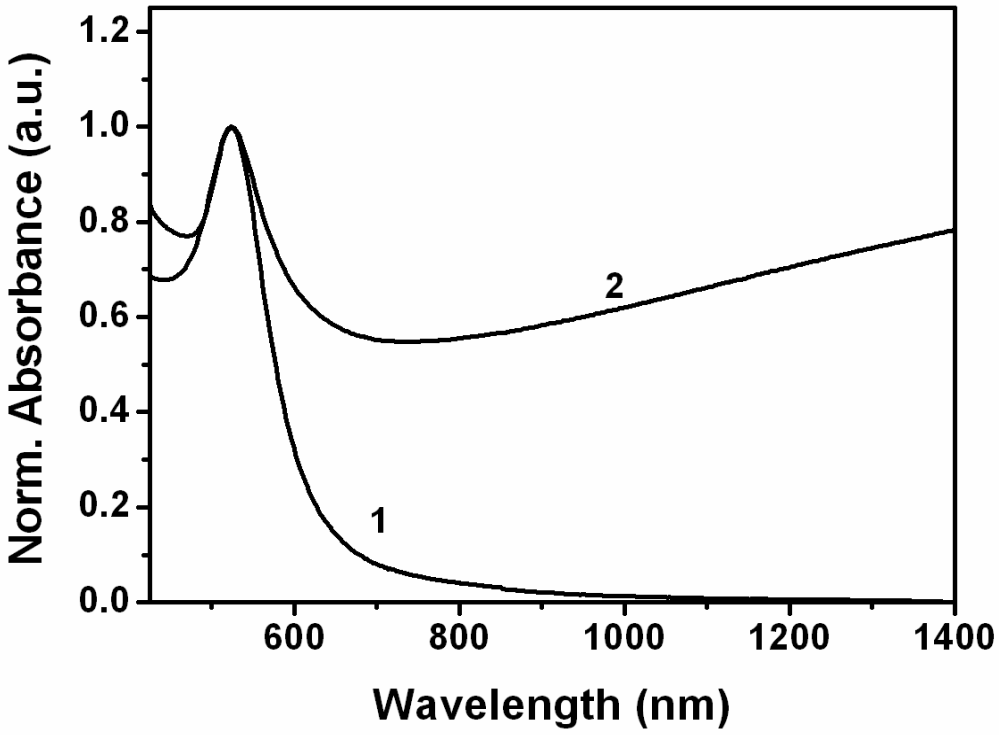

Figure 2.21: *UV-visible-NIR absorbance spectra of nanoparticles (2) formed when 2AAIP was reacted with hydrophobised chloroaurate ions in the absence of seeds. Curve 1 corresponds to ODA capped gold nanoparticles.*

Reaction of 2AAIP with chloroaurate ion was carried out in the absence of gold nanoparticle seeds to ascertain the role played by the seed particles. The product formed when 10^{-3} M of 2AAIP were reacted with 5 mL of 10^{-3} M chloroaurate ions was characterised using UV-visible-NIR spectroscopy (curve 2, fig. 2.21). For comparison the curve is overlaid with the UV-visible-NIR absorbance profile of ODA capped gold nanoparticles (curve 1, fig. 2.21). The intense absorption in the NIR region reflects the anisotropic nature of the product formed (curve 2, fig. 2.21).

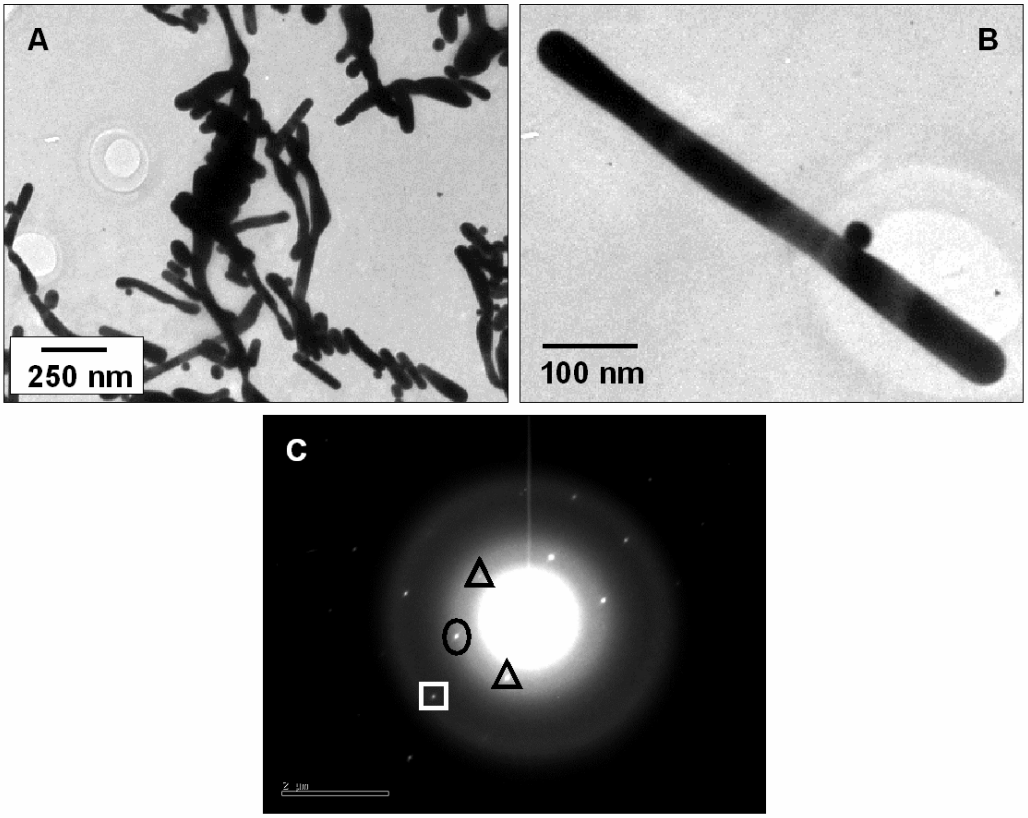

Figure 2.22: *(A) and (B) Representative TEM images show the formation of gold nanorods and elongated structures due to the reductive action of 2AAIP on chloroaurate ions in absence of seed. (C) SAED from a single nanorod as shown in B. Diffraction from {111}, {200} and {311} are highlighted using triangles, oval and square respectively.*

TEM analysis of the product shows formation of gold nanorods and elongated nanostructures (figs. 2.22A and 2.22B) due to the reductive action of 2AAIP on chloroaurate ions. It is seen that the particles are characterised by non uniform surfaces (figs. 2.22A and 2.22B). Such particle surfaces are usually characterised by the presence of atomic steps [5,27]. Also a large population of the structures have a bent shape. These structures justify the UV-visible-NIR profile as seen in fig. 2.21. This is

in concurrence with reports wherein elongated structures and rods with non-uniform surfaces have an intense absorbance in the NIR region [27]. SAED from a single nanorod (fig. 2.22C) shows its single crystalline nature. The pattern here corresponds to a [110] zone axis. The reflections could be indexed to FCC gold and indicate that the surface is comprised of the high energy {220} planes [12a]. Here too we speculate the faceting of the surface of the single crystalline gold nanorod to reveal high energy planes such as the {110} Miller planes which are stabilised by the presence of aliphatic amines (ODA). It is seen here that though gold nanorods and elongated structures are formed in the absence of seed particles, the nanoparticles formed lack a definite shape as is the case with seeded growth (figs. 2.19 and 2.20). Thus, we see that the seed particles play an important role in determining the size, shape and structure of the product. Further studies and HRTEM analysis are required to elucidate the mechanism of formation and stabilisation of the gold nanorods formed due to the reductive action of the ascorbic acid derivative 2AAIP.

2.4. Conclusions

The chapter describes two novel methods for seed mediated growth of gold nanostructures, with particular interest in gold nanorods, formed in organic media such as chloroform and toluene. In the first case where HDA capped gold nanoparticles are used as seeds the nanorods formed are composed of five single crystal variants. Each of these is separated by {111} twin boundaries. They have a five-fold symmetry and evolve from decahedral multiply twinned particles as they grow in the common [110] direction. The nanorods are bound at the tips by five {111} faces and at the sides by {100} faces. Considerable evidence has been presented to show that the nanorods grow under the shape directing influence of alkylamines that stabilize the high energy {100} faces. The concentration of the alkylamine plays a critical role as a higher concentration of the same lead to the predominant formation of spherical nanoparticles. The hydrophobicity of such alkylamines seems to be an important factor as octylamine with a considerably small hydrophobic chain yields negligible quantity of nanorods.

In the second case where reduction of hydrophobised chloroaurate ions was carried out under the influence of an ascorbic acid derivative (2AAIP), single crystalline gold nanorods are formed. The reductive action of 2AAIP in the presence and absence of seed yielded structures with the higher energy faces of FCC gold {200} and {220} being exposed. We speculate the stabilising action of alkylamines used as

phase transfer agents to be responsible for this. However the mechanism of formation of such single crystalline nanorods in this case in comparison to rods comprising of defect structure in the former case needs to be established.

2.5. References

[1] (a) Perez-Juste, J.; Pastoriza-Santos, I.; Liz-Marzan, L. M.; Mulvaney, P. *Coord. Chem. Rev.* **2005**, *249*, 1870. (b) Grzelcak, M.; Perez-Juste, J.; Mulvaney, P.; Liz-Marzan, L. M. *Chem. Soc. Rev.* **2008**, *37*, 1783. (c) Murphy, C. J.; Sau, T. K.; Gole, A. M.; Orendorff, C. J.; Gao, J.; Gou, L.; Hunyadi, S. E.; Li, T. *J. Phys. Chem. B* **2005,** *109,* 13857. (d) Murphy, C. J.; Sau, T. K.; Gole, A. M.; Orendorff, C. J.; Gao, J.; Gou, L.; Hunyadi, S. E.; Li, T. *J. Phys. Chem. B* **2005,** *109,* 13857. (e) Nikoobakht, B.; El-Sayed, M. A. *Chem. Mat.* **2003**, *15*, 1957. (f) Kim, F.; Song, J, H.; Yang, P. *J. Am. Chem. Soc.* **2002**, *124*, 14316.

[2] (a) Murphy, C. J.; Gole, A. M.; Hunyadi, S. E.; Stone, J. W.; Sisco, P. N.; Alkilany, A.; Kinard, B. E.; Hankins, P. Chem. Commun. 2008, 544. (b) Sudeep, P. K.; Joseph, S. T. S.; Thomas, K. G. *J. Am. Chem. Soc.* **2005**, *127*, 6516. (c) Eustis, S.; El-sayed, M. A. *Chem. Soc. Rev.* **2006**, *35*, 209. (d) Hutter, E.; Fendler, J. H. *Adv. Mater.* **2004**, *16*, 1685.

[3] Lofton, C.; Sigmund, W. *Adv. Func. Mater.* **2005**, *15*, 1197.

[4] Perez-Juste, J.; Liz-Marzan, L. M.; Carnie, S.; Chan, D. Y. C.; Mulvaney, P. *Adv. Funct. Mater.* **2004**, *14*, 571.

[5] Liu, M.; Guyot-Sionnest, P. *J. Phys. Chem. B* **2005**, *109*, 22192.

[6] Murugadoss, A.; Pasricha, R.; Chattopadhyay, A. *J. Colloid Interface Sci.* **2007**, *311*, 303.

[7] Miranda, O. R.; Dollahon, N. R.; Ahmadi, T. S. *Cryst. Growth Des.* **2006**, *6*, 2747.

[8] (a) Pastoriza-Santos, I.; Perez-Juste, J.; Liz-Marzan, L. M. *Chem. Mater.* **2006**, *18*, 2465. (b) Mitamura, K.; Imae, T.; Saito, N.; Takai, O. *J. Phys. Chem. B* **2007**, *111*, 8891.

[9] Jana, N. R.; Gearheart, L.; Murphy, C. J. *Chem. Mater.* **2001**, *13*, 2313.

[10] (a) Selvakannan, PR.; Mandal, S.; Pasricha, R.; Adyanthaya, S. D.; Sastry, M. *Chem. Commun.* **2002**, 1334. (b) Selvakannan, PR.; Kumar, P. S.; More, A. S.; Shingte, R. D.; Wadgaonkar, P.; Sastry, M. *Adv. Mater.* **2004**, *16*, 966. (c) Subramaniam, C.; Tom, R. T.; Pradeep, T. *J. Nanopart. Res.* **2005**, *7*, 209.

[11] Pong, B. K.; Lee, J. Y.; Trout, B. L. *Langmuir* **2005**, *21*, 11599

[12] (a) Johnson, C. J.; Dujardin, E.; Davis, S. A.; Murphy, C. J.; Mann, S. *J. Mater. Chem.* **2002**, *12*, 1765. (b) Kou, X.; Zhang, S.; Tsung, C. –K.; Yang, Z.; Yeung, M. H.; Stucky, G. D.; Sun, L.; Wang, J.; Yan, C. *Chem. Eur. J.* **2007**, *13*, 2929.

[13] Vemula, P. K.; Aslam, U.; Mallia, V. A.; John, G. *Chem. Mater.* **2007**, *19*, 138.

[14] (a) Yao, H.; Minami, T.; Hori, A.; Koma, M.; Kimura, K. *J. Phys. Chem. B* **2006**, *110*, 14040. (b) Prasad, B. L. V.; Stoeva, S. I.; Sorensen, C. M.; Klabunde, K. J. *Chem. Mater.* **2003**, *15*, 935.

[15] Link, S.; El-Sayed, M. A. *J. Phys. Chem. B* **1999**, *103*, 8410.

[16] Esumi, K.; Matsuhisa, K.; Torigoe, K. *Langmuir* **1995**, *11*, 3285.

[17] Jain, P. K,; Huang, W.; El-Sayed, M. A. *Nano Lett.* **2007**, *7*, 2080.

[18] Chandran, S. P.; Chaudhary, M.; Pasricha, R.; Ahmad, A.; Sastry, M. *Biotechnol. Prog.* **2006**, *22*, 577.

[19] Martin, C. R. *Chem. Mater.* **1996**, *8*, 1739.

[20] Gai, P. L.; Harmer, M. A. *Nano Lett.* **2002**, *2*, 771.

[21] Gao, J.; Bender, C. M.; Murphy, C. J. *Langmuir* **2003,** *19,* 9065.

[22] Elechiguerra, J. L.; Reyes-Gasga, J.; Yacaman, M. J. *J. Mater. Chem.* **2006**, *16*, 3906.

[23] (a) Kumar, A.; Mandal, S.; Selvakannan, PR.; Pasricha, R.; Mandale, A. B.; Sastry, M. *Langmuir* **2003**, *19*, 6277. (b) Leff, D. V.; Brandt, L.; Heath, J, R. *Langmuir* **1996**, *12*, 4723.

[24] Kelly, K. L.; Coronado, E.; Zhao, L. L.; Schatz, G. C. *J. Phys. Chem. B* **2003,** *107,* 668.

[25] Wiley, B.; Sun, Y.; Mayers, B.; Xia, Y. *Chem. Eur. J.* **2005**, *11*, 454.

[26] Lisiecki, I.; Filankembo, A.; Sack-Kongehl, H.; Weiss, K.; Pileni, M, -P.; Urban, J. *Phys. Rev. B* **2000**, *61*, 4968.

[27] Ryu, H. J.; Sanchez, L.; Keul, H. A.; Raj, A, Bockstaller, M. R. *Angew. Chem. Int. Ed.* **2008**, *47*, 7639.

Chapter 3

Interfacial synthesis of Au@Ag core-shell nanoparticles

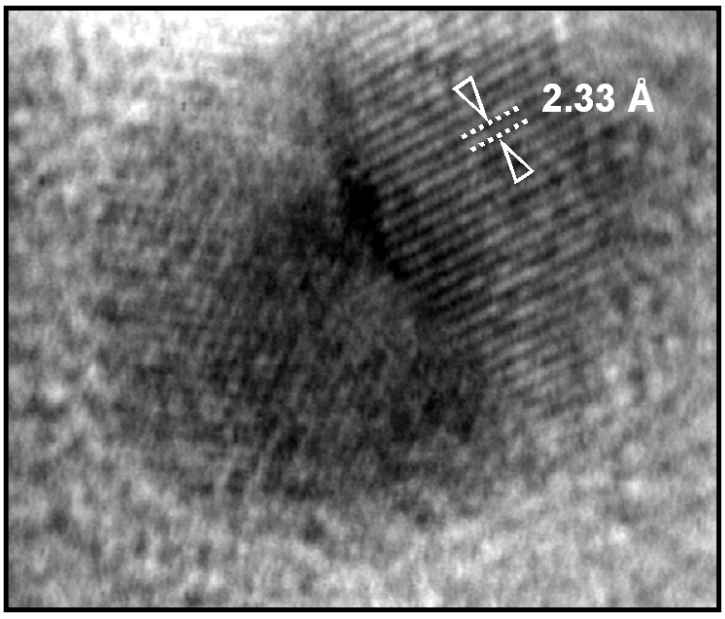

A seed mediated procedure for the synthesis of hydrophobic Au@Ag core-shell nanoparticles in toluene is demonstrated. The reaction proceeds by way of the interfacial reduction of aqueous silver ions by 3-pentadecylphenol followed by their deposition on hydrophobised gold nanoparticles. The reaction that exclusively yields Au@Ag core-shell nanoparticles was studied using UV-visible absorption spectroscopy and FTIR spectroscopy. TEM measurements, as a function of time, showed step-wise growth of the silver layer and examination of HRTEM images confirmed the core-shell morphology. Further evidence for the core-shell structure was obtained using XPS studies.

Part of work discussed in this chapter has been published in

Prathap Chandran, S.; Ghatak, J.; Satyam, P. V.; Sastry, M. *J. Colloid Interface Sci.* **2007**, *312*, 498-505.

3.1. Introduction

Core-shell nanoparticles form an important class of nanostructures where the core and the shell differ in their chemical composition [1]. The ability to design such a multi-component system has enabled their utility in variety of applications such as therapeutics [2-4], design of optoelectronic [5], magnetic [6] and semiconductor [7] materials. Apart from these, interesting applications in phase transfer protocols have been conceptualized. For instance, Sastry and co-workers in an interesting approach coated magnetically important nickel nanoparticles with a thin shell of silver thereby enabling their phase transfer to organic media which is otherwise not possible [8a]. Core shell Au@SiO_2 nanorod structures have also been used to facilitate phase transfer [8b].

Noble metal core-shell nanostructures have attracted attention by virtue of their interesting optical and electronic properties. Both Ag@Au core-shell [9-11] and Au@Ag core-shell [12-17] nanoparticles have been synthesized by a variety of methods. Silver nanoparticles possess relatively less stability in comparison to gold nanostructures and consequently tend to aggregate under biological conditions such as high salt concentration. Depositing a thin layer of gold on silver nanoparticles combines the optical properties of silver (essential for applications such as SERS) and the stability of gold. This enables their usage in applications such as oligo-nucleotide conjugation [11]. Conversely, carefully controlled deposition of silver on gold nanoparticles leading to the preparation of Au@Ag core-shell nanoparticles helps in controlling the SERS signal enhancement seen in such systems [12]. Some of the strategies followed for the synthesis of core-shell structures include deposition of the shell on the surface of a pre-formed seed [9,11], utilization of surface bound reducing agent [16-17], layer by layer deposition [18-19] of the shell material on to the surface of the core nanoparticle to state a few.

Although a variety of strategies exist for the synthesis of noble metal core-shell nanostructures, they have been primarily accomplished in the aqueous phase. Hardly any protocol exists for the synthesis of the same in organic media though utilization of appropriate phase transfer agents has enabled phase transfer of these nanoparticles to the organic media [8,17]. Organic media based procedures are significant due to: relevance in film forming applications, flexibility in surface functionality that can be achieved and catalytic applications [20,21]. Recently however Au@Ag core-shell nanoparticles have been synthesized in the organic media by way of a galvanic

exchange reaction [22]. In this chapter, we investigate an interfacial seed mediated growth procedure leading to the formation of phase pure Au@Ag core-shell nanoparticles in toluene. Gold nanoparticles stabilized in organic media act as seeds for the deposition of metallic silver leading to the formation of Au@Ag core-shell nanoparticles. 3-pentadecylphenol (PDP), which was earlier reported to perform an interfacial reduction to yield silver nanoparticles in the organic phase [23] was used to accomplish the interfacial reduction of silver ions on to gold seeds. The Au@Ag core-shell nanoparticles thus formed have been characterized using UV-visible spectroscopy, TEM and HRTEM measurements. X-ray photoelectron spectroscopy was also used to substantiate the formation of Au@Ag core-shell nanostructures. In the following sections, details of this study are presented.

3.2. Synthesis of Au@Ag core-shell nanoparticles from ODA capped gold nanoparticle seeds

3.2.1. Preparation of ODA capped gold nanoparticles

In a typical reaction, 1 L of 10^{-4} M gold nanoparticles in de-ionised water (Milli-Q®), prepared as was outlined in section 2.2.1, was stirred vigorously with 100 mL of ODA (10^{-3} M) in toluene for 6 h. The complete phase transfer was accompanied by the resultant aqueous solution turning colourless and the toluene phase assuming a deep ruby red colour. The toluene phase was further separated and the concentration of gold nanoparticles was assumed to be 10^{-3} M. The average particle size was determined from TEM images (fig. 3.1A) to be 9.0 ± 1.3 nm (fig. 3.1B).

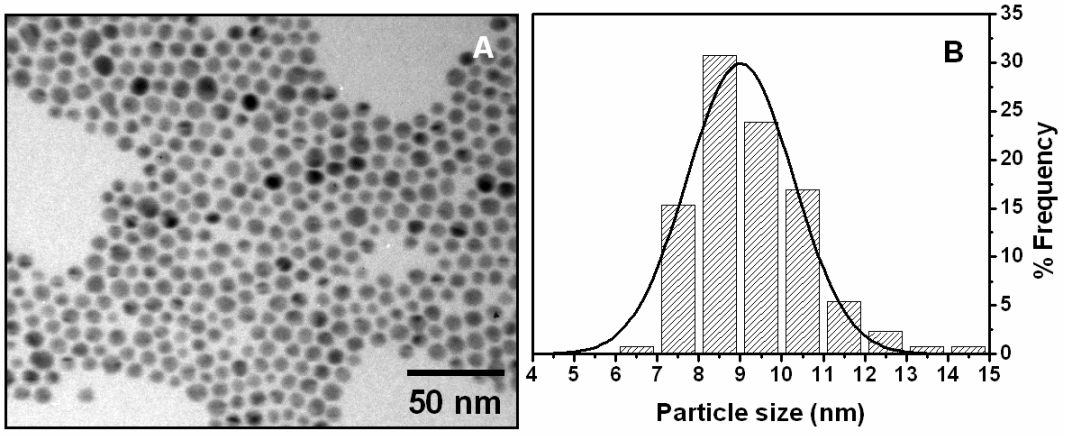

Figure 3.1: *(A) Representative TEM image of ODA capped gold nanoparticles. The size distribution of the ODA capped gold nanoparticles fitted to a Gaussian curve is shown in (B).*

3.2.2. Preparation of hydrophobic Au@Ag core-shell nanoparticles

To 10 mL of 10^{-3} M ODA capped gold nanoparticles in toluene was added 1 mL of 10^{-2} M PDP in toluene (final concentration of PDP is approximately 10^{-3} M). This was stirred against an alkaline aqueous solution of 10 mL 10^{-3} M Ag_2SO_4 (concentration of KOH is 10^{-3} M). The stirring was carried out for a period of 5 h resulting in the formation of a yellowish red colour in the toluene phase. The nanoparticles formed in the toluene phase were periodically removed and analyzed using UV-visible absorbance spectroscopy and TEM measurements.

3.3. TEM characterisation of Au@Ag core-shell nanoparticles

Reduction of aqueous silver ions using PDP in the toluene phase in the presence of ODA capped gold nanoparticle seeds led to transformation of the intense ruby red colour to a yellow brown colour. TEM analysis (fig. 3.2) of the reaction products, formed after 5 h, revealed the formation of spherical nanoparticles with interesting contrast features. The particles show a dark centre and a lighter shell (figs. 3.2A and 3.2B). Inset in fig. 3.2B reveals the sharp change in the contrast of one of the particles.

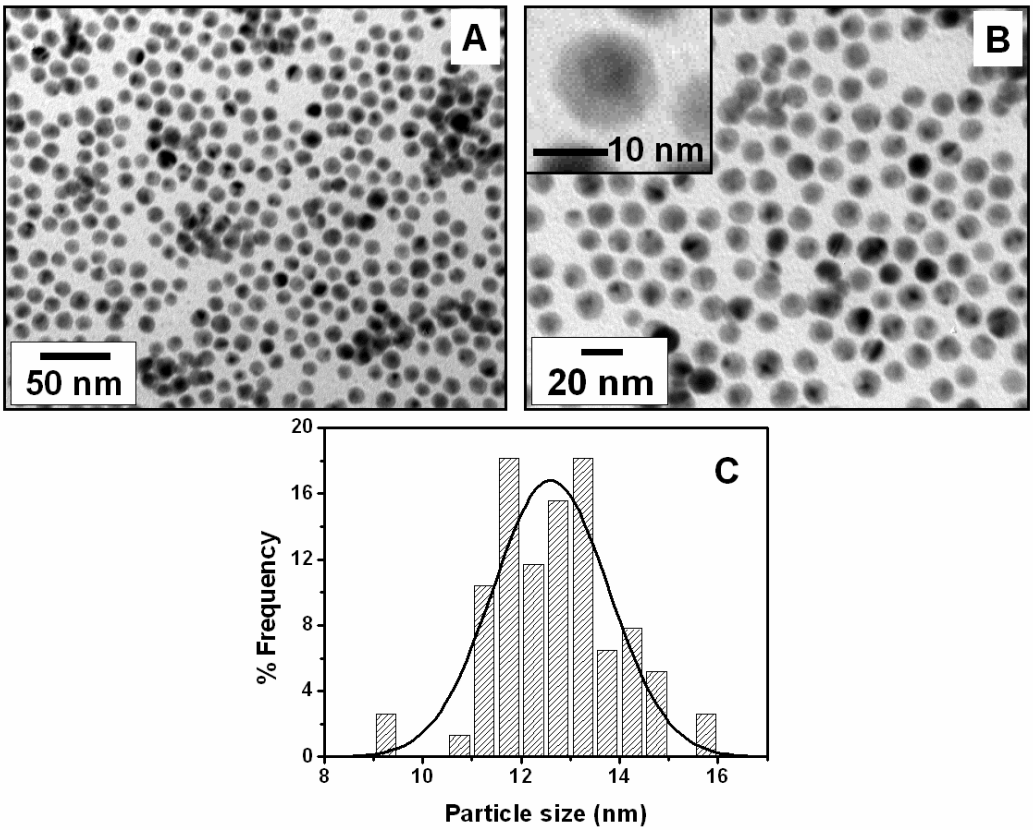

Figure 3.2: *(A), (B) Representative TEM images of Au@Ag core-shell nanoparticles. Size distribution analysis of the same is shown in (C).*

Such a contrast is consistent with Au@Ag core shell nanoparticles observed previously [13,16]. Close inspection of TEM images of the product reveals that all particles have the core-shell architecture. Fig. 3.2C shows the size distribution analysis that was carried out on Au@Ag core-shell nanoparticles formed after 5 h of the reaction. The increased size of Au@Ag core-shell nanoparticles (12.6 ± 1.2 nm – fig. 3.2C) as against that of ODA capped gold nanoparticles (9.0 ± 1.3 nm – fig. 3.1B) indicates that ODA capped gold nanoparticles have acted as seeds for the deposition of reduced silver atoms leading to formation of Au@Ag core-shell nanoparticles.

3.4. Kinetics of formation of Au@Ag core-shell nanoparticles studied using UV-visible absorbance spectroscopy and TEM analysis

Formation of the core-shell nanoparticles was followed by studying UV-visible absorption spectra of the nanoparticle aliquots collected periodically from the organic phase (fig. 3.3). The spectra are normalized with respect to their absorbance maxima in the region from 400 to 600 nm. The absorption spectrum of ODA capped gold nanoparticles reveal a single peak at 524 nm due to the surface plasmon absorbance of

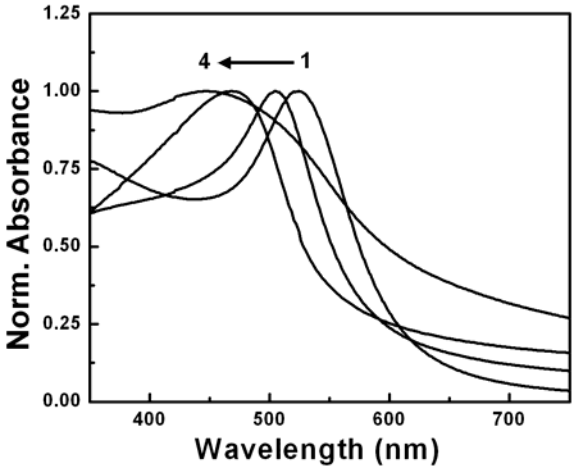

Figure 3.3: *Curve 1 shows the UV-visible absorbance spectra of ODA capped gold nanoparticles. UV-visible absorbance spectra of nanoparticles in the organic phase taken out at different stages of the interfacial reaction: curve 2 – after 2 h, curve 3 – after 5 h, curve 4 – after second round of seeded growth process on nanoparticles corresponding to curve 3. The spectra are normalized w.r.t their respective absorbance maxima in the region from 400 to 600 nm. See text for details.*

gold (curve 1, fig. 3.3). Interfacial reduction of silver ions results in increase of the absorbance intensity at 420 nm (after 2h - curve 2, fig. 3.3). This is in addition to

shifting of the longer wavelength peak (previously at 524 nm) to 520 nm. With time and progress of reaction the absorbance intensity at 420 nm increases (after 5h - curve 3, fig. 3.3) signalling the deposition of silver shell around gold nanoparticle seeds. The absorbance profile observed here indicating two types of collective electron oscillations can be used to conclude the formation core-shell nanoparticles [13]. Increase in absorbance intensity at 420 nm is thus indicative of the growing silver layer on gold seeds. Shifting of the longer wavelength band (initially at 524 nm) to 460 nm after 5 h of reaction (curve 3, fig. 3.3) could also be interpreted as the formation of an alloy phase at the gold-silver interface. This is due to the fact that alloy nanoparticles of gold and silver exhibit a single composition dependent surface plasmon resonance absorbance peak which is intermediate to that of individual gold and silver nanoparticles [24]. It is understood that alloy formation at surface of nanostructures is facile particularly in nanoparticles of size below 10 nm [25]. We believe that the alloy formation could have taken place during the initial phases of the reaction when the surface of ODA capped gold nanoparticle seed was covered by a few atomic layers of metallic silver. Further reduction however could have led to further deposition of metallic silver leading to increase in intensity at 420 nm. The reaction saturates after a period of 5 h and further reaction does not lead to any change in relative intensities of the absorbance bands.

In order to increase the size of the silver shell, a second round of interfacial reduction was carried out on the Au@Ag core-shell nanoparticles obtained after 5h. This was done as follows: Au@Ag core-shell nanoparticles obtained as outlined above were purified using centrifugation (18000 rpm for 20 min; thrice) and redispersed in 10 mL of toluene containing 10^{-3} M PDP. The above nanoparticulate solution was then stirred with 10 mL of 10^{-3} M alkaline Ag_2SO_4 (concentration of KOH is 10^{-3} M) for a period of 5 h. Characterization of the particles formed in the organic phase using UV-visible spectroscopy indicated a further blue shift of the peak to 440 nm with concomitant increase of the absorbance intensity at 420 nm (curve 4, fig. 3.3), indicating an increase in the silver layer thickness. The broad nature of the absorbance band could be due to aggregation of the nanoparticles that are formed.

Formation of individual silver nanoparticles during this process can be ruled out as resultant physical mixtures would show two distinct peaks at 520 nm and 420 nm (curves 1-4, fig. 3.4) due to the surface plasmon resonance of individual gold and silver nanoparticles. To establish this point, the UV-visible absorbance spectra of different

ratios of physical mixtures (fig. 3.4) of ODA capped gold silver nanoparticles [26] were measured. From the spectra it is clear that varying the composition of the physical mixture only alters the relative intensities of the respective surface plasmon resonance peaks without altering the peak positions significantly (curves 1-4, fig. 3.4). In the present case, however, a clear shift in the peak features (curves 1-4, fig. 3.3) is observed ruling out the presence of mixtures of individual gold and silver nanoparticles. This particular reasoning is further supported by TEM analysis.

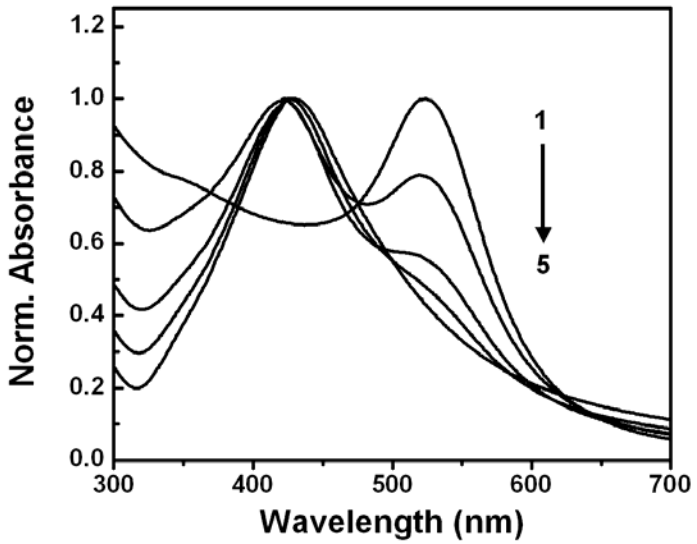

Figure 3.4: *UV-visible absorbance spectra obtained from nanoparticulate solutions comprising different volume fractions of ODA capped gold nanoparticles (10^{-3} M) and ODA capped silver nanoparticles (4×10^{-4} M) (the spectra are normalized w.r.t their respective absorbance maxima in the region 400 to 600 nm): curves 1-5 correspond to mixtures of gold and silver nanoparticulate solutions wherein the gold nanoparticulate solution volume fractions are 100 %, 75 %, 50 %, 25 % and 0 % respectively.*

Aliquots that were collected periodically during the process of the reaction described above were studied using TEM. Examination of TEM images show that ODA capped gold nanoparticles was spherical without any contrast features (fig. 3.5A). The average size of these were determined to be 6.4 ± 0.7 nm (fig. 3.6A). It needs to be noted that the size of the ODA capped gold nanoparticle seeds used in this study of the kinetics of core-shell formation are smaller than what was used earlier (section 3.2.1). Samples collected after 2 h and 5 h revealed presence of spherical particles (figs. 3.5B and 3.5C respectively). As evident from TEM images, particles formed after 5 h of the interfacial reaction show prominent contrast features with the core being darker in

comparison to the shell. However these features are not prominent in the sample collected after 2 h of reaction. This again supports our claim (based on UV-visible spectroscopy) that the initial layers of the silver metal could be involved in an alloying process with the surface atoms of the gold seeds. Therefore they lack distinct contrast features that are seen in particles formed after 5 h.

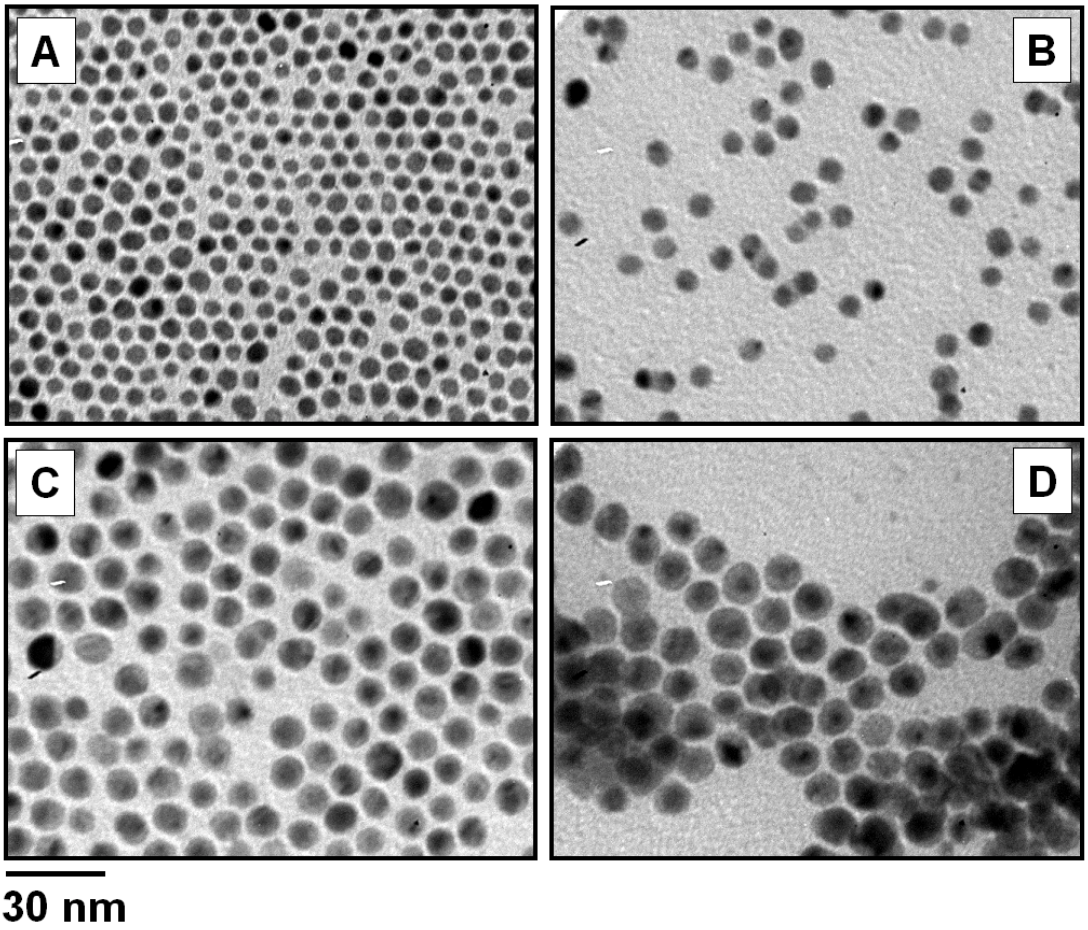

Fig. 3.5: *Representative TEM images of nanoparticles during different stages of the interfacial reaction: (A) ODA capped gold nanoparticle seeds, (B) after 2 h, (C) after 5 h, (D) after second round of seeded growth process on nanoparticles corresponding to (C). Scale bar is common to all the images.*

Samples obtained after 2 h and 5 h however show marked increase in their size (figs. 3.6B and 3.6C respectively) indicating the occurrence of seeded growth leading to Au@Ag core-shell nanoparticles (2 h – 8.2 ± 0.8 nm and 5 h – 10.4 ± 1.1 nm). TEM analysis (fig. 3.5D) was also performed on the sample prepared after a second round of silver deposition (corresponding to curve 4, fig. 3.3). A clear increase in the size of the shell layer in addition to aggregation of some of the particles is evident. The presence

of aggregates also account for broadening of the corresponding UV-visible absorbance (curve 4, fig. 3.3). In fact the size of these particles assumes a bimodal distribution with average diameters of 11.7 ± 0.5 and 13.7 ± 0.5 nm (fig. 3.6D). Shown in fig. 3.6E is a plot of silver layer thickness (determined from average sizes of the nanoparticles formed at different stages of the reaction) versus the intensity of absorbance at 420 nm obtained from the normalized spectra (fig. 3.3). The plot clearly relates increase in intensity at 420 nm to the thickness of the metallic silver layer as the reaction proceeds.

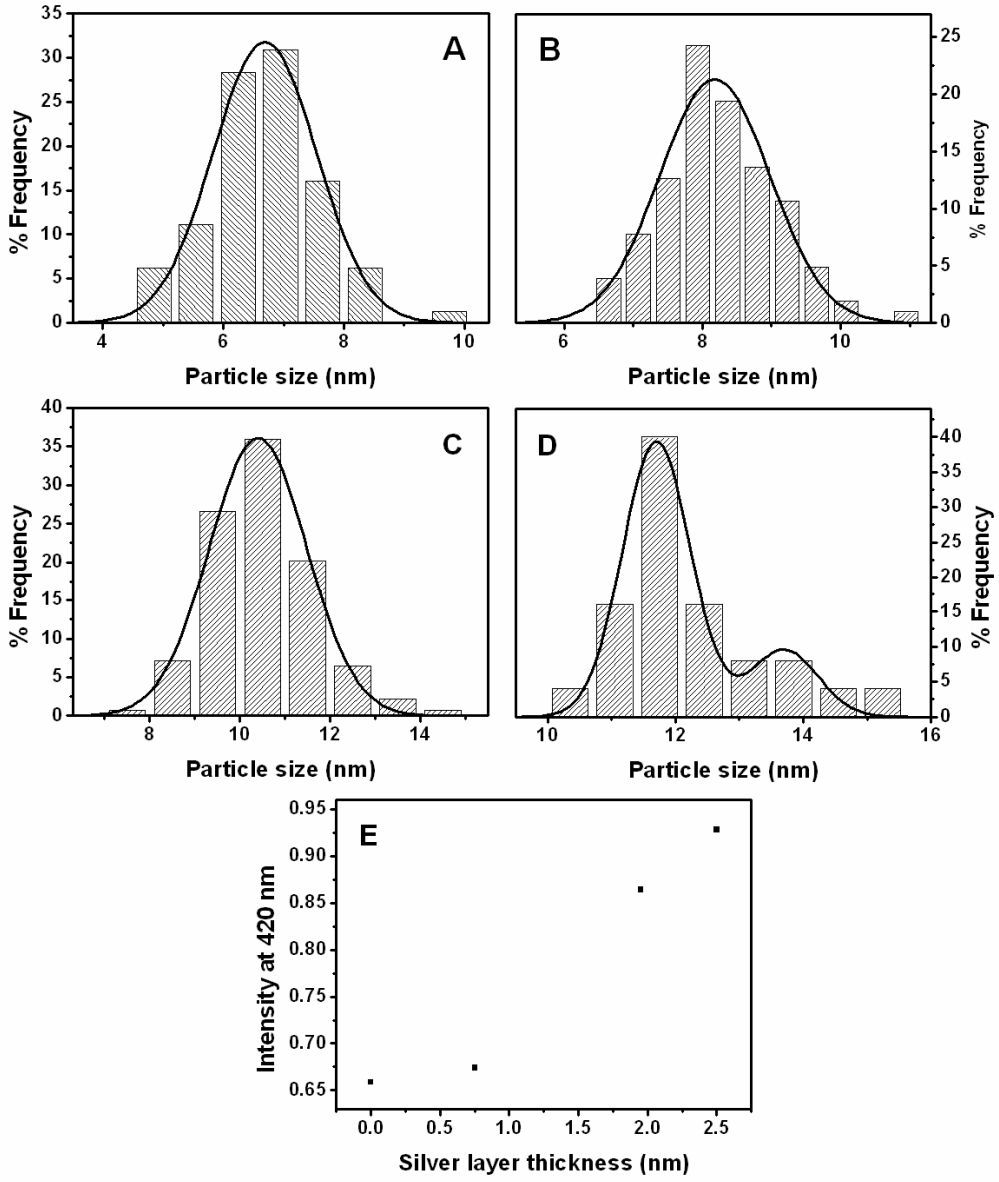

Figure 3.6: *Size distributions of ODA capped gold nanoparticle seeds (A) and Au@Ag core-shell nanoparticles formed after 2 h (B) and 5 h (C) of interfacial reaction. (D) represents the size distribution analysis performed on Au@Ag core-shell nanoparticles formed after the second round of interfacial reaction. (E) illustrates how the surface plasmon feature of silver (at 420 nm) increases with thickness of the silver layer.*

As is characteristic of seeded growth procedures, when the rate of reduction of silver ions was increased, fresh nucleation was also observed. This experiment was carried out with a PDP concentration of 10^{-2} M (10 time excess). Fig. 3.7A presents TEM evidence for the formation of small particles in the size range of 2 to 5 nm. However, the UV-visible absorbance characteristics (curve 1, fig. 3.7B) are similar to those of phase pure Au@Ag core-shell nanoparticles formed when the concentration of PDP was 10^{-3} M (curve 3, fig. 3.3). This could be due to the presence of fewer numbers of individual silver nanoparticles and that too of very small size (less than 5 nm) as is

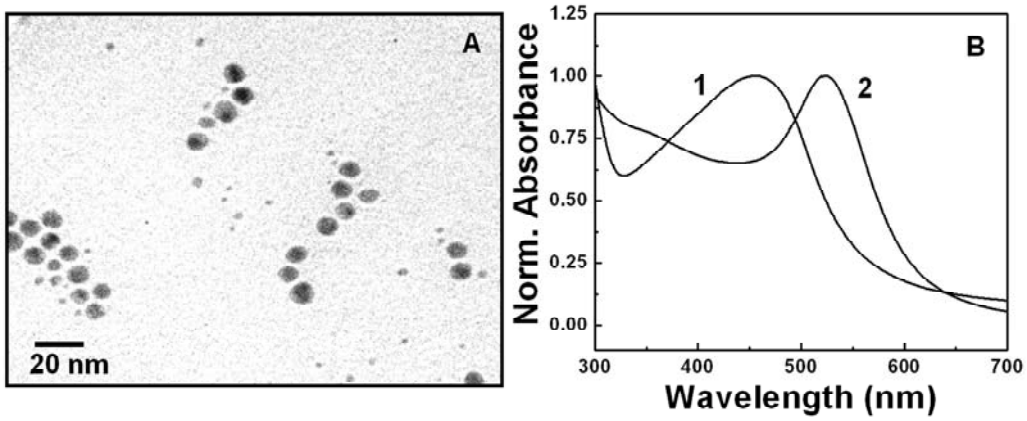

Figure 3.7: *(A) Representative TEM image of nanoparticles formed when 10^{-2}M PDP was used in the interfacial reduction process. (B) Plot comparing the UV-visible spectral characteristics of nanoparticles seen in A (curve 1) and ODA capped gold nanoparticle seeds (curve 2). See text for details.*

evident from fig. 3.7A. The individual silver nanoparticles are formed as a result of fresh nucleation facilitated by the faster reduction in the presence of excess reducing agent. Faster reduction would lead to greater supersaturation of silver atoms and hence favour fresh nucleation [27]. This is in contrary to conditions when the reducing agent concentration was lower leading to seeded growth (fig. 3.5).

3.5. HRTEM analysis Au@Ag core-shell nanoparticles

Further evidence for the formation of the core-shell nanoparticles was obtained based on HRTEM analysis. Fig. 3.8 shows an HRTEM image of the Au@Ag core-shell nanoparticle synthesized from ODA capped gold nanoparticles (after 5 h of reaction). The sharp change in contrast between the dark core and the lighter shell indicates the formation of the silver shell over the gold core. The lattice image of the shell indicates its crystalline nature and the interplanar spacing (d = 0.233 nm) matches well with

standard {111} *d* spacing values of FCC silver [28]. The crystalline nature of the core shell particles is also apparent from the selected area diffraction pattern that was obtained from a collection of Au@Ag core-shell nanoparticles. The rings were indexed based on the FCC structure of gold [28] and silver [28]. It is important to note that the lattice parameters of both FCC gold and silver are identical (4.078 Å and 4.086 Å respectively) [28] and hence their respective Bragg reflections are not distinguishable.

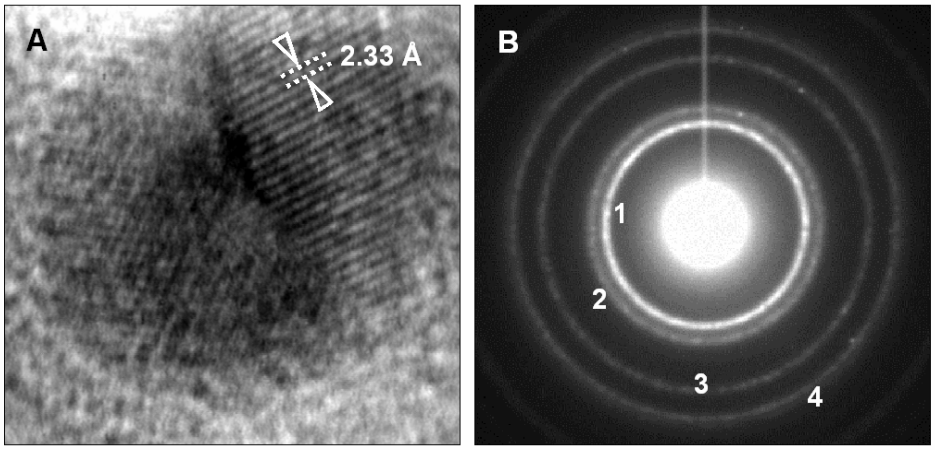

Figure 3.8: *(A) HRTEM image of an Au@Ag core-shell nanoparticle obtained (after 5 h of reaction) from ODA capped gold nanoparticle seeds clearly showing the lattice fringes of the silver shell with "d" spacing corresponding to {111} Miller planes of FCC silver. (B) SAED pattern of Au@Ag core-shell nanoparticles indexed to FCC gold and silver. Rings 1 – 4 correspond to {111}, {200}, {220} and {311} Miller planes.*

3.6. Synthesis of Au@Ag core-shell nanoparticles from HDA capped gold nanoparticle seeds

The effect of capping agent of gold nanoparticle seeds was studied by using HDA capped gold nanoparticles as the starting material for the deposition of the silver shell. HDA capped gold nanoparticles were prepared as described in section 2.2.2. A procedure similar to that described in section 3.2.2 was used for deposition of a silver shell on the HDA capped gold nanoparticle seeds using the reductive action of PDP.

Typically 10 mL of 10^{-3} M HDA capped gold nanoparticles in toluene were added to 1 mL of 10^{-2} M PDP in toluene (final concentration of PDP is approximately 10^{-3} M). This was stirred against an alkaline aqueous solution of 10 mL 10^{-3} M Ag_2SO_4 (concentration of KOH is 10^{-3} M). The stirring was carried out for a period of 25 h resulting in the formation of a yellowish red colour in the toluene phase. The

nanoparticles formed in the toluene phase were periodically removed and analyzed using UV-visible absorbance spectroscopy and TEM measurements.

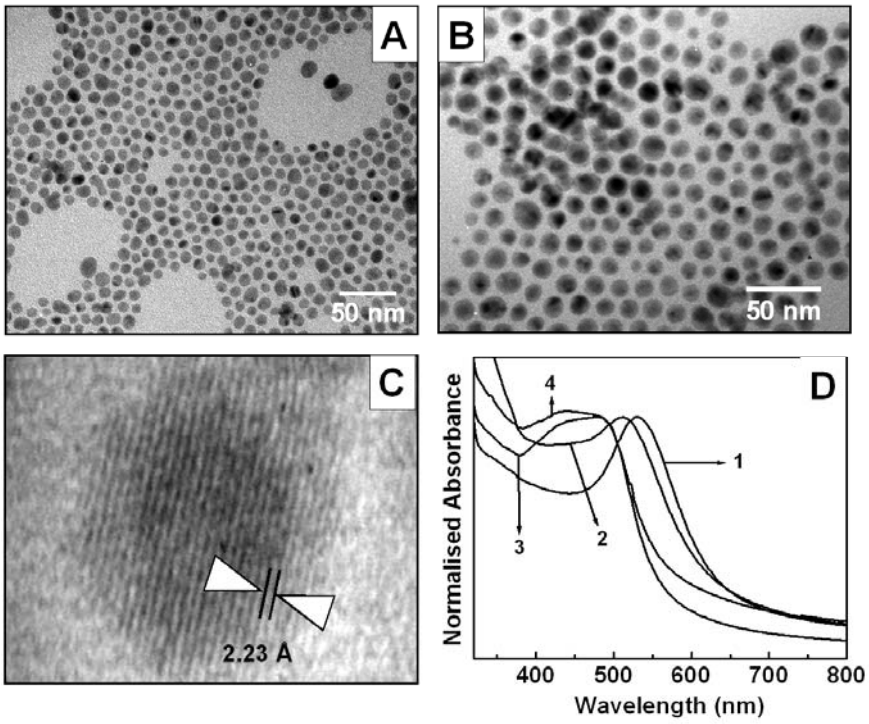

Figure 3.9: *Representative TEM image of HDA capped gold nanoparticles (A) and Au@Ag core-shell nanoparticles (B) obtained from the same. (C) HRTEM image of the Au@Ag core-shell nanoparticles. (D) Normalized UV-visible absorbance spectra of aliquots removed from the organic phase at different stages of reaction; 2 – After 17h of reaction, 3 – After 22h of reaction, 4 – After 25h of reaction. Curve 1 corresponds to HDA capped gold nanoparticles. The spectra are normalized w.r.t their respective absorbance maxima in the 400 – 600 region.*

Similar to the previous case where ODA capped gold nanoparticles were used; formation of Au@Ag core-shell nanoparticles from HDA capped gold seeds was inferred as follows. The TEM image of HDA capped gold nanoparticle seeds (fig. 3.9A) reveals no contrast features. However, contrast features are seen in the nanoparticles obtained after interfacial reduction of silver ions (fig. 3.9B). TEM image (fig. 3.9B) also highlights the phase purity of the core-shell products formed.

The contrast pattern of the particles is seen more clearly in the HRTEM image shown in fig. 3.9C. The crystalline nature of the silver shell is also evident from fig. 3.9C. The interplanar spacing calculated from the HRTEM images (d = 0.223 nm) matches closely with the {111} interplanar distance of FCC silver [28]. UV-visible absorbance spectra were recorded as a function of time to monitor the growth of the

silver shell on the seed. The strong absorbance of HDA capped gold nanoparticles at 530 nm (curve 1, fig. 3.9D) is attributed to the surface plasmon resonance of gold. With progress in reaction, these peaks red shift monotonically (curves 2 to 4, fig. 3.9D) to 480 nm. Accompanying this is the growth of another spectral feature at about 430 nm indicative of the deposition of a silver shell on the seeds (curve 2, fig. 3.9D). With time the intensity of this feature increases relative to the longer wavelength absorbance peak showing the increase in silver shell thickness (curves 2 to 4, fig. 3.9D). The increase in diameter as is evident from the size distributions (fig. 3.10) of HDA capped gold nanoparticle seeds and Au@Ag core-shell nanoparticles (after 25 h of reaction) also supports the above observations.

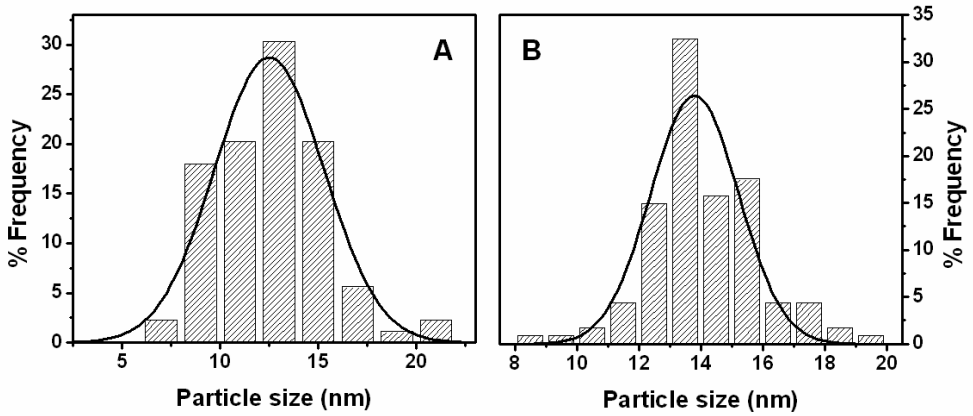

Figure 3.10: *Gaussian fits to the size distributions of HDA capped gold nanoparticles and Au@Ag core-shell nanoparticles obtained from the formed yielded average particle diameters of 12.5 ± 2.8 nm and 13.8 ± 1.4 nm.*

3.7. FTIR analysis

It is known that phenolic compounds, such as PDP [23] and tyrosine [17], reduce silver ions under alkaline conditions. Consequently, they get oxidised to the semiquinone form [17,23]. Here too we speculate formation of semiquinone derivatives. FTIR analysis on the core-shell nanoparticles was performed to ascertain this hypothesis. In this study, particles derived from ODA capped gold seeds were used in order to detect changes to the aromatic ring of PDP. With HDA capped gold nanoparticle seeds, the HDA aromatic ring signals could overlap with that of PDP and products of PDP oxidation making possible interpretation difficult. The nanoparticles were subjected to purification by centrifugation (18000 rpm for 20 min; thrice) and washings with toluene. The purified particles were then dispersed in KBr powder and

subjected to diffuse reflectance FTIR measurements. Similar dispersions of ODA and PDP were prepared in KBr for FTIR study.

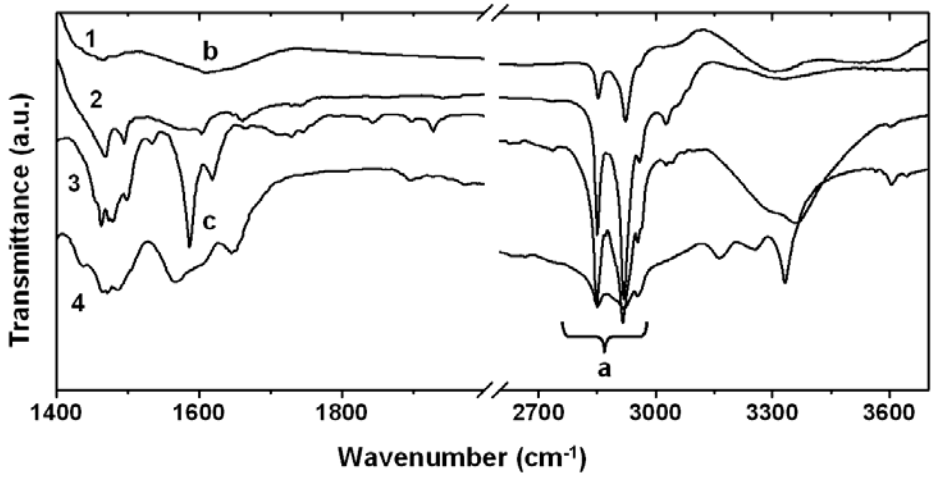

Figure 3.11: *FTIR spectra of (1) Au@Ag core-shell nanoparticles, (2) ODA capped gold nanoparticles, (3) PDP and (4) ODA.*

Fig. 3.11 summarises the FTIR study. Feature labelled "a" representing vibrations at 2844 and 2920 cm^{-1}, corresponding to aliphatic C-H stretching of amphiphiles that cap the gold nanoparticle seeds and Au@Ag core-shell nanoparticles. The features in the region from 1520 to 1725 cm^{-1} provide clues regarding the surface capping of the nanoparticles. The signal centred at ~ 1610 cm^{-1} (labelled "b") in curve 1, is asymmetric towards the higher wavenumber side. The individual components of the signal, however, are not discernible. It is known that the carbonyl stretching of α, β-unsaturated ketones fall in the region from 1685 – 1666 cm^{-1} [17,23,29a]. Here too we believe that carbonyl stretching vibrations of α, β-unsaturated ketones (semiquinone moieties), present capping the Au@Ag core-shell nanoparticles, give rise to signals leading to feature "b". The feature at 1595 cm^{-1} in curve 3 corresponding to PDP (labelled "c") arises due to the C=C ring stretching vibrations [29b]. The same is clearly absent in curve 1 corresponding to Au@Ag core-shell nanoparticles. This observation suggests the destruction of the aromatic ring structure of the phenol and formation of a semiquinone derivative. The fact that signals from ODA and PDP might overlap, makes exact determination of surface composition of Au@Ag core-shell nanoparticles difficult. However in addition to the semiquinone that has been detected, we believe that amines are present capping the Au@Ag core-shell nanoparticles, since they are well known capping agents of noble metal nanoparticles [17,23,26].

3.8. XPS analysis of Au@Ag core-shell nanoparticles

The chemical composition of hydrophobised Au@Ag core-shell nanoparticles synthesized from HDA capped gold seeds and that of the seeds themselves was analyzed using XPS. The spectra were recorded from films of the respective samples prepared by drop coating on to Si (111) wafers. Background correction was performed using the Shirley algorithm [30]. All signals were charge corrected taking the adventitious carbon C1s core level signal observed at 285 eV as reference. Deconvolution of the peaks was performed wherever necessary. Fig. 3.12A shows the photoelectron emission from the Au 4f orbital of HDA capped gold nanoparticles. The Au 4f core level signal could be resolved to be due to emission from two chemically distinct species with Au $4f_{7/2}$ (Au $4f_{5/2}$) binding energies of 84.4 (88) and 86.9 (90.5) eV (curves 1 and 2, fig. 3.12A). These are assigned to metallic (Au^0) and unreduced gold ions (Au^{3+}) respectively indicating that a small percentage of unreduced gold ions are present on the surface of the HDA capped gold nanoparticles [31].

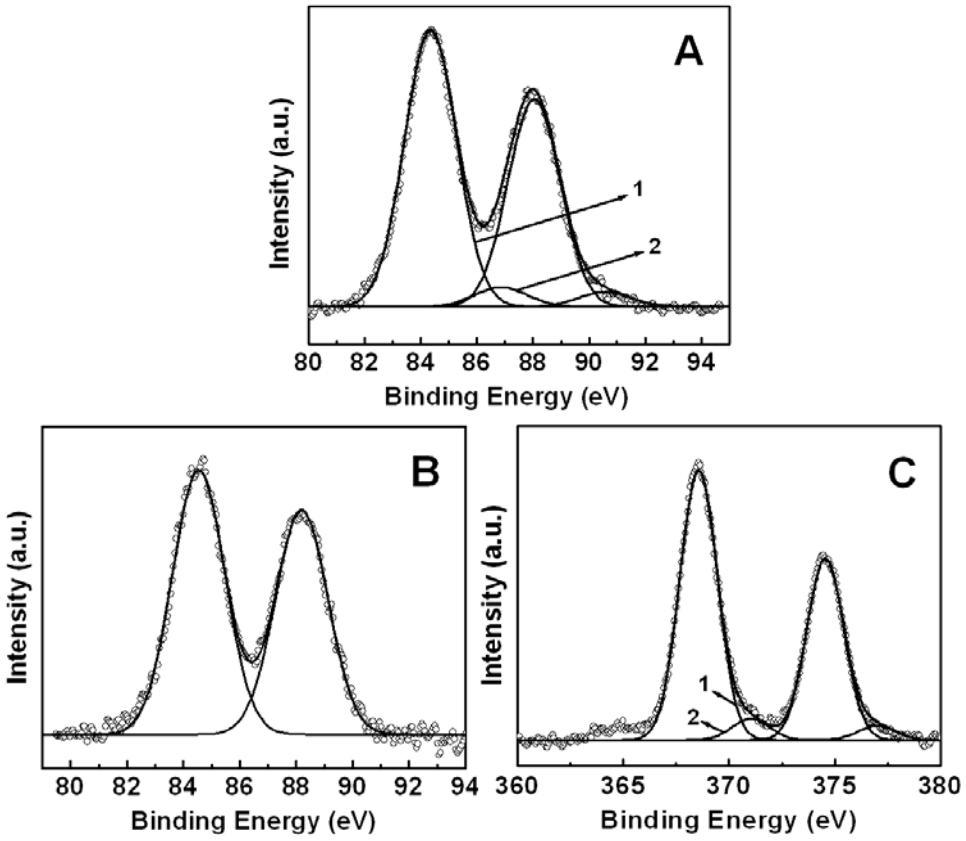

Figure 3.12: *XPS analysis: (A) Au 4f core level spectra recorded from HDA capped gold nanoparticles. Au 4f (B) and Ag 3d (C) core level spectra recorded from Au@Ag core-shell nanoparticles, synthesized from HDA capped gold nanoparticle seeds. The solid lines are non-linear least square Gaussian fits to the background corrected data (hollow circles).*

In case of Au@Ag core-shell nanoparticles the emission from the gold core level occurs at 84.6 eV (Au $4f_{7/2}$) and 88.2 eV (Au $4f_{5/2}$) (fig. 3.12B) indicating the presence of gold in a single form, that of its metallic state. Silver however occurs in two different forms with Ag $3d_{5/2}$ binding energies of 368.6 eV and 371 eV (curves 1 and 2 respectively, fig 3.12C). The lower binding energy component is attributed to metallic silver and the higher binding energy component is attributed to the presence of a small amount of unreduced silver ions. The occurrence of the gold in a single chemical form in Au@Ag core-shell nanoparticles is accounted for as follows. The Au/Au^{3+} redox couple has a higher reduction potential in comparison to that of Ag/Ag^{+} and thus the initially formed layers of metallic silver (following the interfacial reduction of silver ions) tend to reduce the surface bound Au^{3+} ions to their metallic state by way of a galvanic exchange reaction. This is followed by the deposition of more silver to form the shell.

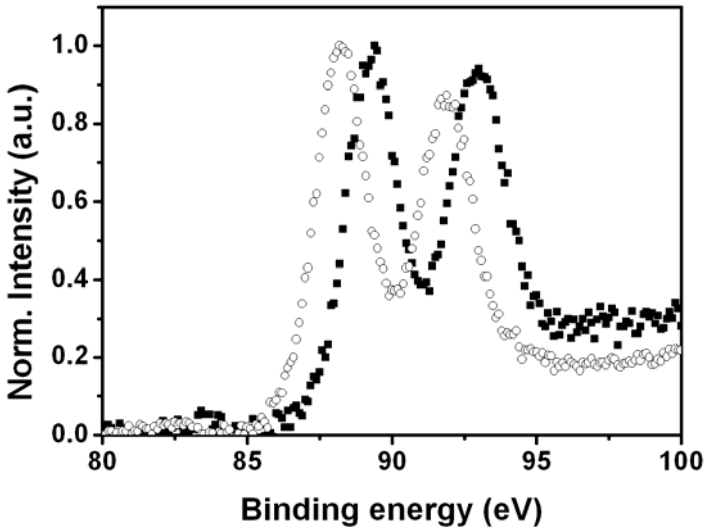

Figure 3.13: *Uncorrected XPS signals from Au 4f core levels of HDA capped gold nanoparticles (■) and Au@Ag core-shell nanoparticles (o). The signals have been normalised w.r.t to their Au $4f_{7/2}$ core level emissions.*

During XPS measurements the ejected photoelectrons tend to loose energy due to inelastic scattering by the surrounding material. This is more so if ionisation occurs at a point beyond the inelastic mean free path (λ) of the material under study. Hence photoelectrons from species situated beyond λ undergo kinetic energy loss and contribute to a background at higher binding energies. From size distribution analysis performed on Au@Ag core-shell nanoparticles (fig. 3.10), the average silver layer

thickness was calculated to be 0.65 nm. This is below the mean free path of Au 4f electrons which is approximately 1.5 nm [32]. Consequently we see a prominent Au 4f signal from the core-shell particles. However the slightly pronounced background (at higher binding energies) seen for the uncorrected Au 4f signal (fig. 3.13) from the Au@Ag core-shell nanoparticles can be attributed to inelastic scattering by the silver shell. Such analysis has been previously used for study of composition profiles in layered materials [33].

3.9. Conclusions

A seed mediated approach was employed to synthesize Au@Ag core-shell nanostructures in toluene. The process proceeds by way of interfacial reduction of silver ions leading to deposition of metallic silver on to hydrophobised gold nanoparticle seeds. Thickness of the silver layer can be controlled by the varying reaction time. Varying the capping agent of hydrophobised gold seeds does not affect formation of the core-shell architecture. The products were conclusively characterized to be core-shell structures using HRTEM and XPS elemental analysis. FTIR analysis was used to conclude that the phenolic amphiphile PDP is involved in an oxidative electron transfer to silver ions resulting in the latter's reduction. PDP itself forms a semiquinone derivative during this process.

3.10. References

[1] Sastry, M.; Swami, A.; Mandal, S.; Selvakannan, PR. *J. Mater. Chem.* **2005**, *15*, 3161.

[2] Oldenburg, S. J.; Averitt, R. D.; Westcott, S. L.; Halas, N. *J. Chem. Phys. Lett.* **1998**, *248*, 243.

[3] Loo, C.; Lowery, A.; Halas, N. J.; West, J.; Drezek, R. *Nano Lett.* **2005**, *5*, 709.

[4] Oh, K. S.; Lee, K. E.; Han, S. S.; Cho, S. H.; Kim, D.; Yuk, S. H. *Biomacromolecules* **2005**, *6*, 1062.

[5] (a) Garca Santamara, F.; Salgueirio Maceira, V.; Lopez, C.; Liz-Marzan, L. M. *Langmuir* **2002**, *18*, 4519. (b) Wang, D.; Li, J.; Chan, C. T.; Salgueirio Maceira, V.; Liz-Marzan, L. M.; Romanov, S.; Caruso, F. *Small* **2005**, *1*, 122. (c) Wang, D.; Salgueirio Maceira, V.; Liz-Marzan, L. M.; Caruso, F. *Adv. Mater.* **2002**, *14*, 908.

[6] Li, G.; Fan, J.; Jiang, R.; Gao, Y. *Chem. Mater.* **2004**, *16*, 1835.

[7] Dabbousi, B. O.; Rodriguez-Viejo, J.; Mikulec, F. V.; Heine, J. R.; Mattousi, H.; Ober, R.; Jenson, K. F.; Bawendi, M. G. *J. Phys. Chem. B* **1997**, *101*, 9463.

[8] (a) Bala, T.; Swami, A.; Prasad, B. L. V.; Sastry, M. *J. Colloid Interface Sci.* **2005**, *283*, 422. (b) Pastoriza-Santos, I.; Perez-Juste, J.; Liz-Marzan, L. M. *Chem. Mater.* **2006**, *18*, 2465.

[9] Mulvaney, P.; Giersig, M.; Henglein, A. *J. Phys. Chem.* **1993**, *97*, 7061.

[10] Srnova-Sloufova, I.; Lednicky, F.; Gemperie, A.; Gemperlova, J. *Langmuir*, **2000**, *16*, 9928.

[11] Cao, Y. W.; Jin, R.; Mirkin, C. A.; *J. Am. Chem. Soc.* **2001**, *123*, 7961.

[12] (a) Freeman, R. G.; Hommer, M. B.; Grabar, K. C.; Jackson, M. A.; Natan, M. J. *J. Phys. Chem.* **1996**, *100*, 718. (b) Cao, Y. C.; Jin, R.; Mirkin, C. A. *Science* **2002**, *297*, 1536.

[13] Hodak, J. H.; Henglein, A.; Giersig, M.; Hartland, G. V. *J. Phys. Chem. B* **2000**, *104*, 11708.

[14] Mallik, K.; Mandal, M.; Pradhan, N.; Pal, T. *Nano. Lett.* **2001**, *1*, 319.

[15] Lu, L.; Wang, H.; Zhou, Y.; Xi, S.; Zhang, H.; Hu, J.; Zhao, B. *Chem. Commun.* **2002**, 144.

[16] Mandal, S.; Selvakannan, PR.; Pasricha, R.; Sastry, M. *J. Am. Chem. Soc.* **2003**, *125*, 8440.

[17] Selvakannan, PR.; Swami, A.; Srisathiyanarayanan, D.; Shirude, P. S.; Pasricha, R.; Mandale, A. B.; Sastry, M. *Langmuir* **2004**, *20*, 7825.

[18] Caruso, F.; Caruso, R. A.; Mohwuld, H. *Science* **1998**, *282*, 1111.

[19] Liang, Z.; Susha, A.; Caruso, F. *Chem. Mater.* **2003**, *15*, 3176.

[20] Sastry, M. *Curr. Sci.* **2003**, *85*, 1735.

[21] Liang, H. P.; Zhang, H. M.; Hu, J. S.; Guo, Y. G.; Wan, L. J.; Bai, C. L. *Angew. Chem. Int. Ed.* **2004**, *43*, 1540.

[22] Yang, J.; Lee, J. Y.; Too, H. *J. Phys. Chem. B* **2005**, *109*, 19208.

[23] Swami, A.; Selvakannan, PR.; Pasricha, R.; Sastry, M. *J. Phys. Chem. B* **2004**, *108*, 19269.

[24] Link, S.; Wang, Z. L.; El-Sayed, M. A. *J. Phys. Chem. B* **1999**, *103*, 3529.

[25] Mulvaney, P. *Langmuir* **1996**, *12*, 788.

[26] ODA capped silver nanoparticles were prepared by a modification of the procedure reported in Kumar, A.; Joshi, H, Pasricha, R.; Mandale, A. B.; Sastry, M. *J. Colloid Interface Sci.* **2003**, *264*, 396. In a typical reaction, 100 mL of 10^{-4} M Ag_2SO_4

was reacted with 0.01 g of $NaBH_4$ and was simultaneously stirred with 50 mL of 10^{-3} M ODA in toluene. Complete phase transfer of silver nanoparticles to the toluene phase occurred due to the capping action of ODA molecules. The concentration of the silver nanoparticles thus obtained was assumed to 4×10^{-4} M.

[27] Burda, C.; Chen, X.; Narayanan, R.; El-Sayed, M. A. *Chem. Rev.* **2005**, *105*, 1025.

[28] (a) *Joint Committee on Powder Diffraction Standards*, File No: 04-0783 for FCC silver. (b) *Joint Committee on Powder Diffraction Standards*, File No: 04-0784 for FCC gold.

[29] (a) Silverstein, R. B.; Webster, F. X. *Spectrometric Identification of Organic Compounds, 6th ed.; John Wiley & Sons, Inc: New York*, **1998**; Chapter 3, p 92. (b) Silverstein, R. B.; Webster, F. X. *Spectrometric Identification of Organic Compounds, 6th ed.; John Wiley & Sons, Inc: New York*, **1998**; Chapter 3, p 89.

[30] Shirley, D. A. *Phys.Rev.B.* **1972**, *5*, 4709.

[31] Liu, Y. C. ; Chuang, T. C. *J. Phys. Chem. B* **2003**, *107*, 12383.

[32] Wagner, C. D.; Riggs, W. M.; Davis, L. E.; Moulder, J. F.; Muilenberg. G. E. (ed.) *Handbook of X-Ray photoelectron spectroscopy, Perkin-Elmer Corporation, Physical Electronics division: 6509 Flying cloud drive, Eden Praire, Minnesota 55344*; **1979**, Chapter 2, p 5.

[33] (a) Idla, K.; Johansson, L. S.; Campbell, J. M.; Inganas, O. *Surf. Interface Anal.* **2000**, *30*, 557. (b) Johansson, L. S.; Juhanoja, J. *Thin Solid Films* **1994**, *238*, 242.

Chapter 4

Synthesis of gold nanotriangles and silver nanoparticles using Aloe vera leaf extract

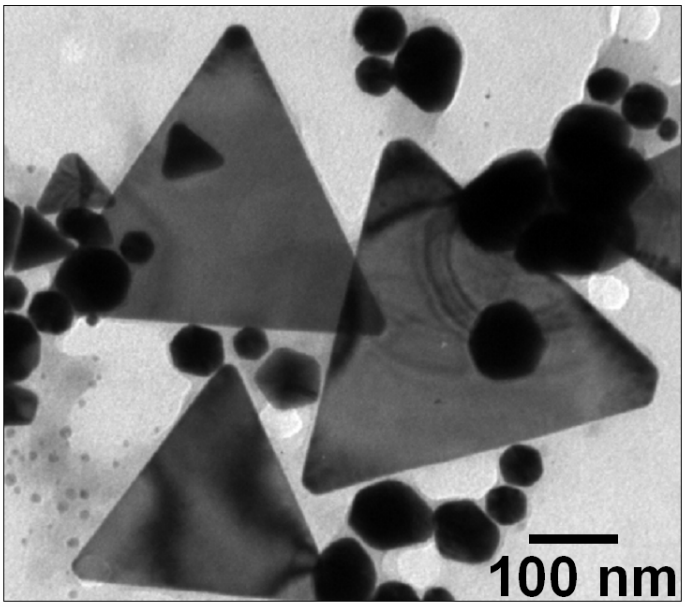

This chapter presents a protocol for the synthesis of single crystalline triangular gold nanoparticles and spherical silver nanoparticles in high yield by the reductive action of the Aloe vera leaf extract. This method offers control over the yield and optical properties of the nanoparticles formed. It is suggested that carbonyl compounds formed during the course of the reaction cause shape transformation of spherical nuclei resulting in formation of gold nanotriangles and hexagons.

Part of work discussed in this chapter has been published in

Prathap Chandran, S.; Chaudhary, M.; Pasricha, R.; Ahmad, A.; Sastry, M. *Biotechnol. Prog.* **2006**, *22*, 577.

4.1. Introduction

Monodispersity of size and selectivity of shape are two key issues that are the focus of nanoparticle synthesis research. Though monodispersity is very critical for device applications [1], the fascinating properties exhibited by anisotropic nanoparticles [2] makes shape selective synthesis important. Shape dependent catalytic properties [3] and the remarkably different optical properties of gold and silver nanotriangles and nanorods (in comparison to spherical nanoparticles) are some examples to this effect [2, 4]. Gold and silver nanotriangles in particular are promising as they could find potential applications that include cancer hyperthermia [5], electromagnetic waveguides [6], SERS [7] and infrared radiation absorbing optical coatings [8]. Consequently, a variety of synthetic procedures leading to planar gold and silver nanostructures have been reported. Methods offering reasonable control over silver nanotriangle edge length [9] and thickness [10] have been reported. These include photochemical transformation of spherical nanoparticles [9] or wet chemical synthesis with [11] or without templates [10, 12]. Similar reports for gold include procedures employing liquid crystal [13] and polymer templates [14] leading to high yields of planar and triangular gold nanostructures. Solution based methodologies such as aspartate reduction [15] and starch mediated reduction [16] among others [17] lead to the production of planar gold nanostructures with reasonable control over their optical properties.

Recently biosynthetic methods employing either microorganisms or plant extracts have emerged as a simple and viable alternative to chemical and physical methods for synthesis and fabrication of nanostructures. Following the initial report on intracellular silver nanoparticle formation in *Pseudomonas stutzeri* by Klaus *et al* [18], many reports on synthesis of metal [19] and semiconductor nanoparticles [20] using fungi or bacteria have appeared. Sastry and co-workers in their quest for new eco-friendly 'green' methods for the synthesis of noble metal nanoparticles have identified fungi [19b, 21], actinomycetes [19c] and plant extracts [5,8,22] for the synthesis of silver and gold nanoparticles. Recently, excellent shape-selective formation of single crystalline triangular gold nanoparticles was observed using the extract of the lemongrass plant (*Cymbopogon flexuosus*) [5]. These nanostructures possess a strong NIR absorbance which could be easily tuned by modifying the experimental conditions [8]. The NIR absorbing properties of the biogenic gold nanotriangles was used to design simple optical coatings for architectural applications [8].

In this chapter, we present a protocol for the synthesis of single crystalline triangular gold nanoparticles and spherical silver nanoparticles in high yield by the reductive action of *Aloe vera* leaf extract. *Aloe vera* has been used in many medical applications due to its antipyretic, antioxidative and cathartic properties [23]. *Aloe vera* exudates are rich in compounds which have oxidisable groups such as the hydroxyl and phenol. Surface active groups such as carbonyls [23,24] are also present. Consequently they are identified as possible candidates for synthesis and shape control of metal nanoparticles. Whereas the reaction of *Aloe vera* extract with gold ions results in the formation of nanotriangles, spherical nanoparticles are formed from silver ion precursors. It is seen that by varying the percentage of the extract in the reaction medium, the percentage of gold nanotriangles to spherical particles as well as the size of the nanotriangles can be modulated. This leads to a significant control over the optical properties of the nanoparticulate solution. Carbonyl compounds formed during the course of the reaction are believed to cause shape transformation of spherical nuclei resulting in formation of gold nanotriangles and hexagons.

4.2. *Aloe vera* extract preparation

30 g of thoroughly washed *Aloe vera* leaves were finely cut and boiled in 100 mL of de-ionised water (MilliQ®). The resulting extract was used for further experiments.

4.3. Synthesis of gold nanotriangles

In a typical experiment, different volumes (0.5 to 4 mL) of the *Aloe vera* extract were added to 6 mL solutions of 10^{-3} M aqueous chloroauric acid ($HAuCl_4$) and the volume was made up to 10 mL by adding appropriate amount of de-ionised water. Volume fraction of the *Aloe vera* extract is thus varied from 5% to 40%. The reaction was allowed to proceed for a period of 30 h during which the colour of the reaction mixture changes to ruby red or purple, depending on the volume fraction of the *Aloe vera* extract. This observation indicates formation of anisotropically shaped gold nanoparticles [5,8].

In order to study the effect of higher temperature on the formation of gold nanotriangles, 1mL of the *Aloe vera* leaf extract (10% volume fraction) was added to 6 mL of 10^{-3} M aqueous $HAuCl_4$ and the volume was made up to 10 mL using de-ionised

water. The reaction here was performed at an elevated temperature of 80 $^{\circ}$C for a period of 30 mins. Formation of a purple coloured solution indicated the formation of gold nanoparticles [4].

4.3.1. UV-visible absorbance studies

Addition of 1 mL of *Aloe vera* extract to 6 mL of 10^{-3} M aqueous $HAuCl_4$ solution (final volume made up to 10 mL) led to the appearance of a brownish red colour in solution after about 5 h of reaction indicating the formation of gold nanoparticles. The UV-visible-NIR absorption spectrum recorded from this solution shows the characteristic surface plasmon resonance (SPR) band of gold nanoparticles centred at 560 nm (curve 1, fig. 4.1). The kinetics of gold nanoparticle formation was followed using UV-visible-NIR spectroscopy (fig. 4.1). It is observed that with the progress of reaction the absorbance intensity at ca. 560 nm increases monotonically with time while a new band centred at 817 nm appears after about 7.5 h of reaction (curve 2, fig. 4.1). With time, the longer wavelength absorption undergoes a further red shift before stabilizing at 1300 nm indicating completion of reaction (curves 3-5, fig. 4.1). These time-dependent features in the UV-visible-NIR spectra are characteristic of aggregated spherical nanoparticles [25] or anisotropic nanostructures whose dimensions change with time [8].

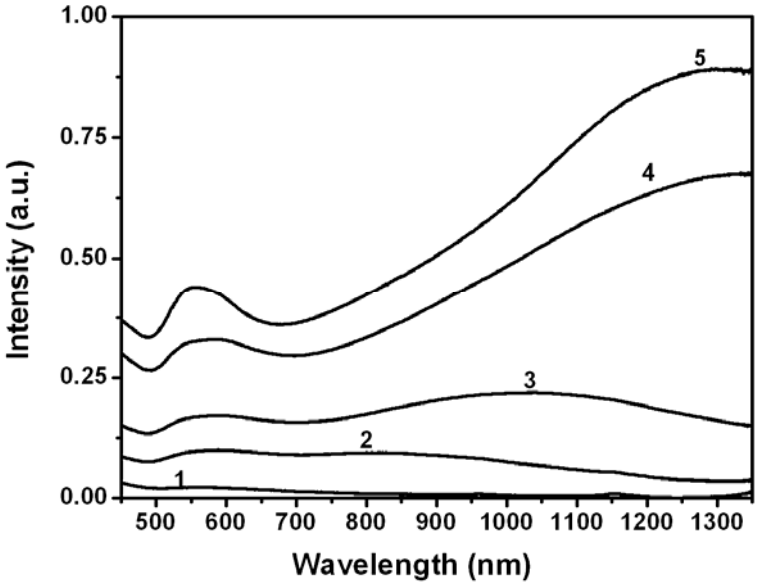

Figure 4.1: *UV-visible-NIR absorption spectra of gold nanoparticles measured during the reaction of 6 mL of 10^{-3} M $HAuCl_4$ with 1 mL Aloe vera extract (final volume of reaction mixture adjusted to 10 mL using de-ionised water) after 5 h, 7.5 h, 8 h, 9 h and 25 h of reaction (curves 1, 2, 3, 4 and 5 respectively).*

Fig. 4.2 shows the UV-visible-NIR absorbance spectra of gold nanoparticles synthesized using different amounts of *Aloe vera* extract recorded after 25 h of the reaction. The inset shows photographs of the nanoparticle solutions thus synthesised. The nanoparticles thus synthesized exhibit two strong absorbance bands; band I centred at ca. 560 nm is a common feature. However, the relative intensity and the position of the second band (band II) that occurs in the NIR region are seen to be a function of the amount of *Aloe vera* extract used in the reaction. It is seen that as the amount of *Aloe vera* extract in the reaction medium increases, band II shifts to smaller wavelengths and weakens in intensity relative to band I (curves 1-6, fig. 4.2). The corresponding solutions show a large variation in colour that ranges from pale pink to dark blue (inset of fig. 4.2). It is well known that rod shaped and flat gold nanoparticles absorb in the NIR region of the electromagnetic spectrum [5, 26]. Such nanostructures exhibit two well separated absorption bands. Herein the shorter wavelength band centred at ca. 520 nm corresponds to the transverse surface plasmon resonance while the longer wavelength component (which could be shifted well into the NIR region) corresponds to the longitudinal surface plasmon absorption [8,26].

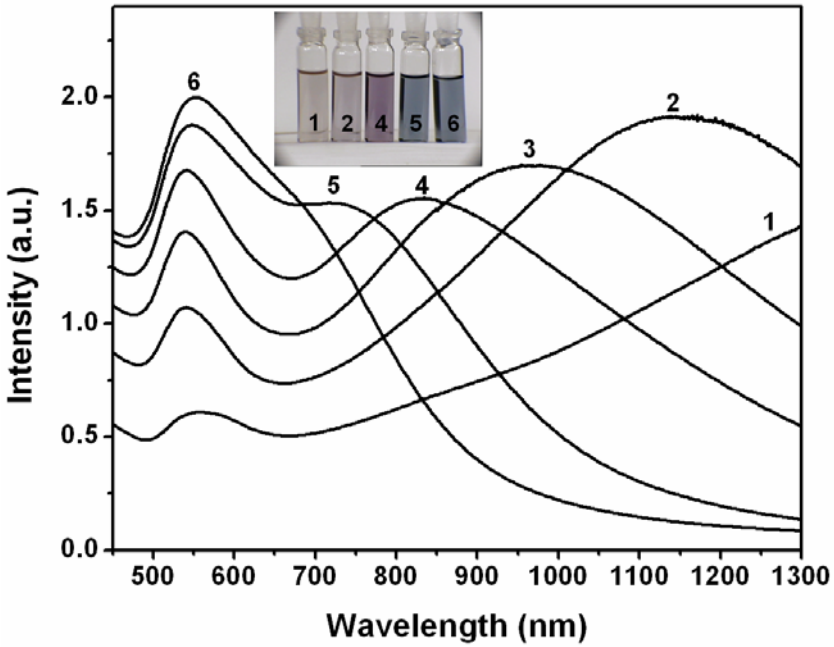

Figure 4.2: *UV-visible-NIR absorbance spectra of gold nanotriangles formed after 25 h of the reaction of 6 mL of 10^{-3} M aqueous $HAuCl_4$ with different amounts of Aloe vera extract: 0.5, 1, 1.5, 2, 3 and 4 mL (curves 1, 2, 3, 4, 5 and 6 respectively; final volume adjusted to 10 mL using de-ionised water). The inset shows a photo of the different nanoparticle solutions after 25 h of the reaction – the labels correspond to spectra shown in the main part of the figure.*

4.3.2. TEM, electron diffraction and AFM studies

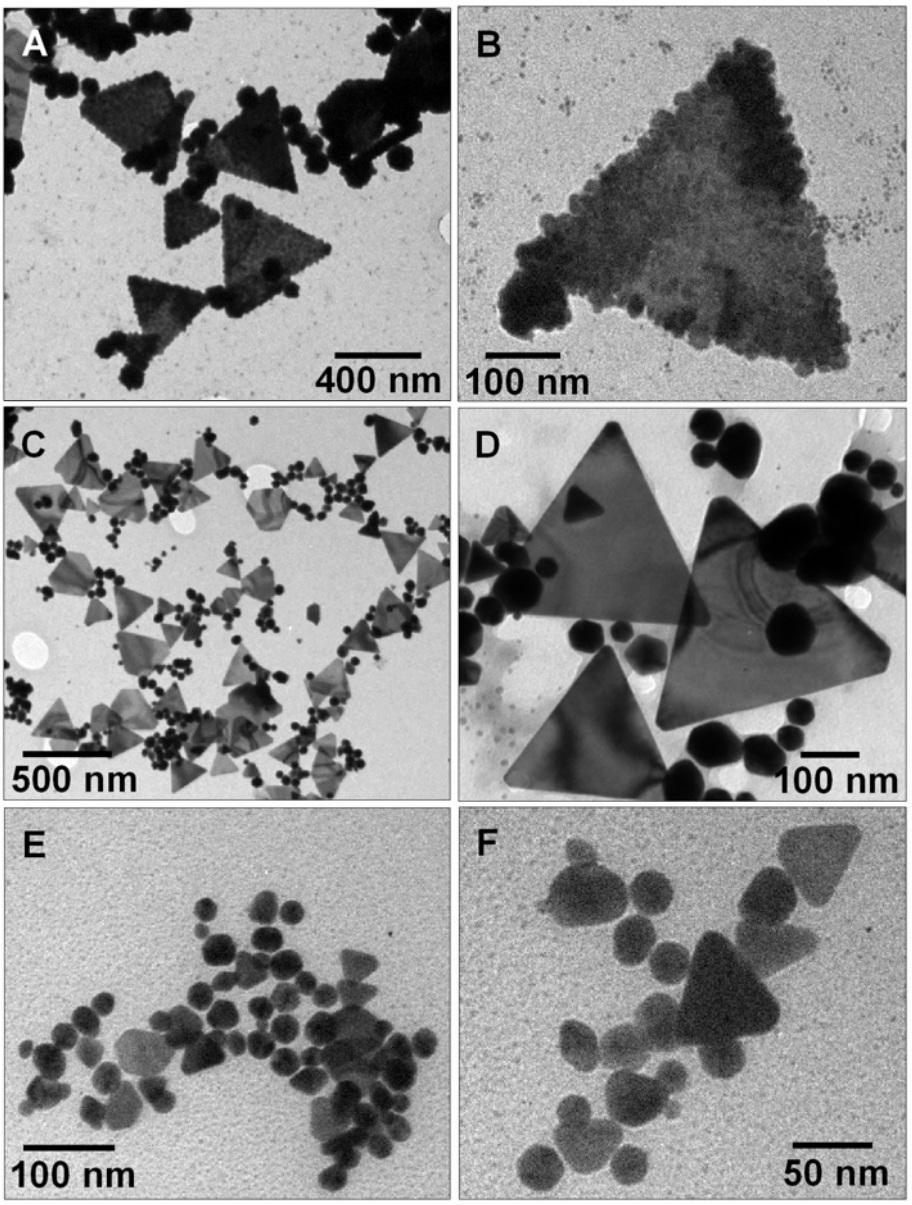

Figure 4.3: *Representative TEM images of gold nanotriangles synthesized using different amounts of Aloe vera extract: (A), (B) - 0.5 mL. (C), (D) - 1 mL. (E), (F) - 4 mL by reaction with 6 mL of* 10^{-3} *M* $HAuCl_4$ *(final volume adjusted to 10 mL wherever necessary).*

Fig. 4.3 shows representative transmission electron microscopy (TEM) images of the nanoparticles synthesized using different amounts of the *Aloe vera* extract. TEM analysis clearly reveals the formation of triangular and a small amount of hexagonal planar gold nanostructures in addition to spherical nanoparticles.

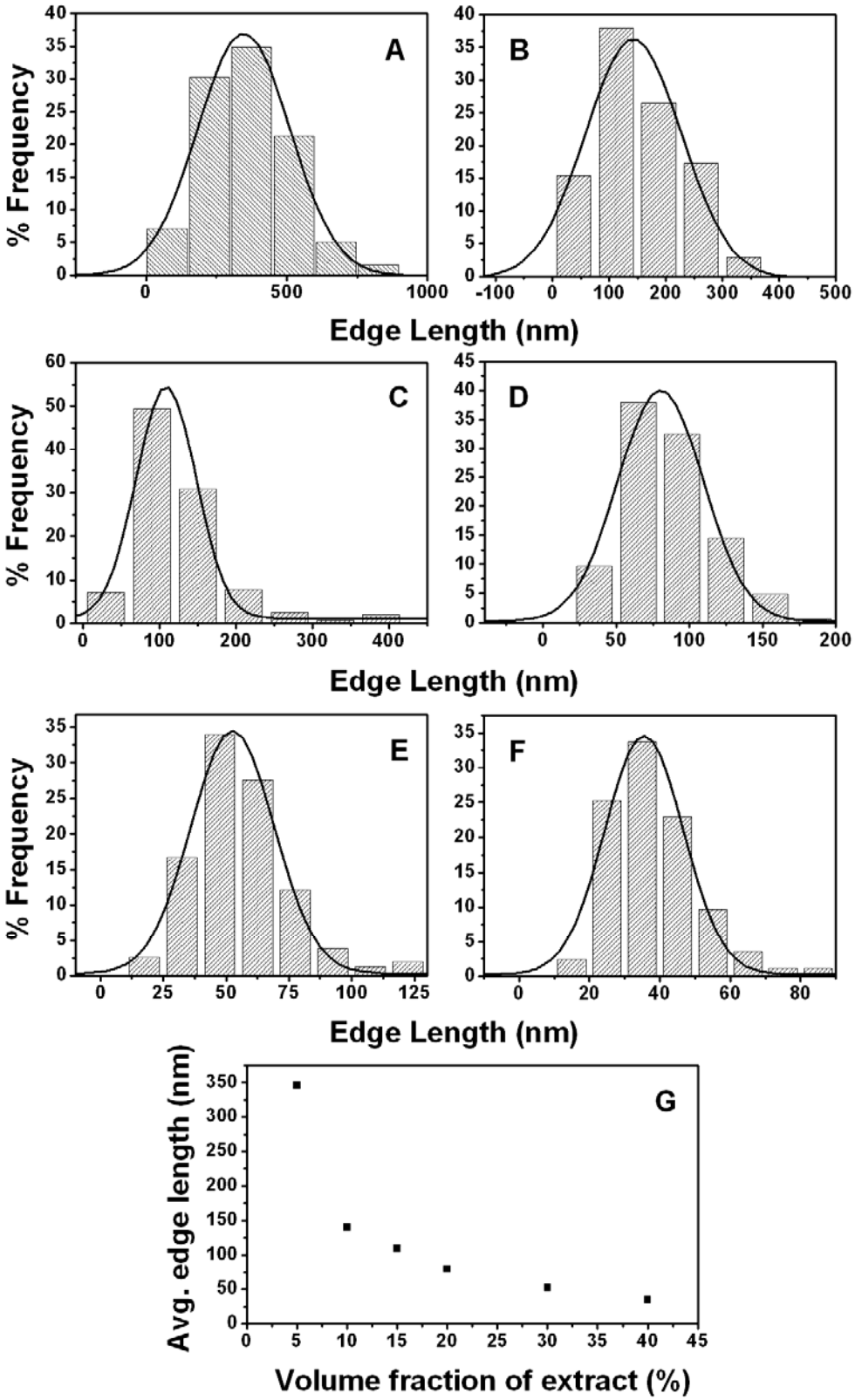

Figure 4.4: *Size distribution analysis on gold nanotriangles formed after 25 h of reaction of 6 mL of 10^{-3} M aqueous $HAuCl_4$ with different amounts of Aloe vera extract: 0.5, 1, 1.5, 2, 3 and 4 mL Aloe vera extract (figures (A), (B), (C), (D), (E) and (F) respectively; final volume adjusted to 10 mL using de-ionised water). (G) summarises the size distribution analysis.*

The contrast patterns that are seen in the TEM images of nanotriangles and hexagons (figs. 4.3C and 4.3D) are attributed to bending contours resulting from the nanometre thickness of the particles [27]. Further analysis shows that reaction with small amounts (0.5 mL) of *Aloe vera* extract leads to the formation of triangular nanoparticles with edge lengths of 346.2 ± 163.5 nm (figs. 4.3A and 4.3B). Fig. 4.4 shows variation in the distribution of gold nanotriangle edge lengths as a function of the extract amount. As the amount of *Aloe vera* extract in the reaction medium is increased to 1 mL, the average edge lengths of the nanotriangles decrease (figs. 4.3C, 4.3D and fig. 4.4B). The same trend is followed on further increase in the amount of *Aloe vera* extract to 4 mL (figs. 4.3E, 4.3F, and figs. 4.4C to fig. 4.4F). Fig. 4.4G summarises the findings of the edge length analysis and clearly shows that the size of the gold nanotriangles can be easily tuned in this protocol.

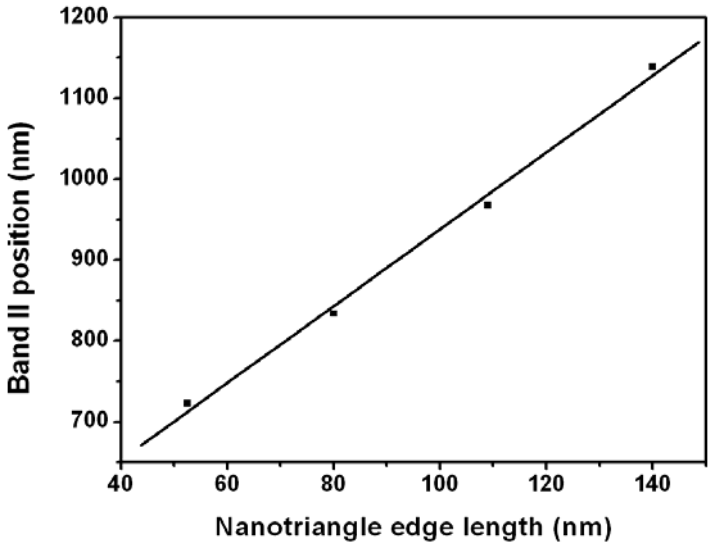

Figure 4.5: *Plot of the longitudinal surface plasmon resonance absorbance band position versus the average edge length of the gold nanotriangles synthesized in experiments containing different amounts of Aloe vera extract.*

It is well known that in triangular nanoparticles of gold the in plane surface plasmon band is a strong function of the edge length of the triangles [4]. This in fact has been found to be the case here with the position of band II showing a direct dependence on the nanotriangle edge length (fig. 4.5). The ability to tune the optical properties of these biogenic gold nanotriangles can be very useful in applications such as cancer cell hyperthermia [5] and architectural optical coatings [8].

An analysis of the percentage of triangles formed in the reaction medium as a function of the *Aloe vera* extract amount reveals that more spherical particles are formed with increasing amount of extract (fig. 4.6). In one particular case wherein we consider the gold nanoparticles synthesized using 5% *Aloe vera* extract, we see a deviation from the above trend with the percentage of gold nanotriangles being much smaller in comparison with reactions employing higher amounts of extract. This may be attributed to the fact that the gold nanotriangles obtained in this case have a very large average size (edge lengths ~ 350 nm) compared to those synthesized using higher amounts of the extract (fig. 4.4G). The fact that increasing amounts of *Aloe vera* extract leads to an increase in the population of the spherical particles is clearly reflected in the UV-visible-NIR absorbance spectra, which show a relative increase in the intensity of the transverse band in comparison with the longitudinal band (fig. 4.2).

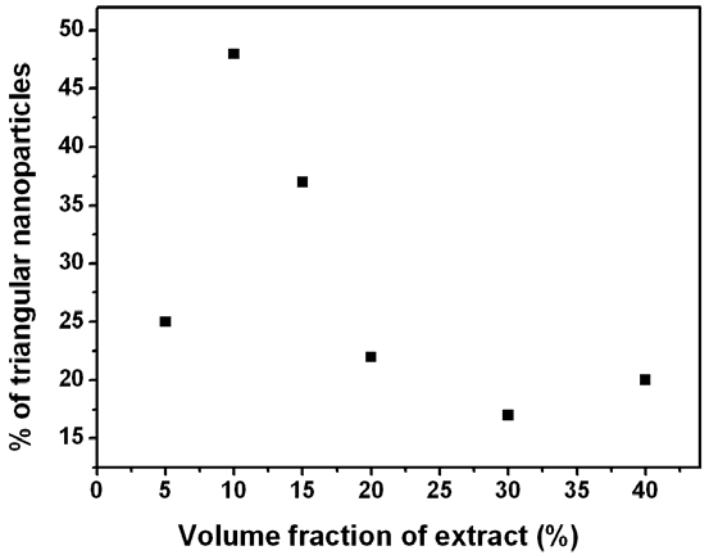

Figure 4.6: *Plot of percentage of triangular nanoparticles formed in the reaction medium versus the amount of Aloe vera extract used.*

The single crystalline nature of the biogenic gold nanotriangles is reflected in the hexagonal nature of the selected area electron diffraction (SAED) spots (fig. 4.7) corresponding to one of the triangles shown in fig. 4.3D. Some of the diffraction spots could be indexed to the face centred cubic (FCC) structure of gold. For instance the spots marked using square and oval are assigned to Bragg reflections from {220} and {311} Miller planes with lattices spacing of 1.44 and 1.23 Å respectively. This shows that the triangles are [111] oriented with the top surface normal to the electron beam [5,28]. The spot marked using the triangle, corresponding to a *d*-spacing of 2.5 Å,

originates due to the presence of a HCP lamellar region in the gold nanotriangles [29]. These emanate from the stacking faults parallel to each other and to the flat {111} surface of the gold nanotriangles. The presence of the reflection corresponding to a *d* spacing of 2.5 Å is a common feature in gold and silver nanotriangles prepared by a variety of methods [5,9a,28].

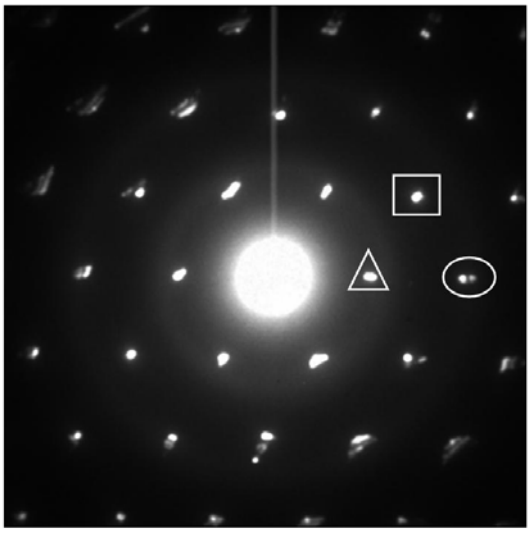

Figure 4.7: *Electron diffraction recorded from a gold nanotriangle shown in Fig. 4.3D. The spots marked using square and oval correspond to Bragg reflections from {220} and {311} lattice planes of FCC gold respectively. The spot marked with the triangle originates due to the presence of HCP lamellar regions in the gold nanotriangles.*

Fig. 4.8A shows representative AFM images of the gold nanotriangles prepared using *Aloe vera* extract. A number of triangular and truncated triangular nanoparticles can be seen overlapping each other. Topographic height analysis of one such truncated triangle is shown in fig. 4.8B. Thickness of the truncated triangle as measured using two sets of points lying on lines 1 and 2 drawn across different areas of the truncated triangle were found to be 2.6 and 7.9 nm respectively (fig. 4.8B).

Though AFM studies suggest presence of a non uniform surface for the nanotriangles, the selected area diffraction pattern (fig. 4.7) observed here is characteristic of gold and silver nanostructures bound by atomically flat surfaces [30]. Thickness of the nanotriangles not being uniform throughout can thus be attributed to the adsorption of biomolecules on to the surface of the gold nanotriangles. Also,

positive evidence for the presence of biomolecules on gold nanotriangle surface can be obtained from XPS measurements (section 4.3.3).

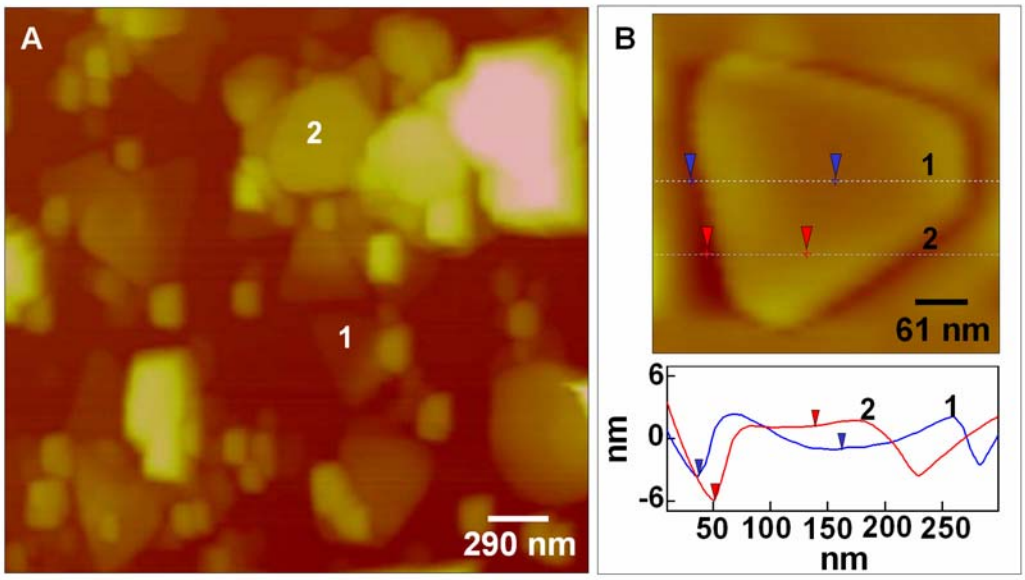

Figure 4.8: *(A) Representative AFM image of Aloe vera reduced gold nanoparticles clearly showing triangular (1) and truncated triangular (2) nanoparticles overlapping each other. (B) Contact mode AFM image of a gold nanotriangle. The lower panel shows the topographic height variation along lines 1 and 2 drawn across different areas of the truncated triangle.*

4.3.3. XPS analysis

Fig. 4.9 summarises the results of X-ray photoelectron spectroscopy (XPS) analysis of the gold nanotriangles. XPS measurements give information on the chemical nature of the surface under investigation. The nanotriangles were prepared by reacting 6 mL of 10^{-3} M $HAuCl_4$ with 1 mL of *Aloe vera* extract (final volume adjusted to 10 mL). The particles thus obtained were purified using centrifugation and redispersion in de-ionised water. The purified nanoparticles were drop coated on a silicon wafer for XPS analysis. All signals obtained were corrected for background contribution using the Shirley algorithm [31] and deconvoluted to their respective Gaussian components. The position of the adventitious carbon signal is used to correct the shift in XPS signals of all elements of the sample that occurs due to charge build up during measurements.

Fig. 4.9A shows the signal arising from the C1s core level. The complex signal is resolved in to five components with binding energies of 280.5, 284, 285, 286 and 288.3 eV. The intense signal at 285 eV is attributed to the adventitious carbon. The

aromatic carbons present in the biomolecules give rise to the lower binding energy signal at 284 eV [32]. The signals at 286 and 288.3 eV are attributed to carbons bound to nitrogen and oxygen [33]. The greater binding energy of the component bound to the oxygen suggests that the carbon is involved in a carbonyl bond [33]. FTIR studies on gold nanotriangles formed using *Aloe vera* extract also support this observation (section 4.3.4). We are unable to account for the strong signal at 280.5 eV.

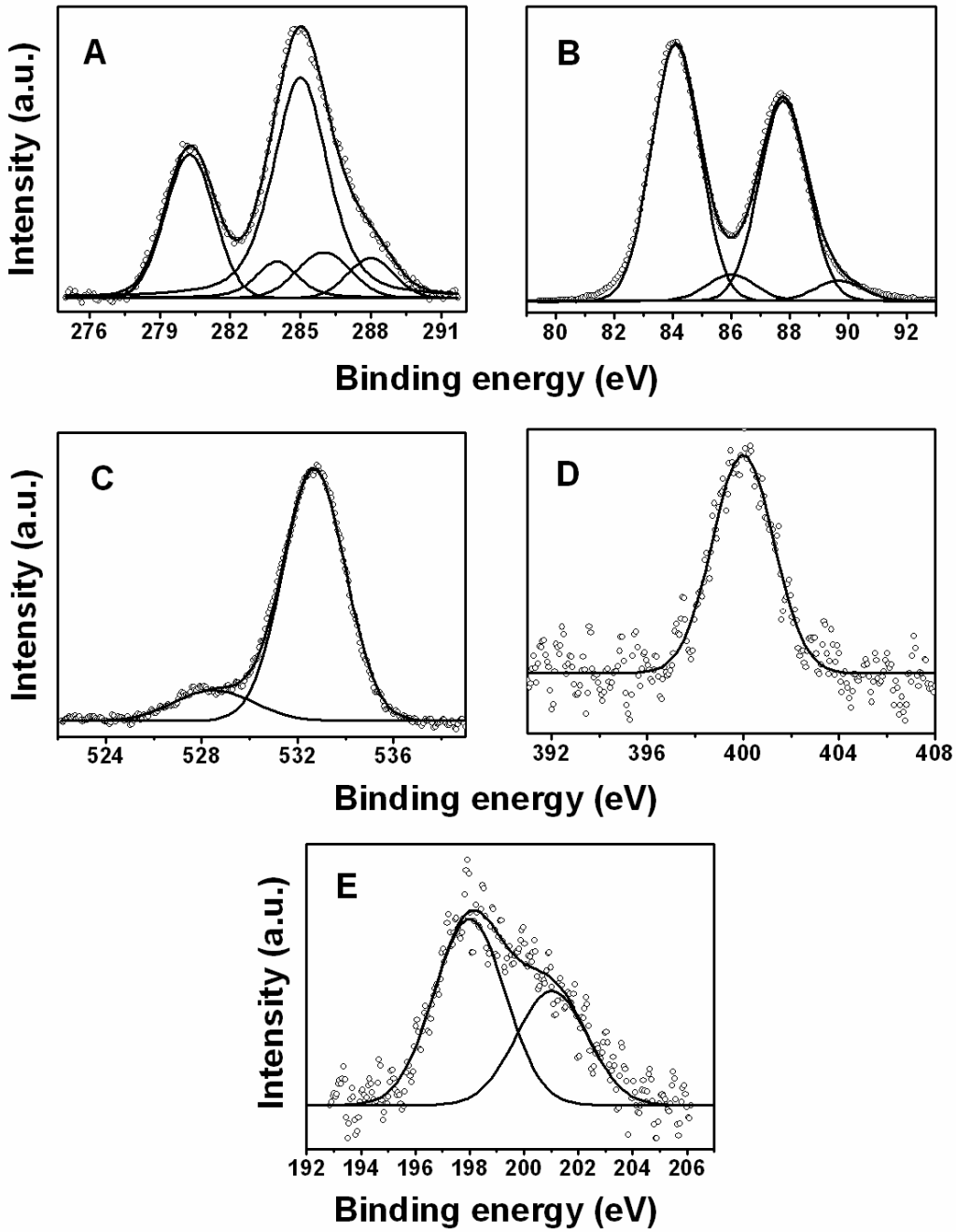

Figure 4.9: *XPS signals from various elements detected in Aloe vera reduced gold nanotriangles: C1s (A), Au4f (B), O1s (C), N1s (D) and Cl2p (E).*

The composite Au 4f signal (fig. 4.9B) is split to two components from metallic and ionic gold. The metallic gold gives rise to signals at 84.1 and 87.8 eV due to the Au $4f_{7/2}$ and Au $4f_{5/2}$ states that arise due to spin orbit coupling. The ionic gold gives rise to higher binding energy signals at 86 (Au $4f_{7/2}$) and 89.8 eV (Au $4f_{5/2}$). The ionic component is attributed to the presence of Au(I) on the surface of gold nanotriangles. Presence of unreduced gold ions is typical of gold nanoparticles and is responsible for their electrostatic stabilisation [8]. Fig. 4.9C shows the signal from O1s core level. The signal is deconvoluted to two components at 528.5 and 532.7 eV. These are attributed to oxygen species in alcohols and carbonyl compounds. The presence of nitrogenous compounds is also seen from the presence of N1s signal at 400 eV (fig. 4.9D). The signal from Cl2p (fig. 4.9E) is deconvoluted to two components centred at 198 and 201 eV originating from the $2p_{3/2}$ and $2p_{1/2}$ core levels. The presence of Cl suggests that the Au(I) detected (fig. 4.9B) is present complexed with the chloride ions on the surface of the gold nanotriangles.

4.3.4. FTIR analysis and mechanism of reduction of gold ions

To study the biomolecules responsible for the formation of gold nanotriangles, the *Aloe* V*era* extract was separated using a 3 kDa nylon membrane (Amicon®). Fraction 1 with molecular weight less than 3 kDa and fraction 2 with molecular weight greater than 3 kDa were obtained. It was observed that only fraction 1 causes reduction of the gold ions, leading to the formation of gold nanoparticles. Fig. 4.10A shows the

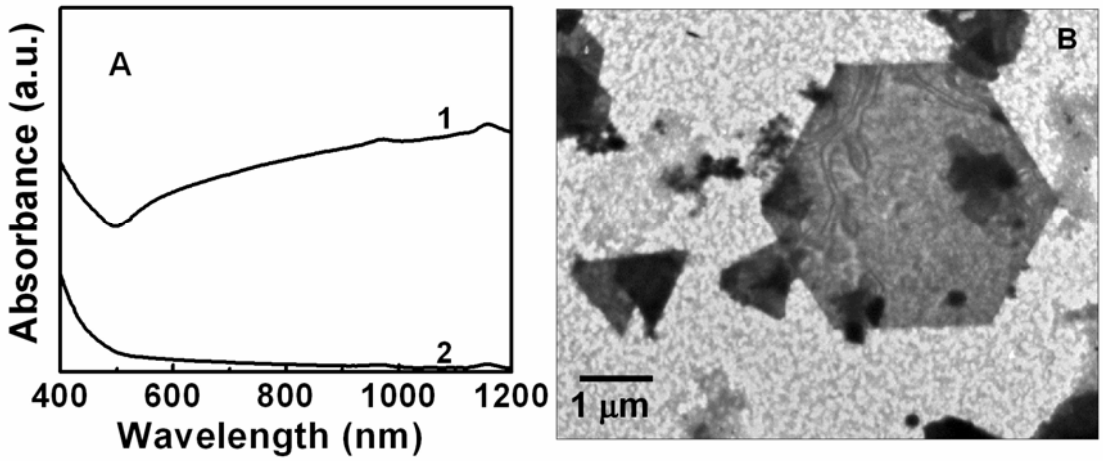

Figure 4.10: *(A) UV-visible-NIR absorbance spectra of solutions obtained on reacting 6 mL of 10^{-3} M aqueous $HAuCl_4$ with 1 mL each of fraction 1 (curve 1) and fraction 2 (curve 2) of the Aloe vera extract (final volume adjusted to 10 mL). (B) Representative TEM image of the nanoparticles formed on reacting 1 mL of fraction 1 with 5 mL of 10^{-3} M aqueous $HAuCl_4$ (final volume adjusted to 10 mL).*

UV-visible-NIR absorbance spectra of gold nanoparticles that have been synthesized on reacting aqueous $HAuCl_4$ with fraction 1 of the *Aloe* V*era* extract (curve 1, fig. 4.10A). The presence of a very broad surface plasmon resonance indicates the reduction of gold ions. The formation of gold nanotriangles is further verified using TEM measurements. Very large triangular and hexagonal gold nanotriangles are seen in addition to smaller nanoparticles (fig. 4.10B). The absence of any distinct absorbance peak in the reaction mixture when fraction 2 was reacted with gold ions lead us to conclude that the reducing and shape-directing agents that cause formation of the nanotriangles have molecular weights less than 3 kDa.

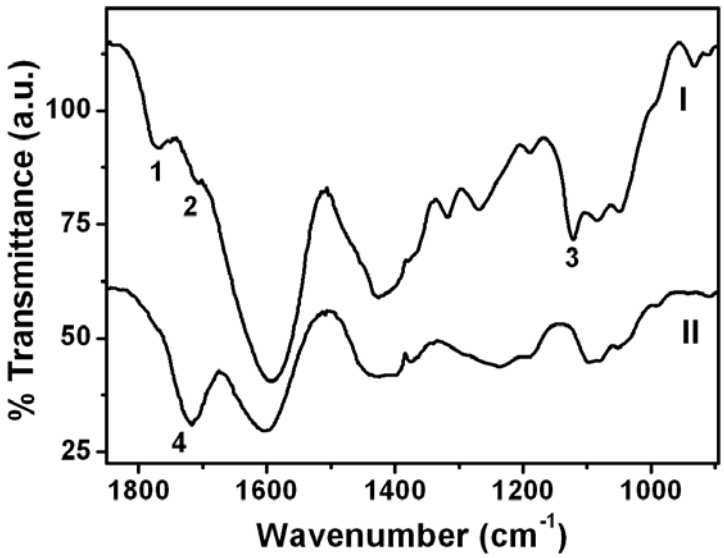

Figure 4.11: *FTIR spectra of fraction 1 of the Aloe vera (curve I) and gold nanoparticles (curve II) synthesized by adding 1 mL of fraction 1 of Aloe vera extract to 6 mL of 10^{-3} M aqueous $HAuCl_4$ solution (final volume adjusted to 10 mL).*

The FTIR spectrum of fraction 1 of the *Aloe Vera* extract is shown in curve I of fig. 4.11. Components of fraction 1, possess weak vibrational peaks at 1770 (peak 1, fig. 4.11) and 1710 cm^{-1} (peak 2, fig. 4.11) apart from a prominent peak at 1120 cm^{-1} (peak 3, fig. 4.11). These indicate the presence of carbonyl and alcoholic groups in the components of fraction 1. After reaction with gold ions (curve II), however, an enhancement in the signal corresponding to a carbonyl group as in aldehydic or ketonic components is observed at 1717 cm^{-1} (peak 4, curve II, fig. 4.11). The presence of carbonyl is also observed in XPS signals of carbon and oxygen (section 4.3.3). The absence of the prominent signal at 1120 cm^{-1} signal in the reaction mixture indicates

that the reduction of the gold ions is coupled to the oxidation of the alcoholic component of fraction 1 of *Aloe* V*era* extract. This observation is similar to previous reports on gold nanotriangle synthesis using lemon grass extract wherein carbonyl groups were found to play an important role in the stabilization and capping of the gold nanotriangles [5,8].

4.3.5. Mechanism of formation of nanotriangles

During the formation of a crystal, greater driving force leads to continuous crystal growth i.e. formation of three-dimensional crystal nuclei and their growth thereof. However, if the driving force for crystal growth is less, layer by layer growth takes place starting from a two-dimensional nuclei [34]. Moreover during nuclei formation and their subsequent growth, the formation or presence of species that retard

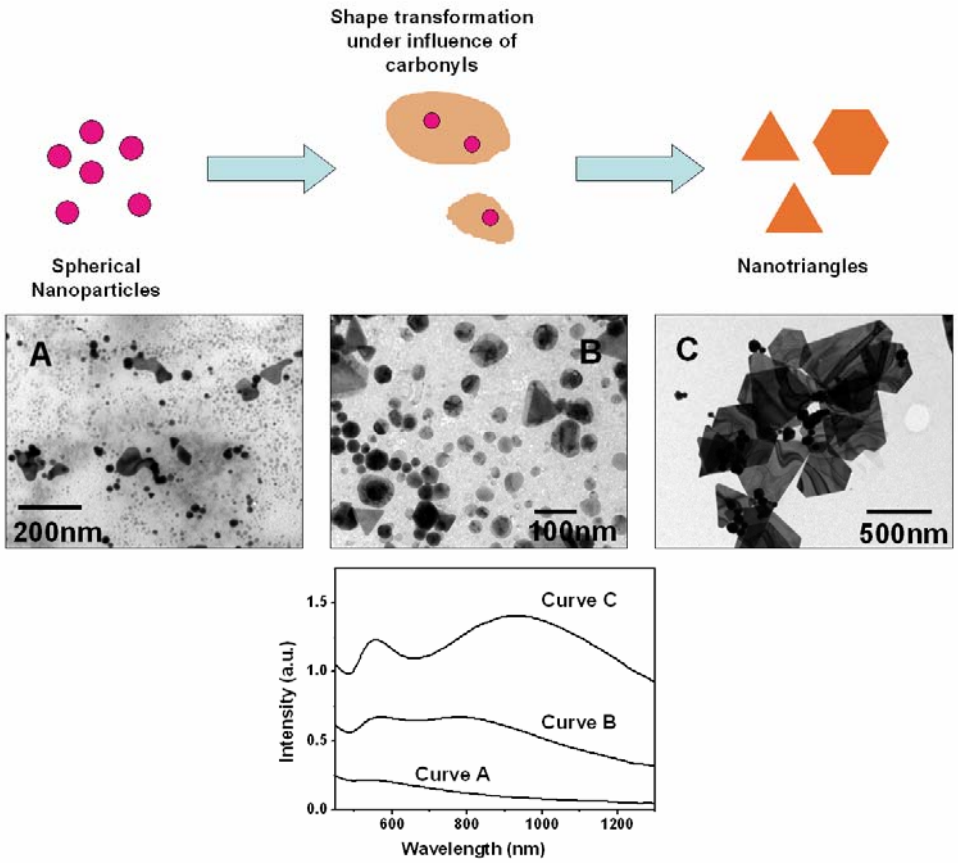

Figure 4.12: *Mechanism of gold nanotriangle formation: It is suggested that, spherical nanoparticles formed initially undergo shape transformation under influence of carbonyl compounds leading to facetted nanotriangles and hexagons. TEM Images shown here were recorded after 1.5 h (A), 3 h (B) and 7 h (C) of onset of reaction. They respectively correspond to curves A, B and C of UV-visible-NIR absorbance spectra. Results obtained are for the reaction where 6 mL of 10^{-3} M $HAuCl_4$ was treated with 1 mL of Aloe vera extract (final volume adjusted to 10 mL).*

three-dimensional growth, could lead to layer by layer or two-dimensional growth.

The mechanism of nanotriangle or hexagon formation here is illustrated in fig. 4.12. Reduction of gold ions leads to the formation of spherical nuclei during the initial stages of the reaction (fig. 4.12A and curve A in fig. 4.12). However accompanying the formation of metallic gold is the formation of carbonyl compounds (peak 4, curve II, fig. 4.11). Carbonyl compounds act on metallic gold and silver nanoparticles [24] and ensure a fluid like surface. Consequently they act as an impediment to the growth or existence of 3D nanostructures [34]. This results in the aggregation of spherical nanoparticles leading to formation of extended flat structures [24]. This is evident from TEM images (fig. 4.12B) and concomitant changes in the UV-visible-NIR spectra (curve B in fig. 4.12). The new structures formed are rich in the stable {111} face. The triangles and hexagons formed are oriented along the <111> direction. This is evident from the observed SAED pattern (section 4.3.2.). The shape transformation process ultimately leads to the formation of faceted triangular or hexagonal structures (fig. 4.12C and curve C in fig. 4.12) keeping with the symmetry of FCC gold.

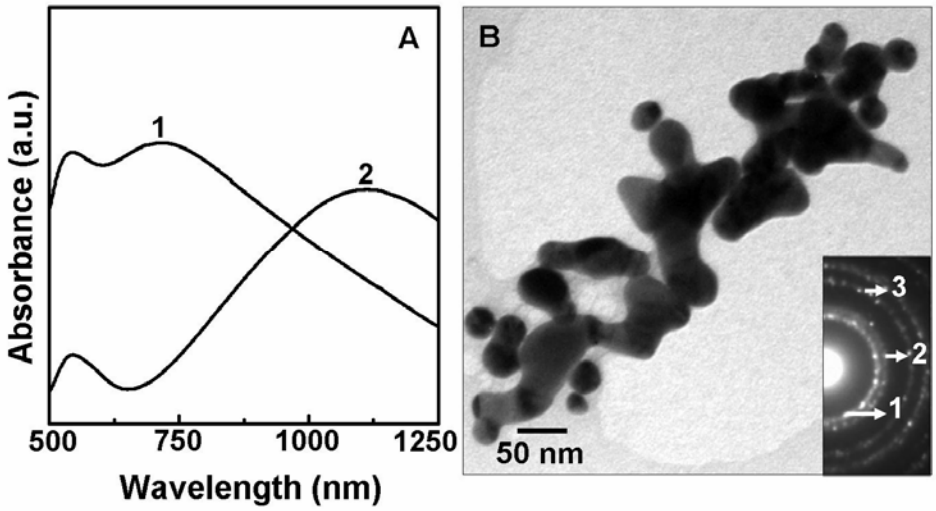

Figure 4.13: *(A) UV-visible-NIR absorption spectra of nanoparticles synthesized by reacting 1 mL of Aloe vera extract with 6 mL of 10^{-3} M $HAuCl_4$ solution (final volume adjusted to 10 mL) at 80 ºC (curve 1) and at room temperature (curve 2). Higher temperature leads to loss of shape control resulting in aggregation (B). The inset shows their SAED pattern. Rings 1, 2 and 3 arise due to Bragg reflections from the {111}, {200} and {220} Miller planes of FCC gold.*

Lower volume fraction of the extract implies a low rate of reaction and supersaturation. This implies that the critical size of the nuclei that can be stabilised before and after shape transformation is small [35]. Conditions that lead to a higher

reaction rates such as higher amounts of *Aloe vera* extract and higher reaction temperature results in an increase in reduction rate and hence the driving force for the formation of 3D nuclei increases. This eventually results in loss of shape control. Thus, higher amounts of *Aloe vera* extract leads to formation of a smaller percentage of smaller gold nanotriangles (fig. 4.6). The same being the case with higher reaction temperature, wherein, apart from the formation of spherical nanoparticles, their aggregation was also observed (fig. 4.13).

4.4. Synthesis of silver nanoparticles

In a typical reaction, 2.5 mL of a 30% ammonia solution in water was added to 5 mL of 10^{-2} M aqueous silver nitrate ($AgNO_3$) solution followed by addition of 5 mL of the *Aloe vera* extract. The concentration of $AgNO_3$ was adjusted to 10^{-3} M by making up the final volume to 50 mL with de-ionised water. The observation of faint yellow colour after 24 h of reaction indicated the formation of silver nanoparticles [4,21].

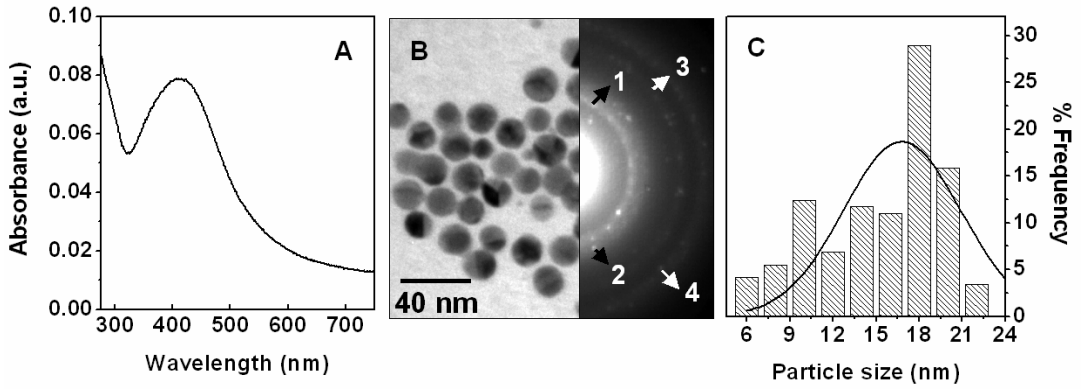

Figure 4.14: *(A) UV-visible absorption spectrum of silver nanoparticles prepared using Aloe vera extract. (B) Representative TEM image and selected area electron diffraction of the same. Rings 1, 2, 3 and 4 arise due to Bragg reflections from {111}, {200}, {220} and {311} Miller planes of FCC silver respectively. (C) Size distribution of silver nanoparticles showing mean size of 15.2 nm ± 4.2 nm.*

The peak at 410 nm (fig. 4.14A) characteristic of silver nanoparticles is due to its surface plasmon absorbance [4,21]. TEM analysis reveals that the silver nanoparticles are predominantly spherical (fig. 4.14B) and the average size of the spherical silver nanoparticles was estimated to be 15.2 nm ± 4.2 nm (fig. 4.14C). Fig. 4.14B also shows the SAED pattern recorded from the silver nanoparticles. The ring-like diffraction pattern indicates that the particles are poly-crystalline. Rings 1, 2, 3 and

4, corresponding to *d*-spacings of 2.33, 2.04, 1.44 and 1.23 nm respectively, are indexed to {111}, {200}, {220}, {311} Miller planes of FCC silver [36]. Unlike reduction of chloroaurate ions which leads to the formation of a large percentage of nanotriangles, such shape control is not exhibited during the formation of silver nanoparticles. A more detailed study is required to fully understand this difference in nanoparticle morphology in these different coinage metals.

4.5. Conclusions

Gold nanotriangles and spherical silver nanoparticles were synthesised using *Aloe vera* leaf extract as the reducing agent. In case of gold, the edge lengths of the [111] oriented nanotriangles could be tuned from 35 to 345 nm. Consequently, the longitudinal surface plasmon resonance band of the nanotriangles could be tuned from the visible to the NIR region of the electromagnetic spectrum. SAED reveals that the atomically flat gold nanotriangles have stacking faults parallel to the [111] surfaces that gives rise to local HCP regions within the nanotriangles. XPS and FTIR spectroscopic studies along with TEM kinetics suggest that carbonyl compounds formed during the course of the reaction cause shape transformation of spherical nuclei resulting in formation of gold nanotriangles and hexagons. It is not clear, at this juncture, why this shape control does not occur during the reduction of silver ions to silver nanoparticles, highlighting the importance of more work needed on this topic.

4.6. References

[1] Fendler, J. H.; Meldrum, F. C. *Adv. Mater.* **1995**, *7*, 607.

[2] El-Sayed, M. A. *Acc. Chem. Res.* **2001**, *34*, 257.

[3] (a) Shi, A.-C.; Masel, R. I. *J. Catal.* **1989**, *120*, 421. (b) Subhramannia, M.; Pillai, V. K. J. Mater. Chem. DOI: 10.1039/b811149a.

[4] Kelly, K. L.; Coronado, E.; Zhao, L. L.; Schatz, G. C. *J. Phys. Chem. B* **2003**, *107*, 668.

[5] Shankar, S. S.; Rai, A.; Ankamwar, B.; Singh, A.; Ahmad, A.; Sastry, M. *Nature Mater.* **2004**, *3*, 482.

[6] Maier, S. A.; Brongersma, M. L.; Kik, P. G.; Meltzer, S.; Requicha, A. A. G.; Atwater, H. A. *Adv. Mater.* **2001**, *13*, 1501.

[7] Dick, L. A.; McFarland, A. D.; Haynes, C. L.; Van Duyne, R. P. *J. Phys. Chem. B* **2002**, *106*, 853.

[8] Shankar, S. S.; Rai, A.; Ahmad, A.; Sastry, M. *Chem Mater*. **2005**, *17*, 566.

[9] (a) Jin, R.; Cao, Y.; Mirkin, C. A.; Kelly, K. L.; Schatz, G. C.; Zheng, J. G. *Science* **2001,** *294*, 1901. (b) Jin, R.; Cao, Y. C.; Hao, E.; Metraux, G. S.; Schatz, G. C.; Mirkin, C. A. *Nature* **2003**, *425*, 487.

[10] Metraux, G. S.; Mirkin, C. A. *Adv. Mater.* **2005**, *17*, 412.

[11] Hao, E.; Kelly, K. L.; Hupp, J. T.; Schatz, G. C. *J. Am. Chem. Soc.* **2002**, *124*, 15182.

[12] I. Pastoriza-Santos, ; Liz-Marzon, L. M. *Nano Lett.* **2002**, *2*, 903.

[13] Wang, L.; Chen, X.; Zhan, J.; Chai, Y.; Yang, C.; Xu, L.; Zhuang, W.; Jing, B. *J. Phys. Chem. B* **2005**, *109*, 3189.

[14] Kim, J.; Cha, S.; Shin, K.; Jho, J. Y.; Lee, J. C. *Adv. Mater.* **2004**, *16*, 459.

[15] Shao, Y.; Jin, Y.; Dong, S. *Chem. Commun.* **2004**, 1104.

[16] Sarma, T. K.; Chattopadhyay, A. *Langmuir* **2004**, *20*, 3520.

[17] Sau, T. K.; Murphy, C. J. *J. Am. Chem. Soc.* **2004**, *126*, 8648.

[18] Klaus, T.; Joerger, R.; Olsson, E.; Granqvist, C. G. *Proc. Natl. Acad. Sci. USA*, **1999**, *96*, 13611.

[19] (a) Gardea-Torresdey, J. L.; Parsons, J. G.; Gomez, E.; Peralata- Videa, J.; Troinai, H. E.; Santiago, P.; Yacaman, M. J. *Nano Lett.* **2002**, *2*, 397. (b) Mukherjee, P.; Ahmad, A.; Mandal, D.; Senapati, S.; Sainkar, S. R.; Khan, M. I.; Ramani, R.; Pasricha, R.; Ajayakumar, P. V.; Alam, M.; Sastry, M. *Angew. Chem. Intl. Ed. Eng.* **2001**, *40*, 3585. (c) Ahmad, A.; Senapati, S.; Khan, M. I.; Kumar, R.; Sastry, M. *Langmuir* **2003**, *19*, 3550. (d) Brown, S.; Sarikaya, M.; Johnson, E. *J. Mol. Biol.* **2000**, *299*, 725.

[20] (a) Dameron, C. T.; Resse, R. N.; Mehra, R. K.; Kortan, A. P.; Caroll, P. J.; Steigerwald, M. L.; Brus, L. E.; Winge, D. R. *Nature* **1989**, *338*, 596. (b) Labrenz, M.; Druschel, G. K.; Thomsen-Ebert, T.; Gilbert, B.; Welch, S. A.; Kemner, K. M.; Logan, G. A.; Summons, R. E.; Stasio, G. D.; Bond, P. L.; Lai, B.; Kelly, S. D.; Banfield, J. F. *Science* **2000**, *290*, 1744. (c) Ahmad, A.; Mukherjee, P.; Mandal, D.; Senapati, S.; Khan, M. I.; Kumar, R.; Sastry, M. *J. Am. Chem. Soc.* **2002**, *124*, 12108.

[21] Mukherjee, P.; Ahmad, A.; Mandal, D.; Senapati, S.; Sainkar, S. R.; Khan, V; Parishcha, R.; Ajaykumar, P. V.; Alam, M.; Kumar, R.; Sastry, M. *Nano Lett.* **2001,** *1*, 515.

[22] (a) Shankar, S. S.; Ahmad, A.; Sastry, M. *Biotechnol. Prog*. **2003**, *19*, 1627. (b) Shankar, S. S.; Ahmad, A.; Pasricha, R.; Sastry, M. *J. Mater. Chem.* **2003,** *13*, 1822.

[23] (a) Shin, K. H.; Woo, W. S.; Lim, S. S.; Shim, C. S.; Chung, H. S.; Kennely, E. J.; Kinghorn, A. D. *J. Nat. Prod.* **1997**, *60*, 1180. (b) Umano, K.; Nakahara, K.; Shoji, A.; Shibamoto, T. *J. Agri. Food Chem.* **1999**, *47*, 3702. (c) Saccu, D.; Bagoni, P.; Procida, G. J. *J. Agri. Food Chem.* **2001**, *49*, 4526.

[24] (a) Li, G.; Lauer, M.; Schulz, A.; Boettcher, C.; Li, F.; Fuhrhop, J-H. *Langmuir* **2003,** *19*, 6483. (b) Smetana, A. B.; Klabunde, K. J.; Marchin, G. R.; Sorensen, C. M. *Langmuir* **2008,** *24*, 7457.

[25] Shipway, A. N.; Lahav, M.; Gabai, R.; Willner, I. *Langmuir* **2000**, *16*, 8789.

[26] Link, S.; El-Sayed, M. A. *Annu. Rev. Phys. Chem.* **2003**, *54*, 331.

[27] Rodriguez-Gonzalez, B.; Pastoriza-Santos, I.; Liz-Marzan, L. M. *J. Phys. Chem. B* **2006**, *110*, 11796.

[28] Germain, V.; Li, J.; Ingert, D.; Wang, Z. L.; Pileni, M. P. *J. Phys. Chem. B* **2003**, *107*, 8717.

[29] Ahrene, D.; Ledwith, D. M.; Gara, M.; Kelly, J. M. *Adv. Func. Mater.* **2008**, *18*, 2005.

[30] Jiang, L-P.; Xu, S.; Zhu, J-M.; Zhang, J-R.; Zhu, J-J.; Chen, H-Y. *Inorg. Chem.* **2004**, *43*, 5877.

[31] Shirley, D. A.; Phys. Rev. B **1972**, *5*, 4709.

[32] Buckel, F.; Effenberger, F.; Yan, C.; Golzhauser, A.; Grunze, M. *Adv. Mater.* **2000**, *12*,901.

[33] Wang, W-C.; Neoh, K-G.; Kang, E-T. *Macromol. Rapid Commun.* **2006**, *27*, 1665.

[34] Vishwanath, B.; Kundu, P.; Mukherjee, B.; Ravishankar, N. *Nanotechnology* **2008**, *19***,** 195603.

[35] Burda, C.; Chen, X.; Narayanan, R.; El-Sayed, M. A. Chem. Rev. **2005,** 105, 1025.

[36] Joint Committee on Powder Diffraction Standards, File No. 04-0783.

Chapter 5

"Click" chemistry based controlled functionalisation of silica nanoparticles and quantification of surface functional groups

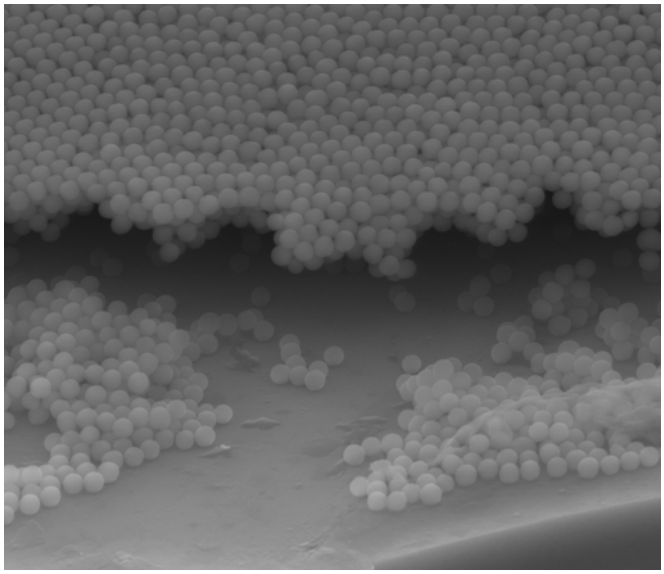

*The first part of this chapter details a methodology to achieve functionalisation of Stober silica nanoparticles using the Huisgen's 1, 3 dipolar cycloaddition, "click" reaction, between surface bound propargyl groups and azide substituted pyrene molecules. The photophysical properties of the pyrene moieties are used to monitor the functionalisation which proceeds in a controllable manner. The surface densities of the fluorophore pyrene moieties are also determined in different samples. In the second part of this chapter, an assay to quantify important functional groups such as amines and azides using (9H-fluoren-9-yl)methyl chloroformate (**FMoC-Cl**) and its derivative is described.*

Part of the work discussed in this chapter has been published in

Prathap Chandran, S.; Hotha, S.; Prasad, B. L. V. *Curr. Sci.* **2008**, 95, 1327.

5.1. Introduction

Silica nanoparticles find varied applications in chromatography [1], bio-separations [2], imaging [3] and synthesis of multifunctional nanocomposites [3,4]. Functionalisation of silica nanoparticle surfaces is commonly achieved using layer by layer assembly [5], physical adsorption [6] and silane coupling agents [7]. Silane functionalisation that proceeds by way of covalent bond formation between surface silanol groups and silane coupling agents has been used widely for silica nanoparticle surface modification. While silanisation can be used to impart a broad range of functionality, the method itself suffers from inherent drawbacks. Factors such as solvent polarity and reaction temperature play complicated and opposing roles in directing the course of reaction [2]. Self condensation of the silane coupling agent poses problems in tuning the density of the surface functionalities and often results in irreproducible surface coverage [2]. Conditions that promote large scale self condensation of silanes in the solvent usually affect the density and uniformity of the surface capping agent.

In this context, the Huisgen's 1, 3 dipolar cycloaddition reaction, one of the popular "click" reactions, between an azide and a terminal alkyne resulting in 1, 2, 3 triazoles [8,9], has been demonstrated to be a versatile tool in organic synthesis [10], material and polymer synthesis [11]. The fact that these reactions proceed to give high yields even under ambient conditions make them popular choices in bioconjugation procedures where pH, medium of reaction and temperature conditions play a crucial role [12]. Moreover the modular nature of a "click" reaction enables imparting of desirable functionalities, without the capping agent undergoing side reactions [9]. There have been few reports that demonstrated the utility of the "click" reaction in preparation of monolayers of surface functionality on silica substrates [13a] and fabrication of silica based particles [1, 13b-d]. However, a systematic study varying the surface density of functional groups on silica nanoparticles using "click" chemistry based protocols has not been carried out.

Addressing this issue, in the first part of this chapter, a "click" reaction based procedure that builds on the functionality imparted by silane coupling agents. The protocol can be used to tune the density of the silica nanoparticle surface capping (scheme 5.1). Standard functionalisation protocols are initially used to graft propargyl groups on to the silica nanoparticle surface. This is followed by reaction with varying amounts of a pyrene chromophore (**PA**) bearing an azide group. The photoactive

capping agent used enables estimation of the amount of fluorophore capping. The utility of the present method in studying the variance in surface functionalisation can easily be validated through pyrene "excimer" emission characteristic of proximity of pyrene molecules to one another. As proposed, we observed that by changing the initial amount of **PA** the density of surface capping can easily be controlled.

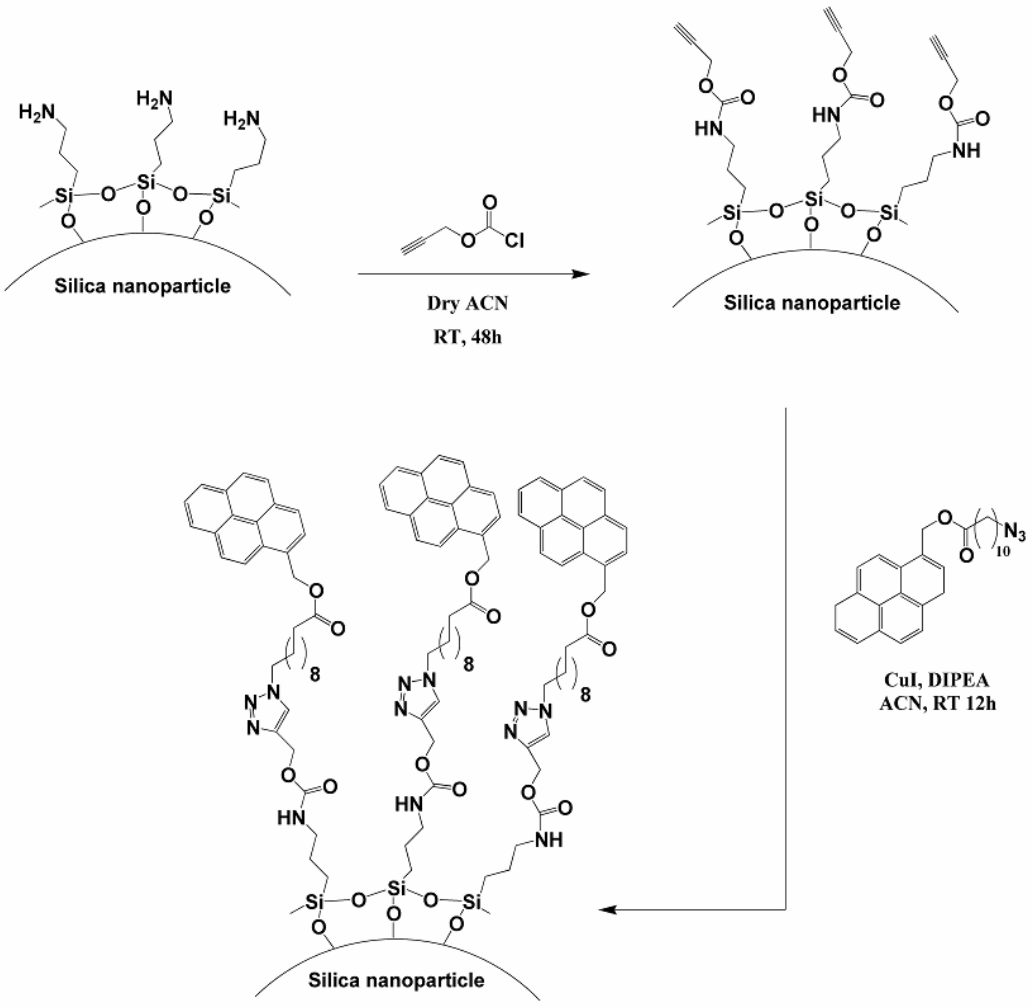

Scheme 5.1: *Salient features of the "click" chemistry protocol for the functionalisation of silica nanoparticles.*

A crucial aspect of functionalisation of nanoparticles and other solid surfaces is the quantification of surface active groups. A variety of techniques have been employed for the same. Combustion analysis has been extensively used to quantify the surface coverage of silica surfaces [1,7a,14]. Chemical methods used include titration against $AgNO_3$ [15] to detect reductive groups such as silyl hydrides, besides others [14a]. Spectroscopic techniques have also been used for this purpose. For instance Hoffman

and co-workers have used quantitative FTIR analysis to study the extent of "click" reactions on functionalized silica surfaces [13]. Thomas et al [16] have estimated the surface density of pyrene chromophores on gold nanoparticles. We have extended the same to a silica nanoparticle system [17] as would be discussed in the first part of this chapter. Kallury and co-workers [18] have used XPS and elemental analysis for surface coverage quantification in combination with NMR and BET isotherm measurements.

Park and co-workers used the reaction between 4-nitrobenzaldehyde and surface amines, leading to formation of a chromophore Schiff's base, to evaluate the surface density of amines in functionalized silica nanoparticles spectroscopically [19]. This method was further utilized by Ian Bruce and co-workers to study the effect of reaction conditions on the surface amine density in silica coated magnetic nanoparticles [2]. Schiff's base formation is highly susceptible to moisture, and so the above procedure requires anhydrous conditions to produce authentic results. It needs to be noted that water itself is formed as a by-product of the reaction.

In a recent study by Cheng et al, fluorene substituted silanes were used to study functionalisation of mesoporous silica [20]. Herein, the UV-visible absorbance of dibenzofulvene (**DBF**), released by fluorenylmethoxycarbonyl derivatives on treatment with secondary amines, was measured to study the differential release rates of the same from inside and outside the pores [20]. In an earlier report, Tirrell and co-workers used flow-cytometry methods to detect azide groups incorporated on to the surface of bacterial cells [22]. In this method, propargylated biotin groups were incorporated on to cell surfaces using "click" chemistry. Tagging of the biotin groups with fluorescent labeled avidin molecules allowed flow cytometry analysis. However, only a semi-quantitative estimation of the surface azide groups was demonstrated [22].

In our study, as detailed in the second part of this chapter we extend the approach of Cheng et al to quantify surface reactive amine and azide groups present on Stober silica nanoparticles. The utility of these groups in functionalisation processes is well documented [8,9,19]. It is common knowledge that **FMoC-Cl** is used for studying functional group loadings in solid state peptide synthesis [21]. The present method bears a very close resemblance to the same. In addition to amine analysis, a propargyl derivative of **FMoC-Cl** was used to detect and quantify the density of azide groups in silica nanoparticles of different sizes.

5.2. "Click" chemistry for surface functionalisation of silica nanoparticles

Scheme 5.1 summarizes the salient features of the "click" reaction based surface functionalisation protocol. In the following sections, the same is described in more detail.

5.2.1. Experimental details

5.2.1.1. Synthesis of silica nanoparticles

Silica nanoparticles were synthesized following the procedure reported by Stober and co-workers [23]. In a typical procedure, 1.5 mL of Tetraethylorthosilicate (TEOS) was added to a mixture of 50 mL absolute ethanol, 2 mL NH_3 (about 30% in water) and 1 mL de-ionised water (Milli-Q®) at 40 °C. After 3 h of reaction at 40 °C, an additional 1 mL of TEOS was added. This was followed by another 3h of reaction at 40 °C. Purification of silica nanoparticles was carried out using three rounds of centrifugation (13000 rpm for 15 mins) interspersed with re-dispersion and washing with absolute ethanol. The size of purified silica nanoparticles was determined to be 61.3 ± 4.2 nm using TEM analysis [24]. The first part of this chapter dealing with pyrene functionalisation of silica nanoparticles is exclusively based on these particles. Table 5.1 shows the size of the silica nanoparticles obtained under different reaction conditions that have been used in this chapter.

Table 5.1: *Silica nanoparticles synthesized under different reaction parameters (T = 40 °C).*

TEOS (mL)	**H_2O (mL)**	**NH_3 (mL)**	**Absolute Ethanol (mL)**	**TEOS added after 3h (mL)**	**Size of SiO_2 nanoparticles (nm)**
1.5	1	1.7	50	1	37.5 ± 1.5
1.5	1	1.8	50	1	51.7 ± 4.7
1.5	1	2	50	1	61.3 ± 4.2
1.5	1	3	50	1	146 ± 6.1
1.5	1	20	50	1	398 ± 10.2

5.2.1.2. Amine functionalisation of silica nanoparticles

(3-aminopropyl)-triethoxy silane (APTES) functionalisation is the most widely used method for obtaining exposed amine groups on silica surfaces. For our study, we

optimized the conditions available in several papers and employed the following procedure [2]. Unfunctionalised silica nanoparticles were dispersed in absolute ethanol (150 mg in 15 mL) followed by the addition of 2% w/v of APTES. The above mixture was stirred for a period of 6 h under reflux conditions. Purification of functionalized silica nanoparticles was carried out using three rounds of centrifugation (13000 rpm for 15 mins) interspersed with re-dispersion and washing with absolute ethanol. Functionalized silica nanoparticles were subjected to TEM characterization after purification.

5.2.1.3. Propargyl functionalisation of silica nanoparticles

In a typical reaction, 250 mg of APTES capped silica nanoparticles were dispersed in 50 mL of dry acetonitrile followed by addition of 0.3 mL propargylchloroformate. The above reaction mixture was stirred for a period of 48 h at RT under nitrogen atmosphere. The propargyl capped silica nanoparticles were purified using multiple rounds of centrifugation and washing with acetonitrile. Purified propargyl capped silica nanoparticles were characterized using FTIR and TEM analysis.

5.2.1.4. Synthesis of pyrene chromophores

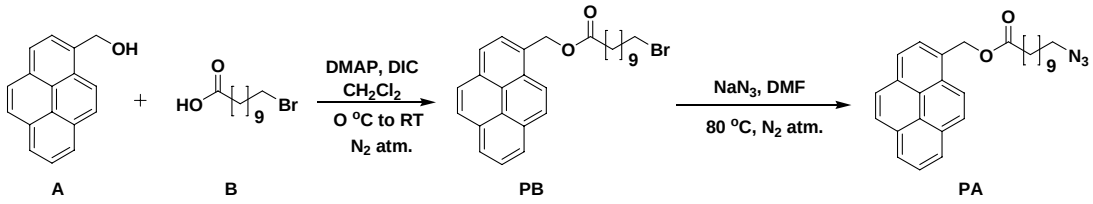

Scheme 5.2: *Protocol for the synthesis of methyl-(1-pyrene)-11-azido-undecanoate (**PA**).*

Synthesis of the organic molecule bearing the azide functionality (**PA)** was accomplished by following standard protocols [25] (scheme 5.2) and its structural authenticity was thoroughly established by various spectroscopic techniques including ^{1}H and ^{13}C NMR spectroscopy and MALDI-TOF mass spectrometry.

5.2.1.4.1. Synthesis of Methyl-(1-pyrene)-11-bromo-undecanoate (PB)

To a solution of 1-pyrene methanol (**A**) (0.69 g, 0.297 mmol) and 11-bromoundecanoic acid (**B**) (0.7876 g, 0.297 mmol) in anhydrous CH_2Cl_2 (15 mL) was

added diisopropylcarbodiimide (DIC) (0.693 mL, 0.445 mmol) and a catalytic amount of 4-N,N-(dimethylamino)pyridine (DMAP) at 0 ^{o}C under nitrogen atmosphere. The resulting solution was brought to room temperature (35 ^{o}C) and stirred vigorously for 2 h. At the end of the reaction, as adjudged by TLC analysis, the reaction mixture was diluted with 50 mL of freshly distilled CH_2Cl_2, washed thoroughly with water and extracted thrice with CH_2Cl_2 (3 x 50 mL). The combined organic layers were dried over anhydrous Na_2SO_4 and filtered. The filtrate was concentrated *in vacuo* to obtain a crude residue which was subsequently purified by silica gel column chromatography using a gradient solvent system starting with 10 % ethyl acetate in petroleum ether and the product (**PB**) (1.31 g, 92 %) was eluted with 30 % ethyl acetate in petroleum ether.

*Characterization data of compound **PB**:*

^{1}H NMR (200.13 MHz, $CDCl_3$): 1.13-1.45 (m, 12 H), 1.56-1.86 (m, 4 H), 2.37 (t, 2 H, *J* = 7.36 Hz), 3.36 (t, 2 H, *J* = 6.81 Hz), 5.83 (s, 2 H), 7.95-8.36 (m, 9 H); *^{13}C NMR* (50.32 MHz, $CDCl_3$): 25.0, 28.1, 28.6, 29.0, 29.1, 29.2, 29.3, 32.8, 33.8, 34.4, 64.5, 122.9, 124.6, 125.4, 125.5, 126.1, 127.3, 127.7, 127.8, 128.1, 129.1, 129.5, 130.7, 131.2, 131.7, 173.8 *Calcd. Mol. Wt.* of $C_{28}H_{31}BrO_2$: 478.15, *Found:* 478.13, 480.13; *FTIR:* 3037 (m), 2916 (s), 2850 (s), 1739 (s) cm^{-1}.

5.2.1.4.2. Synthesis of Methyl-(1-pyrene)-11-azido-undecanoate (PA)

Compound PB (0.84 g, 0.17 mmol) was dissolved in 20 mL of anhydrous DMF and to it NaN_3 (0.911 g, 1.4 mmol) was added under stirring condition. The mixture was heated at 80 ^{o}C for 12 h under nitrogen atmosphere. The volume of the solution was reduced in *vacuo* and the light yellow solid was purified by silica gel column chromatography using a gradient solvent system starting with 10 % ethyl acetate in petroleum ether and the pure product (**PA**) (0.734 g, 95 %) was fully characterized by ^{1}H and ^{13}C NMR spectroscopy and MALDI-TOF spectrometry.

*Characterization data of compound **PA**:*

^{1}H NMR (200.13 MHz, $CDCl_3$): 1.10-1.32 (m, 12 H), 1.45-1.68 (m, 4 H), 2.36 (t, 2 H, *J* = 7.33 Hz), 3.19 (t, 2 H, *J* = 6.89 Hz), 5.81 (s, 2 H), 7.92-8.28 (m, 9 H); *^{13}C NMR* (50.32 MHz, $CDCl_3$): 24.9, 26.4, 28.8, 29.0, 29.1, 29.2, 29.3, 34.3, 51.4, 64.5, 122.9, 124.6, 124.8, 125.4, 125.4, 126.0, 127.3, 127.7, 127.8, 128.1, 129.0, 129.5, 130.6, 131.1, 131.6, 173.8; *Calcd. Mol. Wt. of* $C_{28}H_{31}N_3O_2$: 441.24, *Found:* 441.27; *FTIR:* 3043 (m), 2928 (s), 2853 (s), 2094 (s) [azide stretching], 1733 (s) cm^{-1}.

5.2.1.5. "Click" functionalisation of silica nanoparticles with pyrene units

In a typical reaction, 50 mg of purified propargyl capped silica nanoparticles and 32 mg of CuI were dispersed in 5 mL of acetonitrile. The role of Cu(I) salt here is to catalyze the regioselective reaction between the azide and alkyne to yield 1,4-disubstituted 1,2,3-triazoles rather than 1,5-disubstituted 1,2,3-triazoles [8]. 4 mg of **PA** (1.8×10^{-3} M) and 0.36 mL of DIPEA were added to this mixture of propargyl capped silica nanoparticles and Cu(I). The above constituents were stirred for a period of 12 h at RT. Purification of pyrene capped silica nanoparticles was carried out as follows: 3 rounds of centrifugation interspersed with re-dispersion and washing with acetonitrile. The precipitate obtained thus was re-dispersed in 5 mL of acetonitrile and added to 15 mL of 0.01 N HCl. This leads to the precipitation of silica nanoparticles and dissolution of excess copper(I) iodide. The precipitate is further washed with acetonitrile and chloroform to yield purified pyrene capped silica nanoparticles (**SiPy1**).

The above process is repeated with varying amounts of **PA** (concentrations - 1.8×10^{-4} M and 1.8×10^{-5} M) to yield silica nanoparticles with varying pyrene surface densities (**SiPy2** and **SiPy3** respectively). The nanoparticles thus obtained were characterized using TEM and spectroscopic techniques such as UV-visible absorbance, fluorescence and FTIR.

5.2.2. FTIR characterization

Fig. 5.1 shows FTIR spectra of silica nanoparticles at different stages of functionalisation. Curve 1 in fig. 5.1 shows the FTIR spectra of APTES functionalized silica nanoparticles. On propargyl chloroformate treatment (scheme 5.1) a peak at 1700 cm^{-1} (curve 2, fig. 5.1) attributed to the carbonyl stretching vibrations in urethanes [26] is observed (curve 2, fig. 5.1). This distinguishing feature, absent in curve 1, provides evidence for successful functionalisation of amine capped silica nanoparticles with propargyl groups. The spectrum from pure **PA** reveals a very intense peak at 2100 cm^{-1} due to the azide group stretching. However, the "click" product (**SiPy1**) shows no absorbance at 2100 cm^{-1} indicating the absence of any azide moiety (compare curves 3 and 4, fig. 5.1) in the product. This also rules out the possibility of **PA** capping the silica nanoparticles by way of physical adsorption, in which case the azide group would be detected by FTIR. The spectral feature due to 1, 2, 3 triazole unit, expected around 1650 cm^{-1} [27], is not clearly discernible as it overlaps with the signal at 1650 cm^{-1} characteristic of water present in the silica [28]. Note that the feature at 1650 cm^{-1} is

seen in all silica samples. Conclusive evidence for the formation of the "click" product is, however, obtained from optical characterization.

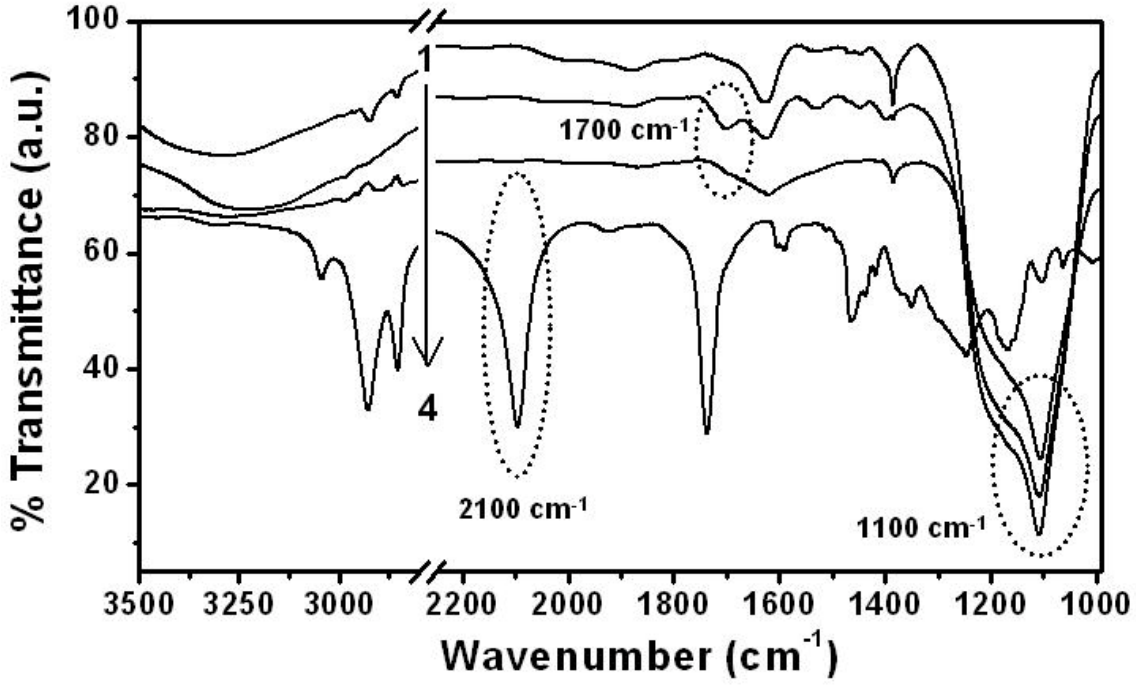

Figure 5.1. *FTIR characterisation of APTES capped silica, propargyl capped silica and* ***SiPy1*** *(curves 1-3 respectively). Note the intense band at 1100 cm^{-1}, which arises due to the siloxane bonds present in silica. Curve 4 corresponds to methyl-(1-pyrene)-11-azido-undecanoate* ***(PA)****.*

5.2.3. UV-visible absorbance, fluorescence and TEM studies

It is important to note that dispersibility of the nanoparticles can be tuned by choosing an appropriate capping agent. Silica nanoparticles obtained as products of the "click" reaction are dispersible in chloroform (due to the non-polar nature of the pyrene capping) indicating change in surface polarity following the reaction. The dispersions in chloroform have been used to estimate concentration of the surface capping agent. Fig. 5.2 shows UV-visible absorbance profiles of pyrene functionalized silica nanoparticles. Curves 1 to 3 corresponding to **SiPy1** to **SiPy3** (see section 5.2.1.5 for details) respectively indicate presence of pyrene moieties on the silica nanoparticle surface. The spectral features at 315, 330 and 346 nm are typical of pyrene chromophores [29]. This observation along with FTIR evidence clearly proves the occurrence of "click" reaction between propargyl functionalized silica nanoparticles

and the azide functionality of **PA**. Varying spectral intensities reflect change in the surface density of pyrene chromophores on the nanoparticle surface.

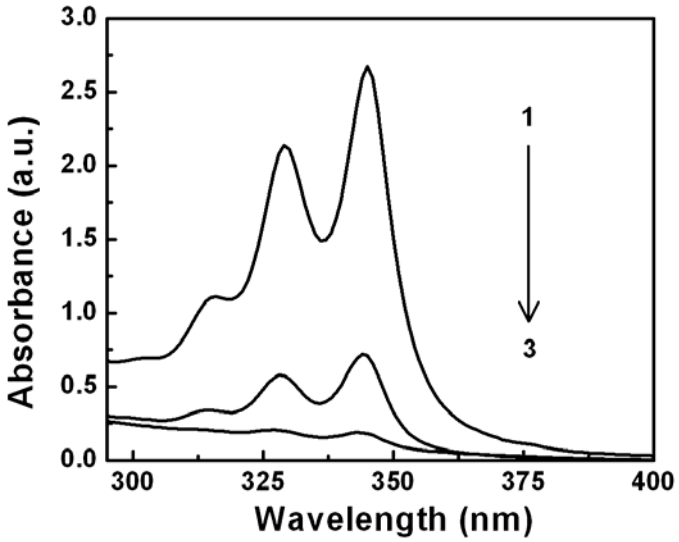

Figure 5.2: *Background corrected UV-visible absorbance profiles of* ***SiPy1****,* ***SiPy2*** *and* ***SiPy3*** *(Curves 1-3 respectively).*

The quantity of pyrene content in the silica composite was determined by measuring the UV-visible absorbance spectra of a dispersion of pyrene functionalized silica nanoparticles (1 mg in 1 mL of $CHCl_3$). The value of absorbance at 346 nm is then used to quantitatively estimate the amount of pyrene present in 1 mg of functionalized silica. The molar extinction coefficient of **PA** in chloroform was determined (ε = 5.9 x 10^4 Mcm^{-1}) from a calibration plot. The amount of pyrene chromophore in 1 mg of the silica composite was estimated, from UV-visible analysis, to be 4.5 x 10^{-8} moles for **SiPy1.** Similarly for **SiPy2** and **SiPy3** the amount of pyrene in 1 mg of the silica composites were determined (table 5.2).

Table 5. 2: *Determination of pyrene content from UV-visible absorbance studies.* ε *= 5.9 x* 10^4 Mcm^{-1} *(at 346 nm in chloroform).*

Sample	Absorbance value at 343 nm	Amount of Pyrene (moles / mg)
SiPy1	2.67	4.5 x 10^{-8}
SiPy2	0.720	1.2 x 10^{-8}
SiPy3	0.19	3 x 10^{-9}

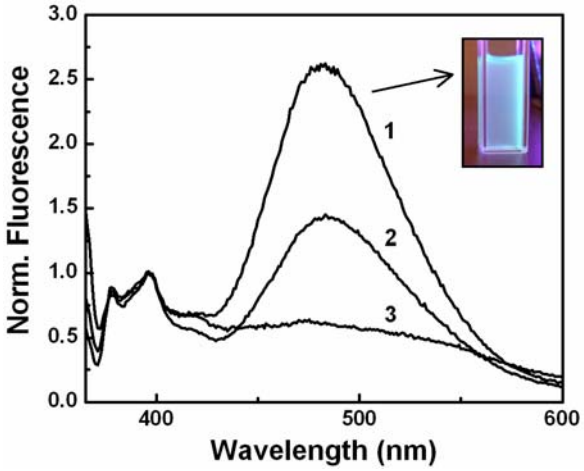

Figure 5.3: *Curves 1-3 show normalized emission profiles corresponding to* ***SiPy1 – 3*** *respectively (excitation at 350 nm; normalization of the signals done w.r.t intensity of emission at 397 nm). Inset shows a picture of* ***SiPy1*** *dispersed in $CHCl_3$ when irradiated with a 365 nm UV lamp.*

Additional evidence for the functionalisation and the ease with which the density of surface groups can be tuned was obtained from fluorescence measurements. Fig. 5.3 shows the emission profiles of pyrene functionalized silica **SiPy1 – SiPy3** (curves 1 – 3 respectively) when excited at 350 nm. Examination of curve 1 (corresponding to emission from **SiPy1**) reveals peaks at 378 and 397 nm in addition to a hump at 389 nm. These emissions of the pyrene fluorophore [16,29,30] provide proof for successful functionalisation of the nanoparticle surface by way of the "click" reaction. Moreover a broad band centered at 480 nm characteristic of the pyrene excimer emission (curve 1, fig. 5.3) is observed [30]. Inset in fig. 5.3 shows the green excimer emission of **SiPy1** dispersed in $CHCl_3$ when excited with a 365 nm UV lamp.

Excimer emission is observed when the concentration of pyrene in a given analyte is either high or when the pyrene moieties are held in close proximity in constrained environments such as micelles and solid surfaces. In such cases, the excited state interaction of pyrene units is permitted leading to the excimer emission [16,30]. Observation of pyrene excimer emission from the silica particles is attributed to the high density of the pyrene fluorophore on the nanoparticle surface. The fall in relative intensity of the excimer emission in comparison to monomer emission in case of **SiPy2** and **SiPy3** (see curves 2 and 3, fig. 5.3 respectively) is attributed to change in the surface density of pyrene fluorophores.

Formation of excimer in **SiPy1** due to aggregation of nanoparticles can be ruled out as all samples have been diluted to the same extent and no aggregates could be

observed either in solution or in TEM images. TEM images, however, indicate a slight increase in the size of the silica nanoparticles occurring accompanying the process of functionalisation (fig. 5.4).

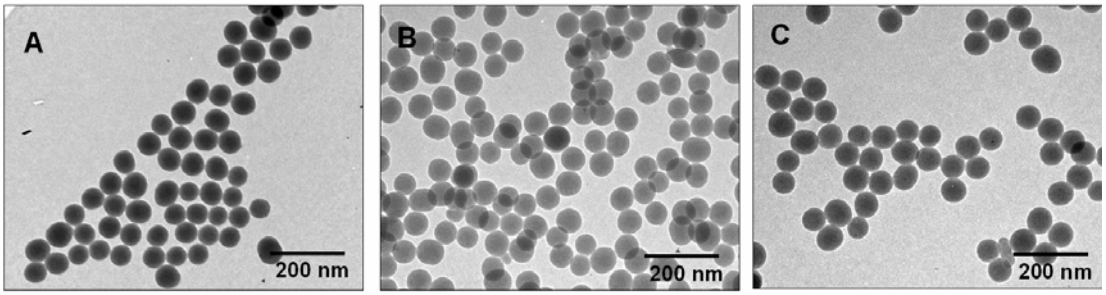

Figure 5.4: *Transmission electron micrographs of functionalized silica nanoparticles: (A) Stober silica, (B) propargyl capped and (C) pyrene capped silica nanoparticles (**SiPy1**).*

The final size of the silica nanoparticles after pyrene functionalisation was determined to be 66.5 ± 3.9 nm. Thus we see an increase of 5.2 nm in the diameter of the silica nanoparticles (see section 5.2.1.1 for comparison) following functionalisation. Such increase in the size of the silica nanoparticles up on functionalisation has been observed earlier [7a,14a,31].

5.2.4. Thermo gravimetric analysis and determination of pyrene density on functionalized silica nanoparticles

TGA studies were carried out to study the varying concentration of the pyrene surface groups [14b]. Fig. 5.5 shows increasing weight loss with increasing functionalisation due to loss of the organic matter. It is seen that **SiPy1** (curve 3) and **SiPy3** (curve 4) recorded 4.5% and 1.5% greater weight loss in comparison to stober silica at 800 °C. These observations were used to determine the surface density of the pyrene chromophores in different silica nanoparticle composites as described below.

The pyrene chromophores are assumed to be uniformly distributed among all the silica nanoparticles and the particles themselves are assumed to be uniform spheres in the following calculations.

Density of Stober silica nanoparticles = 1.98×10^{6} g/m^{3} [17b]

Volume of a Stober silica nanoparticle (diameter – 66.5 nm) = 1.54×10^{-22} m^{3}

Weight of a Stober silica nanoparticle (diameter – 66.5 nm) = 3.1×10^{-16} g

Surface area of a Stober silica nanoparticle (diameter – 66.5 nm) = 1.39 x 10^{-14} m^2

These were incorporated in further calculations summarized in table 5.3.

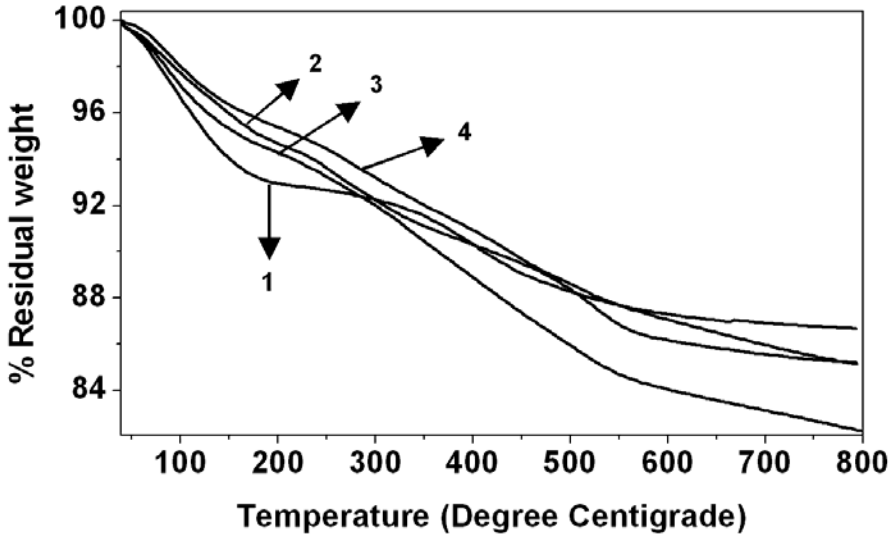

Figure 5.5: *Thermo gravimetric analysis performed on unfunctionalized silica nanoparticles (1), propargyl functionalized silica nanoparticles (2) and samples* ***SiPy1*** *(3) and* ***SiPy3*** *(4).*

Table 5.3: *Surface density of pyrene units on silica nanoparticles under different conditions.*

Sample	Stober silica content per mg of sample	Number of particles per mg of sample	Amount of pyrene per mg of sample	Number of Pyrene units per particle	Surface density of pyrene units (molecules/nm^2)
SiPy1	9.55 x 10^{-4} g	3.35 x 10^{12}	4.5 x 10^{-8} moles	8.1 x 10^3	0.6
SiPy3	9.85x 10^{-4} g	3.46 x 10^{12}	3 x 10^{-9} moles	5.2 x 10^2	0.04

The number of pyrene chromophores on the surface of a single particle was calculated based on these estimates (table 5.3). Typically a single silica nanoparticle in case of **SiPy1** is functionalized to bear 8.1 x 10^3 pyrene units (surface density – 6 x 10^{-1} molecules/nm^2) as compared to 5.2 x 10^2 units on **SiPy3** surface (surface density – 4 x 10^{-2} molecules/nm^2). Thus the "click" based protocol can be used to vary surface

concentration of the capping agent by orders of magnitude with initial concentration of the azide playing a decisive role.

The observations made during fluorescence studies can also be better understood from these calculations. Accordingly, for **SiPy3** having a pyrene surface density of 4 x 10^{-2} molecules/nm^2, an excimer emission of very low intensity (curve 3, fig. 5.3) is observed. However for **SiPy1**, having a higher pyrene surface density of 6 x 10^{-1} molecules/nm^2, an intense excimer emission is observed (curve 1, fig. 5.3). With decreasing surface density the pyrene units are distributed far apart on the surface of the silica nanoparticles preventing them from interacting in the excited state. This leads to a low intensity excimer emission. Consequently, it is seen that in sample **SiPy3**, having a low concentration of pyrene capping, the intensity of the excimer is not significant as in **SiPy2** and **SiPy1**. This particular observation has previously been made in the case of pyrene functionalized gold nanoparticles by Thomas et al [16] and others [32].

5.3. Estimation of reactive functional groups on surface of silica nanoparticles

In the following sections, the results of our experiments to study density variation of surface functional groups on nanoparticles employing the protection-deprotection strategy are described.

5.3.1. Estimation of surface reactive amine groups

The procedure for estimation of amine groups is based on the protection-deprotection strategy employed for the same. (9H-fluoren-9-yl)methyl chloroformate **(FMoC-Cl**) and its derivatives are routinely used for the protection of amine groups in organic synthesis [33] resulting in the formation of a carbamate derivative. After desirable organic transformations a secondary amine is used to cleave the carbamate and achieve near quantitative yield of the deprotected product [33]. Herein, amine functionalized silica nanoparticles are treated with **FMoC-Cl**. This results in all the amine groups on the surface forming a carbamate product. After the removal of excess **FMoC-Cl** from the reaction mixture, the **FMoC** carbamate bearing silica nanoparticles are treated with 1,8-Diazabicyclo[5.4.0]undec-7-ene (**DBU**) - a secondary amine. This leads to release of dibenzofulvene (**DBF**) a photoactive compound [21,33]. Estimation of **DBF** gives the amount of amine present on the silica nanoparticles. The process is summarized in scheme 5.3.

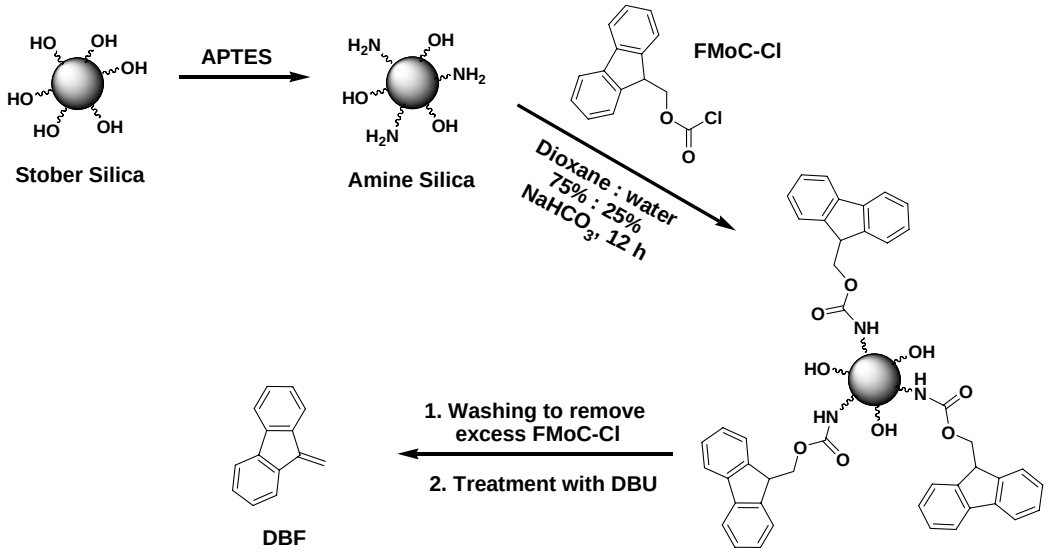

Scheme 5.3: *Estimation of surface active amine groups in silica nanoparticles.*

5.3.1.1. Synthesis of amine capped silica nanoparticles

For the synthesis of amine capped silica nanoparticles, silica nanoparticles of size 51.7 ± 4.7 nm (table 5.1 and fig. 5.6) were used. A procedure similar to that described in section 5.2.1.2 was used for functionalisation. It is well known that change in concentration of the silane capping agent and reaction condition such as temperature brings about a change in density of surface capping [2]. Three samples with varying densities of surface amine were then synthesized by varying the reaction conditions. Table 5.4 provides details of reaction conditions used for amine functionalisation of the silica nanoparticles.

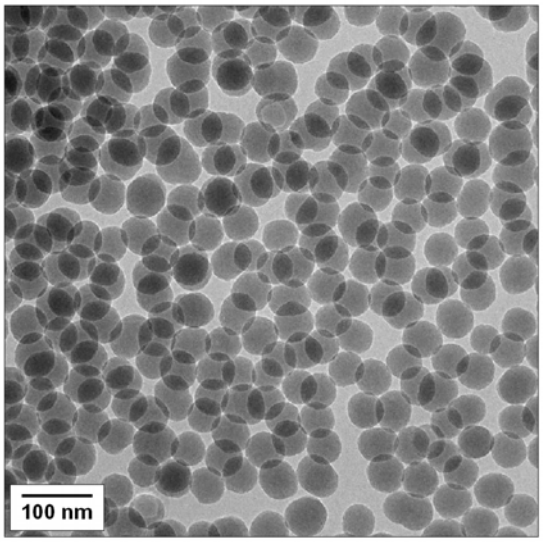

Figure 5.6*: Silica nanoparticles used in the amine assay (size - 51.7 ± 4.7 nm)*

Table 5.4: *Experimental conditions for amine functionalisation of silica nanoparticles.*

Sample	Amount of APTES (weight / volume)%	Temperature
SiO_2NH_2-1	2	reflux
SiO_2NH_2-2	0.2	reflux
SiO_2NH_2-3	0.2	25°C

5.3.1.2. Estimation procedure

In a typical procedure for detection of amine groups, 5 mg of functionalized silica nanoparticles were reacted in 20 mg of **FMoC-Cl** and 10 mg of $NaHCO_3$. The solvent system was 25% de-ionised water in 1,4-dioxane. After reaction for 24 h, and 6 washings with 1,4-dioxane, the silica nanoparticles were treated with **DBU** in 1 mL of DMF. Reaction with **DBU** results in release of **DBF** having a characteristic peak at 306 nm [21]. The molar extinction coefficient of **DBF** in DMF is 7800 Mcm^{-1} at 306 nm [21]. The absorbance at 306 nm (Y) was used to estimate the amount of amine using the formula:

$$[Amine] = Y \times 0.001/ 3.9 \times 10^4 \quad nmoles/mg \ldots\ldots\ldots\ldots (1)$$

This takes in to account dilution factors and the amount of functionalized silica initially used.

5.3.1.3. Results and discussion

Fig. 5.7 shows the spectra of **DBF** released from different silica samples. The varying spectral intensities indicate varying extents of functionalisation of the silica nanoparticles. The results are summarized in table 5.5. It is evident that greater amount of APTES and higher reaction temperature ensures greater density of amine groups. This is in concurrence with previous reports [2]. However, it needs to be noted that the present estimation procedure did not involve any rigorous conditions such as an anhydrous reaction medium [2].

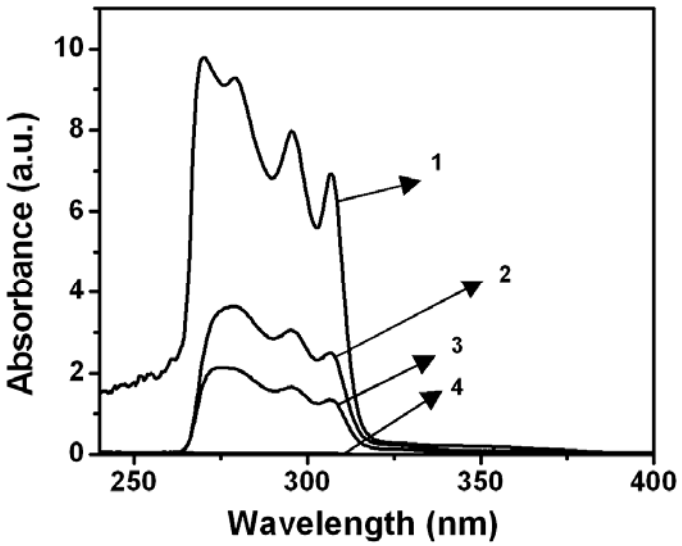

Figure 5.7: *Varying amounts of amine reflected in the varying spectral intensities of DBF released from (1)* ***SiO_2NH_2-1****, (2)* ***SiO_2NH_2-2****, (3)* ***SiO_2NH_2-3*** *and unfunctionalized silica nanoparticles (4). Note that there is no DBF released from unfunctionalized silica nanoparticles ruling out adsorption phenomenon.*

Table 5.5*: Varying amine densities on silica nanoparticles as determine using* ***FMoC-Cl*** *assay. See text for details.*

Sample	Absorbance *(Y)* at 306 nm	Density of amine groups (nmoles/mg)
SiO_2NH_2-1	6.8	175
SiO_2NH_2-2	2.7	70
SiO_2NH_2-3	1.5	35
SiO_2 - unfunctionalised	0	0

Such an assay can be very useful in monitoring the progress of surface reactions involving amines in nanoparticles. This has been demonstrated below for a reaction that was illustrated in scheme 5.1. In this reaction, amine groups on the surface of silica nanoparticles are used to impart propargyl functionality, useful in "click" chemistry, by reaction with propargylchloroformate. The progress of this reaction has been studied using **FMoC-Cl** analysis to determine the amount of free amine groups and propargyl groups exposed. Multiple steps of the reaction were carried out on amine capped silica nanoparticles of size 51.7 ± 4.7 nm (table 5.1) as described in section 5.2.1.3 (scheme

5.4). Free amine groups were determined after each stage and progress of the reaction was monitored.

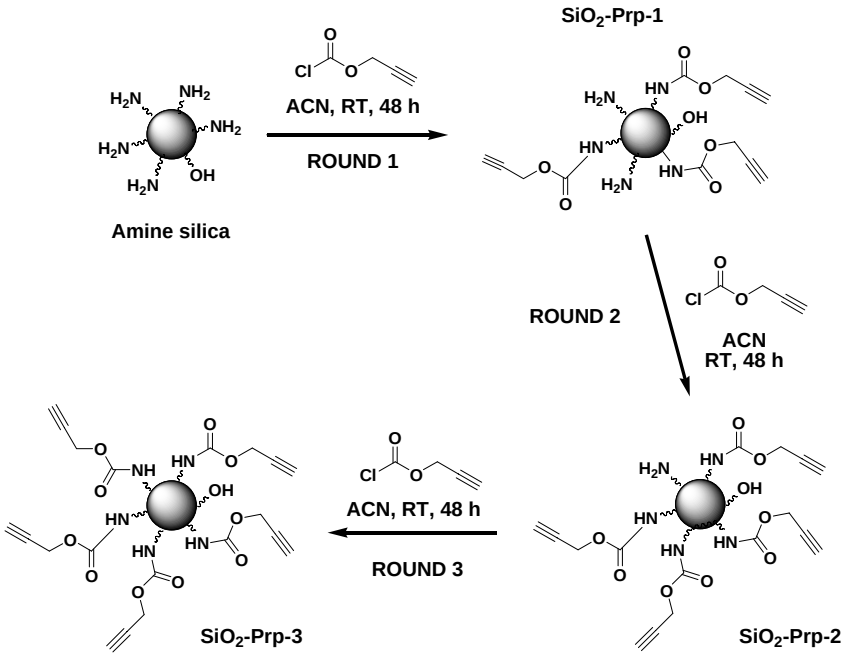

Scheme 5.4: *Stepwise functionalisation of amine groups on the surface of silica nanoparticles.*

Fig. 5.8 clearly shows that as more amount of propargyl groups are incorporated, by controlling the number of steps of propargylation, the free amine on the surface of the silica nanoparticles is consumed. In this case specifically, the density of surface propargyl groups in the silica nanoparticle composites can also be determined indirectly. This is because the propargyl groups were obtained by derivatisation of the free amine groups. Table 5.6 summarizes these results.

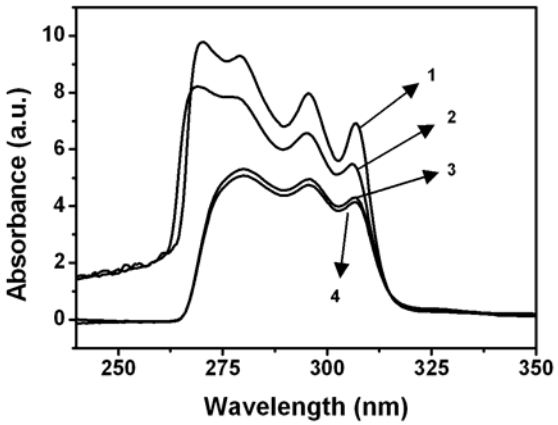

Figure 5.8: *Gradual consumption of surface amine groups during propargylation reflected in the DBF signals from (1) amine capped silica nanoparticles, (2)* ***SiO_2-Prp-1****, (3)* ***SiO_2-Prp-2*** *and (4)* ***SiO_2-Prp-3****.*

Table 5.6*: Consumption of silica nanoparticle surface amine groups during step-wise reaction with propargylchloroformate is shown. See text for details.*

Sample	Absorbance *(Y)* at 306 nm	Density of amine groups (nmoles/mg)	Density of Propargyl groups (nmoles/mg)
SiO_2NH_2	6.8	175	-
SiO_2-Prp-1	5.5	140	35
SiO_2-Prp-2	4.3	110	65
SiO_2-Prp-3	4.1	100	75

5.3.2. Estimation of surface reactive azide groups

A procedure similar to what was described for amine estimation was used for the azide assay. The basis for this assay however is the reaction of azides with alkynes in the presence of Cu(I) leading to the formation of 1,4-disubstituted 1,2,3-triazoles in near quantitative yield [8]. For this purpose, **FMoC-Cl** was reacted with propargylamine to yield (9H-fluoren-9-yl)methyl prop-2-ynylcarbamate (**FMoC-Prp**) as detailed below (scheme 5.5). **FMoc-Prp** is the probe used to detect and quantify the azide groups.

5.3.2.1. Synthesis and characterisation of FMoC-Prp

In a typical procedure (scheme 5.5), 0.25 mL of propargylamine and 1 mL of triethylamine were mixed in 5 mL of dry DCM. To this a solution of **FMoC-Cl** (1 g) in 5 mL of dry DCM was added drop wise with constant stirring at 0 °C. Following this, the reaction was allowed to proceed for 12 h at room temperature under nitrogen atmosphere. The reaction was followed by TLC to completion. Following this the reaction mixture was diluted with 50 mL of freshly distilled CH_2Cl_2, washed

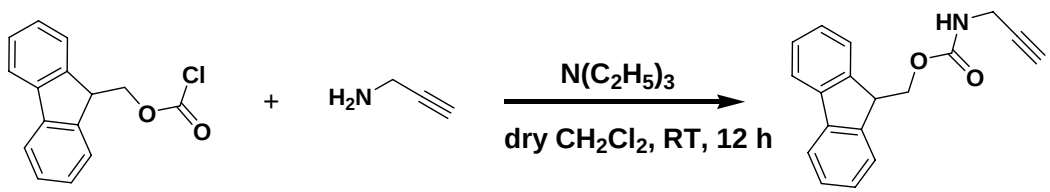

FMoC-Cl **Propargylamine** **FMoC-Prp**

Scheme 5.5: *Synthesis of FMoC-Prp*

thoroughly with water and extracted thrice with CH_2Cl_2 (3 x 50 mL). The combined organic layers obtained following extraction with CH_2Cl_2 were dried over anhydrous Na_2SO_4 and filtered. The filtrate was concentrated *in vacuo* to obtain a crude residue which was subsequently purified by silica gel column chromatography using a gradient solvent system starting with 5 % ethyl acetate in petroleum ether and the product was eluted with 10 % ethyl acetate in petroleum ether.

*Characterisation of **FMoC-Prp**:*

^{1}H NMR (200.13 MHz, $CDCl_3$): δ 2.23 (t, 1H, J = 2.5 Hz), 3.95 – 4.10 (m, 2H), 4.19 (t, 1H, J = 7.0 Hz), 4.41 (d, 2H, J = 7.0 Hz), 5.03 (bs, 1H), 7.20 – 7.45 (m, 4H), 7.59 (2 doublets, 2H, J = 8Hz), 7.75 (2 doublets, 2H, J = 8Hz). *Calcd. Mol. Wt. of* $C_{18}H_{15}N_1O_2$: 277.31, *Found:* 277.23; *FTIR:* 3300 (s) [≡C-H stretch], 3040 (m), 2920 (s), 2853 (2), 2110 (m) [C≡C stretching], 1705 (s) cm^{-1}.

5.3.2.2. Synthesis of azide functionalized silica nanoparticles

Azide functionalisation of silica nanoparticles (scheme 5.6) was accomplished using a previously reported two step procedure with slight modifications [31]. In the first step 1 g of unfunctionalised silica nanoparticles (section 5.2.1.1) were dispersed in 150 mL of dry toluene using sonication under a nitrogen atmosphere. Following this, a solution of 2 mL of 3-bromopropyltrichlorosilane in 10 mL dry toluene was added drop wise to the above dispersion under refluxing conditions. The reaction was allowed to continue for 24 h. Repeated (thrice) centrifugation and redispersion in toluene was done to wash off excess 3-bromopropyltrichlorosilane. This yields bromide capped silica nanoparticles. The substitution of the bromide with azide groups was achieved in the second step. For this, 0.5 g of bromide capped silica nanoparticles and 2 g of NaN_3 were dispersed in 40 mL of dry DMF using sonication. The dispersion was then heated at 80 °C for 12 h. Repeated (thrice) centrifugation and redispersion in DMF yielded purified azide capped silica nanoparticles. The particles were characterized using FTIR spectroscopy as shown in fig. 5.9. Azide functionalisation was performed on silica nanoparticles of sizes 37.5 ± 1.5 nm (***SiO_2-N_3-1***), 146 ± 6.1 nm (***SiO_2-N_3-2***) and 398 ± 10.2 nm (***SiO_2-N_3-3***) (table 5.1 and fig. 5.9).

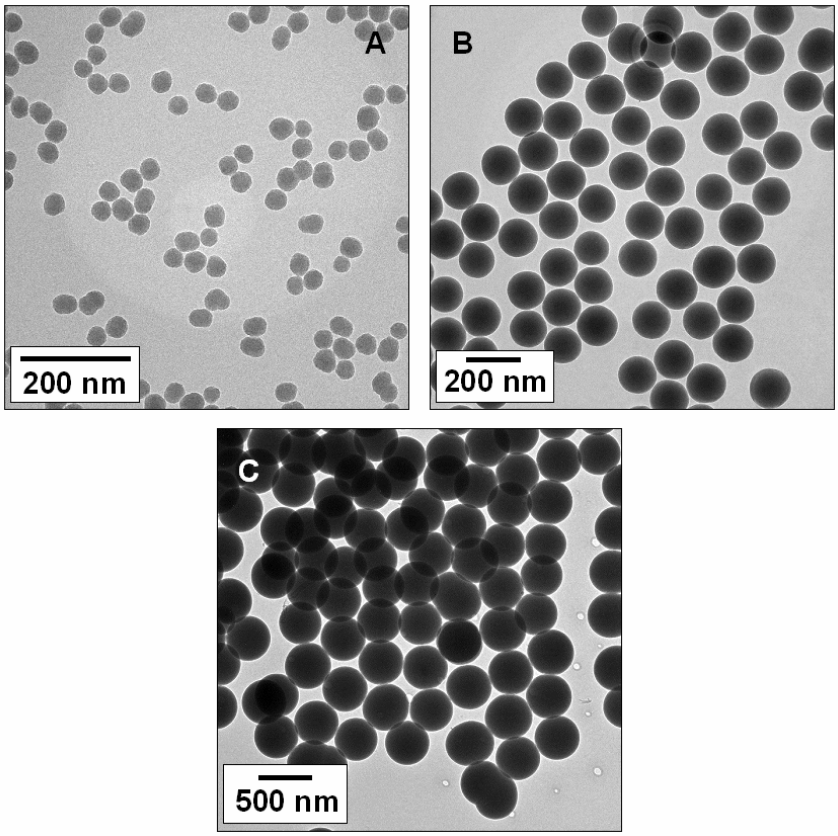

Figure 5.9: *TEM images of silica nanoparticles used for azide functionalisation and subsequent experiments. See text for details. Average size: (A) 37.5 ± 1.5 nm, (B) 146 ± 6.1 nm and (C) 398 ± 10.2 nm.*

5.3.2.3. Estimation procedure

The typical procedure for detection of reactive surface azide groups is outlined in scheme 5.6. Typically, 5 mg of functionalized silica nanoparticles were reacted with 14 mg of **FMoC-Prp** in the presence of 20 m of sodium ascorbate and 9 mg of $CuSO_4$. The solvent system used was de-ionised water (750 µL) - 1,4-dioxane (750 µL) mixture. After reaction for 24 h, three washings with 1,4-dioxane and de-ionised water were given. The silica nanoparticles were further treated with sodium diethyldithiocarbamate (1 mL of 0.1 M solution in methanol) for 30 mins for removal of excess copper(I) [34]. This was followed by washings with methanol and acetone. This procedure for copper removal was repeated thrice. After copper(I) removal the silica nanoparticles were treated with **DBU** in 1 mL of DMF. Reaction with **DBU** results in release of **DBF** having a characteristic peak at 306 nm. The absorbance at 306 nm (Y) was used to estimate the amount of amine using the formula:

$$[Azide] = Y \times 0.001/3.9 \times 10^{4} \quad nmoles/mg \ldots\ldots\ldots\ldots (2)$$

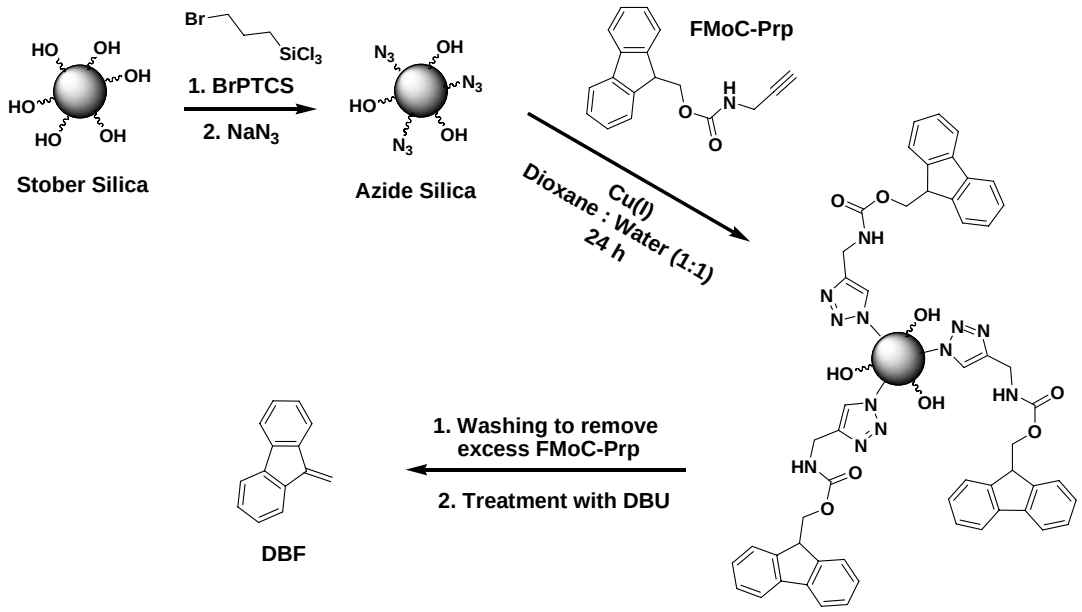

Scheme 5.6: *Estimation of surface active azide groups on silica nanoparticles.*

5.3.2.4. Results and discussion

The veracity of this azide estimation procedure depends on the efficiency of the "click" reaction between **FMoC-Prp** and the azide functionalized silica nanoparticles. The FTIR signal at 2100 cm^{-1} a characteristic of azide group stretching is often used to study the efficiency of a "click" reaction [13].

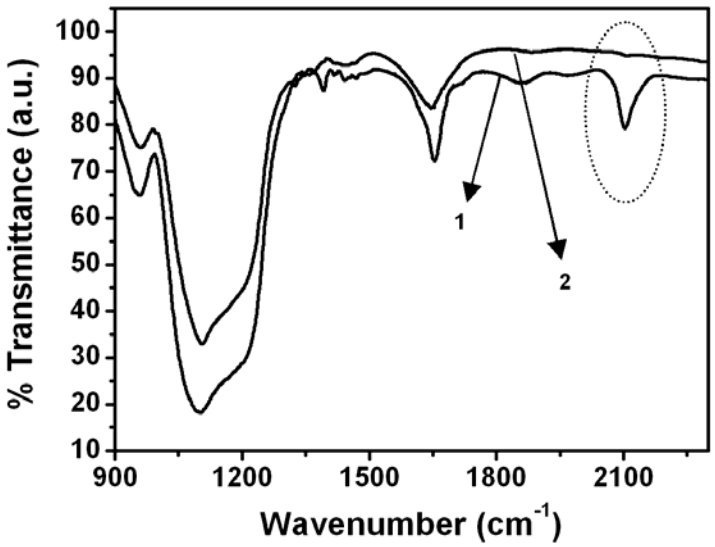

Figure 5.10: *FTIR spectra showing near complete consumption of azide groups (feature at 2100 cm^{-1}) following "click" reaction. Curves 1 and 2 correspond to* ***SiO_2-N_3-1*** *before and after reaction with* ***FMoC-Prp*** *respectively.*

We monitor the azide stretching before (curve 1, fig. 5.10) and after (curve 2, fig. 5.10) the "click" reaction to detect unreacted azide groups in ***SiO_2-N_3-1***. It is seen from fig. 5.10 that following reaction with **FMoC-Prp**, there is near complete consumption of azide groups as indicated by the absence of the signal at 2100 cm^{-1} (curve 2, fig. 5.10). This observation confirms the efficiency of the "click" reaction in this assay.

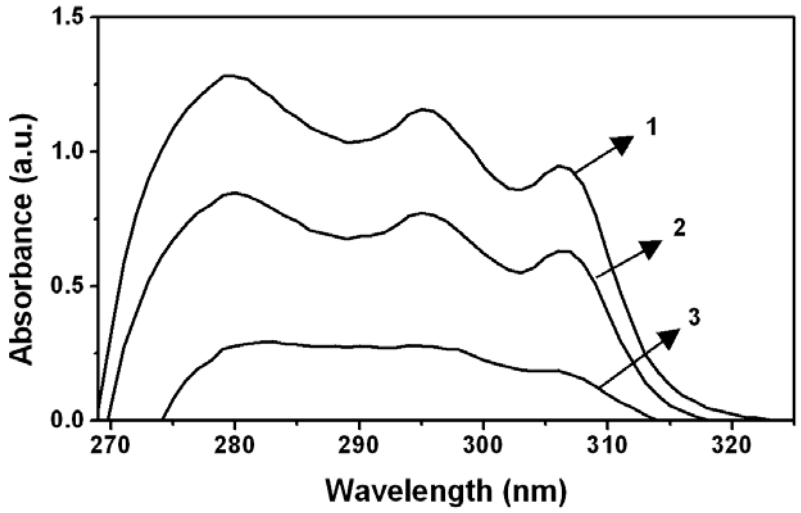

Figure 5.11: *UV-visible absorption spectra of* ***DBF*** *released from azide capped silica nanoparticles of varying sizes. Curves 1 to 3 correspond to* ***DBF*** *released from samples* ***SiO_2-N_3-1****,* ***SiO_2-N_3-2*** *and* ***SiO_2-N_3-3*** *respectively.*

Fig. 5.11 shows that varying amounts of **DBF** are released from samples of different sizes though the functionalisation conditions were identical. As seen from table 5.7, smaller nanoparticles possess greater density of azide groups due to greater surface area. Thus it is seen that the azide assay can be effectively used for detecting the density of surface functional groups in silica nanoparticle.

Table 5.7*: Varying azide densities on silica nanoparticles of varying size as determine using* ***FMoC-Prp*** *assay. See text for details.*

Sample	Absorbance *(Y)* at 306 nm	Density of azide groups (nmoles/mg)
SiO_2-N_3-1	0.95	24
SiO_2-N_3-2	0.63	16
SiO_2-N_3-3	0.19	4

5.4. Conclusions

It is demonstrated that "click" chemistry can be used as a versatile tool for functionalisation of silica nanoparticles. By this procedure, the surface density of the pyrene capping agent can be tuned by varying the initial concentration of reactants. UV-visible absorbance and fluorescence spectrophotometry in combination with FTIR analysis were used to study the reaction. The procedure presented here is general and could be extended to impart desired functionality on to the nanoparticle surface by choosing appropriate coupling molecules having the azide functional group. Similar results can be obtained by starting with azide bearing silica and alkyne functionalized capping molecule as will be demonstrated in chapter 6. In addition, a method to determine the surface density reactive amine and azide groups, using **FMoC-Cl** and its derivative has been demonstrated. The procedure is based on the protection-deprotection strategy employed in organic synthesis. This procedure can be extended to any nanoparticle or solid state system to quantify surface active groups and hence can be of general use in material science.

5.5. References

[1] Guo, Z.; Lei, A.; Liang, X.; Xu, Q. *Chem. Commun.* **2006**, 4512.

[2] (a) Campo, A. D.; Sen, T.; Lellouche, J. P.; Bruce, I. J. *J. Magn. Magn. Mater.* **2005**, *293*, 33. (b) Bruce, I. J.; Sen, T. *Langmuir* **2005**, *21*, 7029.

[3] Burns, A.; Ow, H.; Weisner, U. *Chem. Soc. Rev.* **2006**, *35*, 1028.

[4] Kim, J.; Lee, J. E.; Lee, J.; Jang, Y.; Kim, S. W.; An, K.; Yu, J. H.; Hyeon, T. *Angew. Chem. Int. Ed.* **2006**, *45*, 4789.

[5] Johnston, A. P. R.; Read, E. S.; Caruso, F. *Nano Lett.* **2005**, *5*, 953.

[6] Roth, I.; Simon, F.; Bellmann, C.; Seifert, A.; Spange, S. *Chem. Mater.* **2006**, *18,* 4730.

[7] (a) Philipse, A. P.; Vrij, A. *J. Colloid lnterface Sci.* **1989***, 128,* 121. (b) Van Blaaderen, A.; Vrij, A. *J. Colloid lnterface Sci.* **1993***, 156,* 1.

[8] Rostovtsev, V. V.; Green, L. G.; Fokin, V. V.; Sharpless, K. B. *Angew. Chem. Int. Ed.* **2002**, *41*, 2596.

[9] Kolb, H. C.; Finn, M. G.; Sharpless, K. B. *Angew. Chem. Int. Ed.* **2001**, *40*, 2004.

[10] Zhang, L.; Chen, X.; Xue, P.; Sun, H. H. Y.; Williams, I. D.; Sharpless K. B.; Fokin, V. V.; Jia, G. *J. Am. Chem. Soc.* **2005**, *127*, 15998.

[11] Binder, W. H.; Sachsenhofer, R. *Macromol. Rapid Commun.* **2007**, *28*, 15.

[12] Lewis, W. G.; Green, L. G.; Grynszpan, F.; Radic, Z.; Carlier, P. R.; Taylor, P.; Finn, M. G.; Sharpless, K. B. *Angew. Chem. Int. Ed.* **2002**, *41*, 1053.

[13] (a) Lummerstorfer, T.; Hoffmann, H. *J. Phys. Chem. B* **2004**, *108*, 3963. (b) Ortega-Munoz, M.; Lopez-Jaramillo, J.; Hernandez-Mateo, F.; Santoyo-Gonzalez, F. *Adv. Synth. Catal.* **2006**, *348*, 2410. (c) Rajan, R.; Brittain, W. J. *Macromolecules* **2007**, *40*, 6217. (d) Lin. P.; Ueng, S.; Yu, S.; Jan, M.; Adak, A. K.; Yu, C.; Lin, C. *Org. Lett.* **2007**, *9*, 2131.

[14] (a) Ketelson, H. A.; Brook, M. A.; Pelton, R. H. *Chem. Mater.* **1995**, *7*, 1376. (b) Abu-Reziq, R.; Alper, H.; Wang, D.; Post, M. L. *J. Am. Chem. Soc.* **2006**, *128*, 5279.

[15] Reed-Mundell, J. J.; Nadkarni, D. V.; Kunz Jr, J. M.; Fry, C. W, Fry, J. L. *Chem. Mater.* **1995**, *7*, 1655.

[16] Ipe, B. I.; Thomas, K. G. *J. Phys. Chem. B* **2004**, *108,* 13265.

[17] Chandran, S. P.; Hotha, S.; Prasad, B. L. V. *Curr. Sci.* **2008**, *95*, 1327.

[18] Kallury, K. M. R.; Macdonald, P. M.; Thompson, M. *Langmuir* **1994**, *10*, 492.

[19] Moon, J. H.; Shin, J. W.; Kim, S. Y.; Park, J. W. *Langmuir* **1996**, *12*, 4621.

[20] Cheng, K.; Landry, C. C. *J. Am. Chem. Soc.* **2007**, *129*, 9674.

[21] Newcomb, W. S.; Miller, D. W.; Porco, J. A. *Biotechnol. Bioeng.* **1998**, *61*, 55.

[22] Link, A. J.; Vink, M. K. S.; Tirrell, D. A. *J. Am. Chem. Soc.* **2004**, *126*, 10598.

[23] Stober, W.; Fink, A.; Bohn, E. *J. Colloid lnterface Sci.* **1968***, 26,* 62.

[24] The particle size distribution obtained following measurements from TEM images were fitted to Gaussian curves to obtain the mean diameters.

[25] Hotha, S.; Anigundi, R. I.; Natu, A. *Tetrahedron Lett.* **2005**, *46*, 4585.

[26] Yilgor, E.; Burgaz, E.; Yurtsever, E.; Yilgor, I. *Polymer* **2000**, *41*, 849.

[27] Hotha, S.; Kashyap, S. *J. Org. Chem.* **2006**, *71*, 364.

[28] Prado, A. G. S.; Airoldi, C. *J. Colloid lnterface Sci.* **2001***, 236,* 161.

[29] Ipe, B. I.; Thomas, K. G.; Barazzouk, S.; Hotchandani, S.; Kamat, P. V. *J. Phys. Chem. B* **2002**, *106,* 18.

[30] (a) Milosavljevict, B. H.; Thomas, J. K. *J. Phys. Chem.* **1988**, *92,* 2997. (b) Thomas, J. K. *Chem. Rev.* **2005**, *105*, 1683. (c) Yamazaki, T.; Tamai, N. Yamazaki, I. *Chem. Phys. Letters* **1986**, *124*, 326.

[31] Rajan, R.; Brittain, W. J. *Macromolecules* **2007**, *40*, 6217.

[32] Montalti, M.; Prodi, L.; Zaccheroni, N.; Battistini, G. *Langmuir* **2004**, *20*, 7884.

[33] Greene, T.; Wuts, P. G. M. Protective Groups in Organic Synthesis, 4th Ed.; Wiley. New York, **2006**.

[34] Terry, T. J.; Stack, T. D. P. *J. Am. Chem. Soc.* **2008**, *130*, 4945.

Chapter 6

Silane and "click" chemistry based functionalisation of inorganic nanoparticles

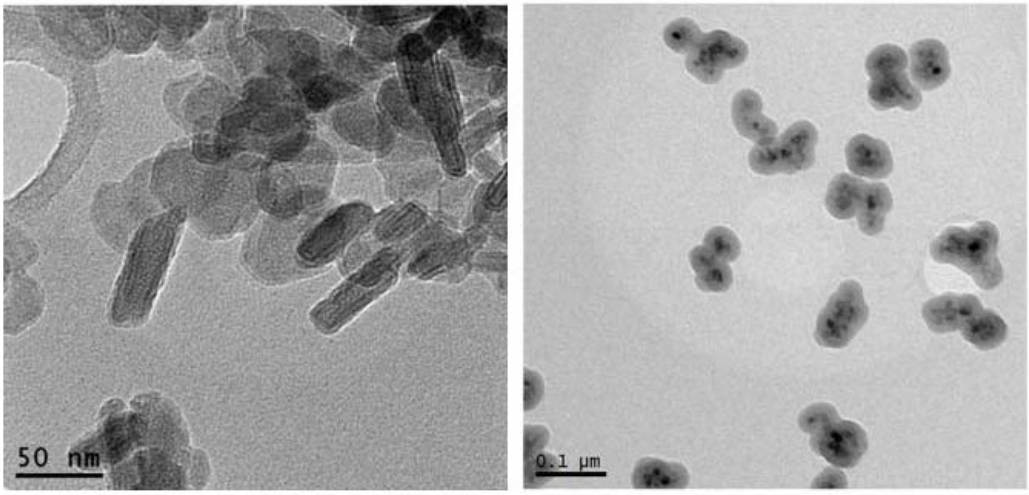

In this chapter, we demonstrate that silica chemistry in combination with the [3 + 2] Huisgen's cycloaddition could be used to effectively functionalize a variety of inorganic nanoparticles. We illustrate three examples in this regard. The first deals with the synthesis of a biologically active silica based nanocomposite prepared by grafting azide bearing berberine alkaloids on to the surface of alkyne functionalized silica nanoparticles. In another set of experiments, boehmite nanoparticles are coated with a thin layer of silica prior to their surface functionalisation with fluorescent pyrene groups. These nanoparticles are then dispersed in liquid crystalline matrices and the resulting composite is examined using optical microscopy. Finally, silica based bi-functional nanocomposite that incorporates magnetic and fluorescence functionality is synthesized using iron oxide nanoparticles as seeds. The surface density of the fluorescent pyrene capping is tuned using the "click" protocol. These nanomaterials could find applications in biology, materials science and catalysis.

Part of the work discussed in this chapter has been published in

Halimani, M.; Prathap Chandran, S.; Kashyap, S.; Jadav, V. M.; Prasad, B. L. V.; Hotha, S.; Maiti, S. *Langmuir* (in print) DOI: 10.1021/la802761b.

6.1. Introduction

The importance of silica nanoparticles and silane coatings has already been discussed in chapter 1 and chapter 5. Silica coatings have been accomplished on a variety of materials including noble metal [1], semiconductor [2] and oxide [3] nanoparticles. From narrowing the polydispersity in size of nanoparticles [4] to concealing their toxic constituents [5], silica coatings serve a variety of purposes. However their major advantage is the versatility that they bring to the surface functionalisation process. Briefly, silanisation in combination with techniques such as the "click" reaction could serve as a generic procedure for the controlled functionalisation of nanomaterials [6,7].

Herein we functionalize silica nanoparticles and silica coated inorganic nanomaterials using "click" chemistry. Three cases are dealt with:

- Functionalisation of silica nanoparticles with berberine – a known anti-cancer drug.
- Pyrene functionalized γ-AlOOH@SiO_2 nanoparticles
- Pyrene functionalized iron oxide@SiO_2 nanoparticles

These materials could find applications in varied fields that include drug delivery, liquid crystal base composites and catalysis.

In the first case, we synthesize silica nanoparticles functionalized with berberine derivatives (scheme 6.1). Berberine is a natural isoquinoline alkaloid present in medicinal plants such as *Coptis chinensis* (Coptis or goldenthread), *Berberis aquifolium* (Oregon grape), *Berberis vulgaris* (barberry), and *Coscinium fenestratum* [8] and found to have anti-diarrheal, anti-arrhythmic and anti-tumor activities [9]. These drug molecules are grafted onto silica nanoparticles using the "click" reaction incorporating spacer molecules of differing chain lengths. Such berberine functionalized nanoparticles are characterized using FTIR, UV-visible absorbance spectroscopy and TGA analysis. It was observed that long and flexible spacer molecules facilitate better berberine loading on to the silica nanoparticles. Subsequently, the biological activity of these nanoconjugates was studied [10]. It needs to be noted that silica nanoparticles, due to their biocompatibility, have been widely used for biological applications [5b].

In the second example the surface modification of anisotropic boehmite (γ-AlOOH) nanoparticles with pyrene fluorophores is illustrated (scheme 6.2). Boehmite is known to exhibit liquid crystalline activity [11]. Silica coating and pyrene functionalisation thereof were accomplished on the boehmite nanoparticles following the Stober process and "click" chemistry protocol respectively. Aluminum oxides including boehmite have earlier been coated with silica [12]. Apart from modulating the interaction between the cores [12c], silica surface functionalisation enables modulation of their interaction with solvent molecules [12c]. Integration of optical properties such as fluorescence [12a,13] has also been demonstrated. The nanoparticles fabricated here have been characterized using TEM, XRD, XPS, FTIR and UV-visible absorbance and fluorescence spectroscopy. The hydrophobic pyrene capped nanoparticles were dispersed in a cyanobiphenyl (E7) liquid crystalline matrix to demonstrate the utility of a fluorescent shell. Apart from altering the surface chemistry, the pyrene groups also facilitate monitoring of internal structure of the composite using fluorescence microscopy.

The third class of nanomaterials that we focus in this chapter is magnetic nanomaterials which have attracted attention [14]. Here too functionalisation prior to their application is critical. Silica based magnetic nanocomposites [3,14] have been extensively studied. In addition to facilitating surface functionalisation, incorporation of other assets such as luminescence and catalytic properties [15] has been demonstrated. Indeed such multifunctional nanomaterials have donned roles in bio-separations, drug delivery, cancer hyperthermia, magnetic resonance imaging and catalysis [15,16]. Procedures that enable tuning of the magnetic properties [17] and also the position of the luminescence [18] have been designed. Magnetic nanoparticles have already been subjected to "click" functionalisation with [7f, i-l] or without [7h] silica coating and have been applied in catalysis [7j,l] and spectroscopy [7i] and site specific bioconjugation [7f]. In this regard, we demonstrate that the surface functionality of silica coated magnetic iron oxide can be effectively tuned using the "click" chemistry protocol (scheme 6.3). These fluorescence incorporated multifunctional nanomaterials have been characterized using TEM, XRD and XPS. The tunability of the surface coverage has been demonstrated by studying FTIR and UV-visible spectroscopy.

6.2. Berberine capped silica nanoparticles

Our investigation of berberine functionalisation on silica nanoparticles is delineated in the following section.

6.2.1. Synthesis of functionalised silica nanoparticles

Unfunctionalised Stober silica nanoparticles (**1**) were synthesized following the procedure reported by Stober and co-workers [19]. Purification of silica nanoparticles was carried out using three rounds of centrifugation (13000 rpm for 15 min) interspersed with redispersion and washing with absolute ethanol.

The functionalisation procedure employed is summarised in scheme 6.1.

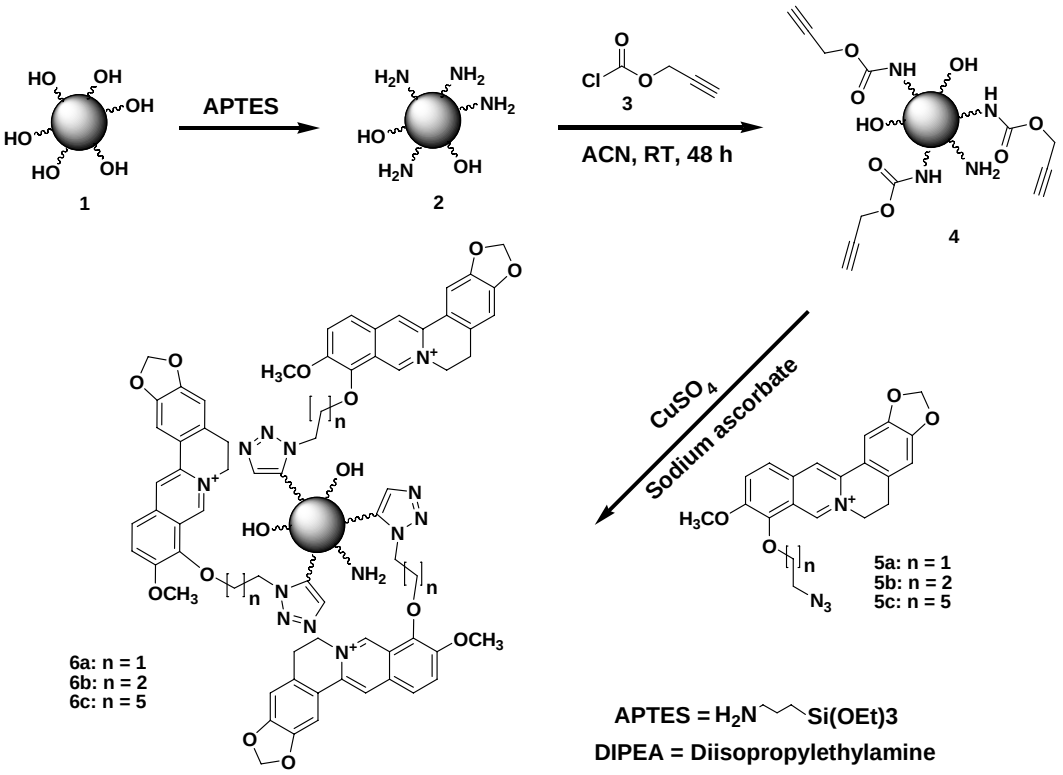

Scheme 6.1: *Berberine functionalisation of silica nanoparticles using the "click" reaction.*

6.2.1.1. Synthesis of amine functionalized silica nanoparticles

Bare silica nanoparticles (**1**) were dispersed in absolute ethanol (150 mg in 15 mL) followed by the addition of 2% w/v of APTES. The above mixture was stirred for a period of 6 h under reflux conditions. Purification of amine functionalized silica nanoparticles (**2**) was carried out using three rounds of centrifugation (13000 rpm for 15 mins) interspersed with re-dispersion and washing with absolute ethanol.

6.2.1.2. Synthesis of propargyl functionalized silica nanoparticles

In a typical reaction, 250 mg of amine functionalized silica nanoparticles (**2**) were dispersed in 50 mL of dry acetonitrile followed by addition of 0.3 mL of propargylchloroformate (**3**) [20]. The above reaction mixture was stirred for a period of 48 h at room temperature under nitrogen atmosphere. These silica nanoparticles were purified using three rounds of centrifugation (13000 rpm for 15 mins) and washings with acetonitrile. The size of the silica nanoparticles at this stage was determined to be about 54.4 ± 5.7 nm from TEM studies (fig. 6.1). Purified propargyl capped silica nanoparticles (**4**) obtained thus were characterized using FTIR spectroscopy.

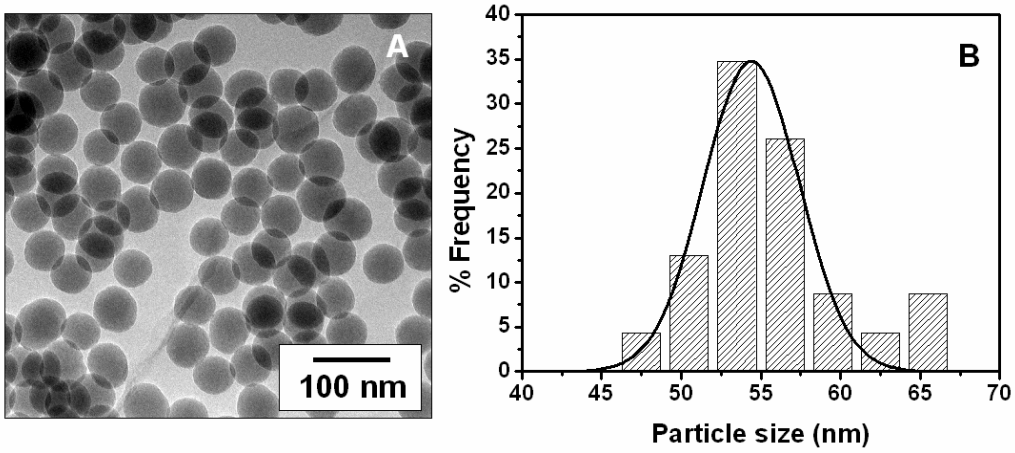

Figure 6.1: *(A) Representative TEM images of propargyl functionalised silica nanoparticles. (B) Size distribution analysis of propargyl functionalised silica nanoparticles fitted to a Gaussian curve yields average size to be 54.4 ± 5.7 nm.*

6.2.2. Synthesis of berberine derivatives

Berberine derivatives (scheme 6.1) were provided by Dr. S. Hotha's group at NCL Pune, India. The following is the characterisation data for the same: ^{1}H NMR spectra were recorded on 200.13 MHz for ^{1}H NMR spectrometers. Chemical shifts (δ_H) are quoted in ppm and are referenced to tetramethylsilane (internal). Mass spectra were recorded on a Q Star Pulsar LC-MS-MS-TOF machine.

Characterization data for compound ***5a****:* ^{1}H NMR (200.13 MHz, DMSO-d^6-CD_3OD (4:1)): δ 3.28 (t, 2 H, *J* = 6.4 Hz), 3.92 (t, 2 H, *J* = 4.4 Hz), 4.09 (s, 3 H), 4.65 (t, 2 H, *J* = 4.4 Hz), 5.12 (t, 2 H, *J* = 6.4 Hz), 6.10 (s, 1 H), 6.84 (m, 1 H), 7.33 (s, 1 H), 7.43 (s, 1 H), 7.92 (d, 1 H, *J* = 3.92 Hz), 7.98 (s, 1 H), 8.39 (s, 1 H), 10.12 (s, 1 H); Anal. Calcd

for $C_{21}H_{19}N_4O_4$: C, 64.44; H, 4.89; N, 14.31. Found: C, 64.94; H, 5.71; N, 14.87; FT-IR (NUJOL): 2948.96, 2921.95, 2852.52, 2154.41, 1633.59, 1602.74, 1594.37, 1469.69, 1461.94, 1454.23, 1377.08, 1274.86, 1037.63, 929.63, 721.33, 683.39 cm^{-1}.

*Characterization data for compound **5b**:* ^1H NMR (200.13 MHz, DMSO-d^6-CD_3OD (4:1)): δ 2.28 (m, 2 H), 3.28 (t, 2 H, *J* = 5.80 Hz), 4.09 (s, 3 H), 4.21 (m, 1 H), 4.52 (t, 2 H, *J* = 6.2 Hz), 5.10 (t, 2 H, *J* = 6.2 Hz), 6.10 (s, 2 H), 6.86 (s, 1 H), 7.36 (s, 1 H), 7.45 (s, 1 H), 7.93 (s, 1 H), 7.95 (s, 1 H), 8.42 (s, 1 H), 9.91 (s, 1 H); Anal. Calcd for $C_{22}H_{21}N_4O_4$: C, 65.17; H, 5.22; N, 13.82. Found: C, 64.38; H, 5.93; N, 14.53; FT-IR (NUJOL): 2950.89, 2920.03, 2850.59, 2135.05, 1602.74, 1469.69, 1461.94, 1454.23, 1377.08, 1301.86, 1274.86, 1035.70, 927.70, 721.33, 683.39 cm^{-1}.

*Characterization data for compound 5**c**:* ^1H NMR (200.13 MHz, DMSO-d^6-CD_3OD (4:1)): δ 1.58 (m, 6 H), 2.17 (m, 2 H), 3.33 (m, 3 H), 4.09 (s, 3 H), 4.42 (t, 2 H, *J* = 6.7 Hz), 5.04 (t, 2 H, *J* = 6.2 Hz), 6.11 (s, 2 H), 6.88 (s, 1 H), 7.43 (s, 1 H), 7.51 (s, 1 H), 7.98 (m, 2 H), 8.51 (s, 1 H), 9.76 (s, 1 H); Anal. Calcd for $C_{25}H_{27}N_4O_4$: C, 67.10; H, 6.08; N, 12.52. Found: C, 66.52; H, 6.47; N, 12.98; FT-IR (NUJOL): 2954.74, 2921.95, 2852.52, 2140.84, 1666.38, 1660.60, 1650.95, 1503.30, 1461.94, 1456.16, 1377.08, 1342.36, 1301.86, 1276.79, 1234.36, 1101.28, 1039.56, 721.33, 683.39 cm^{-1}.

6.2.3. Synthesis of berberine capped silica nanoparticles using Huisgen's dipolar cycloaddition

In a typical reaction, 100 mg of purified propargyl capped silica nanoparticles (**4**) were dispersed in 10 mL of 1:1 absolute ethanol – de-ionised water mixture along with $CuSO_4$ (4.7mg) and sodium ascorbate (3.7 mg) [21]. This was followed by the addition of 7.8 mg of berberine-9-*O*-ethylazide (**5a**), dissolved in 1 mL of de-ionised water, accompanied by vigorous stirring under ambient conditions for 24 h. Purification of **6a** was carried out using three rounds of centrifugation (13000 rpm for 15 mins) interspersed with redispersion and washing with de-ionised water. Similar procedures were employed for surface functionalisation of propargyl capped silica nanoparticles (**4**) with propyl (**5b**) and hexyl (**5c**) azide substituted berberine to give **6b** and **6c**, respectively (scheme 6.1). The molar concentration of berberine analogues was 10^{-5} M in all cases. The berberine functionalized silica nanoparticles (**6a** and **6c**) thus prepared were subjected to TGA characterization after purification.

6.2.4. Characterisation of berberine capped silica nanoparticles

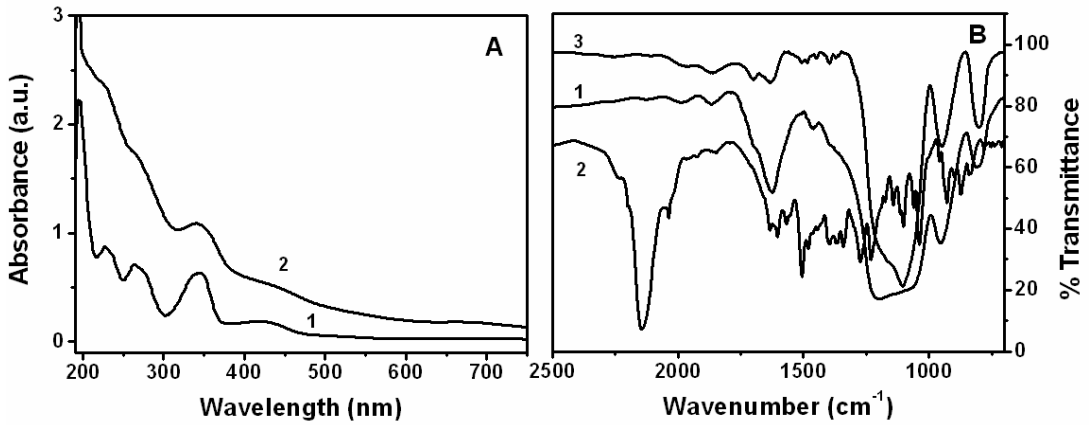

Figure 6.2: *UV-visible absorption (A) and FTIR (B) spectral characterisation of berberine functionalised silica nanoparticles.*

UV-visible absorbance spectrum of **5a** showed absorbance maxima at 226, 263, 342 and 420 nm (curve 1, fig. 6.2A). Similar spectral signatures were observed in **6a** confirming the successful functionalisation of silica nanoparticles with 9-*O*-ethyl berberine (curve 2, fig. 6.2A). In **6a,** these features ride on a baseline due to scattering from silica nanoparticles. An FT-IR spectrum of **5a** showed an intense peak at 2100 cm^{-1} attributed to the stretching vibrations of the azide moiety (curve 2, fig. 6.2B). The same however is absent in the spectrum of **5a** functionalized silica nanoparticles (**6a**) (curve 3, fig. 6.2B). This shows that binding of the berberine units is through a triazole linkage formed due to the "click" reaction. Spectral features of the triazole moiety

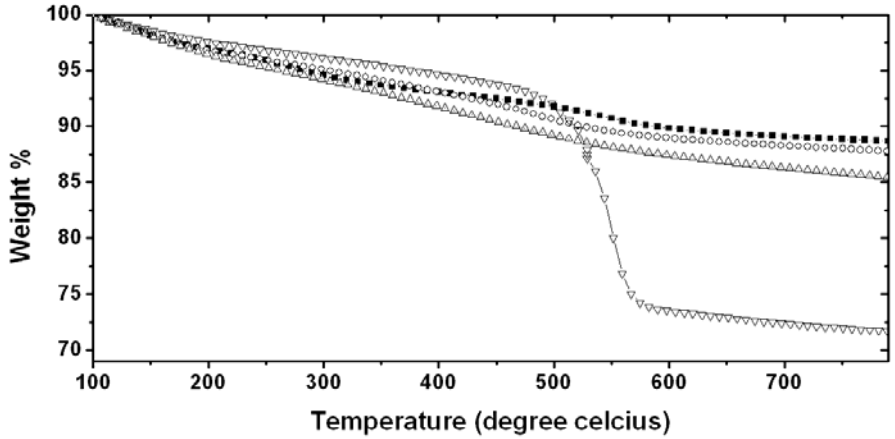

Figure 6.3*: Thermo gravimetric analysis of propargyl silica nanoparticles (square) before and after functionalisation with ethyl (circle), propyl (triangle) and hexyl (inverted triangle) berberine.*

(1650 cm^{-1}) are not discernible in the FTIR spectra due to overlap with the intense silica signal [7g]. Comparison of FTIR spectra of propargyl functionalized silica (**4**) (curve 1, fig. 6.2B) with berberine functionalized silica (**6a**) (curve 3, fig. 6.2B) showed additional spectral features between 1510 and 1340 cm^{-1}. These features characteristic of **5a** provided further proof for the presence of berberine units on silica nanoparticle surface.

Furthermore thermo gravimetric analysis (TGA) for determination of the berberine surface density (mole of berberine/mg of silica-berberine nanoconjugates) was performed. TGA has been routinely used for determination of functional group densities and carbon content in silica systems [22]. Representative TGA plots along with the data are presented in fig. 6.3 and table 6.1 respectively. It was found that surface density of berberine for silica-berberine nanoconjugates with ethyl linker (**6a**) was 2×10^{-5} mol/mg nanoconjugates whereas surface density of berberine for silica-berberine nanoconjugates with hexyl linker (**6c**) was 3.8×10^{-4} mol/mg nanoconjugates. This result signifies that higher surface density can be achieved by changing the linker length in between nanoparticles and the respective ligands. This may be because of the

Table 6.1: *TGA analysis of berberine functionalized silica nanoparticles*

Sample	**Molecular weight of corresponding free berberine derivative**	**Residual weight % at 790°C**	**Weight loss % at 790°C**	**Weight loss w.r.t propargyl silica**	**Amount of berberine derivative per mg of silica berberine composite**	**Density of berberine derivative per mg of silica berberine composite**
Propargyl silica (**4**)	-	88.7	11.3	-	-	-
Ethyl berberine functionalised silica (**6a**)	391	87.3	12.2	0.9	0.009mg	2×10^{-5} moles
Propyl berberine functionalised silica (**6b**)	405	85.4	14.6	3.3	0.033mg	8.2×10^{-5} moles
Hexyl berberine functionalised silica (**6c**)	447	71.7	28.3	17.7	0.17mg	3.8×10^{-4} moles

better flexibility of the six carbon spacer facilitating better surface conjugation in comparison to the ethyl spacer.

The effect of these nanoconjugates on the cell proliferation, cell cycle profile and apoptosis/necrosis in the Human cervical carcinoma cell line (HeLa), Human hepatocellular liver carcinoma cell line (HepG2) and Human embryonic kidney (HEK) 293T cell lines were studied. Biological studies show that nanoconjugates have similar pharmacological function but are more effective than free berberine due to possible dendritic effect. The results of experiments performed using these nanoconjugates have been published [10].

6.3. Pyrene capped γ-AlOOH@SiO_2 nanoparticles

To demonstrate the versatility of the "click" functionalisation procedure on materials other than pure stober silica nanoparticles, we illustrate two examples. In these experiments, silica is coated on to different inorganic nanoparticles. Following this, "click" chemistry is used to functionalize the nanocomposite surface with pyrene groups. The first example deals with pyrene functionalisation of γ-AlOOH@SiO_2 nanoparticles.

6.3.1. Synthesis of γ-AlOOH@SiO_2 core shell nanoparticles

γ-AlOOH (boehmite) nanoparticles (**7**) were commercially obtained from Sasol ® Germany, (DISPAL 11 N7-12) as an aqueous dispersion. These were used for further experiments following characterisation using TEM, XRD, XPS and FTIR studies. The functionalisation procedure employed is summarised in scheme 6.2.

For silica coating, 5 mL of the commercially obtained dispersion of (**7**) was dispersed in 80 mL of absolute ethanol containing 10 mL of NH_3 (about 30% in water). This dispersion was sonicated for a period of 10 minutes. Silica coating was performed by addition of 3 mL of TEOS (16.6 μL/min) to the above dispersion accompanied by vigorous stirring. The reaction was performed for a period of 3 h. Following this the nanoparticles obtained (**8**) were purified using centrifugation (12000 rpm for 15 min) interspersed with redispersion and washing with absolute ethanol. The particles thus obtained were characterized using TEM, XRD, XPS and FTIR spectroscopy.

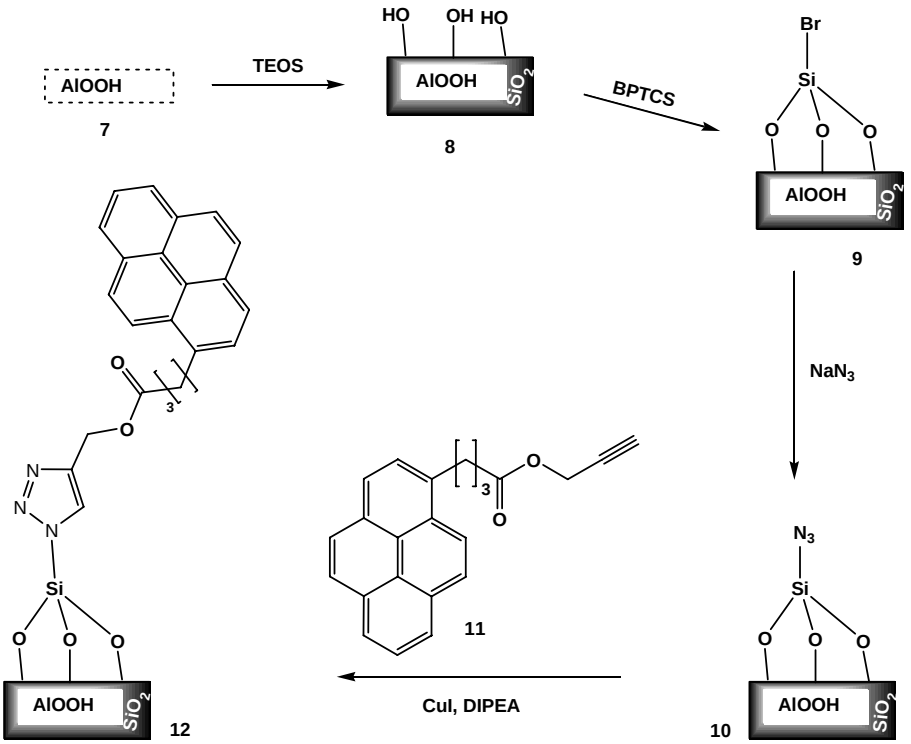

Scheme 6.2: *Cartoon illustrating the "click" functionalisation of γ-AlOOH@SiO_2 nanoparticles with pyrene derivatives.*

6.3.1.1. TEM and XRD analysis of γ-AlOOH and γ-AlOOH@SiO2 nanoparticles

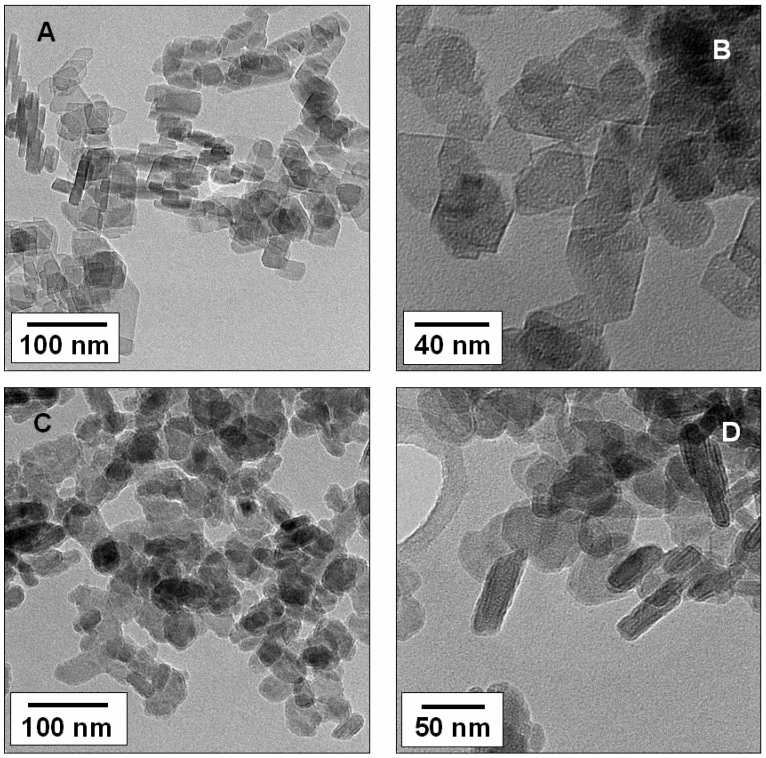

Figure 6.4: *TEM micrographs of (A), (B) γ-AlOOH (**7**) and (C), (D) γ-AlOOH@SiO_2 (**8**) nanoparticles.*

Fig. 6.4 presents TEM evidence for the coating of **7** with SiO_2. Figs. 6.4 A and B show the TEM image of **7**. The particles were a mixture of rods and discs. Their average size was about 50 nm. Following the coating procedure (figs. 6.4 C and D), a thin shell of SiO_2 is evident (**8**). The particles now have slightly serrated edges and the contrast pattern is characteristic of core-shell systems. The thickness of the shell was determined to be ~ 3.5 nm.

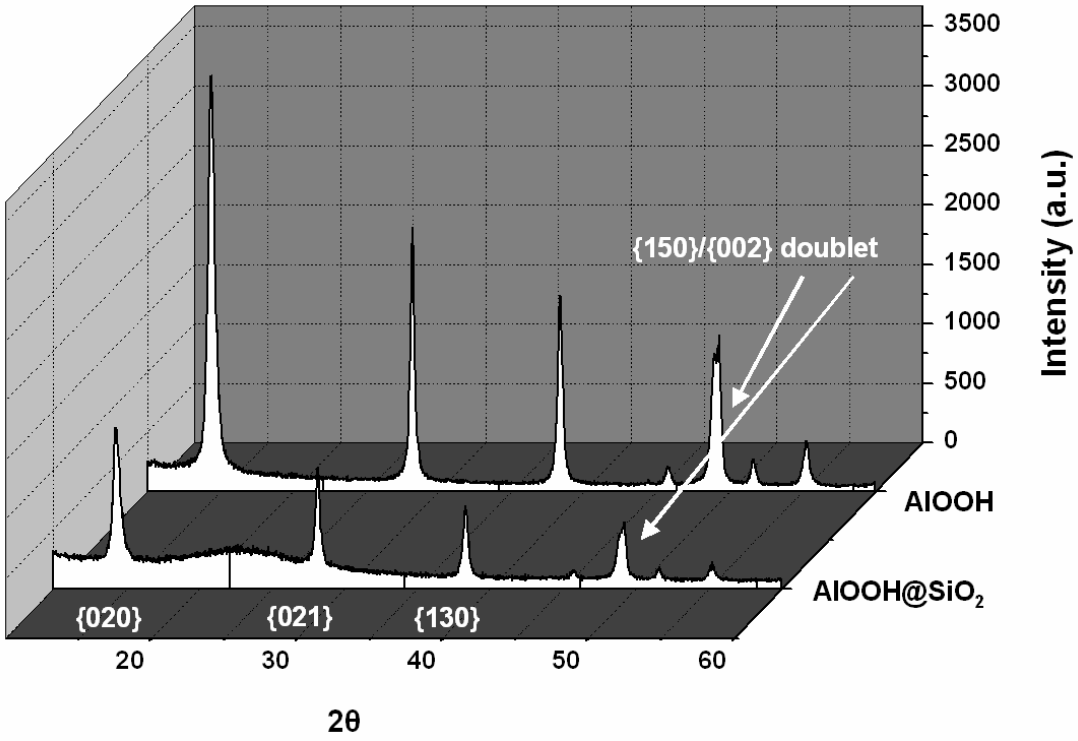

Figure 6.5: *XRD patterns of γ-AlOOH (**7**) and γ-AlOOH@SiO_2 nanoparticles (**8**).*

Fig. 6.5 shows the XRD patterns corresponding to **7** and **8**. The signals could be indexed to the orthorhombic crystal structure of γ-AlOOH (boehmite) [23]. The structural integrity of the core is preserved even after the SiO_2 coating procedure as can be seen from the identical nature of the Bragg reflections from both the samples.

6.3.1.2. XPS characterisation of γ-AlOOH and γ-AlOOH@SiO2 nanoparticles

XPS analysis was performed to study the change in surface elemental composition of **7** and **8**. Fig. 6.6 A shows the Al 2p signal from **7** fitted to a single curve (curve a, fig. 6.6A) at 74 eV [24]. As is characteristic of the Al 2p core level [25], spin orbit splitting is not evident from the recorded signal. The O 1s signal could be deconvoluted to two components corresponding to two kinds of oxygen species, Al-O-Al and Al-O-H, present in γ-AlOOH systems. Their respective binding energies are

530.5 and 531.9 eV (curves 1 and 2, fig. 6.6B) [24]. Table 6.2 presents a summary of the XPS results.

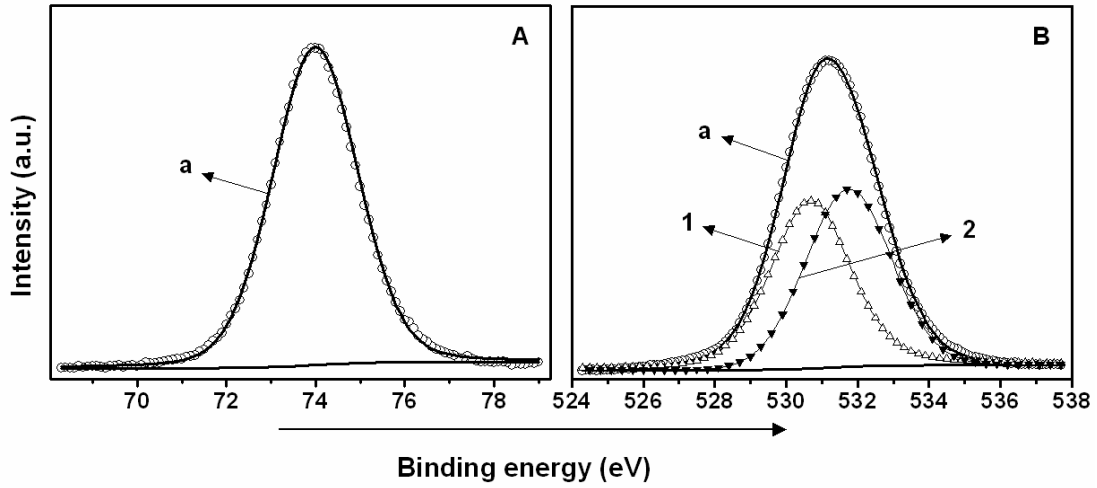

Figure 6.6: *XPS signals from (A) Al 2p and (B) O 1s core levels of γ-AlOOH (**7**). Curve a represents composite fit to the raw signal (hollow circles) in all cases. See text and table 6.2 for details.*

Table 6.2: *Summary of XPS analysis of γ-AlOOH (**7**).*

Element core level	**Binding energy (eV)**	**Assignment**
C 1s	285	Adventitious carbon C-H
	289	CO_3^{2-} adsorbed impurities
Al 2p	74	AlOOH
O 1s	530.5	AlOAl
	531.9	AlOH and adsorbed CO_3^{2-} impurities

Following SiO_2 coating, the Al 2p signal intensity (curve 1, fig. 6.7A) is negligible in comparison to sample **7** (curve 2, fig. 6.7A). This can be attributed to the fact that the photoelectrons from Al 2p core level of **8** get inelastically scattered by the 3.5 nm thick SiO_2 layer present on the surface of each boehmite nanoparticle. The inelastic scattering mean free path is estimated to be less than 2 nm for electrons from

Al 2p core level for a Mg-Kα X-ray source [25]. Consequently, photoelectrons evolving from below this depth do not contribute to a core level signal. This explains the absence of an Al 2p signal after silica coating.

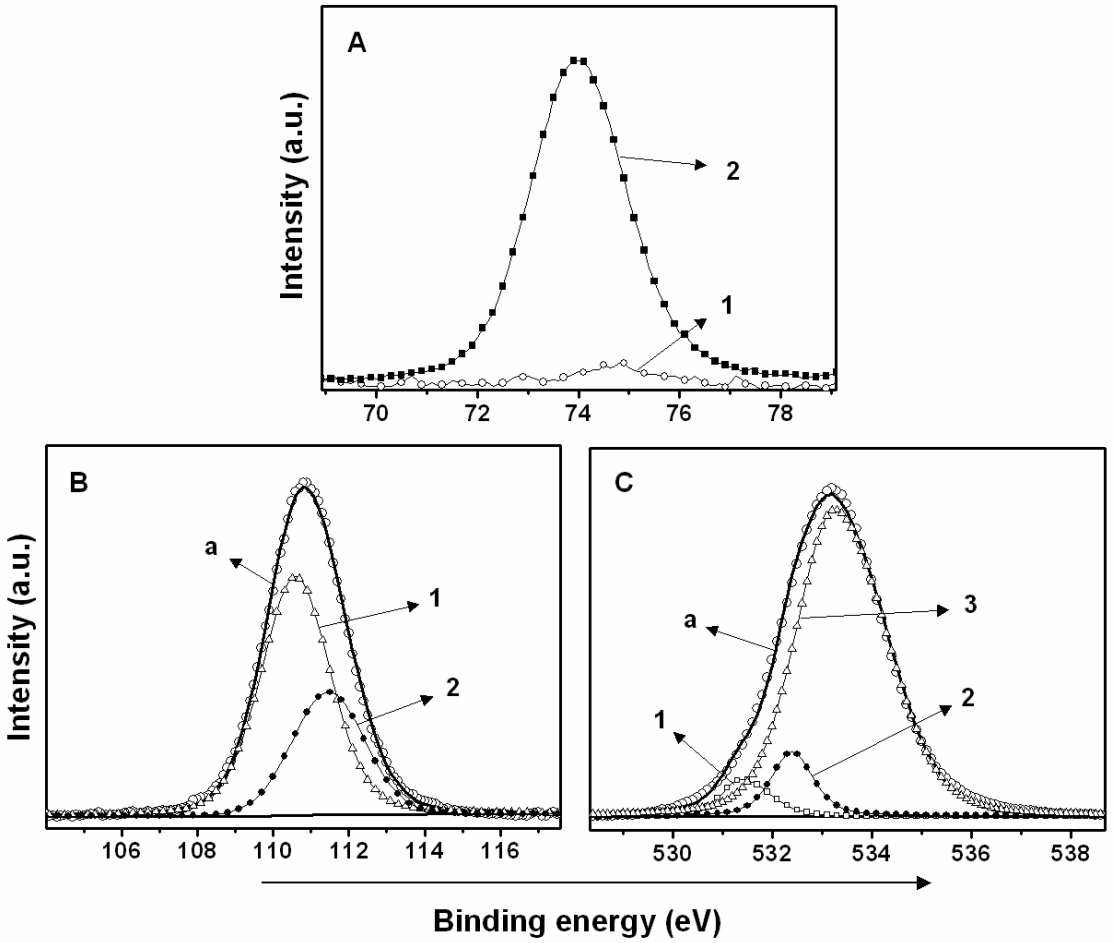

Figure 6.7: *(A) Comparison of raw XPS signals from Al 2p core levels of γ-AlOOH@SiO_2 (**8**) (curve 1) and γ-AlOOH (**7**) (curve 2) nanoparticles. XPS signals from (B) Si 2p and (C) O 1s core levels of γ-AlOOH@SiO_2 (**8**). Curve a represents composite fit to the raw signal (hollow circles) in all cases. See text and table 6.3 for details.*

The Si 2p composite signal from the silica shell could be deconvoluted to two components, 103.5 and 104.4 eV (curves 1 and 2, fig. 6.7B), corresponding to the Si $2p_{3/2}$ and Si $2p_{1/2}$ spin orbit coupling pairs. The binding energy values confirm to reported values of silica species [24]. This observation further confirms presence of a surface SiO_2 layer. The O 1s composite signal could be stripped to three components. The signal at 532.3 eV (curve 2, fig. 6.7C) is assigned to the oxygen in Si-O-C and surface Si-O-H substructures. The signal at 533.2 eV (curve 3, fig. 6.7C) has been attributed to the oxygen species of the Si-O-Si units present in silane materials [24]. In

addition a small component from adsorbed carbonate impurities is also included at 531.3 eV (curve 1, fig. 6.7C). Due to weak signal from the Al 2p in **8**, oxygen species of γ-AlOOH core structure have not been included in interpreting of the composite O 1s signal from **8**. Table 6.3 summarizes these results. These observations confirm the γ-AlOOH@SiO_2 core-shell structure (figs. 6.4C and D) of **8**.

Table 6.3: *Summary of XPS analysis of* ***8****.*

Element core level	Binding energy (eV)	Assignment
C 1s	285	Adventitious carbon C-H
	286.4	C-O-Si
	289.4	Adsorbed CO_3^{2-} impurities
Si 2p	103.5	$2p_{3/2}$ of Si
	104.4	$2p_{1/2}$ of Si
O 1s	531.3	adsorbed CO_3^{2-} impurities
	532.3	Si-O-C and Si-O-H
	533.2	Si-O-Si

6.3.2. Synthesis of azide functionalized γ-AlOOH@SiO_2 nanoparticles (10)

Azide functionalisation of **8** (scheme 6.2) was accomplished using previously reported two step procedure with slight modifications [7e]. In the first step, 0.6 g of **8** was dispersed in 80 mL of dry toluene using sonication under a nitrogen atmosphere. Following this, a solution of 1.2 mL of 3-bromopropyltrichlorosilane (BPTCS) in 5 mL dry toluene was added drop wise to the above dispersion under refluxing conditions. The reaction was allowed to continue for 8 h. Repeated (thrice) centrifugation (12000 rpm, 15 mins) and redispersion in toluene was done to remove excess 3-bromopropyltrichlorosilane. This yields bromide capped γ-AlOOH@SiO_2 (**9**) nanoparticles.

The substitution of the bromide with azide groups was achieved in the second step. 0.3 g of bromide capped silica nanoparticles and 0.4 g of NaN_3 were dispersed in

40 mL of dry DMF using sonication. The dispersion was then heated at 80 °C for 10 h. Repeated (thrice) centrifugation (15000 rpm, 20 mins) and redispersion in DMF yielded purified azide capped silica nanoparticles. The azide capped γ-AlOOH@SiO_2 nanoparticles (**10**) thus synthesized were used for "click" functionalisation with pyrene moieties.

6.3.3. Synthesis of prop-2-ynyl 4-(pyren-1-yl)butanoate (11)

Synthesis of the organic molecule bearing the propargyl functionality (**11)** was accomplished by following standard protocols [26] (scheme 6.3) and its structural authenticity was thoroughly established by various spectroscopic techniques including ^{1}H NMR spectroscopy and MALDI-TOF mass spectrometry.

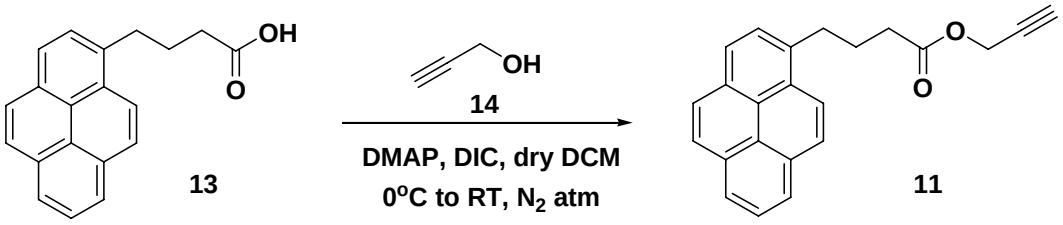

Scheme 6.3: *Synthesis of prop-2-ynyl 4-(pyren-1-yl)butanoate (**11**)*

To a solution of 4-(pyren-3-yl)butanoic acid (**13**) (0.87 g, 3 mmol) and propargyl alcohol (**14**) (0.17 g, 3 mmol) in anhydrous CH_2Cl_2 (15 mL) was added diisopropylcarbodiimide (DIC) (0.76 mL, 0.6 mmol) and a catalytic amount of 4-N,N-(dimethylamino)pyridine (DMAP) at 0 ^oC under nitrogen atmosphere. The resulting solution was brought to room temperature (35 ^oC) and stirred vigorously for 2 h. At the end of the reaction, as adjudged by TLC analysis, the reaction mixture was diluted with 50 mL of freshly distilled CH_2Cl_2, washed thoroughly with water and extracted thrice with CH_2Cl_2 (3 x 50 mL). The combined organic layers were dried over anhydrous Na_2SO_4 and filtered. The filtrate was concentrated *in vacuo* to obtain a crude residue which was subsequently purified by silica gel column chromatography using a gradient solvent system starting with 10 % ethyl acetate in petroleum ether and the product (**11**) (0.73 g, 75%) was eluted with 30 % ethyl acetate in petroleum ether.

*Characterization data of compound **11**:*

^{1}H NMR (200.13 MHz, $CDCl_3$): 2.23 (quintet, 2H, J = 7 Hz), 2.45-2.60 (m, 3H), 3.41 (t, 2H, J = 7 Hz), 4.73 (d, 2H, J = 2.5 Hz), 7.86 (d, 1H, J = 8 Hz), 7.99 (d, 1H, J = 8

Hz), 8.04 (s, 2H), 8.15 (d, 1H, J = 2 Hz), 8.17 (d, 1H, J = 2 Hz), 8.20 (s, 1H), 8.31 (d, 1H, J = 8 Hz); Anal. *Calcd. Mol. Wt*. of $C_{23}H_{18}O_2$: 326.37, *Found:* 326.35; *FTIR:* 3249 (s), 3038 (m), 2958 (m), 2939 (m), 2880 (m), 2126(m), 1736 (s) cm^{-1}.

6.3.4. "Click" functionalisation of azide capped γ-AlOOH@SiO_2

Huisgen's 1, 3 dipolar "click" cycloaddition of **10** with **11** (scheme 6.2) was accomplished as follows. Typically 50 mg of purified azide capped γ-AlOOH@SiO_2 nanoparticles (**10**) and 32 mg of CuI were dispersed in 15 mL of acetonitrile. This was followed by the addition of 85 mg of **11** (concentration - 0.3 M) and 0.36 mL of DIPEA. The above constituents were stirred for a period of 12 h at RT. Purification of pyrene capped γ-AlOOH@SiO_2 nanoparticles (**12**) was carried out using three rounds of centrifugation (15000 rpm, 20 minutes) interspersed with re-dispersion and washing with acetonitrile. The above purification steps were repeated with chloroform. The nanoparticles (**12**) were further treated with sodium diethyldithiocarbamate (1 mL of 0.1 M solution in methanol) for 30 mins for removal of copper(I) [27]. This was followed by washings with methanol and acetone. This purification cycle was repeated thrice. The nanoparticles thus obtained (**12**) were characterized using spectroscopic techniques such as UV-visible absorbance, fluorescence and FTIR analysis.

6.3.5. UV-visible and FTIR studies of pyrene capped γ-AlOOH@SiO_2

Curve 1, fig. 6.8 shows the UV-visible absorbance spectra of **12.** The peaks at 330 and 348 nm characteristic of pyrene chromophores [28] confirm the functionalisation of γ-AlOOH@SiO_2 with pyrene. The high density of pyrene chromophores is evident from the features seen in the fluorescence emission (curve 2, fig. 6.8) of pyrene capped γ-AlOOH@SiO_2 nanoparticles (**12**). Spectral features at 378, 389 and 397 nm that are characteristic of monomer pyrene emission are diminutive in comparison to the excimer emission at 480 nm. The high relative intensity of the excimer emission in comparison to the monomer emission is characteristic of densely packed pyrene units on solid substrates or concentrated pyrene solutions [29]. It needs to be noted that the density of the chromophores can be tuned by changing the initial concentration of the reactants as has been demonstrated in chapter 5.

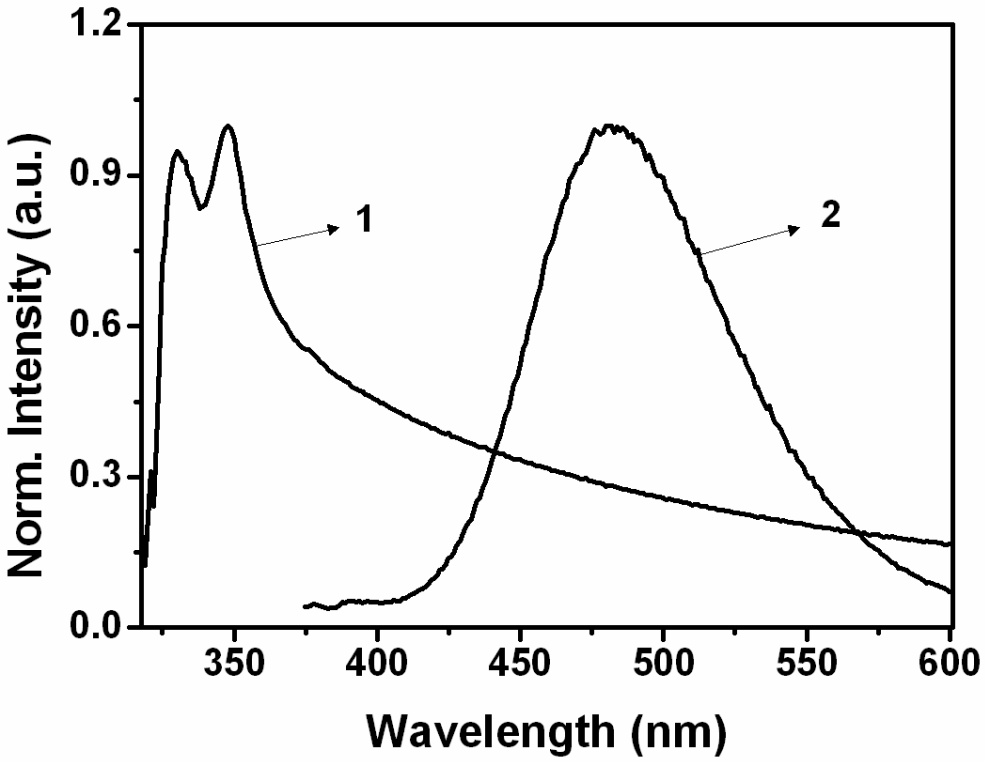

Figure 6.8: *UV-visible absorbance (curve 1) and fluorescence emission (curve 2) of* ***12****. The nanoparticles were excited at 350 nm to record the fluorescence spectra. Normalisation was carried out w.r.t to the 350 nm absorbance peak and the 480 nm pyrene fluorescence peak.*

The entire functionalisation process can be monitored by close scrutiny of FTIR features of respective nanoparticles (fig. 6.9). Following the coating of **7** with a SiO_2 layer, features that are characteristic of silane materials are incorporated in the nanoparticle systems **9**, **10** and **12**. The spectral features in the region from 1000 to 1300 cm^{-1} display a distinct silane character (fig. 6.9A) [30]. The curve with hollow circle is that of unfunctionalised Stober silica nanoparticles and is shown for comparison. The spectra of γ-AlOOH systems were normalized w.r.t the signal at 3294 cm^{-1}, characteristic of the OH stretching vibration (fig. 6.9C) [31]. The signal at 2097 cm^{-1} is characteristic of γ-AlOOH systems [31] and it coincides with the stretching vibration of azides (2100 cm^{-1}) (fig. 6.9B). However on azide functionalisation of γ-AlOOH@SiO_2, there is a significant increase in intensity accompanied by sharpening of the spectral feature indicating successful functionalisation. The same is quenched following "click" reaction with **11**. This is seen in FTIR spectra of pyrene capped AlOOH@SiO_2. It is thus demonstrated here that silica coatings effectively facilitate "click" chemistry functionalisation of γ-AlOOH nanoparticles.

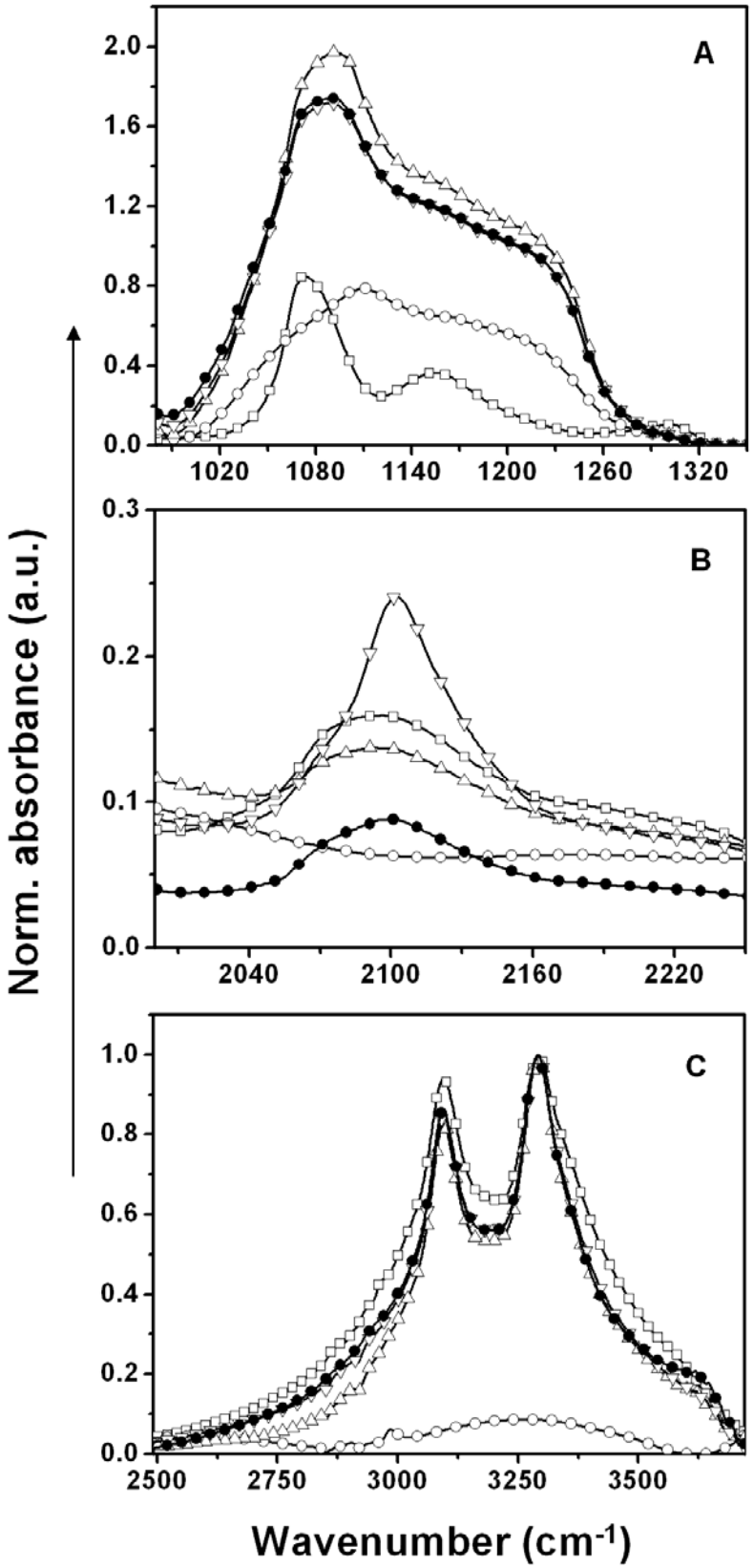

***Figure 6.9**: FTIR characterisation of AlOOH (**7**) (square), SiO_2 (hollow circle), bromide capped AlOOH@SiO_2 (**9**) (hollow triangle), azide capped AlOOH@SiO_2 (**10**) (inverted triangle) and pyrene capped AlOOH@SiO_2 (**12**) (solid circle) nanoparticles. Spectra of AlOOH systems have been normalized w.r.t signal at 3294 cm^{-1}.*

6.3.6. Dispersion of pyrene capped γ-AlOOH@SiO_2 in cyanobiphenyls

The fluorescence of **12** can also be used to study the organization of such nanoparticles in liquid crystalline systems. In earlier reports, the fluorescence incorporated in polystyrene micro spheres, using surface modification procedures, was used to monitor their behavior at the oil water interface [32]. Nanoparticulate systems wherein the surface chemistry is modified have been used for studying self organization in complex fluids [33].

Figs. 6.10A and B respectively show an optical micrograph of cyanobiphenyls in the absence and presence of 480 nm excitation. Fig. 6.10C shows a dispersion of pyrene capped γ-AlOOH@SiO_2 in cyanobiphenyl (E7) observed in absence of 480 nm excitation. The contrast patterns of cyanobiphenyls are apparent in fig. 6.10C, as in fig. 6.10A, making observation of the nanoparticles difficult. The presence of pyrene chromophores, however, enables selective observation of the **γ-**AlOOH@SiO_2 nanoparticles and their organization under 480 nm excitation. The marked regions in fig. 6.10D (oval and arrow) indicating fluorescence emission from surface pyrene show places of nanoparticle organization. The corresponding regions in fig. 6.10C are also marked for reference. Thus the fluorescence capping incorporated using "click" chemistry enables selective observation of nanoparticles in LC matrices.

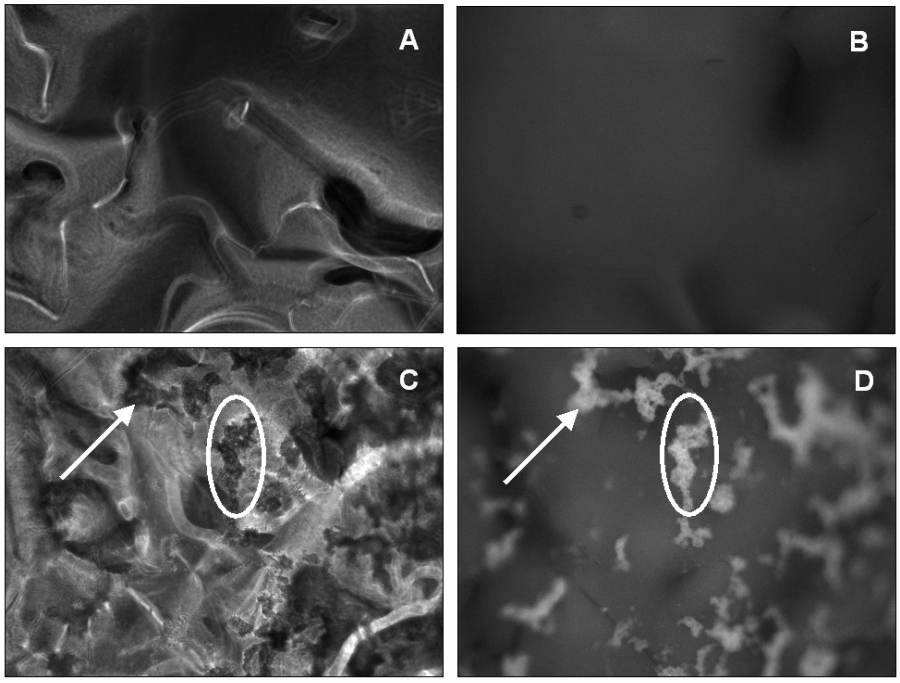

Figure 6.10*: Optical micrographs of cyanobiphenyl (E7) observed in absence (A) and presence (B) of pyrene excitation. Optical micrographs of dispersion of pyrene capped AlOOH@SiO_2 in cyanobiphenyl (E7) observed in absence (C) and presence (D) of pyrene excitation. The magnification is 20X in all cases. See text for details.*

6.4. Pyrene capped iron oxide@SiO_2 nanoparticles

In the final set of experiments we demonstrate that silica coatings in combination with "click" chemistry can be used to tune the density of functional groups on magnetic iron oxide.

6.4.1. Synthesis of iron oxide nanoparticles

Iron oxide nanoparticles were prepared using a simple co-precipitation method reported earlier [34]. Typically, 0.86 g of $FeCl_2$ and 2.35 g of $FeCl_3$ were mixed in 40 mL of de-ionized water (Milli-Q®) and heated to 80 °C under argon in a three necked flask. To the above solution under stirring condition was added 5 mL of NH_3 (about 30% in water). The heating was continued for 30 mins followed by addition of 1 g of citric acid (dissolved in 2 mL of de-ionized water). The temperature was then raised to 95 °C and the stirring continued for an additional 90 mins. The iron oxide nanoparticles prepared thus were purified using six rounds of centrifugation (15000 rpm for 40 mins) and redispersion in de-ionized water.

6.4.2. Synthesis of interconnected iron oxide@SiO_2 nanostructures (15)

The silica coating of iron oxide is well established [3,14,17]. The method used here is a modification of the same. 100 mg of iron oxide nanoparticles obtained as described above were dispersed, using sonication, in a mixture of 10 mL of de-ionized water, 3 mL of NH_3 and 38 mL of absolute ethanol. To this mixture, under stirring conditions, was added a stock solution of TEOS (1 mL in 30 mL of absolute ethanol), at the rate of 0.5 mL/ min. At different stages of addition of the TEOS stock solution, aliquots were removed from the reaction mixture and characterized (fig. 6.12) to monitor the growth of silica shell on the iron oxide core. Following addition of TEOS, the reaction was allowed to continue for a period of 24 h. After this, the nanoparticles were purified using centrifugation (15000 rpm, 40 minutes, thrice) and washings with absolute ethanol.

6.4.2.1 TEM and FTIR studies of iron oxide and interconnected iron oxide@SiO_2 nanostructures

In concurrence with the reported procedure [34], the mean size of the iron oxide nanoparticles was determined from TEM studies (fig. 6.11A) to be 12.2 ± 2.7 nm (fig. 6.11B). The purified iron oxide@SiO_2 nanoparticles were examined using TEM. It was

seen that interconnected iron oxide@SiO_2 core-shell nanostructures were formed. The core-shell structure is evident from the contrast pattern (fig. 6.12). The shell thickness was determined to be ~ 13 nm in these nanostructures.

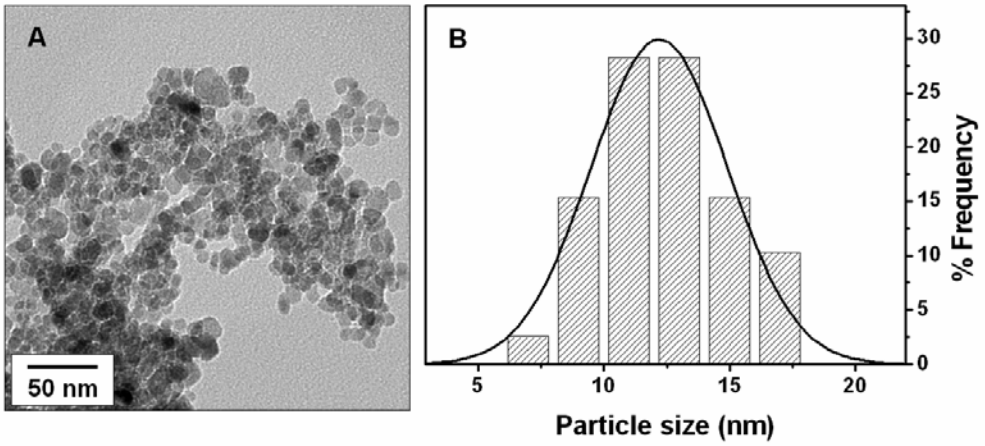

***Figure 6.11**: Representative TEM image (A) and size distribution (B) of iron oxide nanoparticles (average size - 12.2 ± 2.7 nm).*

It needs to be noted that the nanoparticles are linked to each other (fig. 6.12) in a quasi linear fashion [14b]. Earlier reports note that magnetic nanoparticles have been found to be present in the form of ordered arrays due to magnetic dipolar forces [35]. Here too we believe that the interconnected structures formed could be due the assembly of initially formed iron oxide@ SiO_2 nanoparticles. These nanostructures bound by magnetic forces could have been fused to each other by further coating of silica facilitated by excess TEOS.

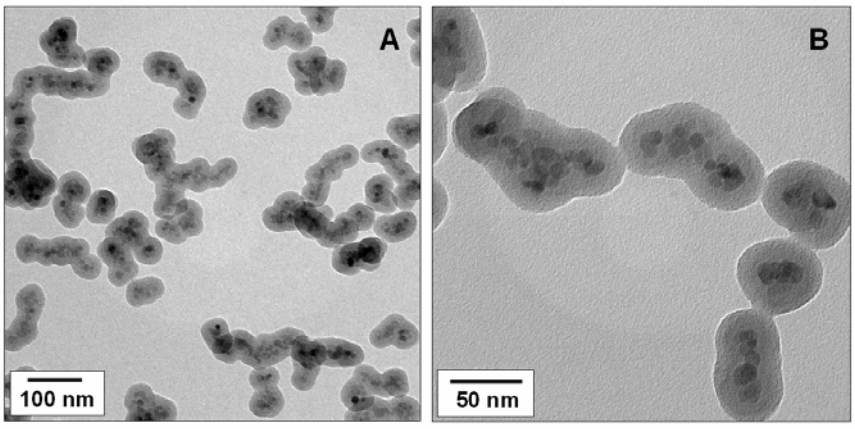

***Figure 6.12**: Representative TEM images of iron oxide@SiO_2 nanostructures.*

FTIR studies shed light on the phase purity of iron oxide and also growth of silica shell on the iron oxide nanoparticles. From fig. 6.13A it can be seen that the citrate capped iron oxide nanoparticles have features extending from 530 to 690 cm^{-1}

with maxima at 580 and 630 cm^{-1}. It is reported that magnetite - Fe_3O_4 does not have a feature at 630 cm^{-1} [36]. This feature is however characteristic of the Fe-O stretching vibrations of maghemite (γ-Fe_2O_3) [36]. This indicates a mixed phase of Fe_3O_4 and γ-Fe_2O_3 in the present case.

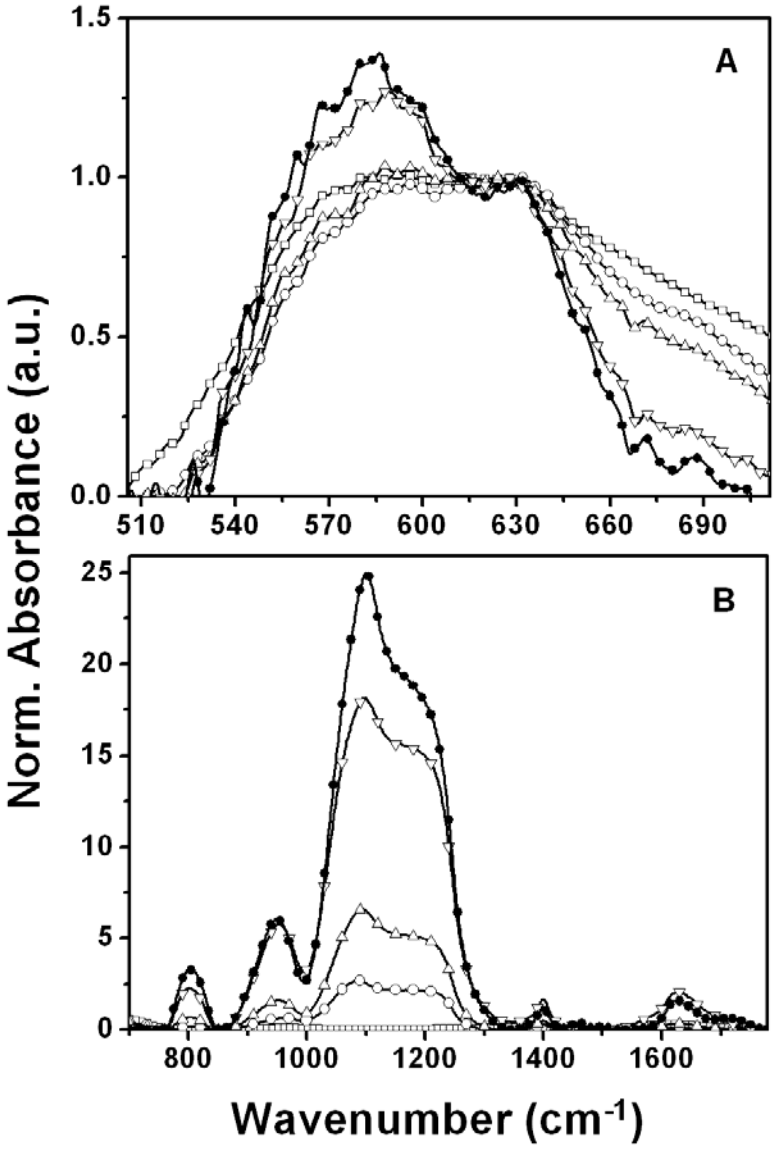

Figure 6.13: *FTIR analysis: Curve with hollow square corresponds to iron oxide nanoparticles. Curves with hollow circle, triangle, inverted triangle and solid circle correspond to iron oxide@SiO_2 nanostructures formed following addition of 4.3, 12.5, 19.5 and 31 mL of the TEOS stock solution to alkaline iron oxide dispersion. Spectra have been normalized w.r.t the Fe-O stretching vibration signal at 630 cm^{-1}. Increasing silica content is evident from signal growth at 1100 cm^{-1} corresponding to Si-O-Si bending vibrations. See text for details.*

The signals of iron oxide and silica coated iron oxide nanoparticles, removed from the reaction mixture at different stages of the silica coating procedure, are

normalized w.r.t the signal at 630 cm^{-1}. The growth of the silica shell is evident from the increase of the intensity of the peak at 1100 cm^{-1} (fig. 6.13B). Increasing intensity of this feature, characteristic of the siloxane (Si-O-Si) bending vibrations, indicates growth of the silica shell on the iron oxide nanoparticles. Further proof for silica growth is seen from the increase in intensity of the feature at 580 cm^{-1} (fig. 6.13A). Silica's overlapping vibration with the Fe_3O_4 signal is responsible for this spectral evolution [30,36].

XRD patterns (fig. 6.14) from iron oxide and iron oxide@SiO_2 nanostructures indicate that the structural integrity of the iron oxide core in the silica coated structures is preserved. All the Bragg reflections could be indexed to the cubic structure of Fe_3O_4 [37]. However, it needs to be noted that certain peaks are common to both cubic Fe_3O_4 [37] and cubic γ-Fe_2O_3 [38] and therefore, both these phases could be present in the system reported here. This observation is in concurrence with results of FTIR analysis wherein a mixture of iron oxide phases was observed.

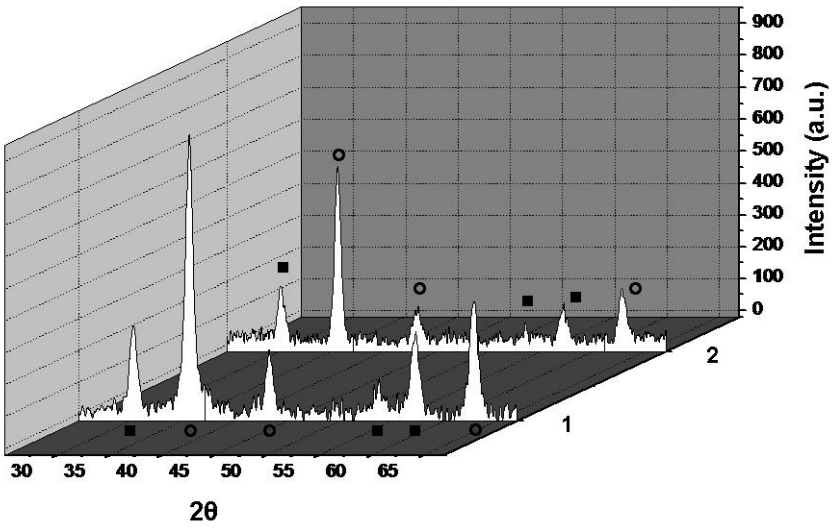

Figure 6.14: *XRD patterns corresponding to iron oxide (curve 1) and iron oxide@SiO_2 nanostructures (curve 2). Peaks marked with hollow circles arise from cubic Fe_3O_4. Those marked with solid squares arise from both cubic Fe_3O_4 and cubic γ-Fe_2O_3.*

6.4.2.2. XPS studies of iron oxide and interconnected iron oxide@SiO_2 nanostructures

XPS analysis, apart from confirming the presence of a silica shell in **15,** proves the existence of a γ-Fe_2O_3 phase. Fig. 6.15A shows signals from the Fe 2p core-levels of iron oxide nanoparticles. The composite signal could be deconvoluted to two spin

orbit coupling pairs. The Fe $2p_{3/2}$ (Fe $2p_{1/2}$) components occurring at 709.7 (732.1) and 711.3 (724.8) eV originate from the Fe^{2+} (curve 1, fig. 6.15A) and Fe^{3+} (curve 2, fig. 6.15A) species of iron oxide. In addition to this, satellite features at 718.9 and 732.4 eV were also recorded (curve 3, fig. 6.15A). The satellite features provide proof of existence of a γ-Fe_2O_3 phase. It is reported that Fe_3O_4 does not exhibit satellite peaks [39]. Moreover, the difference in binding energy between the Fe $2p_{3/2}$ core level of Fe^{3+} and the satellite at 718.9 eV matches with reported values of Fe_2O_3 [39]. The ratios of Fe^{3+} and Fe^{2+} peak area in Fe_3O_4 is 2. In the present case, it is 2.6 indicating an excess Fe^{3+} population from the γ-Fe_2O_3 phase. These observations confirm a mixed phase of γ-Fe_2O_3 and Fe_3O_4 in our iron oxide conclusively. The actual reported synthetic procedure was, however, nonconclusive about the phase purity of the iron oxide nanoparticles [34]. It needs to be noted that both Fe_3O_4 and γ-Fe_2O_3 are magnetic and hence serve our purpose. No effort was therefore made to purify this biphasic system.

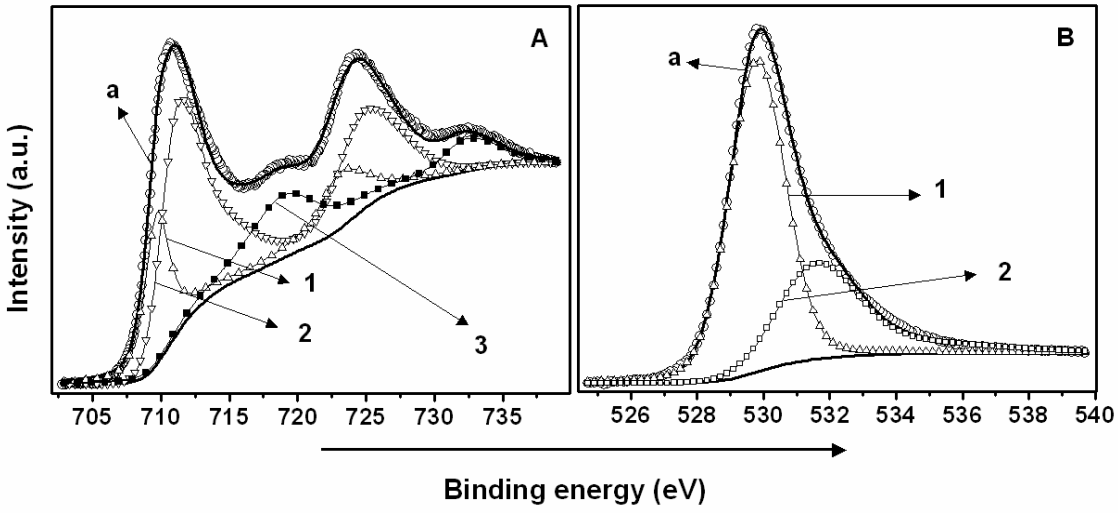

Figure 6.15: *XPS signals from (A) Fe 2p and (B) O 1s core levels of iron oxide nanoparticles. Curve a represents composite fit to the raw signal (hollow circles) in all cases. See text and table 6.4 for details.*

The composite O 1s signal could be deconvoluted to two components at 529.7 (curve 1, fig. 6.15B) and 531.6 eV (curve 2, fig. 6.15B) arising from lattice O_2^{2-} of iron oxide and surface hydroxyl of iron oxide respectively. The XPS values of iron oxide matches with earlier reports [24] and table 6.4 summarizes these results.

Table 6.4: *Summary of XPS analysis of iron oxide nanoparticles.*

Element core level	Binding energy (eV)	Assignment
C 1s	285	Adventitious carbon C-H
	288.2	C of acid group in citrate
Fe 2p	709.7 and 723.1	$2p_{3/2}$ and $2p_{1/2}$ of Fe^{2+} respectively
	711.3 and 724.8	$2p_{3/2}$ and $2p_{1/2}$ of Fe^{3+} respectively
	718.9 and 732.4	Satellite peaks
O 1s	529.7	Lattice O_2^{2-} of Fe_3O_4
	531.6	Surface hydroxyl of Fe_3O_4 and citrate capping

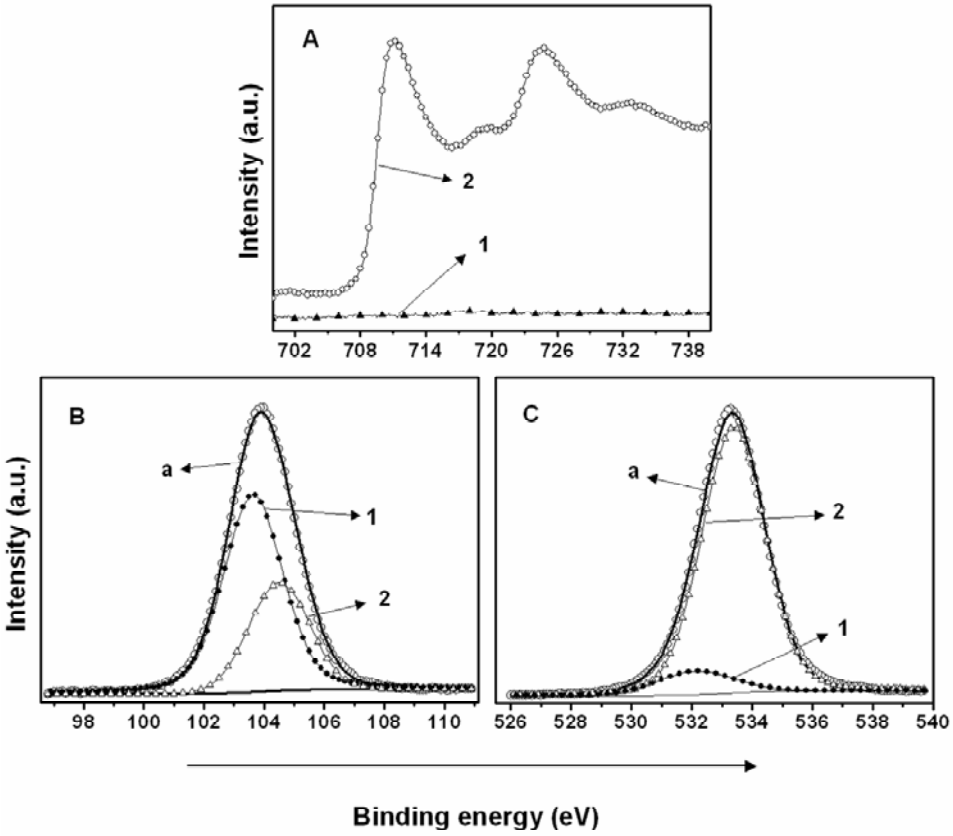

Figure 6.16: *(A) Comparison of raw XPS signals from Fe 2p core levels of iron oxide (curve 1) and iron oxide@SiO_2 (curve 2) nanoparticles. (B) Si 2p and (C) O 1s core levels of iron oxide@SiO_2. Curve a represents composite fit to the raw signal (hollow circles) in all cases. See text and table 6.5 for details.*

Table 6.5: *Summary of XPS analysis of iron oxide@SiO_2 nanoparticles.*

Element core level	Binding energy (eV)	Assignment
C 1s	285	Adventitious carbon C-H
	286.3	C–O-Si bond
Si 2p	103.6	$2p_{3/2}$ of Si
	104.4	$2p_{1/2}$ of Si
O 1s	532.3	Si-O-C and Si-O-H
	533.2	Si-O-Si

As was the case for Al 2p signal from AlOOH@SiO_2 (**8**) nanoparticles (fig. 6.7A), the signal from Fe 2p core level in interconnected iron oxide@SiO_2 nanostructures is not detected (compare curves 1 and 2, fig. 6.16A). This is despite the fact that XRD and FTIR analysis confirm presence of iron oxide in **15**. This is due to the presence of a 13 nm thick layer of SiO_2 on the iron oxide nanostructures (fig. 6.12) effectively scattering the photoelectrons from the Fe 2p core level. This is in confirmation with similar observations in previous reports of silica coated hematite nanoparticles [40].

The signals from Si 2p core level conform to reported values of SiO_2 species (figs. 6.16 B and C). The Si 2p composite signal from the silica shell could be deconvoluted to two components, 103.6 and 104.4 eV (curves 1 and 2, fig. 6.7B), corresponding to the Si $2p_{3/2}$ and Si $2p_{1/2}$ spin orbit coupling pairs. The O 1s core level signal could be deconvoluted to two components. The component at 532.3 eV (curve 2, fig. 6.7C) is assigned to the oxygen in Si-O-C and surface Si-O-H substructures. The component at 533.2 eV (curve 3, fig. 6.7C) has been attributed to the oxygen species of the Si-O-Si units present in silane materials [24]. A summary of these results is shown in table 6.5.

6.4.3. Tunable "click" functionalisation of interconnected iron oxide@SiO_2 nanostructures with pyrene chromophores

The functionalisation of **15** to yield azide capped nanostructures **16** was accomplished by following a procedure just as outlined in section 6.3.2. Functionalisation of **16** with **11** (prop-2-ynyl 4-(pyren-1-yl)butanoate) was accomplished using the "click" reaction. Typically 50 mg of **16** was dispersed in 5 mL

of acetonitrile using sonication in the presence of 32 mg of CuI and 0.36 mL of DIPEA. To this was added 30 mg of **11** dissolved in 1 mL of $CHCl_3$. The reaction mixture was stirred for a period of 24 h. Purification of the functionalised nanoparticles was carried out as was done for pyrene capped $AlOOH@SiO_2$ nanoparticles (**12**) (section 6.3.4). Excess pyrene chromophores (**11**) and Cu(I) were thus removed. The sample obtained here is referred to as iron oxide@SiO_2@pyrene-1 (**17**). The same procedure was repeated with 3 and 0.3 mg of **11** (other conditions being identical) to yield iron oxide@SiO_2@pyrene-2 (**18**) and iron oxide@SiO_2@pyrene-3 (**19**).

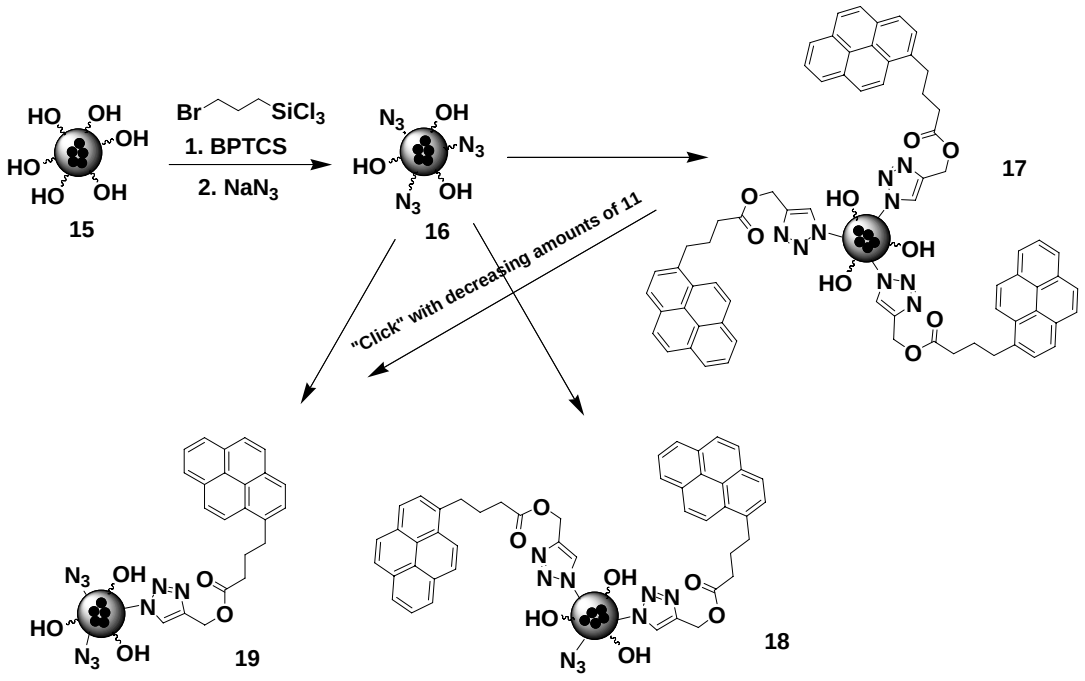

Scheme 6.4: *Cartoon illustrating the "click" functionalisation of iron oxide@SiO_2 nanoparticles with pyrene derivatives. See text of details.*

6.4.4. FTIR and UV-visible characterisation of pyrene capped interconnected iron oxide@SiO_2 nanostructures

A qualitative picture of the tunability of surface coverage can be obtained by monitoring the azide and pyrene signatures in FTIR and UV-visible absorbance spectroscopic techniques respectively.

When the FTIR spectra of **16**, **17**, **18** and **19** were normalized w.r.t the Si-O-Si spectral signature at 1100 cm^{-1} (fig. 6.17), the variation in the intensity of the azide signature at 2100 cm^{-1} is evident (inset of fig. 6.17). It can be seen that from samples **16** to **19**, the signal intensity at 2100 cm^{-1} progressively decreases. The relative percentage of free azide groups in each sample, w.r.t t **16**, can be obtained by calculating the area

of the azide feature in each sample and normalizing the same w.r.t the Si-O-Si

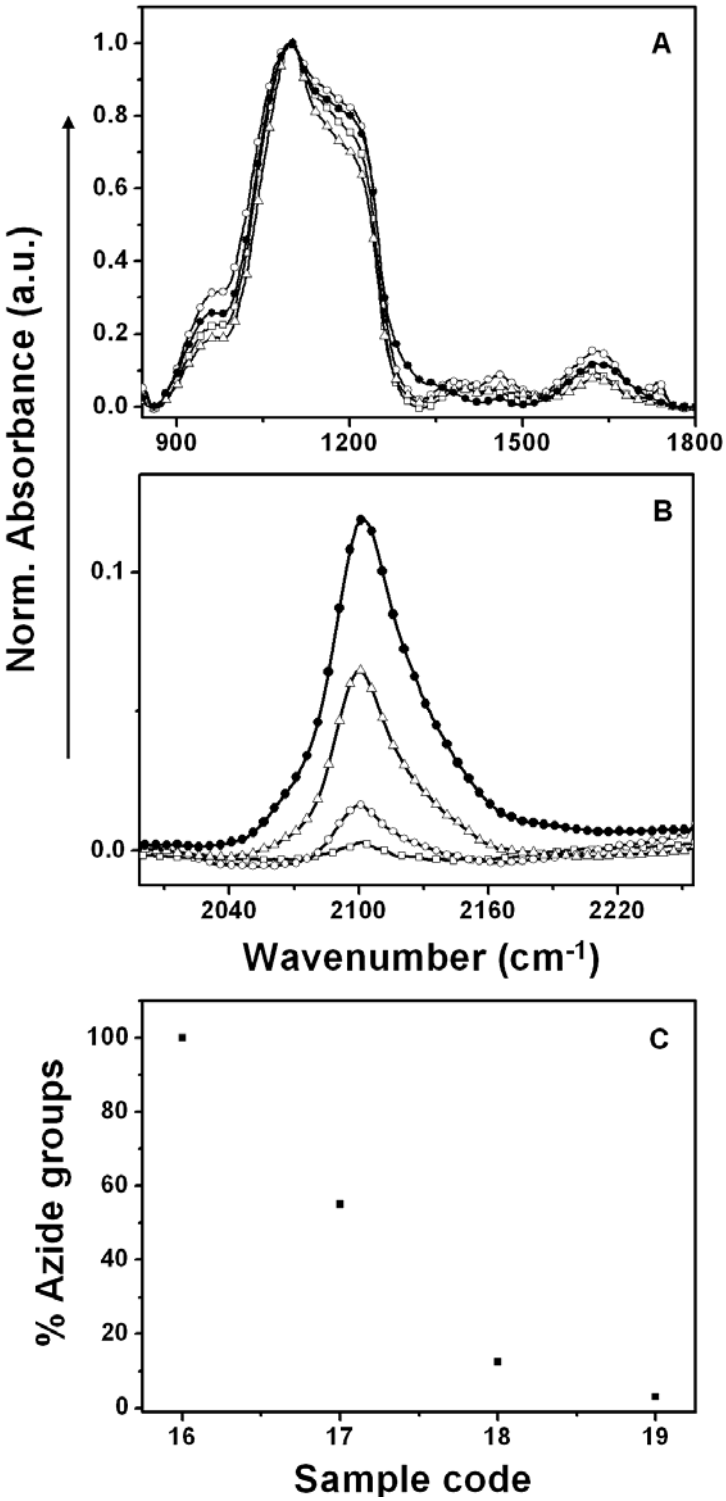

***Figure 6.17**: FTIR analysis: curves with solid circles, squares, hollow circles and triangles correspond to azide capped iron oxide@SiO_2 (**16**), iron oxide@SiO_2@pyrene-1 (**17**), iron oxide@SiO_2@pyrene-2 (**18**) and iron oxide@SiO_2@pyrene-3 (**19**) nanostructures respectively. (B) shows depleting signal intensity at 2100cm^{-1} (corresponding to azide vibration) indicating greater extents of "click" reaction. Normalisation w.r.t to Si-O-Si bending vibrations at 1100 cm^{-1} has been performed. (C) shows amount of free azide groups in each sample.*

signature. Fig. 6.17C shows the results of such an analysis. This shows that greater amounts of pyrene are bound to the surface of iron oxide@SiO_2 as we increase the amount of **11** during the "click" reaction.

UV-visible signatures (at 315, 330 and 348 nm) from the pyrene chromophores increase in intensity from samples **17**, **18** and **19** (curves 3 to 1, fig. 6.18). Measurements from dispersions of 1 mg of the pyrene capped nanoparticles in 1 mL of chloroform were carried out here. These studies provide evidence that silica coating on magnetic iron oxide nanoparticles facilitates tunable surface functionalisation through the "click" chemistry pathway. As noted earlier such nanoparticles with suitable capping would find applications in bio-separations, drug delivery, cancer hyperthermia, magnetic resonance imaging and catalysis [16].

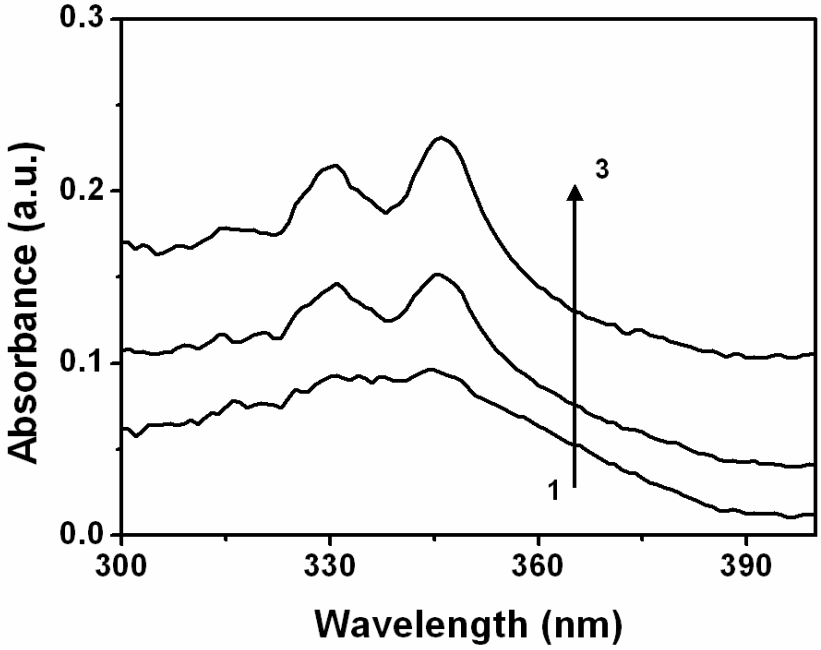

Figure 6.18: *UV-visible absorbance spectral signatures corresponding to pyrene from iron oxide@SiO_2@pyrene-3 (**19**), iron oxide@SiO_2@pyrene-2 (**18**) and iron oxide@SiO_2@pyrene-1 (**17**) nanostructures is shown in curves 1, 2 and 3 respectively.*

6.5. Conclusions

In this chapter, we have demonstrated that by using a combination of silane coatings and "click" chemistry a variety of functional inorganic nanomaterials could be synthesized. Berberine capped silica nanoparticles, pyrene capped AlOOH@SiO_2 and pyrene capped iron oxide@SiO_2 have been fabricated and thoroughly characterized

using analytical techniques such as TEM, XRD, XPS, FTIR, UV-visible and fluorescence spectroscopy.

6.6. References

[1] Liz-marzan, L. M.; Giersig, M.; Mulvaney, P. *Langmuir* **1996**, *12*, 4329.

[2] Selvan, S. T.; Tan, T. T.; Ying, J. Y. *Adv. Mater.* **2005**, *17*, 1620.

[3] Rebolledo, A. F.; Bomati-Miguel, O.; Marco, J. F.; Tartaj, P. *Adv. Mater.* **2008**, *20*, 1760.

[4] Aliev, F. G.; Correa-Duarte, M. A.; Mamedov, A.; Ostrander, J. W.; Giersig, M.; Liz-Marzan, L. M.; Kotov, N. A. *Adv. Mater.* **1999**, *11*, 1006.

[5] (a) Gerion, D.; Pinaud, F.; Williams, S. C.; Parak, W. J.; Zanchet, D.; Weiss, S.; Alivisatos, A. P. *J. Phys. Chem. B* **2001**, *105*, 8861. (b) Sun, C.; Lee, J. S. H.; Zhang, M. *Adv. Drug. Deliver. Rev.* **2008**, *60*, 1252.

[6] Moses, J. E.; Moorhouse, A. D. *Chem. Soc. Rev.* **2007**, *36*, 1249.

[7] (a) Halas, N. J.; *ACS Nano* **2008**, *2*, 179. (b) Lummerstorfer, T.; Hoffman, H. *J. Phys. Chem. B* **2004**, *108*, 3963. (c) Ortega-Munoz, M.; Lopez-Jaramillo, J.; Hernandez-Mateo, F.; Santoyo-Gonzalez, F. *Adv. Synth. Catal.* **2006**, *348*, 2410. (d) Guo, Z.; Lei, A.; Liang, X.; Xu, Q. *Chem. Commun.* **2006**, 4512. (e) Rajan, R.; Brittain, W. J. *Macromolecules* **2007**, *40*, 6217. (f) Lin. P.; Ueng, S.; Yu, S.; Jan, M.; Adak, A. K.; Yu, C.; Lin, C. *Org. Lett.* **2007**, *9*, 2131. (g) Chandran, S. P.; Hotha, S.; Prasad, B. L. V. *Curr. Science* **2008**, *95*, 1327. (h) White, M. A.; Johnson, J. A.; Koberstein, J. T.; Turro, N. J. *J. Am. Chem. Soc.* **2006**, *128*, 11356. (i) Polito, L.; Colombo, M.; Monito, D.; Melato, S.; Caneva, E.; Prosperi, D. *J. Am. Chem. Soc.* **2008**, *130*, 12712. (j) Schatz, A.; Grass, R. N.; Stark, W. J.; Reiser, O. *Chem. Eur. J.* **2008**, *14*, 8262. (k) Polito, L.; Monito, D.; Caneva, E.; Delnova, E.; Russo, G.; Prosperi, D. *Chem. Commun.* **2008**, 621. (l) Lv, G.; Mai, W.; Jin, R.; Gao, L. *Synlett* **2008**, *9*, 1418.

[8] (a) Stermitz, F. R.; Lorenz, P.; Tawara, J. N.; Zenewicz, L. A.; Lewis, K. *Proc. Natl. Acad. Sci. U S A* **2000**, *97,* 1733. (b) Rojsanga, P.; Gritsanapan, W.; Suntornsuk, L. *Med. Princ. Pract.* **2006**, *15*, 373.

[9] (a) Newman, D. J.; Cragg, G. M.; Snader, K. M. *J. Nat. Prod.* **2003**, *66*, 1022. (b) Mantena, S. K.; Sharma, S. D.; Katiyar, S. K. *Carcinogenesis* **2006**, *27*, 2018.

[10] Halimani, M.; Prathap Chandran, S.; Kashyap, S.; Jadav, V. M.; Prasad, B. L. V .; Hotha, S.; Maiti, S. *Langmuir* DOI: 10.1021/la802761b.

[11] Davidson, P.; Batail, P.; Gabriel, J. C. P.; Livage, J.; Sanchez, C.; Bourgaux, C. *Prog. Polym. Sci.* **1997**, *22*, 913.

[12] (a) Philipse, A. P.; Nechifor, A.; Patmamanoharan, C. *Langmuir* **1994**, *10*, 4451. (b) Graf, C.; Vossen, D. L. J.; Imhof, A.; Blaaderen, A. V. *Langmuir* **2003**, *19*, 6693. (c) Wijnhoven, J. E. G. J. *Chem. Mater.* **2004**, *16*, 3821.

[13] Bruggen, M. P. B. V. *Langmuir* **1998**, *14*, 2245.

[14] (a) Lu, A.; Salabas, E. L.; Schuth, F. *Angew. Chem. Int. Ed.* **2007**, *46*, 1222. (b) Philipse, A. P.; van Bruggen, M. P. B.; Pathmamanoharan, C. *Langmuir* **1994**, *10*, 92.

[15] Kim, J.; Lee, J. E.; Lee, J.; Jang, Y.; Kim, S.; An, K.; Yu, J. H.; Hyeon, T. *Angew. Chem. Int. Ed.* **2006**, *45*, 4789.

[16] (a) Pankhurst, Q. A.; Connolly, J.; Jones, S. K.; Dobson, J. *J. Phys. D: Appl. Phys.* **2003**, *36*, R167. (b) Quarta, A.; Corato, R. D.; Manna, L.; Ragusa, A.; Pellegrino, T. *IEEE Trans. Nanobioscience* **2007**, *6*, 298.

[17] Tartaj, P.; Gonzalez-Carreno, T.; Serna, C. *Adv. Mater.* **2001**, *13*, 1620.

[18] Zhang, M.; Shi, S.; Meng, J.; Wang, X.; Fan, H.; Zhu, Y.; Wang, X.; Qian, Y. *J. Phys. Chem. C* **2008**, *112*, 2825.

[19] Stober, W.; Fink, A.; Bohn, E. *J. Colloid lnterface Sci.* **1968***, 26,* 62.

[20] Ramesh, R.; Bhat, R. G.; Chandrasekaran S. *J. Org. Chem.* **2005**, *70*, 837.

[21] Hotha, S.; Kashyap, S. *J. Org. Chem.* **2006**, *71*, 364.

[22] (a) Philipse, A. P.; Vrij, A. *J. Colloid lnterface Sci.* **1989***, 128,* 121. (b) Ketelson, H. A.; Brook, M. A.; Pelton, R. H. *Chem. Mater.* **1995**, *7*, 1376. (c) Abu-Reziq, R.; Alper, H.; Wang, D.; Post, M. L. *J. Am. Chem. Soc.* **2006**, *128*, 5279.

[23] *Joint Committee on Powder Diffraction Standards*, File No: 21-1307.

[24] *NIST X-ray Photoelectron Spectroscopy Database*, Version 3.5 (National Institute of Standards and Technology, Gaithersburg, 2003); http://srdata.nist.gov/xps/

[25] Wagner, C. D.; Riggs, W. M.; Davis, L. E.; Moulder, J. F.; Muilenberg. G. E. (ed.) *Handbook of X-Ray photoelectron spectroscopy, Perkin-Elmer Corporation, Physical Electronics division: 6509 Flying cloud drive, Eden Praire, Minnesota 55344*; **1979**, p 50.

[26] Hotha, S.; Anigundi, R. I.; Natu, A. *Tetrahedron Lett.* **2005**, *46*, 4585.

[27] Terry, T. J.; Stack, T. D. P. *J. Am. Chem. Soc.* **2008**, *130*, 4945.

[28] Ipe, B. I.; Thomas, K. G.; Barazzouk, S.; Hotchandani, S.; Kamat, P. V. *J. Phys. Chem. B* **2002**, *106,* 18.

[29] (a) Milosavljevict, B. H.; Thomas, J. K. *J. Phys. Chem.,* **1988**, *92,* 2997. (b) Yamazaki, T.; Tamai, N. Yamazaki, I. *Chem. Phys. Letters,* **1986**, *124*, 326. (c) Ipe, B. I.; Thomas, K. G. *J. Phys. Chem. B* **2004**, *108,* 13265. (d) Thomas, J. K. *Chem. Rev.,* **2005**, *105*, 1683.

[30] Prado, A. G. S.; Airoldi, C. *J. Colloid lnterface Sci.* **2001***, 236,* 161.

[31] Trombetta, M.; Busca, G.; Willey, R. J. *J. Colloid Interface Sci.* **1997**, *190*, 416.

[32] Zeng, C.; Bissig, H.; Dinsmore, A. D. *Solid State Commun.* **2006**, *139*, 547.

[33] Loudet, J. C.; Barois, P.; Auroy, P.; Keller, P.; Richard, H.; Poulin, P. *Langmuir*, **2004**, *20*, 11336.

[34] Sahoo, Y.; Goodarzi, A.; Swihart, M. T.; Ohulchanskyy, T. Y.; Kaur, N.; Furlani, E. P.; Prasad, P. N. *J. Phys. Chem. B* **2005**, *109*, 3879.

[35] Li, H.; Wang, C.; Zhao, Q.; Li, H. *Appl. Surf. Sci.* **2008**, *254*, 7516.

[36] Namduri, H.; Nasrazadani, S. *Corros. Sci.* **2008**, *50*, 2493.

[37] *Joint Committee on Powder Diffraction Standards*, File No: 19-0629.

[38] *Joint Committee on Powder Diffraction Standards*, File No: 39-1346.

[39] (a) Muhler, M.; Schlogl, R.; Ertl, G. *J. Catal.* **1992**, 138, 413. (b) Yamashita, T.; Hayes, P. *Appl. Surf. Sci.* **2008**, *254*, 2441.

[40] Xu, X.; Cortie, M. B. *J. Phys. Chem. C* **2007**, *111*, 18135.

Chapter 7

Conclusions

This chapter summarizes salient features of the work embodied in this thesis. In addition, scope for future work relevant to the present study is discussed.

The objective of this thesis work as explained in chapter 1 was the synthesis of anisotropic and core-shell nanoparticles of gold and silver, particularly in the organic media. In addition, effective methods for nanoparticle surface functionalisation and quantification of surface functional groups were envisaged. Herein a summary of the thesis work and scope of future work are presented.

The salient features of the results are as follows:

- New methods were investigated for the synthesis of gold nanorods and Au@Ag core-shell nanoparticles in organic media.
- A biogenic method for the synthesis of gold nanotriangles was demonstrated with ability to control the nanotriangle dimensions and hence their optical properties.
- "Click" chemistry on silica surfaces was demonstrated as a method to achieve tunable surface functionalisation of inorganic nanoparticles.
- A new method to quantify reactive surface functional groups in nanoparticles was demonstrated.

Thus development of novel methodologies for synthesis and tunable functionalisation of nanoparticles was the focus of this thesis work. It needs to be noted though that the findings do indicate good potential for future applications. For example, it was demonstrated that pyrene coated γ-AlOOH@SiO_2 nanoparticles could be used to study the internal organisation of nanoparticles in liquid crystalline (LC) matrices. However, there was no ordered assembly that was observed. Incompatibility between the surface pyrene groups and the LC matrix used in this case (cyanobiphenyl-E7) could have resulted in aggregation of the nanoparticles. In this regard, a careful study involving varying surface functionality and different LC matrices could result not only in better ordered assemblies but would also facilitate in-situ observation of the phase transitions that resulted in the assemblies at the first place.

The amine and azide quantification procedures that were demonstrated using FMoC derivatives can be extended to other functional groups such as alkyne and thiol. Therefore, they can serve as viable alternatives to presently employed combustion analysis procedures which fail to differentiate between bulk and surface functionalities.

Another avenue with scope for improvement is the synthesis of anisotropic nanostructures in organic media. While two new methods were explored, the results are

not as would be desired of a good synthetic procedure. Consequently, a more detailed study as to what affects the same can be undertaken. For example, the seed nanoparticles' crystal structure has been found determine the product of the seeded growth. A method wherein gold seeds with well defined and uniform crystal structure are used could give desired yields of gold nanorods or other anisotropic nanostructures. The same was not investigated in the present work.

The reduction of gold ions using ascorbic acid derivatives was under-investigated. A bright indication to the latent potential of this method towards anisotropic synthesis in organic media is the high nanorod yield obtained under certain reaction conditions even in the absence of seeds. Establishment of reliable protocols for synthesis of anisotropic and core-shell nanoparticles in organic media has great potential in fields such as SERS, sensor technology, controlled assembly and synthesis of functional organic-inorganic hybrid materials.

Appendix 1: Instrumental and experimental details

Atomic force microscope:

A VEECO Digital Instruments multimode scanning probe microscope equipped with a Nanoscope IV controller was used for AFM measurements. Samples were drop coated on to a Si (111) substrate and were analyzed using contact mode AFM using long silicon nitride probes (100 μm). The height data was collected at a scanning frequency of 1Hz.

Fluorescence spectrophotometer:

Measurements were carried out on a Perkin Elmer LS55 fluorescence spectrophotometer with slit widths of 5 nm. Alternatively spectra were recorded on a Varian Cary Eclipse fluorescence spectrophotometer with slit widths of 5 nm.

FTIR spectrophotometer:

FTIR spectra were recorded on a Perkin Elmer Spectrum One FTIR spectrophotometer in diffuse reflectance mode, operating at a resolution of 4 cm^{-1}.

Mass spectrometer:

Mass spectra were recorded on a Q Star Pulsar LC-MS-MS-TOF machine. Alternatively, MALDI–TOF mass spectra were recorded on a VOYAGER-DE-STR instrument.

Transmission electron microscope:

TEM measurements were performed on a JEOL Model 1200EX instrument operated at an accelerating voltage of 80 kV. HRTEM measurements were carried out using a JEOL–JEM-2010 UHR instrument operated at an acceleration voltage of 200 kV with a lattice image resolution of 0.14 nm. In addition, for HRTEM measurements, a TECHNAI G2 F30 S-TWIN instrument (Operated at an acceleration voltage of 300 kV with a lattice resolution of 0.14 nm and a point image resolution of 0.20 nm) was also employed. The same set of instruments was used for electron diffraction analyses. TEM samples were prepared by placing drops of dispersed samples over carbon coated copper grids and allowing the solvent to evaporate.

Thermo gravimetric analyser:

The TGA experiments were carried out on a Mettler Toledo TGA Instrument (TGA/SDTA 851e) controlled by STARe software (Mettler Toledo GmbH, Switzerland).

UV-visible-NIR spectrophotometry:

UV- Spectroscopic measurements were carried out on a JASCO model V-570 dual-beam spectrophotometer operated at a resolution of 2 nm.

X-ray photoelectron spectroscopy:

Measurements were carried out on a VG MicroTech ESCA 3000 instrument at a pressure better than 10^{-9} Torr. The spectra were recorded with un-monochromatized Mg*Kα* radiation (photon energy = 1253.6 eV) at a pass energy of 50 eV, electron takeoff angle (angle between electron emission direction and surface plane) of 60° and a resolution of 0.1 eV. The core level spectra were background corrected using the Shirley algorithm and the chemically distinct species resolved using a nonlinear least squares curve fitting procedure. The core level binding energies (BEs) were aligned with respect to the C 1s binding energy (BE) of 285 eV.

X-ray diffraction:

The diffractograms were recorded on a PANalytical Xpert pro machine using a CuKα source and operating conditions of 40 mA and 30 kV at a scan rate of 4.66 theta/min.

Organic synthesis:

During synthesis of organic compounds, the following guidelines were followed. All reactions were performed under nitrogen atmosphere. Removal of solvent *in vacuo* refers to distillation using a rotary evaporator attached to an efficient vacuum pump. Products obtained as solids or syrups were dried under high vacuum. Analytical thin-layer chromatography was performed on pre-coated silica plates (F_{254}, 0.25 mm thickness); compounds were visualized by UV light, iodine chamber or by staining with anisaldehyde or ninhydrin solution. NMR spectra were recorded on 200.13 MHz or 300 MHz for ^{1}H and 50.32 MHz for ^{13}C species. Chemical shifts (δ_H) are quoted in ppm and are referenced to tetramethylsilane (internal).

List of abbreviations:

ACN: Acetonitrile

AFM: Atomic force microscope/microscopy

APTES: (3-aminopropyl)-triethoxy silane

Atm.: Atmosphere

BDSAC: benzyldimethylstearylammonium chloride

BET: Brunauer-Emmett-Teller

BPTCS: (3-bromopropyl)-trichloro silane

CTAB: Cetyl trimethylammonium bromide

DBF: Dibenzofulvene

DBU: 1,8-Diazabicyclo[5.4.0]undec-7-ene

DIC: N,N'-diisopropylcarbodiimide

DIPEA: N,N-(diisopropyl)-ethylamine

DMAP: 4-N,N-(dimethylamino)pyridine

DMF: N,N-(dimethyl)-formamide

DMSO: Dimethyl sulfoxide

DNA: Deoxyribonucleic acid

EDTA: Ethylenediaminetetraaceticacid

EFGP: Enhanced green fluorescence protein

EPL: Expressed protein ligation

FCC: Face centred cubic

FMoC: Fluorenylmethoxycarbonyl

FRET: Fluorescence resonance energy transfer

FTIR: Fourier-transform infra-red

HCP: Hexagonal closed packing

HDA: 4-(hexadecyl)-aniline

HRTEM: High resolution transmission electron microscope/microscopy

LC: Liquid crystal

LC-MS-MS: Liquid chromatography-mass spectrometry-mass spectrometry

MALDI – TOF: Matrix-assisted laser desorption/ionisation-time of flight

MBP: Maltose binding protein

MEF: Metal enhanced fluorescence

NIR: Near infra-red

NMR: Nuclear magnetic resonance

Norm.: Normalised

ODA: n-octadecylamine

PDP: 3-(pentadecyl)-phenol

PET: poly(ethylene terephthalate)

PTA: Phosphotungstic acid

PVP: poly(vinyl pyrrolidone)

Rpm: Rotations per minute

RT: Room temperature

SAED: Selected area electron diffraction

SAM: Self assembled monolayer

SERS: Surface enhanced Raman spectroscopy

SPR: Surface plasmon resonance

TEM: Transmission electron microscope/microscopy

TEOS: Tetraethylorthosilicate

TGA: Thermo gravimetric analysis

TLC: Thin layer chromatography

TOAB: Tetraoctylammoniumbromide

UV: Ultra-violet

XPS: X-ray photoelectron spectroscopy

XRD: X-ray diffraction

List of publications:

1. Synthesis of Gold Nanotriangles and Silver Nanoparticles Using *Aloe vera* Plant Extract
Prathap Chandran, S.; Chaudhary, M.; Pasricha, R.; Ahmad, A.; Sastry, M.
Biotechnol. Prog. **2006**, *22*, 577.

2. Synthesis of Gold Nanorods in Organic Media
Prathap Chandran, S.; Pasricha, R.; Bhatta, U. M.; Satyam, P. V.; Sastry, M.
J. Nanosci. Nanotechnol. **2007**, *7*, 2808.

3. Interfacial deposition of Ag on Au seeds leading to Au@Ag core-shell nanoparticles in organic media
Prathap Chandran, S.; Ghatak, J.; Satyam, P. V.; Sastry, M.
J. Colloid Interface Sci. **2007**, *312*, 498.

4. Tunable surface modification of silica nanoparticles through “click” chemistry
Prathap Chandran, S.; Hotha, S.; B. L. V. Prasad.
Curr. Science **2008**, *95*, 1327.

5. Dendritic Effect of Ligand-Coated Nanoparticles: Enhanced Apoptotic Activity of Silica-Berberine Nanoconjugates
Halimani, M.; Prathap Chandran, S.; Kashyap, S.; Jadav, V. M.; Prasad, B. L. V .; Hotha, S.; Maiti, S.
Langmuir (in print) DOI: 10.1021/la802761b.